REVEALING PHYSIOLOGY OF CRANIOFACIAL GROWTH ZONES THROUGH PATHOLOGY

BY

DANIELA MARTA ROTH

A thesis submitted in partial fulfillment of the requirements for the degree of
Doctor of Philosophy
in
Oral Biology

Medical Sciences - Dentistry
University of Alberta

ABSTRACT

This thesis addresses critical gaps in our foundational understanding of craniofacial biology, particularly in elucidating the cellular responses in mechanically loaded craniofacial growth zones. By bridging disparate yet interconnected fields, it aims to provide a comprehensive insight into cell behavior within craniofacial structures. Specifically, this study delves into the dynamics of sutures separating different craniofacial bones, highlighting two understudied sutures: the internasal and mid-palatal sutures.

In the introductory literature reviews comprising Chapters 1 and 2, I explored the significance of mechanistic biological reasoning and its integration into clinical interpretation and treatment. I synthesized evidence of shared biological principles across research disciplines, specifically focusing on their application to cranial sutures. Chapter 1 introduces cranial sutures and explores the biological mechanisms underlying their pathophysiological widening, emphasizing the diversity of modalities leading to a shared clinical outcome. Chapter 2 delves into the current body of knowledge on mechanotransduction, its integration with major signaling pathways, and their synergistic control over cell differentiation within sutures. The methodology used in the primary research chapters is summarized in Chapter 3.

The experimental studies in results Chapters 4 and 5 investigated cellular and molecular responses to the deletion of specific Bone Morphogenetic Protein (Bmp) family members, focusing on *Bmp2* and *Bmp7* and their implications for suture biology. Chapter 4 presents a high-resolution study of the internasal suture deviation in Bmp7 neural crest knockout mice, revealing Bmp7's role in localized osteoblast differentiation signaling and facial symmetry. My follow-up study, detailed in Chapter 5, describes the effects of deleting *Bmp7* or *Bmp2* from *Gli1*+ osteoprogenitor cells. The most prominent

malformation was observed at the cranial base synchondroses, another type of craniofacial growth zone. Comparison with global or neural crest-specific *Bmp2* and *Bmp7* deletions showed distinct morphological and molecular changes affecting embryonic and postnatal cranial base development. These findings underscore the diverse functional roles of Bmp family members beyond ossification, with implications for oromaxillofacial reconstruction and potential off-target effects. Importantly, suture obliteration due to premature ossification was not observed in any of the genetic models utilized in this thesis. This allowed for an examination of osteogenic regulation within a distorted yet intact developmental system using a multiomic approach. Finally, in Chapter 6, I investigated suture establishment in the palate in a wild type model. The study of the mid-palatal suture provided insights into suture patency, forces in morphogenesis, and the establishment of osteogenic structures. This enabled a reciprocal comparison to cranial sutures, revealing significant overlap in pathways, including known craniosynostosis risk genes and hypothesized patency factors.

In the final chapter, this thesis provides a comprehensive discussion of paradigms in suture biology, examining snapshots across the suture's natural lifespan. A key message is that the broad usage of the term 'patency' hinders collective interpretation of the dynamic nature of craniofacial growth zones, including suture morphogenesis, functional growth, and the concept of quiescence. The results in this thesis underscore the importance of further translational studies linking clinical pathology to context-based osteoprogenitor behavior at a foundational level.

PREFACE

This thesis is an original work by Daniela Marta Roth with contributions from collaborators at several institutions outlined below. The research projects, of which this thesis is a part, received animal ethics approval from the University of Alberta Animal Care and Use Committee (ACUC), Animal Use Protocol #1149 (Chapters 4,5) or the National Institute of Child Health and Human Development ACUC, Animal Study Protocol #21-031 (Chapters 4,6).

Some of the chapters in this thesis have been published. Chapter 1 has been published as D.M. Roth, J.O. Piña, M. MacPherson, C. Budden, and D. Graf, "Physiology and Clinical Manifestations of Pathologic Cranial Suture Widening", *The Cleft Palate Craniofacial Journal*. DMR performed the literature search, wrote the text, and created all figures. JOP, MM, CB, and DG revised the manuscript and provided clinical and foundational perspectives on the principles presented. DG was the supervising author. Chapter 2 was published as D.M. Roth, K. Souter, and D. Graf, "Craniofacial sutures: Signaling centres integrating mechanosensation, cell signaling, and cell differentiation" as part of a special issue of the *European Journal of Cell Biology* titled "Cell mechanics and mechanobiology", vol. 101, issue 3. DMR wrote the text, with contributions from KS to the introduction and "The suture as a specialized inter-bone interface", and DG to "Principles of mechanotransduction" and "Conclusions and outlook". All figures were generated by DMR, and DG was the supervising author. Chapter 4, "Regulation of symmetric internasal suture architecture by *Bone Morphogenetic Protein 7*", was conceptualized and written by DMR and DG, with contributions from others. Most experiments were performed, analyzed, and visualized by DMR with assistance from KS and JOP. MVG developed and performed the midfacial suture morphometric pipeline, under the supervision of BH. Sequencing preparation and initial data generation were done by FF and JI at the NICHD Molecular Genomics Core. Transcriptomic analysis was done by DMR. Funding was acquired by RDS and DG. The study described in Chapter 5, "Bmp2 and Bmp7 are independent regulators of bone formation at craniofacial growth zones", was authored by Roth, D.M., Souter, K., Lin, H., Alexiou, M., and Graf, D. The project was conceptualized and written by DMR and DG. DMR performed most experiments, analysis, visualization, and wrote the first draft of the manuscript. KS assisted

with most experiments and was responsible for embryonic micro-computed tomography scanning and analysis, under DMR's supervision. HL prepared samples for sequencing, after which the University of Alberta and the University of British Columbia sequencing cores fulfilled barcoding, library preparation, and sequencing steps. MA assisted with CT scanning for Gli1-CreERT2 samples. DG supervised the project and secured funding.

The research conducted for Chapter 6 of this thesis forms part of an international research collaboration, led by Dr. R.N. D'Souza at the Eunice Kennedy Shriver National Institute of Child Health and Human Development, with Dr. D. Graf being the lead collaborator at the University of Alberta. An updated version of Chapter 6 has been posted in pre-print form to the bioRxiv.org server as Roth, D.M, Piña, J.O.*, Raju, R.*, Iben, J., Faucz, F., Makareva, E., Leikin, S., Graf, D.[§], D'Souza, R.[§], "Mesenchymal Expression of Tendon-Associated Genes Precedes Osteogenesis in Mid-palatal Suture Establishment" (Roth et al., 2024). *These authors contributed equally. [§]Co-corresponding authors. Conceptualization: DMR, JOP, and RDS. Investigation: DMR, JOP, RR, FF, EM. Methodology: DMR, JOP, RR, EM, SL, JI, FF. Data curation: DMR, JI. Visualization: DMR. Writing – original draft: DMR. All authors reviewed the manuscript. Supervision: DG and RDS. Resources: FF, SL, DG, RDS. Funding acquisition: DG, RDS.

DEDICATION

kill the imposter

ACKNOWLEDGEMENTS

None of the work that you read herein would have been possible without the endless font of support I have found in my community. First and foremost, I owe a tremendous debt of gratitude to Dr. Daniel “Necropsy Will Show” Graf – my PhD supervisor. His optimistic, creative, and clever approach to science will continue to inspire my work for years to come. Thank you for always making time for interesting questions. To my supervisory committee, Drs. Anastassia Voronova and Fred Berry: thank you for your guidance on this journey. My world has been shaped in beautiful ways by the many mentors I have been so fortunate to know: Dr. Lakshmi Puttagunta, who taught me to believe my eyes and love histology; Farah Eaton, who kept a whole lab of mad scientists sane; Edmonton’s Marias (Drs. Maria Alexiou and Maria Febbraio), who each helped me feel heard and supported in their own ways; Dr. W. Ted Allison, who introduced me to the EvoDevo puzzle; Dr. Rena D’Souza and her team, who showed me a new world in Bethesda. Your lessons will stay with me as I navigate this exciting and challenging terrain. To my peers in dentistry, development, and bone, far and wide: our conversations and experiments have inspired me more than I’ll ever be able to express. Thank you Shaun, Pranidhi, Jeremie, Resmi, Garett, Emma, and Meng – to name just a few of you. I am also grateful to those who shared their equipment with me throughout these projects: the Voronova lab, the D’Souza lab, the NICHD microscopy core and Dr. Vincent Schram, the Leiken lab and Dr. Ed Mertz, the Centre for Prions and Protein Folding Diseases, Dr. Vardit Kram and the NIDCR, Hilmar and Kiera at the Katz Cell Imaging Core, and the University of Alberta School of Dentistry.

My genetic inclination for science is no small secret, and for that I have several generations of biologists (and biologist-enthusiasts) to thank, as well as my siblings Adam and Gabriela, who had no choice in the matter. Thank you, Stem Champ, for teaching me to rock through the chaos and that loud synth can cure anything. With my whole heart, thank you Sammy. We met when the world was ending, but for us it went on.

Most importantly, to the heroes of my world –
the mice and those who care for them.

The research in this thesis was made possible by funding for the Alberta Dental Association and College Chair in Oral Health Research, the Natural Science and Engineering Research Council of Canada (NSERC) RGPIN-2014–06311, the Women and Children's Health Research Institute (WCHRI) Discovery grants, the Gilbert K. Winter Fund through the Department of Medical Genetics, all to Dr. Daniel Graf. I am grateful to have been supported by a collection of scholarships from the University of Alberta – the Dean's Doctoral Student Award, the Marie Louise Imrie Graduate Student Award, the Alberta Graduate Excellence Scholarship, the Graduate Recruitment Scholarship, and two consecutive Medical Sciences Graduate Program Scholarships. Thank you also to the University of Alberta School of Dentistry for awarding me a Geoffrey & Robin Sperber Fund for Dentistry project grant as co-PI with DG to support the work in Chapter 4, as well as previous Fund for Dentistry grants to DG through the Department of Dentistry.

The work in Chapter 6 constitutes a collaboration between the University of Alberta and the National Institutes of Health in Bethesda, MD and was supported by a Pre-Doctoral Intramural Research Training Award (IRTA) Traineeship (to DMR) and a National Institute of Child Health and Human Development (NICHD) Research Grant to Dr. Rena D'Souza (Identifier ZIA HD009015). I am endlessly grateful to Dr. D'Souza and the National Institute of Child Health and Human Development for the transformative time I spent in Maryland.

TABLE OF CONTENTS

LIST OF TABLES

Page

LIST OF FIGURES

Page

LIST OF COMMON ABBREVIATIONS

Abbreviation	Definition
ACUC	Animal Care and Use Committee
Alk	ALK receptor tyrosine kinase
Alpl	Alkaline phosphatase
Alx	ALX homeobox
Ankrd	Ankyrin repeat domain
AUP	Animal Use Protocol
Axin	Axis inhibition protein
Bglap/Ocn	Osteocalcin
Bmp	Bone morphogenetic protein
Bmpr	Bone morphogenetic protein receptor
BMSC	Bone marrow mesenchymal stromal cell
BSA	Bovine serum albumin
Ca^{2+}	Calcium ion
Cacna1g	Calcium voltage-gated channel subunit alpha1 G
Chodl	Chondrolectin
cko	Conditional knockout (Gli1-CreERT2)
CL/P	Cleft lip with/without cleft palate
Col1a1	Collagen type I alpha 1 chain
Col2	Collagen II
ColX	Collagen X
Cre	Cre recombinase
CTGF	Connective tissue growth factor
Ctrl	Control
Ctsk	Cathepsin K
CXCL	C-X-C motif chemokine ligand
DABCO	Triethylenediamine
DAPI	4',6-diamidino-2-phenylindole
Dcn	Decorin
Dig	Digoxigenin
Dkk1	Dickkopf WNT signaling pathway inhibitor 1
DMEM	Dulbecco's Modified Eagle Medium
Dmp1	Dentin matrix acidic phosphoprotein 1
DNA	Deoxyribonucleic acid
Dsh	Dishevelled
ECM	Extracellular matrix
EDS	Ehlers Danlos syndrome
EDTA	Ethylenediaminetetraacetic acid
Efnb1	Ephrin B1

Eln	Elastin
EMT	Epithelial-mesenchymal transition
ER	Endoplasmic reticulum
ERF	ETS2 repressor factor
ERK	Extracellular signal-regulated kinases
EtOH	Ethanol
FA	Focal adhesion
FAK	Focal adhesion kinase
FBS	Fetal bovine serum
FFPE	Formalin fixed paraffin embedded
Fgf	Fibroblast growth factor
Fgfr	Fibroblast growth factor receptor
Fmod	Fibromodulin
FOXO	Forkhead box O
Fzd	Frizzled
GFP	Green fluorescent protein
GH	Growth hormone
Gli	GLI family zinc finger
GO	Gene Ontology
GPCR	G protein-coupled receptor
GSK	Glycogen synthase kinase
H&E	Hematoxylin and eosin
HDAC	Histone deacetylase
Hh	Hedgehog
HPP	Hypophosphatasia
HRP	Horseradish peroxidase
IF	Immunofluorescence
IFT	Intraflagellar transporter
IGF	Insulin like growth factor
IgG	Immunoglobulin G
Ihh	Indian hedgehog
IL	Interleukin
imm	Immune
ins	Internasal suture
IP	Intraperitoneal
ISH	*In situ* hybridization
ISS	Intersphenoidal synchondrosis
Itm2a	Integral membrane protein 2A
Jnk	Mitogen-activated protein kinase 8
k/o	Global knockout
Krt	Keratin

Lef1	Lymphoid enhancer binding factor 1
LIF	LIF interleukin 6 family cytokine
LINC	Linker of nucleoskeleton and cytoskeleton
LMNA	Lamin A/C
Lrp	LDL receptor related protein
Lum	Lumican
mAb	Monoclonal antibody
MAPK	Mitogen-activated protein kinase
MARPE	Miniscrew-assisted rapid palatal expansion
MES	Midline epithelial seam
MFH	Midface hypoplasia
Mgp	Matrix gla protein
miRNA	MicroRNA
Mkx	Mohawk (aka Iroquois homeobox protein-like 1)
MMP	Matrix metalloproteinase
mRNA	Messenger RNA
MRTF	Myocardin related transcription factor
MSC	Mesenchymal stem/stromal cell
mT/mG	Tandem dimer Tomato (mT)/membrane-targeted green fluorescent protein (mG)
mTOR	Mechanistic target of rapamycin kinase
NCC	Neural crest cell
ncko	Neural crest knockout
NDD	Neurodevelopmental disorder
Opg	Osteoprotegerin
OTM	Orthodontic tooth movement
Pax	Paired-box
PBS	Phosphate-buffered saline
Pcna	Proliferating cell nuclear antigen
PCR	Polymerase chain reaction
PDGF	Platelet derived growth factor
PDGFR	Platelet derived growth factor receptor
PDL	Periodontal ligament
PFA	Paraformaldehyde
PI3K-Akt	Phosphatidynlinositol 3-kinase-protein kinase B
Piezo	Piezo type mechanosensitive ion channel component
Pkd1	Polycystin 1
PLC	Phospholipase C
PNT	Pseudo-neotendon
Postn	Periostin
PRS	Pierre-Robin sequence

PTH	Parathyroid hormone
Ptn	Pleiotropin
RANKL	TNF superfamily member 11
REF	Rat embryonic fibroblasts
rhBMP-2/7	Recombinant Bone morphogenetic protein 2/7
RNA	Ribonucleic acid
Rock/ROCK	Rho associated coiled-coil containing protein kinase
RPM	Revolutions per minute
RTK	Receptor tyrosine kinase
Runx	Runt-related transcription factor
SARME	Surgically-assisted rapid maxillary expansion
scRNA-seq	Single-cell RNA sequencing
Scx	Scleraxis
Sfrp	Secreted frizzled related protein
Six2	SIX homeobox 2
SLC	Solute-carrier
Smad	Mothers against decapentaplegic homolog
snRNA-seq	Single-nucleus RNA sequencing
SOS	Spheno-occipital synchondrosis
Sost	Sclerostin
Sox	SRY-related HMG-box
Sparc	Secreted protein acidic and rich in cysteine (aka Osteonectin)
SSC	Skeletal stem/stromal cell
Svil	Supervillin
Taz	Transcriptional coactivator with PDZ-binding motif
TBST	Tris-buffered saline with Triton
Tcf	T-cell factor
TGF-β	Transforming growth factor beta
Thsd	Thrombospondin
TLC	Tendon-like cells
TMJ	Temperomandibular joint
TNAP	Tissue-nonspecific alkaline phosphatase
TNF	Tumor necrosis factor
Tnn	Tenascin N
TOR	Target of rapamycin
TRAP	Tartrate-resistant acid phosphatase
TRP	Transient receptor potential
Twist1	Twist family BHLH transcription factor 1
UMAP	Uniform manifold approximation and projection
w/v	Weight per volume
Wnt	Wingless-type MMTV integration site family

Yap	Yes1 associated transcriptional regulator
YVS	Yunis-Varón syndrome
µCT	Micro-computed tomography

INTRODUCTION

Craniofacial research is a field which is often split between foundational and clinical disciplines – but also lacks translation from other biological systems, like long bones, early developmental biology, cardiovascular disease, and cancer. These interconnected areas hold significant potential to inform each other. Despite the growing adoption of translational approaches by many research groups, a noticeable gap persists within craniofacial research. This gap becomes apparent when assessing current clinical practices and envisioning future therapeutic innovations. The prospect of transformative discoveries in human health, especially within the craniofacial complex, is substantial when grounded in mechanistic biology. The studies presented in this thesis are designed to encourage future exchange of ideas between experimental systems in the laboratory and practical applications in clinical settings, fostering a bidirectional translational pathway.

0.1 Midfacial growth

Embryonic morphogenesis of the face and skull is a complex, tightly regulated process that involves many axes of growth and remodeling. Moreover, dimensional changes in the craniofacial complex continue far beyond birth. An important phase in postnatal craniofacial growth and maturation is the advancement of the midface until 15 to 17 years of age in humans and about 14 to 30 days of age in mice (Enlow & Hunter, 1966; Maga, 2016; Vora et al., 2016). Insufficient outgrowth of the midface can lead to midface hypoplasia (MFH, which is particularly problematic due to its effects on patency of the airway, association with dental crowding, and aesthetic implications. In severe cases, correction is achieved with distraction osteogenesis with or without surgical intervention such as Le Fort osteotomy. These treatments may be part of the extensive surgical history ahead of children born with pathogenic craniofacial differences and should be minimized in light of the psychosocial and physiological burden accompanying repeat surgeries (Bemmels et al., 2013). There are two main accepted drivers of midfacial growth – expansion of the maxilla and anteroposterior growth of the cranial base. However, a third underacknowledged contributor may be growth at the midfacial sutures, which are numerous in this region (Enlow & Hunter, 1966; M. M. Wang et al., 2022). Furthermore, the growth zones of the skull which contribute to both the etiology of MFH and regeneration following surgery are highly mechanosensitive: they form through precise,

yet incompletely understood, biomechanical patterning and tuning, and are subject to continuously dynamic stresses and strains. This thesis addresses craniofacial growth in each of these three regions: the midfacial sutures, the cranial base, and the maxilla.

Cranial sutures are the physical connections between skull bones, functioning as stem cell niches with significant capacity for integrated bone formation and remodeling responsible for secondary growth of the skull bones. Bone growth occurs through intramembranous appositional growth at the suture sites. The majority of this work focuses on craniofacial sutures as models of the intersection between osteochondroprogenitor differentiation, mechanotransduction, signaling networks, and extracellular matrix composition. The importance of cranial sutures in secondary craniofacial growth is best evidenced by the severe morphological changes resulting from craniosynostosis, which is characterized by premature and hence pathologically ossified sutures and is associated with neurological implications as sequelae. This congenital anomaly has led to sutures being primarily described as synostosed (fused) or patent (open, unfused). Significant advances have been made in suture biology over the last 25 years with the use of animal models of craniosynostosis (Bourgeois et al., 1998; L. Chen et al., 2003; Eswarakumar et al., 2004; Mai et al., 2010; Twigg et al., 2009; Yin et al., 2008; Y.-X. Zhou et al., 2000) and genetic study of human risk factors (Goos et al., 2016; Jabs et al., 1993; Sharma et al., 2013; Wilkie, 1997; Wilkie et al., 2017), though description of their nature and pathology dates back to 17th century B.C. medical papyri (described in Elsberg, 1931). However, the strict distinction between patent and fused sutures does not recognize the different possible states of patent sutures: actively growing, responding to mechanical dysregulation, or quiescent/resting. The presence of numerous sutures in the midfacial region, including the metopic, frontonasal, internasal, nasomaxillary, and frontomaxillary sutures (midfacial sutures labeled in Figure 0.1), suggests that the growth of midfacial structures could be rapidly achieved at these sites. Variation in sutural growth and timing of suture fusion will determine the appearance of the midface, i.e. modulating width and depth.

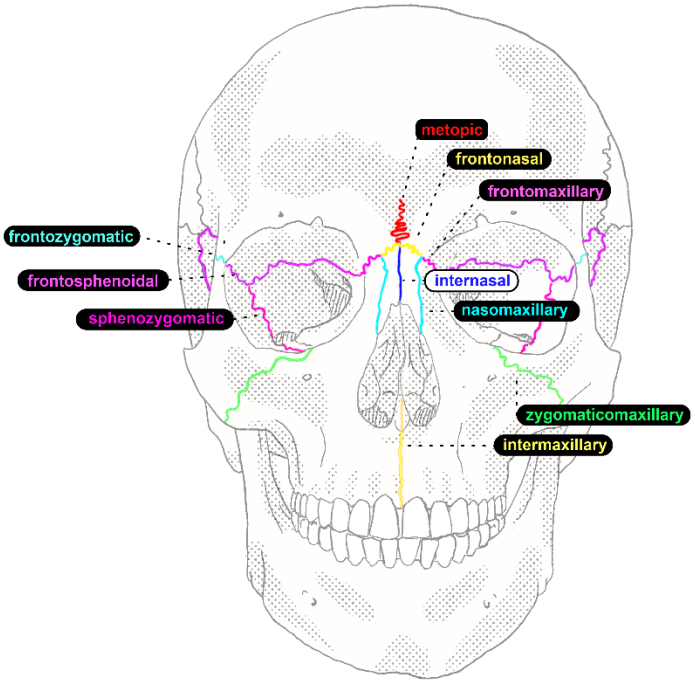

Figure 0.1 Illustration of externally visible midfacial sutures in human skull. Other midfacial sutures can be seen through cross-section or examination of the cranial base. Annotations based on Wang et al., 2022.

In addition to the intramembranous appositional growth that occurs at cranial sutures, midfacial outgrowth is strongly influenced by the growth of the cranial base through the process of endochondral ossification at the cranial base synchondroses (Figure 0.2). Here, bone growth is coordinated through sequential chondrocyte differentiation and subsequent ossification within a bidirectional growth plate. The most mature hypertrophic chondrocytes will either die through apoptosis and be replaced by osteoblasts or will transdifferentiate into osteoblasts (Clarkin & Olsen, 2010; Maes et al., 2010; X. Zhou et al., 2014). Several craniofacial disorders involving premature fusion of these synchondroses result in the manifestation of MFH as well as craniosynostosis (Driessen et al., 2017; Layton et al., 2023; Sorice et al., 2012; Tahiri et al., 2014). It is challenging to separate cause and consequence in these cases, as the same gene regulatory networks are involved in cranial suture patency as well as in cranial base growth.

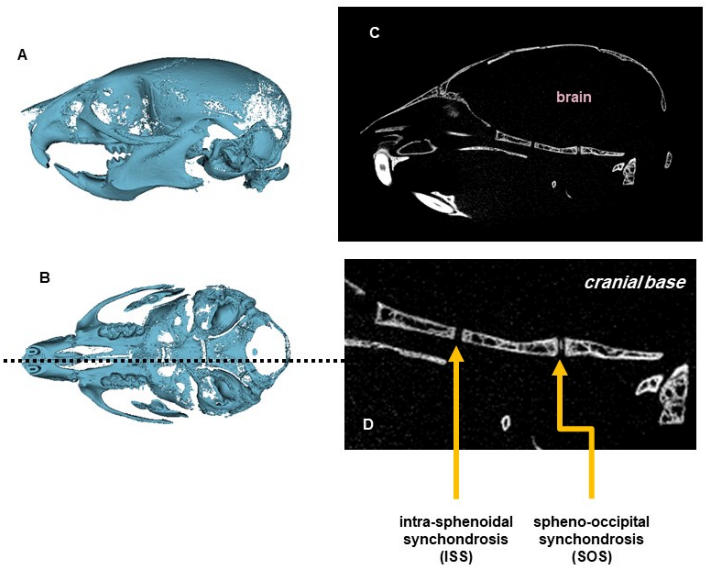

Figure 0.2 Mouse cranial base anatomy.
A) Sagittal view of 3D-rendered micro-computed tomography scan of a 21 day old mouse. B) Inferior view of the scan shown in A). Black dotted line indicates plane of section shown in orthogonal slices through CT scan in C,D). D) Cropped view of cranial base supporting brain in C). The intra- or inter-sphenoidal synchondrosis (ISS) appears as a gap between bones as indicated by the most anterior arrow (left). The spheno-occipital synchondrosis (SOS) is positioned posteriorly.

0.2 Bone Morphogenetic Proteins

Bone Morphogenetic Proteins (BMPs) were first identified in 1965 by M. Urist as a bone-derived factor that could induce ectopic bone formation when injected into rats subcutaneously (Urist, 1965), hence their "bone morphogenetic" moniker (Urist & Strates, 1971). A paradigm shift followed in the 1980/90s upon the discovery of Bmp2/4 and Bmp5/6/7/8 orthologues in *Drosophila* – dpp and gbb respectively (Sekelsky et al., 1995; Wharton et al., 1999). BMPs were found to be highly evolutionarily conserved with notably non-osteogenic roles across invertebrates, like *C. elegans*, and in higher vertebrates, including humans (Newfeld et al., 1999). Of the >30 BMPs that have been identified thus far, seven have been described to initiate bone growth, including Bmp2 and 7 (Sampath & Reddi, 1983, 2020). These two BMPs are considered particularly relevant for osteogenesis due to their approval for clinical use in bone regeneration (Ong et al., 2010). OP-1 (rhBMP-7, Stryker Biotech) was approved by the FDA in 2001 for long bone nonunion application and InFUSE (rhBMP-2, Medtronic Sofamor Danek) was approved in 2002 for spinal fusions. Later, both were approved for further uses and were mainly used for off-label applications – though not without complications (K.-B. Lee et al., 2012; Shields et al., 2006; Vaidya et al., 2008; Zara et al., 2011). The only FDA-approved BMP product in use at the time of writing is rhBMP-2/InFUSE; rhBMP-7/OP-1 was discontinued in 2014 following failure to obtain FDA Premarket Approval in 2009 (Vaccaro et al., 2008),

acquisition of the OP-1 assets by Olympus Biotech Corp. In 2010, and subsequent discontinuation of all Olympus Biotech products in the US by 2014 (Bialy et al., 2017).

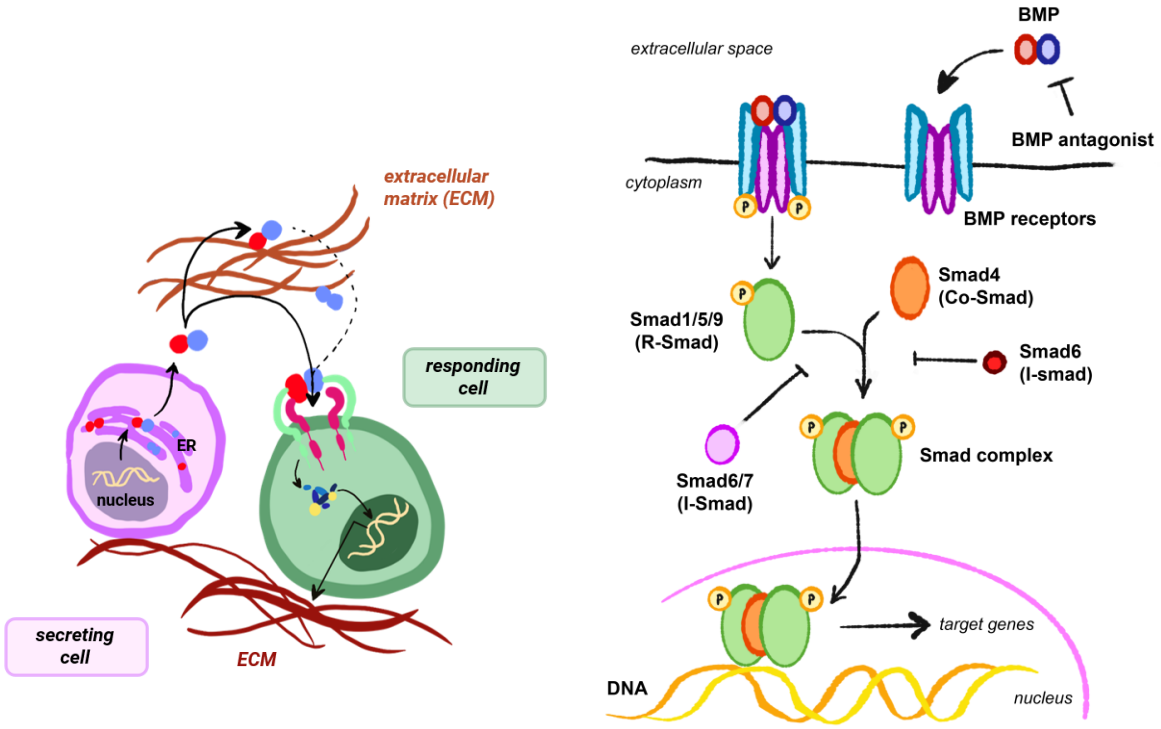

Figure 0.3 Bone Morphogenetic Protein secretion and cellular response.
Left: Summary graphic of the relationship between BMP-secreting cells (purple), the extracellular matrix (ECM), and BMP-responsive cells (green). BMPs are assembled into homo- or hetero-dimers in the endoplasmic reticulum (ER), then secreted by the secreting cell. BMPs may bind to the ECM directly, slow as they pass through dense matrix, and/or bind to the responding cell at the transmembrane receptors. The signaling cascade then may proceed to alter the behavior of the responding cell, which could further change the surrounding ECM. Right: BMP signaling cascade. BMP dimers bind to transmembrane receptor complexes in the cell membrane, unless antagonized in the extracellular space. Once bound, the type II receptors transphosphorylate the type I receptors, beginning a cascade of Smad protein phosphorylation which ends with translocation of the phosphorylated R-Smad/Co-Smad complex to the nucleus where it binds DNA. I-Smads may inhibit this process through several mechanisms.

Belonging to the TGFβ superfamily, BMPs are secreted signaling molecules that canonically exert a transcriptional effect through a cascade of Smad protein phosphorylation events involving receptor-regulatory Smads (R-Smad, Smad1/5/9), co-mediating Smad (Co-Smad, Smad4), and inhibitory Smads (I-Smad, Smad6/7) (Bai et al., 2000; Massagué, 2000) (Figure 0.3). Signaling also occurs through a variety of non-Smad protein phosphorylation events ("non-canonical" BMP signaling). These pathways are not often used as direct readouts for the pathway as they are not BMP-specific. Thus there are

only a few genes that are recognized as “BMP-specific”, including a member of the Inhibitor of Differentiation family (Id1-4) (Hollnagel et al., 1999). A common readout for BMP signaling is the presence of nuclear Smad 1/5/9 phosphorylated at Ser463/465 (Smad1/5) and Ser465/467 (Smad9) (Massagué et al., 2005).

BMPs are synthesized as monomers which dimerize in the endoplasmic reticulum, combining into homo- or heterodimers covalently bound by a disulfide bridge (Gipson et al., 2020). These dimers are then secreted into the extracellular space, where following controlled cleavage of the pro-form they gain the ability to bind to their heterotetrameric BMP receptors. BMPs can bind to two serine/threonine transmembrane receptors, either type I or type II, which have protein kinase activity (Heldin et al., 1997; Koenig et al., 1994; Miyazono et al., 2010; ten Dijke et al., 1994). The seven type I receptors in TGFβ signaling are Alk1-7; Alk2/3/6 have been reported to play overlapping roles in skeletal development and bear the most relevance for BMP signaling (Rigueur et al., 2015; Yi et al., 2000; Yoon et al., 2005). BMPs may bind type I receptors without the presence of type II, but type II receptors are also required for signal transduction due to their transphosphorylation of the type I receptor for intracellular signaling (Ten Dijke et al., 1994; Wrana et al., 1994). There are only three type II receptors for mammalian BMPs: BMPR-II, ActR-II, and ActR-IIB. BMPR-II is reported to be specific for BMP signaling, though the other two receptors are utilized for activin and myostatin signaling as well (S.-J. Lee et al., 2020). It is important to recognize that these receptors are not exclusively used by the BMP signaling pathway.

In addition to the variable signaling activation generated through different combinations of dimer and receptor composition (Feng & Derynck, 2005; P. B. Yu et al., 2005), BMPs are also tightly regulated in the extracellular space by several BMP antagonists (ie Noggin, Gremlin, Chordin, members of the DAN family) and the composition of the extracellular matrix (ECM) itself (Ramirez & Rifkin, 2009). For example, the Bmp7 pro-domain binds to fibrillin microfibrils in the extracellular space (Gregory et al., 2005), conferring spatial restriction as well as latency to this growth factor. Expression of *Bmp7* is induced under mechanical stimulation, indicating a mechanoregulatory role (Santos et al., 2011). The dynamic of secreted growth factor interaction with the matrix is particularly relevant for ECM-rich structures like the fibrous

sutures and cartilaginous cranial base, as this will result in an additional level of local molecular control.

0.3 Biomechanical integration

The study of dysmorphology and the use of genetic models have significantly advanced our understanding of the genetic basis of craniofacial growth and how anomalies occur. However, for some structures, there is still insufficient knowledge of the underlying biophysical processes controlling physiological development. The murine mid-palatal suture is a beautiful example of this process.

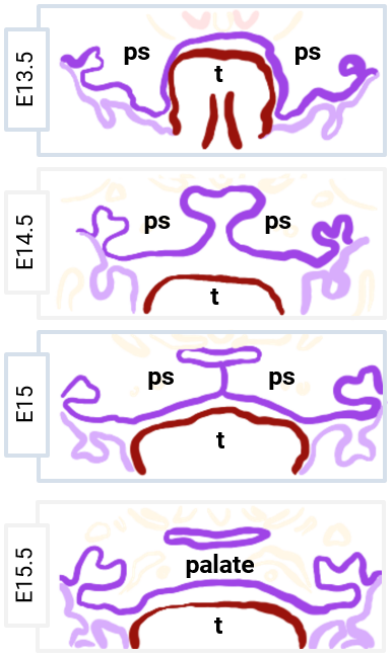

Figure 0.4 Palatal shelf development.
The palate forms from two mesenchymal structures, palatal shelves (ps), which are situated on either side of the tongue (t) by embryonic day 13.5 (E13.5). These shelves elevate to a horizontal orientation above the tongue by E14.5, and contact by E15. The bordering palatal epithelium (dark purple) then breaks down by E15.5, resulting in a continuous mesenchymal palate. Illustration is based on coronal plane of sectioning.

The palatal shelves, which elevate and fuse to form a barrier between the oral and nasal cavities in the embryo, are initially composed of soft mesenchymal tissue lined with epithelium. There is a series of precisely timed developmental events that enables the transition from soft mesenchyme with intervening epithelium to a robust hard bony palate (Figure 0.4). The exact mechanisms guiding the expansion of the osteogenic centers of the maxilla and osteogenic cell differentiation are not yet clear. The behavior of progenitor cells in this region is likely informed by the complex mechanical environment of the developing craniofacial complex, including early suckling *in utero*, expansion of the brain and other osteogenic centers, development of the neurovascular system, and so on (Figure 0.5). Osteochondrogenic progenitor cells are known to be highly sensitive to the stiffness of their surrounding matrix and contact with other cells, influencing their commitment to bone, cartilage, or adipose. Transformative gene regulatory networks including BMP, FGF, Wnt (reviewed in Chapter 2) can be modulated or induced by force and are key to mechanical integration in the craniofacial complex.

There is a definite clinical need for integration of foundational principles of mechanoregulatory elements in osteodifferentiation in dentistry. Orthognathic treatment for maxillary insufficiency, for example, involves physical separation of the maxillary bone with expander devices in an attempt to stimulate osteogenesis to bridge the gap. This technique makes use of the tendency of osteogenic cells to deposit matrix along a surface under tension, returning the bone environment to a more neutral, static state. While distraction osteogenesis and rapid maxillary expansion are largely effective short-term, the expansion may not be maintained over the years to follow, especially in the case of syndromic patients (Gurel et al., 2010; Herring et al., 2024; Scolozzi, 2008). Further understanding of the biological determinants of osteogenic capacity and potentially inhibitory genetic tendencies is necessary to solve this problem.

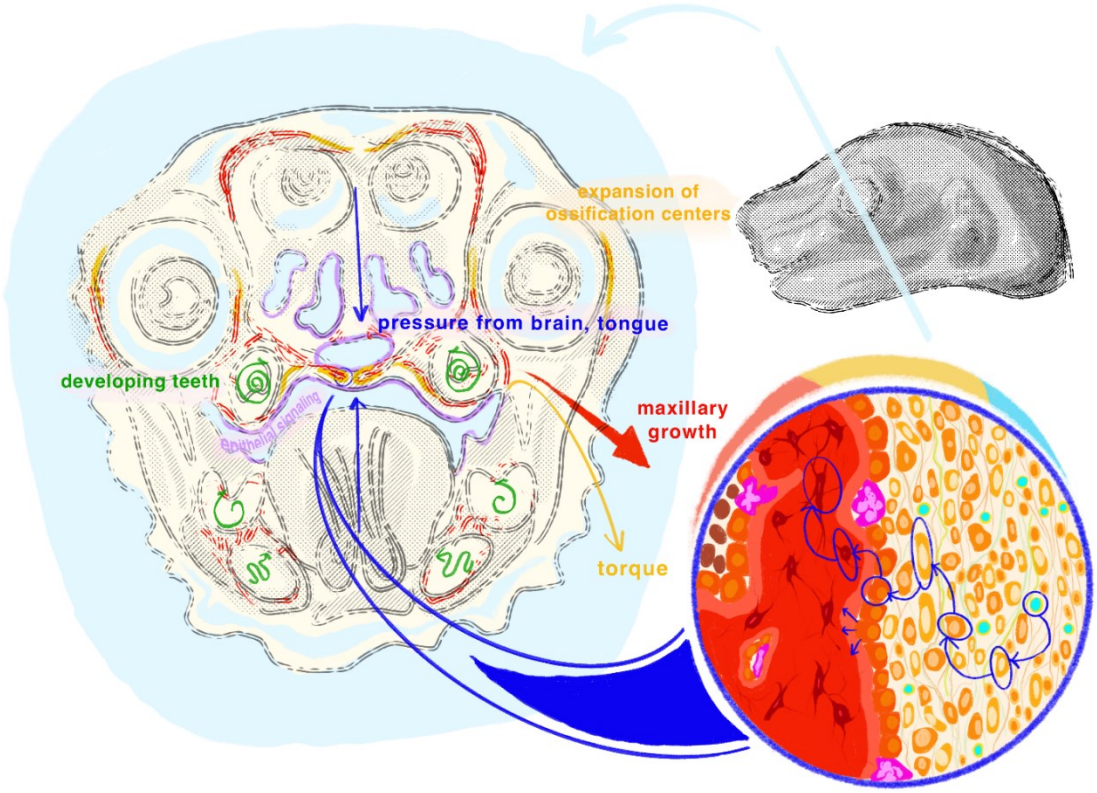

Figure 0.5 Mechanical forces in the developing craniofacial complex and osteogenic differentiation.
The embryonic skull is subject to many diverse mechanical stresses and strains over development. In particular, the palate at embryonic day 17.5 may be influenced by pressure from the expanding brain as neurodevelopment proceeds. Similarly, the tongue is a major contributor of pressure as suckling behavior begins *in utero.* The developing teeth, in green, form through complex epithelial folding and expansion of mesenchymal and epithelial domains. The expanding maxilla and calvarial ossification centers also apply elements of torque, pressure, and strain as the dimensions of the skull change dynamically. The combinatorial effect of these forces likely contributes to the fate and differentiation of cells in the mid-palatal suture mesenchyme (illustrated in the blue circle inlay) as progenitor cells differentiate into osteogenic precursors, osteoblasts, and osteocytes. Furthermore, bone remodeling is accomplished in tandem with osteoclasts, which are recruited in high-loading environments.

0.4 Study design

In the first chapter of this thesis, I conducted a literature review of a less-studied clinical outcome: pathologic cranial suture widening. This study aimed to draw high-level connections between cranial suture physiology from a biology-driven perspective with clinical relevance. I identified that suture physiology was, at that time, incompletely understood beyond the association of genetic variants with craniosynostosis and that further research into the biological underpinnings of broader suture pathology was still required.

Cranial suture physiology, at its core, relies on osteogenesis and bone remodeling, extracellular matrix modulation, cell differentiation and survival, and the ability to transduce physical stimuli into cell function. These principles overlap with physiological functions at many sites in the body, including long bones and the cardiovascular system. Manipulation of these axes of cell biology has been reported in clinical settings, as in orthodontic tooth movement, and *in vitro* models, such as primary osteoblast culture. There were clear gaps in the translation of these shared concepts to craniofacial sutures, which led me to conduct my second literature review (Chapter 2). I aimed to 1) contextualize mechanotransduction in cranial suture physiology, and 2) relate findings from non-calvarial studies to provide further insight into mechanobiology of sutures.

The data chapters in this thesis aim to elucidate determinants of growth in the midfacial sutures, cranial base synchondroses, and maxillary mid-palatal suture through integration of molecular, cellular, and extracellular contributions to secondary growth. The etiology of midface hypoplasia (MFH) and its correlation with calvarial suture malformation, cranial base deficiency, and cleft lip/palate (CL/P) repair is still unknown, necessitating further study of midfacial sutures and craniofacial growth zones (Celie et al.,

2024; Cha et al., 2018; Fariña et al., 2022; Katzen & McCarthy, 2000; Kulczyk et al., 2018; Lowe et al., 2000; Tong et al., 2019). Each chapter explores distinct physiological processes within the midfacial sutures and cranial base in the hope of identifying core developmental paradigms for craniofacial growth. I hypothesized that reciprocal interactions between osteochondrogenic cells and the matrix are at the core of mechanically loaded growth zone function and pathology. To this end, I utilized a combination of wild type mice and several transgenic mouse lines with craniofacial anomalies to address specific questions relating to growth zone physiology in sutures and the cranial base.

Chapter 4 addresses midfacial suture contribution to MFH and provides an example of the consequences of disrupting the fine regulation of osteogenesis. Specifically, it investigates the role of a single Bmp (Bmp7) in the regulation of suture morphology and associated nasal bone growth. The entry-point for this study was previous findings in the lab that deletion of Bmp7 from neural crest cells (Bmp7 ncko) causes MFH in mice (Baddam 2021). My preliminary observations of the irregularity of midfacial sutures and persistence of supernumerary sutural Wormian bones in Bmp7 ncko mice led me to hypothesize that suture malformation contributed to the development of MFH, which I characterized in Chapter 4. I found that loss of *Bmp7* resulted in an asymmetry of the internasal suture that was already detected at birth. Over time, this resulted in an asymmetric and hence dysfunctional suture with suture deviation and asymmetric bone remodeling. These observations are suggestive of an altered mechanical environment.

Chapter 5 asked whether *Bmp2* and *Bmp7* have independent or redundant roles in cranial bone growth. My preliminary data showed that *Bmp2* and *Bmp7* have different expression patterns in sutures over postnatal development of the skull, with the persistence of *Bmp2*-lacZ reporter staining into adulthood (but not *Bmp7*). Neural crest-specific deletion of *Bmp2* is lethal at birth which prevents the study of postnatal growth zone development. To overcome this, I used the Gli1-CreERT2 system to target suture progenitor cells (Zhao et al., 2015) to specifically delete *Bmp2* and *Bmp7* from these sutures. This approach also enabled dissection of complex phenotypes into more discrete elements, such as the influence of internasal suture pathology on nasal bone deviation from that of neighboring structures, like the nasal septum. Deletion of *Bmp2* or *Bmp7* from Gli1+ cells (Bmp2/7 cko) was induced in embryonic (e15.5), early postnatal (P10), and adult (2

month+ old) mice followed by morphometric and histochemical phenotyping of the whole skull. I hypothesized that deletion of either *Bmp2* or *Bmp7* would cause individually distinct but quantifiable phenotypic changes to the cranial sutures, with greater effects of Bmp7 cko in younger mice and Bmp2 cko in older mice. I observed that Bmp2 and Bmp7 cko resulted in differences in suture development and maintenance, with internasal suture deviation in Bmp7 cko adults only, and not Bmp2 cko. Variable phenotypic changes were also observed at the cranial base in both Gli1-CreERT2 mutant lines (which was not observed in Bmp7 ncko mice). Cranial base synchondroses are subject to both extrinsic forces (i.e. brain, spinal cord) and intrinsic forces (bilateral osteochondrodifferentiation from within). This study unequivocally revealed independent roles of Bmp2 and Bmp7 in the cranial base synchondroses, another midfacial growth zone.

Chapter 6 characterizes the establishment of the mid-palatal suture in wild type mice to understand contributors to suture formation and maxillary midfacial growth. After mesenchymal shelf continuity is established by palatal shelf fusion around embryonic day 15.5, two osteogenic fronts emerge medially from the maxillary bone and progress toward the midline, ultimately approximating by day 18.5. In Chapter 6 of this thesis, I employed multimodal transcriptomic techniques to describe the maturation of the midpalate following the fusion of the palatal shelves. The mid-palatal suture had not been described at the same molecular level as cranial sutures, despite their shared mechanoresponsive nature and potential for hypoplasticity. I hypothesized that the mid-palatal suture would share key characteristics with cranial sutures, including cell composition, sequence of formation, and gene regulatory networks. Secondarily, I hypothesized that the midline mesenchyme would bear distinct characteristics compared with the advancing osteogenic front. To this end, I utilized multimodal transcriptomic techniques to build a subcellular profile of early suture formation. In agreement with my hypothesis, I found that the mid-palatal and cranial sutures were composed of comparable cell populations, and the midline mesenchyme of each had distinct transcriptomic features. Additionally, I identified a tendon-like mesenchymal population of cells (pseudo-neotendon, PNT) between the advancing osteogenic front and midline mesenchyme of the mid-palatal suture, which may influence and/or reflect the heterogeneous mechanical environment across the palatal shelf. The PNT and midline mesenchyme were separately enriched for genes encoding

transformative factors like BMPs, Wnts, Fgfs, and Igfs, suggesting that extracellular matrix composition and cell signaling have morphogenic roles in suture establishment. The expression pattern of *Bmp2* suggests that it contributes not only to bone formation, but likely also to the formation of the midline/PNT interface. The hitherto unexplored contribution of tendon-like cells to palatal growth should be investigated further in the context of midface hypoplasia and cranial suture formation.

Together, these data chapters add to the knowledge of the development of anatomical contributors to midfacial growth through the study of the midfacial internasal suture, the cranial base synchondroses, and the maxillary mid-palatal suture. Each chapter illustrates how matrix-producing cells are central to the development and function of craniofacial growth zones (internasal suture osteoprogenitors, synchondrosis chondroprogenitors and chondrocytes, mid-palatal tenocyte-like cells). Regulation of mechanically loaded growth zones is under highly local control, with patterning and symmetry determined within only a few cell layers. These studies bring to light further complexity of growth at suture and synchondrosis sites, which must be considered in clinical settings of surgical intervention or application of exogenous growth factors for bone induction.

CHAPTER 1
PHYSIOLOGY AND CLINICAL MANIFESTATIONS OF PATHOLOGIC CRANIAL SUTURE WIDENING

The majority of clinical translation from suture research is traditionally focused on craniosynostosis, characterized by the premature bony fusion of cranial sutures. In contrast, other suture pathologies – such as widened cranial sutures or incomplete closure of the anterior fontanelle – are not well understood from a foundational perspective. This gap of knowledge formed the basis of this review, which sought to summarize and apply biological principles to features shared by several types of clinical cases. Our approach involved a structured literature search to identify conditions in which widened cranial sutures and/or persistent anterior fontanelle were frequently described. Through this search, we presented four examples to exemplify the different underlying biological drivers between them, with commentary from authors experienced in basic science, medical genetics, and plastic surgery. This review was published in the Cleft Palate Craniofacial Journal, delivering a research-driven translational review to clinicians and translational researchers (Roth et al., 2023)*. The interwoven scientific rationale with clinical examples emphasizes the importance of familiarity with physiology and genetic determinants when approaching suture malformations beyond craniosynostosis. This article was tailored to a broad biomedical audience and thus did not discuss foundational suture biology in great detail beyond the integration of core physiological principles and exemplary studies.*

1.1 Abstract

Cranial sutures are complex structures integrating mechanical forces with osteogenesis which are often affected in craniofacial syndromes. While premature fusion is frequently described, rare pathological widening of cranial sutures is a comparatively understudied phenomenon. This narrative review aims to bring to light the biologically variable underlying causes of widened sutures and persistent fontanelles leading to a common outcome. The authors herein present four syndromes, selected from a literature review, and their identified biological mechanisms in the context of altered suture physiology, exploring the roles of progenitor cell differentiation, extracellular matrix production, mineralization, and bone resorption. This article illustrates the gaps in understanding of complex craniofacial disorders, and the potential for further unification of genetics, cellular

biology, and clinical pillars of health science research to improve treatment outcomes for patients.

1.2 Introduction

Cranial sutures, the fibrous joints connecting skull bones, have been the object of craniofacial study for millennia, with the earliest categorization of their number and arrangement dating back to the Hippocratic era (Dimopoulos et al., 2007). Since these early morphological descriptions, the function of cranial sutures as secondary growth zones of calvaria has been uncovered (Opperman, 2000). The cranial vault is composed of paired frontal, parietal, and temporal bones, and a single posterior occipital bone. These membranous bones, called calvaria, are separated by cranial sutures, which intersect each other at fontanelles.

Critical for expansion of the skull throughout development, sutures represent a complex system in which mechanical forces interface with osteogenesis. Suture patency is mainly governed by stem and progenitor cells residing within the suture, which differentiate along the intramembranous ossification pathway toward bone-forming osteoblasts that line the bone (Fig. 1.1) (Menon et al., 2021). Other factors influence suture development and function, such as signals and cells from the dura mater and periosteum (B. Li et al., 2021). Bone and stem cell biology thus weave into the cranial suture system, and many suture malformations can be traced to abnormalities in key gene regulatory networks and processes.

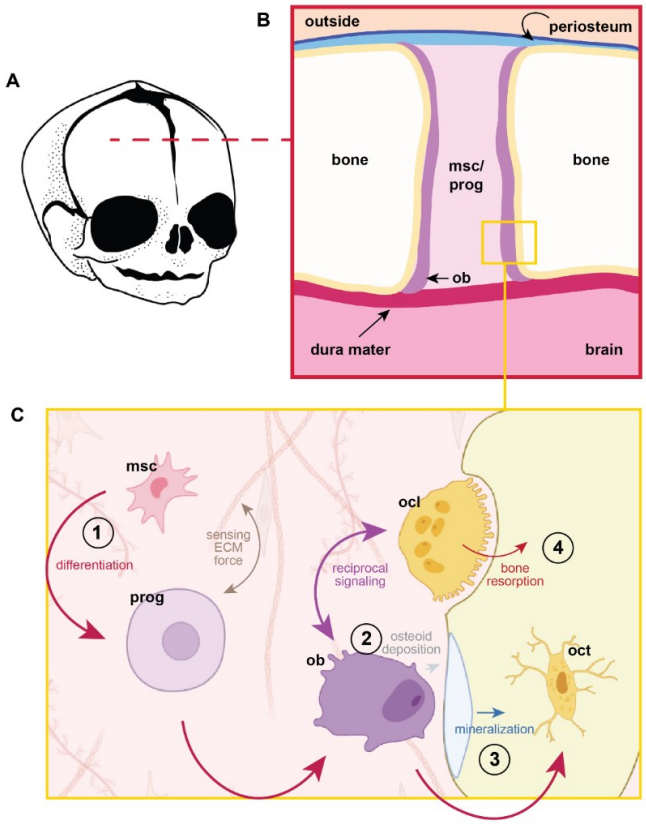

Figure 1.1 Cranial suture milieu.
(A) Diagram of human fetal skull with red dotted line indicating plane of sectioning represented in B. (B) Diagrammatic representation of major components seen in coronal section of an abutting cranial suture. The paired bones are separated from each other by a fibrous joint, the cranial suture (light and dark purple), and from the brain by the dura mater (magenta). The bone surface is covered by the periosteum. The main osteogenic cell types populating the suture space, or mesenchyme, are mesenchymal stem cells and progenitors (msc/prog) and osteoblasts (ob). (C) Diagram of cells found in yellow rectangle in B. Mesenchymal stem cells (msc) differentiate into osteoprogenitors (prog), osteoblasts (ob), and osteocytes (oct) sequentially. The extracellular matrix surrounding these cells includes collagen fibers, proteoglycans, and fibroblasts. Cells in the suture mesenchyme sense and respond to forces from the extracellular matrix. Reciprocal signaling also influences recruitment of bone resorbing osteoclasts and formation of new bone by osteoblasts. Numbers indicate order of processes addressed in this review: 1) Progenitor cell differentiation, 2) Extracellular matrix production, 3) Mineralization, and 4) Bone resorption. Illustration made using BioRender.

The clinical significance of cranial sutures is mainly attributed to abnormalities in their intrinsic growth potential. Normal sutures and fontanelles fuse according to a predictable timeline throughout development; the anterior fontanelle ossifies in children around 10 months of age (Boran et al., 2018; Rice, 2008). Suture-related disorders involve either reduced or overactive bone formation within this niche, with major overall physiological implications. Craniosynostosis, for example, is a result of premature obliteration of the cranial sutures by bone, preventing appropriate expansion of the skull to

accommodate mounting intracranial pressures with brain development. Common outcomes of craniosynostosis are facial and skull deformities and a host of neurological symptoms, such as raised intracranial pressure, seizures, developmental delay, and behavioral effects often accompanied by failure to thrive, though cause and consequence can be difficult to separate in syndromic cases (Fotouhi et al., 2022).[1]

The craniosynostotic skull and its bony sutures have attracted significant study of cranial suture malformation and treatment modalities to return or enhance obliterated suture function (E. Stanton et al., 2022). A comparatively understudied phenomenon is the widening and persistence of the cranial suture space, seen clinically in several rare bone disorders (Table 1.1[2]). This narrative review aims to present exemplary cases of different causes for similarly widened cranial sutures due to defects in progenitor cell differentiation (cleidocranial dysplasia), extracellular matrix production (Yunis-Varón syndrome), mineralization (hypophosphatasia), and bone resorption (pycnodysostosis) selected from recent reports in the literature. These examples highlight the importance of early, precise diagnosis to determine the correct treatment modality, bearing in mind potentially overlapping clinical signs. While sutures and fontanelles are not necessarily the same structure, for simplicity we consider expanded or abnormally persistent fontanelles to be an extension of, or variation on, widened cranial sutures.

Table 1.1 Recent literature describing craniofacial conditions involving widened or persistent cranial suture(s) and/or fontanelle(s).

[1] While elevated intracranial pressure is a primary outcome of suture fusion due to constriction of the developing brain, it should be noted that many causative genes in both craniofacial and neurodevelopmental disorders are shared (eg *SOX6*, *FGFR2, TWIST1*) (Fan et al., 2021; Stevens et al., 2023; Timberlake et al., 2022; Tolchin et al., 2020). Furthermore, neural tissue is known to participate in cross-talk with overlying calvaria through osteokines, nerve- and vascular-derived growth factors, and other cytokines (Opperman et al., 1995, 1996; Tower et al., 2021; Xu et al., 2022). In Foutouhi et al., 2022, the authors reference neurological evidence of damage that may not be alleviated after surgical craniosynostosis correction. Interestingly, experimental cranial suture regeneration following craniosynostosis excision in *Twist1* heterozygous mice returns compromised neurocognitive function (M. Yu et al., 2021). Recent findings characterizing channels connecting the endocranial, ectocranial, and trabecular portions of the bone with underlying tissue (like the brain) suggest a closer physical relationship between the skull and brain than previously appreciated, beyond shared genetic mechanisms alone (Herisson et al., 2018; Mazzitelli et al., 2022).

[2] This table of relevant conditions is not an exhaustive list and only captures a portion of the literature according to the search terms defined in the methodology. Some additional conditions to consider include Weidemann-Rauten Strauch syndrome (biallelic *POLR3A* variants) (Wambach et al., 2018), Craniolenticulosutural dysplasia (inherited *SEC23A* variants) (Cisarova et al., 2022), and Cutis Laxa type IIA (loss of function mutations in *ATP6VOA2*) (Kornak et al., 2008), which all share presentation of widened anterior fontanelles and delayed suture closure. The FGFR-related syndromes also often have widened fontanelles with delayed closure (Goyal et al., 2020; Krakow et al., 2016).

Name of condition	Gene affected	Wide suture(s)	Persistent fontanelle(s)	References
Cleidocranial dysplasia	*RUNX2*	✓	✓	(Farrow et al., 2018; Hordyjewska-Kowalczyk et al., 2019; Jirapinyo et al., 2020; Lotlikar et al., 2018)
Pycnodysostosis	*CTSK*	✓	✓	(Otaify et al., 2018; X. Shi et al., 2017; Thomas et al., 2019)
Mandibuloacral dysplasia	*ZMPSTE24* or *LMNA*	✓		(Haye et al., 2016; Hitzert et al., 2019; Ozer et al., 2016)
Kenny-Caffey syndrome	*FAM111A*	✓	✓	(Cheng et al., 2021; Turner et al., 2020)
KBG syndrome	*ANKRD11*		✓	(Low et al., 2016; Roth, Baddam, et al., 2021)
20p3 microdeletion syndrome	*SOX12* *NRSN2*		✓	(Fang et al., 2019)
De novo partial distal 1q trisomy	*unknown*		✓	(J. Wang et al., 2016)
Hypophosphatasia	*ALPL*	✓	✓	(Di Rocco et al., 2017; Nahabet et al., 2016)
Teebi hypertelorism syndrome	*SPECC1L*	✓	✓	(T. Zhang et al., 2020)
Metopism	*unknown*	✓		(Vinchon, 2019)
Cranium bifidum occultum	*unknown*		✓	(Dossani et al., 2017)
CDAGS syndrome	*unknown*	✓	✓	(Pastrana-Ayala et al., 2017)
Autoimmune thyroiditis	*unknown*		✓	(Marzuillo et al., 2016)
Ehlers-Danlos syndrome	*CHST14*		✓	(Minatogawa et al., 2021)
Dysosteosclerosis	*SLC29A3*		✓	(Uludağ Alkaya et al., 2021)
Caput membranaceum	*ZIC1*	✓	✓	(Sasaki et al., 2020)
Neonatal polycystic kidney disease	*unknown*	✓	✓	(Mchaile et al., 2020)
Neonatal diabetes and hypothyroidism syndrome	*GLI3*		✓	(Dimitri et al., 2016)

1.3 Methods

The disorders discussed in this narrative review were identified through a targeted literature search in PubMed using the following search terms: (((“delayed closure” OR wide* OR dysplasia OR persistent) AND (“cranial suture*” OR “fontanelle”)) AND (patent)) AND ((“2016/01/01"[Date—Publication]: “2022/01/01"[Date—Publication])). 90 results were obtained over the 7-year period. Of those, 28 articles were considered relevant to the topic of this article based on abstract review. These studies were reviews or case reports describing 18 conditions that manifest with widened sutures and/or persistent fontanelles, summarized in Table 1.1. Subsequent un-restricted literature search conducted in PubMed, Web of Science, and Ovid databases targeted pertinent cranial suture descriptions, etiology, and findings from the clinic and experimental systems based on the disorders identified in the preliminary search. The four clinical examples investigated in this review were chosen to illustrate independent biological principles of suture malformation.

1.4 Biologically contextualized clinical examples

Cranial suture development and function are governed by distinct biological processes, including progenitor cell differentiation, extracellular matrix production and maturation, mineralization, and bone remodeling and resorption. The following clinical examples of suture widening are organized by these key processes in suture biology, illustrating that distinct underlying mechanisms can result in convergence of clinical phenotypic presentation.

1.4.1 Progenitor cell differentiation – Cleidocranial Dysplasia

Cleidocranial dysplasia (CCD) is a skeletal dysplasia with a frequency of one in one million individuals worldwide (Machol et al., 2017). Clinically, individuals with CCD present with a triad of delayed closure of the cranial sutures and the anterior fontanelle, hypoplastic or aplastic clavicles, and dental abnormalities. Other features include delayed ossification of the skull, maxillary hypoplasia, moderate short stature, and other skeletal abnormalities. Interestingly, Wormian bones are a common feature in CCD, which have been proposed to stabilize the skull anatomy in cases of delayed suture closure (Barberini et al., 2008).

The bony changes underlying CCD are due to autosomal dominant pathogenic variants of *RUNX2*. RUNX2 is a transcription factor critical for osteoblast progenitor proliferation and differentiation in both intramembranous and endochondral ossification

(Jaruga et al., 2016; Komori, 2019). It is considered a master organizer of bone formation, which through cooperative binding to DNA sequences regulates the transcription of a variety of osteogenic genes (Schroeder et al., 2005). The pathogenic variants identified in patients with CCD are most commonly located in the Runt domain of the gene, which abolishes the transactivation potential of the protein resulting in functional haploinsufficiency (M.-S. Han et al., 2010). As a result, complexes of RUNX2 with other transcriptional co-activators required for cell differentiation cannot efficiently bind to osteogenic target genes, as RUNX2 on its own is a weak transcriptional regulator (T. M. Liu & Lee, 2013).

For patients with CCD, treatment is largely symptomatic as a team of craniofacial specialists is required to address multiple head and neck implications. A primary challenge is dental crowding, which requires orthodontic interventions (Roberts et al., 2013). If expansion of the cranial sutures is severe, a protective device or helmet may be required (Machol et al., 2017). Normally, the anterior fontanelle closes around 10–24 months of age; in CCD, this closure is delayed, sometimes resulting in a persistent anterior fontanelle into adulthood (Boran et al., 2018; Gömleksiz et al., 2014). Some studies warn clinicians to weigh risks and benefits of repair of bone defects in individuals with CCD due to compromised RUNX2 activity (Q. Tu et al., 2007). However, cranioplasty techniques using autologous and alloplastic materials have been successful and non-union in the axial skeleton has been treated with vascularized free fibula grafts (Jung et al., 2015; Shimizu et al., 2021). Older patients are monitored and commonly administered preventative treatment for osteoporosis. Better understanding of how pathogenic variants of *RUNX2* affect osteogenic capacity is required to develop precision treatments and assess their compatibility in the clinic.

1.4.2 Extracellular Matrix Production–Yunis-Varón Syndrome

Yunis-Varón syndrome (YVS) is a multisystem disorder with characteristic persistent, large fontanelles, hypoplastic clavicles, a characteristic facial appearance, digit abnormalities, and brain malformations resulting from an organelle-level (lysosome) disruption leading to abnormal extracellular matrix production (Campeau et al., 2013). Abnormalities of the central nervous system or neurological issues can result in

feeding and respiratory difficulties in infants with this condition (Basel-Vanagaite et al., 2008). In some cases, patients with YVS have life-threatening complications.

YVS is caused by bi-allelic pathogenic variants in *FIG4* or *VAC14* (Lines et al., 2017). *FIG4* encodes for a phosphoinositide phosphatase and its loss compromises formation of PI(3,5)P2 (Cao et al., 2023; Nakajima et al., 2013); *VAC14* encodes an adaptor protein which interacts with FIG4**.** Phosphoinositides are important for vesicle trafficking (Baulac et al., 2014). *Drosophila* Fig4 null animals accumulate enlarged lysosomes in muscle and neural cells. Thus, it is thought that FIG4 is important for lysosomal membrane homeostasis (Bharadwaj et al., 2016). Recent work indicates that VAC14-FIG4 is part of a complex which participates in vesicular organization and PI3K/Akt signaling (Qiu et al., 2021). *Fig4*-null mice have generally normal morphology of hard tissue structures, but greatly reduced bone mineral density with porous bones. This defect has been attributed to extensive vacuolization of osteoblasts due to impaired vesicle transport (Basel-Vanagaite et al., 2008). The vacuolization of osteoblasts likely impairs their ability to form bone*,* though this has not been demonstrated *in vivo*. Lysosomes are also important for osteoclast function, hence the hypothesis of imbalanced bone remodeling due altered physiology of osteoblasts and osteoclasts resulting in impaired production or resorption of extracellular matrix (Lacombe et al., 2013). The need for proper extracellular matrix homeostasis in bone is clear, and dysregulation of this axis will likely impair overall bone physiology. However, as with many animal models of human disease, it is important to note that the *Fig4*-null mouse model recapitulates important aspects of the YVS bone phenotype, but not all clinical features (Lenk & Meisler, 2014).

YVS is an ultra-rare disorder and follows an autosomal recessive inheritance pattern; only about 25 cases have been described since 1980 (Lines et al., 2017)[3]. Most individuals with YVS have a shortened lifespan due to respiratory insufficiency, swallowing, and feeding difficulties. It is difficult to inform future patient management based on such a limited number of clinical descriptions. However, a promising recent study has indicated that chloroquine can correct the enlarged lysosome phenotype in mice, at least temporarily (Lenk & Meisler, 2022). It is currently unknown whether this treatment translates to clinical use.

[3] Reference was incorrectly attributed to Low et al., 2016 in original publication.

1.4.3 Mineralization–Hypophosphatasia

Hypophosphatasia (HPP) is a well-characterised autosomal recessive or autosomal dominant inborn error of metabolism that results in under-mineralized bones and teeth (Root & Levine, 2023). In severe forms of the condition, the bones are weak and soft resulting in skeletal dysplasia and life-threatening complications (M. T. Collins et al., 2022). HPP is caused by loss-of-function pathogenic variants in the *ALPL* gene (Oheim et al., 2022). *ALPL* encodes for tissue non-specific alkaline phosphatase (TNAP), an enzyme that hydrolyzes inorganic pyrophosphate, pyridoxal-5'-phosphate, and phosphoethanolamine (PEA) (J. Liu et al., 2014). Loss of this enzymatic activity leads to elevated levels of these substrates. Inorganic pyrophosphate inhibits mineralization and is produced by chondrocytes and osteoblasts (Foster et al., 2014; Salles, 2015). Characteristics of the condition are low levels of alkaline phosphatase in serum and high plasma and urine levels of PEA (Svejcar & Walther, 1975). The mechanism proposed for HPP involves impaired TNAP function inside bone progenitor cells, involved in mitochondrial respiration and ATP production (Z. Zhang et al., 2021). For this reason, therapeutic replacement of TNAP enzyme does not alter incidence of craniosynostosis despite improvement of skeletal mineralization, motor, and cognitive function (Whyte et al., 2012).

Severe forms of HPP are estimated to occur at a frequency of 1 in 100, 000 (Mornet, 2007). HPP has several phenotypes with varying severity: neonatal, infantile, late, and latent (Hepp et al., 2022). While all forms show evidence of defective mineralization, early infantile hypophosphatasia has the appearance of widened sutures due to large patches of unmineralized skull (Svejcar & Walther, 1975); this neonatal form is lethal and is associated with multiple fractures[4]. In a cohort study of 25 patients by Kozlowski et al., all subjects had widened cranial sutures (Kozlowski et al., 1976). Functional craniosynostosis occurs in these hypomineralized regions, causing a characteristic bulging anterior fontanelle. Precise diagnosis is especially critical in rare bone disorders to guide medical management (Foster et al., 2014). For example, high intracranial pressures in the HPP skull indicate a need for skull expansion, in contrast to frequent cranioplasty in CCD to

[4] The word "of" has been removed from the following sentence for this thesis: "While all forms [of] show evidence of defective mineralization…"

reconstruct skull defects (Jung et al., 2015; Kosnik-Infinger et al., 2015; McGuire et al., 2007). Improper management due to incorrect diagnosis can thus induce significant harm to the patient (Mohn et al., 2011).

1.4.4 Bone Resorption – Pycnodysostosis

Pycnodysostosis is an autosomal recessive skeletal dysplasia with craniofacial and skeletal features including skull deformities, delayed suture closure, osteosclerosis, acro-osteolysis and bone fragility (Appelman-Dijkstra & Papapoulos, 2016). In infants, pycnodysostosis manifests as open fontanelles and sutures, frontal and parietal bossing, and maxillary and mandibular hypoplasia (Hald et al., 2023). Open cranial sutures have also been observed to persist into adulthood (Kundu et al., 2004; X. Shi et al., 2017). Osteosclerosis - abnormal hardening of the bone - advances with growth in pediatric patients and bears increased risk of fracture due to the bone's brittle nature (Romans et al., 2020). With approximately 200 patients described in the literature, this rare disorder has a predicted prevalence of about 1.7 cases per million and can necessitate surgical management of craniofacial hypoplasia (LeBlanc & Savarirayan, 2020).

Individuals with pycnodysostosis have higher bone mineral density due to loss-of-function pathogenic variants in the *CTSK* gene, which encodes for Cathepsin K. Cathepsin K is a collagenase required for osteoclastic bone resorption (Mijanović et al., 2022). It is synthesized as a pro-enzyme and is activated by lysosomal cleavage (Sait et al., 2021). Quantitative computed tomography (CT) evaluation of bone mineral density in patients with pycnodysostosis shows increased bone volume, which can be explained by the impaired ability of osteoclasts to break down type I collagen matrix (Ferlias et al., 2021). The high susceptibility to fractures may also be due to reduced bone remodeling. However, osteomalacia can also be observed in patients with *CTSK* variants, suggesting an additional role in bone mineralization (Schilling et al., 2007). Cathepsin K in osteocytes is likely to play an important role in the suture biology underlying pycnodysostosis and has been hypothesized to be central in mechanosensation and communication with osteoblasts to activate osteogenesis (Dai et al., 2020; L. Qin et al., 2020). The loss of Cathepsin K could influence bone formation and remodeling on several levels, beyond what is discussed in the literature.

1.5 Discussion

This literature review presents examples of clinical widening of cranial sutures and fontanelles contextualized within key elements of suture biology, illustrating the variety of causes for similar suture malformations. Cranial sutures exemplify a dynamic continuum between bone formation and resorption. Disruption of the genetic drivers of cell differentiation, extracellular matrix production, mineralization, bone resorption, or any combination can manifest as dramatic craniofacial changes (Roth, Souter, et al., 2022). Suture malformations demonstrate how specific cellular changes can lead to major physiological consequences.

It is unsurprising that the outcome of widened sutures or a persistent fontanelle can arise in multiple ways, given the range of factors governing normal suture development and function, as well as bone formation as a whole. A 1992 case study of an 11-month-old boy with undiagnosed hypophosphatasia further underscores the concept of careful differential diagnosis. The patient was given a presumptive diagnosis of rickets, due to his widened fontanelle, and was treated with high doses of calcium and vitamin D supplementation as a result. However, eventual lab testing revealed reduced ALP levels, hypercalcemia, hypercalciuria, low parathyroid hormone (PTH), and normal levels of vitamin D, which were suggestive of HPP instead of the previously diagnosed rickets (Mohn et al., 2011). While both rickets and HPP are disorders of bone mineralization, in this case severe clinical complications resulted from indiscriminate treatment.

It is critical to consider the molecular mechanisms underpinning a disorder. Some treatments may not be effective due to mutations in critical pathways. How do the genetic changes underlying the suture malformation interact with the selected treatment modality? This is a crucial element of precision therapeutics, in which clinicians' evolving ability to ascertain genetic or physiological characteristics of patients can streamline treatment of complex conditions. For example, stimulation of bone formation with a growth factor is dependent on the osteoblast's ability to respond to the factor (Maciel et al., 2023). Disruption of a critical process like cellular metabolism, as in HPP, impacts other structures in addition to the suture phenotypes described herein (Langeveld & Hollak, 2018). An understanding of underlying bone biology, including gene regulatory networks facilitating normal development, can benefit clinical treatment of rare bone disorders,

furthering the field of personalized medicine by carefully considering treatment modality and mechanism in the context of the disordered system. This attention to biological detail can help clinicians to identify the most effective treatments, avoiding those that could cause inadvertent harm.

Study of conditions in which there are abnormal suture outcomes has furthered our understanding of the molecular biology of normal suture development; this is the basis of animal modeling of craniofacial anomalies. In addition to its direct benefit to patients, the study of rare disease biology can also help inform treatments for more common conditions (E. Stanton et al., 2022). Thus, there is value in studying rare conditions such as those presented in this review. Indeed, the literature describes several bone disorders presenting with widened cranial sutures with undetermined mechanisms (Chaisrisawadisuk et al., 2021; Chirathivat & Post, 1980; Lucas-Herald et al., 2019; Nelke et al., 2014; Pascual-Castroviejo et al., 1975; Pochedly et al., 1974). In addition to the direct effects of gene disruption on osteogenesis or mineralization, ubiquitous facets of cell biology such as epigenetics or mechanotransduction also influence the phenotype (Alamer et al., 2021; Di Pietro et al., 2021). An example is Craniostenosis, Deafness, Anal abnormalities, and Genitourinary malformations with Skin rash (CDAGS) syndrome, in which disruption of nuclear RNA and intron splicing due to a rare biallelic variant in the RNU12 gene causes a suite of multi-system malformations, including delayed closure of cranial sutures (Xing et al., 2021). While the underlying spliceosomopathy has been identified, the downstream effect of minor spliceosome alteration on bone formation leading to delays in CDAGS syndrome is still unknown. The mechanism by which metopism, a persistent metopic suture, occurs is similarly unclear. Genetic underpinnings are the most likely explanation, especially in the context of evolution (Holloway et al., 2014; Zdilla et al., 2018).

Biology is rarely linear, and these disorders are likely the result of compounding effects of the gene variant or variants on several interacting gene regulatory networks or biological processes. Hence, the identification of the gene affected by pathogenic variation may not be sufficient to fully understand the underpinnings of disordered bone.

The four cases presented in this narrative review illustrate concepts of progenitor cell differentiation, bone mineralization and resorption, and extracellular matrix production; however, these processes do not exist in isolation. The interconnected nature

of bone biology dictates additional axes of involvement in craniofacial suture widening. Cleidocranial dysplasia is directly connected to *RUNX2* pathogenic variants clinically, but little exploration of the interplay of abnormal *RUNX2* with other processes and gene regulatory networks is evidenced in the clinical literature. In contrast, foundational research on *Runx2* and understanding of this master bone regulatory gene in non-clinical contexts is vast (Karsenty, 2008). Epigenetic regulation of *Runx2* through transcriptional silencing, poising cells for expression, and induction of osteoblast differentiation is intricately connected at many levels, which should be considered in the context of the processes and disorders discussed in this review (Montecino et al., 2021). Other overarching processes governing cell-cell interaction and response to the environment, such as mechanotransduction or lineage commitment, may influence the phenotype or severity of the effects of pathogenic variants (Al-Rekabi et al., 2017). Nevertheless, it is clear from *in vitro* studies replicating the *in vivo* suture microenvironment that countless unidentified factors and forces influence bone differentiation (Pereira et al., 2021; Yuste et al., 2021).

When a clinician is presented with a patient with widened sutures or fontanelles with delayed closure, it warrants a thorough pediatrics assessment. The mean age of closure for the anterior fontanelle is approximately 14 months of age. By 2 years of age the anterior fontanelle is closed in 96% of children (Kiesler & Ricer, 2003). Non-genetic causes of a large fontanelle include hydrocephalus, hypothyroidism, and rickets. It is important not to miss these treatable conditions. If these conditions have been ruled out and the fontanelle is open after 2 years of age, consideration should be given to an evaluation by a medical geneticist. Red flags that warrant medical genetics consultation, including early referral, are dysmorphic features, developmental delay, congenital anomalies, or additional skeletal anomalies such as unusual body proportions. Genetic testing may involve chromosomal microarray, single gene testing, gene panel testing or exome sequencing depending on the findings of the assessment. The results of genetic testing not only aid the diagnosis of rare diseases but also help inform recurrence risks for future pregnancies. The challenge with rare genetic disease is that there are very few cases and there are rarely established medical management guidelines. Frequently, the natural history of these conditions is not well established. Treatment and surveillance are typically tailored to the individual patient. We highlighted several conditions in this narrative review. The only condition we reviewed for

which a targeted therapeutic intervention exists is hypophosphatasia. The therapeutic intervention consists of an enzyme replacement therapy for the infantile and juvenile types, which should be initiated early for best outcomes[5]. Cleidocranial dysostosis, Yunis-Varón syndrome, and pycnodysostosis do not currently have medical management guidelines. While the enlarged fontanelle may eventually close over time in these conditions, there are individuals with cleidocranial dysostosis whose fontanelle remains open throughout life. Individuals with these conditions are managed in a multidisciplinary team with a considered approach to surgical intervention when appropriate. Identification and proactive consideration of underpinning genetic mechanisms should inform these personalized, interdisciplinary treatment plans whenever possible.

The future of bench-to-bedside translation of knowledge and clinical intervention options for patients affected by cranial dysmorphology is teeming with potential. The combination of foundational principles observed and capitulated in pre-clinical animal models with known clinical phenotypes and outcomes from affected patient populations will ignite novel avenues of diagnostic and therapeutic exploration. Drawing from recent successes in preclinical animal models of craniosynostosis, similar efforts may be possible to drive homeostatic maintenance of cranial sutures which fail to grow properly (M. Yu et al., 2021). Future pathophysiological studies will provide a better understanding of suture maintenance, stem cell biology, and osteogenic differentiation cues in the context of pathologically widened cranial sutures. Importantly, the convergence of clinical, basic science, and medical engineering experts is crucial to the development of disease mechanism-based therapeutics to help translate improved treatment to patients with cranial suture pathologies.

1.6 Conclusions

Widening of cranial sutures is a rare craniofacial outcome revealing what is not yet known about the causes and implications of cranial suture malformation. The spectrum of craniofacial disorders involving widened sutures described here is caused by pathogenic variants in genes required for the cellular processes governing suture formation and function. Each of the cases presented in this review shares a common feature: widened

[5] This sentence was corrected for grammar from the original publication: "…[we] should be initiated early for best outcomes." now reads "…[which] should be initiated early for best outcomes.".

cranial sutures, or a persistent anterior fontanelle. However, each pathology arises from a different underlying biological perturbation. Whereas distinctions between causes of suture widening are difficult to make clinically, a wholistic view of the disorder and potential biologically relevant causes is required for effective personalized treatment plans for individual patients. Importantly, widened cranial sutures or persistent fontanelles are not simply the inverse of craniosynostosis. This paradigm emphasizes consideration of the underlying biology as patient-specific interventions evolve. This narrative review has illustrated significant gaps in understanding of complex craniofacial disorders in the context of pathologically widened cranial sutures, highlighting avenues for exciting future work to unite foundational biology with clinical practice.

CHAPTER 2

CRANIOFACIAL SUTURES: SIGNALING CENTRES INTEGRATING MECHANOSENSATION, CELL SIGNALING, AND CELL DIFFERENTIATION

While the mechanoresponsive nature of craniofacial sutures has been demonstrated experimentally, this concept is not fully understood nor commonly integrated into functional suture studies. However, principles of mechanotransduction have been studied across several physiological systems using a multitude of experimental models. This gap in knowledge necessitated the synthesis of principles from diverse physiological systems' mechanotransduction studies. Our approach in this narrative review dissected suture fundamental concepts of suture biology, providing a comprehensive commentary on related literature spanning the craniofacial complex and beyond. By summarizing the impacts of varied mechanical loading across systems, we connected overarching principles to suture biology fundamentals. This review expanded the sometimes narrow scope of suture biology by emphasizing translation from diverse bone-related and non-osteogenic systems. Our discussion underscored the importance of contextual understanding when delving into the complexities of suture biology, paving the way for broader perspectives and innovative insights in this field.

2.1 Abstract

Cranial sutures are dynamic structures in which stem cell biology, bone formation, and mechanical forces interface, influencing the shape of the skull throughout development and beyond. Over the past decade, there has been significant progress in understanding mesenchymal stromal cell (MSC) differentiation in the context of suture development and genetic control of suture pathologies, such as craniosynostosis. More recently, the mechanosensory function of sutures and the influence of mechanical signals on craniofacial development have come to the forefront. There is currently a gap in understanding of how mechanical signals integrate with MSC differentiation and ossification to ensure appropriate bone development and mediate postnatal growth surrounding sutures. In this review, we discuss the role of mechanosensation in the context of cranial sutures, and how mechanical stimuli are converted to biochemical signals influencing bone growth, suture patency, and fusion through mediation of cell differentiation. We integrate key knowledge from other paradigms where mechanosensation forms a critical component, such as bone

remodeling and orthodontic tooth movement. The current state of the field regarding genetic, cellular, and physiological mechanisms of mechanotransduction will be contextualized within suture biology.

2.2 Introduction

Cranial sutures are a fascinating model system demonstrating cellular integration of mechanical forces with physiology. These fibrous joints between skull bones are more than just a physical connection; sutures are also a highly plastic mesenchymal stem cell niche. While a suture is patent, or un-fused, its cells lay down new bone to accommodate needs for craniofacial growth or remodel to increase suture interdigitation in response to stresses or strains. Over their lifetime, sutures can remain patent or fuse through replacement of the fibrous material with bone.

Initial interest in sutures was driven by a clinical need to understand premature suture fusion in cases of craniosynostosis, which can lead to life-threatening conditions in affected children. Sutures are considered viscoelastic structures that are exposed to three overall types of strain: impact loading, cyclic loading, and quasi-static strain (Herring, 2008; Herring & Teng, 2000)[6]. Instances of adaptive refinement of sutures in response to micromechanical forces via remodeling processes have been well-documented, with original publications as early as 1957 describing changes to suture interdigitation with manipulation (Moss, 1957). It is now known that suture interdigitation, which is prominent in the palatal sutures and the frontonasal suture, enhances shock absorptive capacity via increase in collagen surface area to dissipate strain (Byron et al., 2004; Jaslow & Biewener, 1995; Rafferty & Herring, 1999). Tension leads to wider sutures with thinner, more elongated bones, with the opposite occurring with compression (Herring, 2008). Fetal constraint of the skull or postnatal force restricting growth of the craniofacial complex leads to craniosynostosis (Jacob et al., 2007; Oppenheimer et al., 2009). In this context, it is important to consider Wolff's law, which states that function dictates form (Wolff, 1986, translation of the original text from 1886). The morphology of cranial sutures and the surrounding bones are molded by cues from their mechanical environment. Analysis of the

[6] It should be noted that these three types of strain are not necessarily active in all sutures. Different regions of the skull experience greater magnitudes or frequencies of mechanical loading. For example, the facial sutures are more directly subjected to cyclical loading from mastication than the calvarial sutures.

effects of forces on sutures in vivo demonstrates that bone formation and the suture signaling milieu are influenced by tensile forces (Herring, 2008). It was previously assumed that force-induced bone growth is the result of osteodifferentiation of suture resident progenitors. Recent direct evidence for this has now been provided by lineage-tracing suture progenitor cells in the context of external mechanical force application (Huang et al., 2021; Jing et al., 2022). Taken together, these observations establish the mechanotransducive capacity of cranial sutures, and may lead one to pose the questions: how do suture cells detect changes in strain, which cells respond to changes in strain, and how are cell biological responses regulated to allow subsequent morphological change?

The traditional understanding of sutures as flexible, fibrous joints is complicated by the presence of stem cells required for bone growth at sutures through the process of intramembranous bone formation (Opperman, 2000). Cellular or genetic changes that interfere with the ordered process of cellular differentiation typically result in premature suture fusion, a relatively prevalent condition. Thus, sutures are an elegant system to study the effects of mechanotransduction on cell biology and genetics in the context of progenitor cell differentiation, both in vivo and in vitro.

Clinical suture studies often focus on identification of major genetic or physiological differences between patent and synostosed sutures, as craniosynostosis occurs spontaneously through de novo mutations in about 85% of patients (Timberlake & Persing, 2018). But what differentiates a patent, mechano-responsive suture from a functionally compromised suture that does not fuse prematurely, but cannot respond to ossification cues (Fig. 2.1A)? The answers to these subtleties may lie in the integration of multidimensional influences such as strain and gene regulatory network signaling on cell differentiation.

This review aims to explore the mechanisms enabling mechanosensation of individual cells within sutures and their interactions. We will present the current body of knowledge surrounding mechanotransduction, how this integrates with major signaling pathways, and how together they form a synergistic system that controls cell differentiation within sutures.

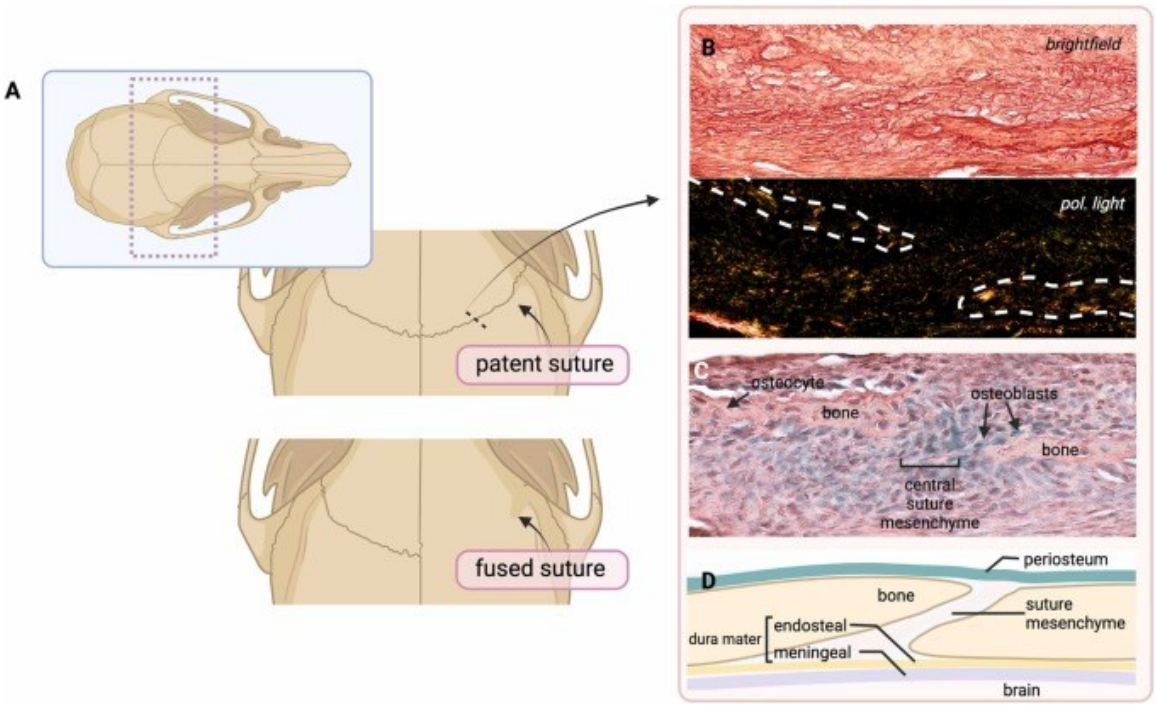

Figure 2.1 Cranial suture patency.
(A) Illustration depicting partial craniosynostosis of the mouse coronal suture. (B) Picrosirius red stain of 1-week-old mouse coronal suture under brightfield light (top) and polarized light (bottom), demonstrating dense cellularity and intricate collagen fibril organization between cranial bones with connections into the suture midline. (C) General cell populations composing sutures can be distinguished with histological techniques. Orcein histological stain with methylene counterstain of 1-month old mouse coronal suture. The central suture mesenchyme, a mix of fibroblasts, mesenchymal stromal cells, and progenitors, is flanked on either side by a single-cell layer of osteoblasts lining the adjacent bones. Within the bones, osteocytes and their lacunocanaliculi are seen.

2.3 The suture as a specialized inter-bone interface

The precise cellular and molecular events required for the establishment of a suture remain unclear. When osteogenic fronts of growing bones meet, they can either fuse, as in the case of the pterygoid processes of the sphenoid bone, or they develop a fibrous suture between opposing bones (e.g. sagittal suture separating parietal bones) (Fig. 2.1B). Cells within the suture have a characteristic hierarchical arrangement with respect to the various differentiation stages of intramembranous bone formation. Immature progenitor cells are typically found in the center of a suture, with more differentiated cells contributing to the formation of new bone lining the outer edges of the suture (Fig. 2.1C, 2.2). Cells within the suture are supported by the surrounding periosteum and the underlying dura (Fig. 2.1D). A detailed single-cell atlas identifying the various cell populations found in the coronal suture was recently reported (Farmer et al., 2021).

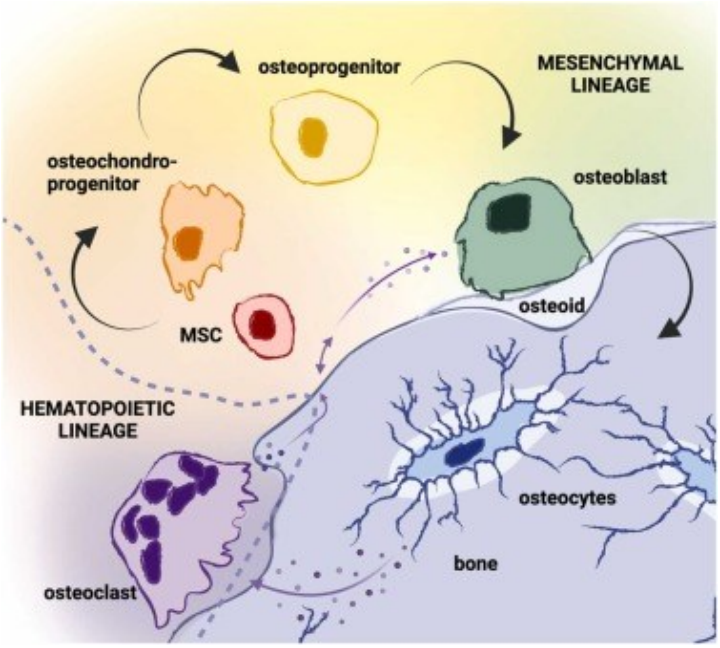

Figure 2.2 Osteodifferentiation pathway in sutures.
Graphic representation of progressive differentiation of mesenchymal stromal cells (MSCs) to osteocytes. Resident MSCs in the cranial suture mesenchyme differentiate into osteochondroprogenitor cells, osteoprogenitor cells, and osteoid-depositing osteoblasts. Terminally differentiated osteocytes, responsible for initiating osteoclast maturation, reside within the mineralized matrix in lacunocanaliculi. Mature osteoclasts, arising from the hematopoietic cell lineage, remodel bone surfaces. Reciprocal communication by secreted factors also occurs between osteoclasts and osteoblasts, mediating a balance between bone formation and resorption. Direction of differentiation is indicated with black arrows between cell types; purple arrows represent reciprocal signaling with osteoclasts, which lie outside of the mesenchymal cell lineage.

The bones on either side of the coronal suture are of different embryonic origin: mesoderm-derived parietal bone and neural crest-derived frontal bone (X. Jiang et al., 2002; Yoshida et al., 2008). Each bone domain expands from within its primordium between the dermal and meningeal mesenchymal layers establishing a sutural space for continued growth. Inability to maintain this boundary in *Twist1*+/- mice is associated with craniosynostosis (Merrill et al., 2006). In Fuz mutant embryos, these boundaries fail to develop and lead to the development of a single cranial bone pair that encases the forebrain (Tabler et al., 2013, 2016; Yannakoudakis & Liu, 2013). Premature suture fusion engages the same cellular processes as physiological fusion, at least in the case of the *Twist*+/- mouse (Behr et al., 2011).

Patent cranial sutures maintain a niche for mesenchymal stromal cells (MSCs), a cell population with stem cell characteristics (Ambrosi et al., 2019; Zhao et al., 2015). Gli1 and Axin2 have been used to identify these MSCs (Maruyama et al., 2016; Zhao et al.,

2015). Axin2, a downstream mediator of Wnt signaling, marks slow cycling cells in the suture midline (Maruyama et al., 2016). Gli1, a downstream marker of Hh signaling, identifies progenitor cells with high proliferative potential (Zhao et al., 2015). Axin2+ MSCs have been used to address the question of what maintains suture patency. A decrease and/or imbalance in this cell population appears to underlie craniosynostosis (Menon et al., 2021).[7]

Surgical separation of prematurely fused cranial bones carries significant risk of re-synostosis, indicating a failure to re-establish a functional suture space (E. Stanton et al., 2022). However, implantation of Gli1+ MSCs into a surgically excised synostosed suture in Twist1+/- mice allowed successful suture re-establishment (M. Yu et al., 2021). Regeneration of the MSC niche required physical contact with the underlying dura (M. Yu et al., 2021). The crosstalk between suture-derived osteoprogenitor cells and the dura appeared to be bi-directional. It was required both for maturation of cerebral veins in the dura as well as maintenance of stem cells within the suture space, which is supported by previous literature relating loss of signaling between the suture and dura with cerebral vein malformation (Tischfield et al., 2017). Interestingly, when Gli1+ MSCs were lineage traced within the re-established suture, it was found that they were derived both from the transplanted MSC as well as from the underlying dura (M. Yu et al., 2021). The detailed relationship between Gli1+ and Axin2+ cells and defined stem and progenitor cell subsets, and their roles in this specialized interface, has yet to be established.

2.4 The suture as a mechano-sensitive structure[8]

The requirements to form and maintain a functional suture are well-studied. However, the intersection of mechanical forces with mechanotransducive abilities of individual cells within a suture is less clear.

The forces experienced by sutures are often considered from an engineering perspective, defined as strain – a parameter that is distinct from unmeasurable stress (Z. Q.

[7] Precise balance of osteogenesis is a requirement for suture patency and craniofacial bone ontogeny. The studies described in this section illustrate two variations on this concept. On one hand, boundaries must be established and maintained, which is disrupted in *Twist1* knockdown mice. It is also critical that differentiation of osteoprogenitor cells is controlled to enable bone formation at the appropriate times and locations, evidenced by *Axin2* and *Gli1* interventions affecting mesenchymal progenitor cells. Current understanding of the contribution of cells from different embryonic origin (e.g. neural crest cell-derived vs. mesodermal) is still evolving (Doro et al., 2024).

[8] This section heading was published as “The suture as mechano-sensitive structure”.

Zhang & Yang, 2015). A major force exerted on sutures is from the growing brain, which increases intracranial pressure. External pressure from birth, compression, and traumatic impact also occurs as well as normal physiological processes like mastication. During mastication, different sutures can experience tensile or compressive strains, or both (Rafferty & Herring, 1999). Cranial sutures have an important role in absorbing these forces and lending the skull flexibility (B. Li et al., 2021). Mechanotransduction is known to regulate many cellular processes including cell proliferation, lineage commitment, differentiation, and death (F.-X. Yu & Guan, 2013). Clinical practice of bone healing and regeneration has established the critical importance of an appropriate mechanical environment, such as rigid fixation. Skeletal tissue growth and differentiation has been proposed to similarly depend on the type of stress and strain, notably exemplified in distraction osteogenesis (Carter et al., 1998). Accordingly, in the context of sutures, the sites of bone formation are predicted to experience low to moderate tensile strain, whereas the fibrous elements would be expected to experience moderate to high strain (Carter et al., 1998). Thus, mechanical stimulation is expected to directly influence the differentiation of the various skeletal stem and progenitor cells. Regulation of osteogenic fate over adipogenesis or chondrogenesis from tripotent MSCs is well documented, however the mechanism underlying control of differentiation into the appropriate cell lineage in the context of high stress environments like sutures is an emerging topic (Kelly & Jacobs, 2010; J. Li et al., 2015; Sen et al., 2008; Y. Sun et al., 2022).

Each cell component along the intramembranous bone formation pathway bears the ability to sense mechanical force. The interplay between the forces experienced by the sutures of the craniofacial complex, resting tension forces, and subcellular force generation likely play a more significant role in suture biology than is recognized (Romani et al., 2021).

Osteocytes found in mature bone are regarded as the bone's "mechanosensors". They coordinate bone remodeling in response to mechanical loading through an interlocking network of fluid-filled lacuno-canaliculi. The canalicular fluid within enables transport of chemical messengers, oxygen, and nutrients, concentrating the physical transduction of force (L. Qin et al., 2020). Osteoblasts are the actual bone-forming cells that deposit osteoid, which in turn mineralizes to form bone. When comparing proteomes

from patent and synostosed sutures, the majority of differentially expressed proteins belonged to osteoblasts (Bala et al., 2021). The effect of mechanical stimulation of osteoblast cell lines has been established in numerous studies (Aryaei & Jayasuriya, 2015; Kang et al., 2011), though in vivo understanding is still expanding.

An important next step to advance our understanding of craniofacial development will be synthesis of literature describing the mechanobiology of individual cells with principles of the physical suture environment. Specifically, secretion of signaling molecules has been shown to be stimulated by extracellular matrix stretching (Romani et al., 2021). *In vitro* studies have identified the potential for stiffness of a substrate to influence cell differentiation and the response of the cell (Discher et al., 2017); an element of "mechanical memory" is reported to enhance MSC stemness during *in vivo* engrafting after soft *in vitro* culture (Gilbert et al., 2010). In the context of regeneration, this concept could be key to the success of a suture re-establishment treatment, with cell fate potentially decided by the setting that the graft originates from or is cultured in[9]. Lastly, consideration must also be given to the physical link between extra- and intracellular components, including the nuclear membrane and cytoskeleton, in a cell's response to mechanosensation (Uhler & Shivashankar, 2017). While the specific machinery within different cell types may vary, the physical linkage of the nucleus and cell wall through the cytoskeleton is a common quality required for internal force generation and detection of cell deformation (Petzold & Gentleman, 2021).

2.5 Principles of mechanotransduction

Cells continuously probe their environment for changes to ECM and physical properties, as well as mechanical forces. At the same time, they define the mechanical and structural properties of their surroundings by modulating the extracellular matrix. These properties are particularly important in sutures, which contain a fibrous, flexible core that is lined by bone. Cells have a plethora of mechanisms to sense and respond to their mechanical environment. There is evidence for activity of most of these mechanisms in sutures. Key players in these processes are the primary cilia, which integrate mechanosensing and chemical sensing, the integrin and cytoskeleton interactions that transduce substrate

[9] This concept does not exclude the possibility of influence on grafting by the inherent environment of the tissue in which the graft is placed.

stiffness defined by ECM to the nucleus, as well as dedicated cell-surface mechanosensitive receptors like Piezo and Pkd1. In this section, we will primarily discuss principles of mechanotransduction in the context of the primary cilium, illustrating the complexity of cell mechanobiology.

2.5.1 The primary cilium as a signaling hub

Primary cilia are singular, antenna-like non-motile structures present on the surface of most cells. They extend into the extracellular space, can sense flow kinetics, and serve as signaling hubs for several major signaling pathways (Anvarian et al., 2019). The basal body of the cilium is centrosome-derived, a structure that is required for mitotic spindle formation during cell division (Basten & Giles, 2013). The existence of the cilium is thus mutually exclusive with active cell division. The cellular protrusion, the axoneme, is composed of microtubules and requires intraflagellar transport (IFT) proteins for antero- and retrograde transport of cargo proteins. The cilium is a junction point for many signaling pathways with critical involvement in suture function and bone physiology, including Hedgehog (Hh), Wnt, TGFβ/BMP, Notch, Hippo, PDGF and FGF, GPCR, and mTOR (Wheway et al., 2018). At the same time, it is a mechanosensitive structure able to detect changes in extracellular fluid. Defects in ciliary formation, motility, or function cause ciliopathies, often multi-systemic genetic disorders with frequent involvement of craniofacial structures (Anvarian et al., 2019). Craniosynostosis is the second most prevalent congenital craniofacial malformation after cleft lip/cleft palate. A review of genes identified in craniosynostosis mapped 18 out of 91 genes to the cilium (Tiberio, Parolini, et al., 2021)[10]. Thus, cilium dysfunction appears to be tightly associated with suture pathologies, in particular premature suture fusion. This association is not surprising given the tight association of Hh and Wnt signaling with normal cilium formation, and the appearance of the transcriptional targets of these pathways, Gli1 and Axin2, in suture progenitor cells (Maruyama et al., 2016; Zhao et al., 2015).

[10] Tiberio et al. performed an ontological analysis and interpretation of craniosynostosis-associated genes identified in the literature, specifically focusing on those which have published roles in primary cilium structure, function, and pathophysiology. Of note, analysis of Gene Ontology terms reflects the current body of published knowledge and the interpretation of individual studies, which is not necessarily a complete or fully accurate depiction of gene/protein function. This article should be treated as a narrative review discussing the potential involvement of cilia in human craniosynostosis disorders.

2.5.2 Interactions between mechanosensation and growth factor signaling

While the association of cilium dysfunction with impaired mechanosensation is well defined, it is not clear if changes in mechanosensation directly lead to alterations in growth factor signaling. Similarly to Hh signaling, synergistic mechano-chemical sensing has been demonstrated in BMP signaling (Vion et al., 2018). Endothelial cells adapt growth factor signaling in response to shear stress. Low shear stress is sensed by primary cilia and in response leads to enhanced sensitivity to vascular Bmp9 involving the Bmp receptor Alk1, preferentially located at the base of the cilium. Wnt signaling is also tightly linked to the basal body/cilium. In the presence of Wnt ligands, the Frizzled (Fzd) receptor protein anchors Dishevelled (Dsh), resulting in blockage of the β-catenin destruction complex. The resultant cytoplasmic accumulation of non-phosphorylated β-catenin, upon translocation to the nucleus, regulates gene expression via Tcf/Lef1 (Houschyar et al., 2019). Cilium integrity is critical for normal signaling, and deletion of Tctn3 (Tectonic 3), a gatekeeper protein at the base of the cilium that regulates protein transport within the cilium, leads to changes in the amount of Gli1 and Hh receptor Ptch1 (Gong et al., 2018)[11]. Wnt molecules also bind to Polycystin 1 (Pkd1) that may be located on the cilium stalk to induce Ca2+ influx through the Pkd1/Trpp2 complex (S. Kim et al., 2016). This process is independent of Fzd, but involves Inversin (Inv). Inv can target Dsh for degradation in a Ca2+-dependent manner. Thus, the switch between canonical β-catenin-dependent Wnt signaling and non-canonical Wnt signaling is controlled by Ca2+ signaling via Polycystins in the cilium stalk (Simons et al., 2005). Activation of the mechanosensitive domain of Pkd1 *in vitro* modulates activation of osteoinductive Runx2 and expression of osteocalcin (Katsianou et al., 2021).

2.5.3 Canonical and non-canonical Wnt signaling at the cilium

Context is a central factor for Wnt signaling action. While non-canonical Wnt signaling is associated with cell polarization and migration, canonical Wnt signaling is associated with various aspects of bone formation and remodeling. Canonical Wnt signaling is modulated

[11] This sentence has been corrected for grammar from the original published version: "Cilium integrity is critical for normal signaling and deletion of Tctn3 (Tectonic 3), a gatekeeper protein at the base of the cilium that regulates protein transport within the cilium and leads to changes in the amount of Gli1 and Hh receptor Ptch1 (Gong et al., 2018)."

by Lrp5/Lrp6, two low density lipoprotein receptor-related proteins that are associated with various bone mass disorders including osteoporosis (Balemans & Van Hul, 2007). While the importance of Lrp5/Lrp6 for the regulation of bone mass is well-established, and Lrp5 is involved in mechanotransduction in bone cells (Kang & Robling, 2015), their involvement in sutures is less clear. Bone-related studies in mice typically focus on the appendicular skeleton and unfortunately rarely report on changes in craniofacial bones or sutures. It might be that suture phenotypes have been overlooked, or that this pathway that is so important for the regulation of bone mass plays a minor role in craniofacial bone formation. While craniosynostosis has been associated with missense mutations in LRP5 (Kwee et al., 2005), this is not a frequent manifestation. In a mouse model for Apert syndrome, a craniofacial syndrome caused by mutations in *FGFR2* in which craniosynostosis is a principal clinical feature, aberrant activation of Wnt/β-catenin signaling involving Lrp5/Lrp6 has been reported (Min Swe et al., 2021). Similarly, a mutation in *AXIN2*, a negative regulator of canonical Wnt signaling, was recently associated with craniosynostosis (Yilmaz et al., 2018).

2.5.4 Receptor tyrosine kinase signaling at the cilium

Primary cilia also coordinate receptor tyrosine kinase (RTK) signaling pathways (Christensen et al., 2012). Engagement of RTK activates a series of signaling cascades, including the phosphatidylinositol 3-kinase-protein kinase B (PI3K-Akt), the phospholipase C (PLC), and mitogen-activated protein kinase (MAPK) pathways (Christensen et al., 2012). With respect to bone formation and remodeling, the PDGFRα, FGF, and IGF pathways are best understood. Often, specific representatives of a particular class of RTKs exist at the cilium (e.g. PDGFRα), while the rest of the cell surface is covered by another RTK (e.g. PDGFRβ) (Schneider et al., 2005). Dysregulated activity of PDGFRα leads to craniosynostosis of coronal sutures (He & Soriano, 2017). Abnormal expansion and premature differentiation of progenitor cells is observed as a consequence of increased signaling activity of PDGFRα. The cartilage anlagen that underlie the coronal suture are expanded, indicating that they directly contribute to morphogenesis and maintenance of calvarial sutures (He & Soriano, 2017). FGF signaling also plays a major role in suture formation, as predominantly gain-of-function mutations in *FGFR1–3* are associated with syndromic craniosynostoses, namely Apert syndrome, Pfeiffer syndrome, and Crouzon

syndrome (Melville et al., 2010). Modulators of intracellular modifiers of RTK-signaling, such as the negative regulators of the Sprouty family, have also been associated with skeletal phenotypes resembling ciliopathies (Hruba et al., 2021).

2.5.5 Notch signaling at the cilium

Notch signaling, a pathway involved in the specification of cell boundaries (Regan and Long, 2013), is also initiated at the primary cilium. Notch (Notch 1–4)/Notch ligands (Jagged 1/2 and Delta-like 1/3/4) are involved in juxtracrine signaling between cells. While Notch signaling is not well investigated in suture biology, it is tempting to speculate that well-arranged cell hierarchies within sutures are in part mediated by Notch signaling. Indeed, mutations in *JAGGED1* cause Alagille syndrome, in which craniosynostosis is a lesser observed feature. Loss of mesodermal but not neural crest-derived Jagged1 leads to craniosynostosis in mice (Yen et al., 2010). Jagged1 has an epistatic relationship with Twist1, a transcription factor widely associated with craniosynostosis (Yen et al., 2010) and helps specify the non-osteogenic/osteogenic boundary.

2.5.6 Signal integration at the cilium

The physical proximity of several signaling pathways along the cilium-centrosome axis allows for integration of the different signaling pathways and mechanosensation to enable intricate regulation of cellular differentiation processes. For example, in the limb, osteoblast cell fate specification by canonical Wnt signaling requires Bmp2 (Salazar et al., 2016). The BMP2 pathway has been associated with craniosynostosis (Timberlake et al., 2016), albeit its precise role in sutures remains unclear. Blocking of Noggin, a downstream target of FGF signaling in sutures, leads to craniosynostosis (Warren et al., 2003). Bmp2 might encourage osteoblasts toward increased ossification or lead to enhanced osteogenic fate induction and subsequent loss of progenitor cells. The consequence of either would be a loss of suture patency and synostosis. Interestingly, the linker domain of Smad1, a key mediator of canonical Bmp signaling, integrates RTK and Wnt signals that, when absent, allow nuclear translocation of pSmad1, but in their presence direct pSmad to proteasome degradation (Fuentealba et al., 2007).

The previous sections establish the importance of cilium-associated signaling pathways and offer a glimpse at how the integration of signaling pathways allows for fine-

tuning of cell differentiation. However, mechanotransduction is typically initiated in response to environmental mechanical stimuli. The following sections will explore the environmental angle of cell biology.

2.5.7 Mechanosensation and the environment

A second major component for mechanosensation is the ability of cells to detect material stiffness or attachment to their environment in processes independent of the primary cilium. This involves sensing of overall isometric forces representative of the environment or cyclic forces that reflect mechanical loading of tissues. Cells sense the stiffness of their surroundings by applying forces and evaluating contractile tension in relation to changes in cell shape. The micro-stiffness is defined as the mechanical stress needed for a cell to induce a fractional change in length (Irianto et al., 2016). Each tissue has a characteristic micro-stiffness landscape. Depending on their location within the suture, cells can face hard bone matrix laterally or encounter relatively soft fibrous tissue medially. Stem cells, including those resident in sutures, use this mechanism to control lineage differentiation in addition to the well-established influence of growth factors (Engler et al., 2006). The actual force is sensed via myosin type II mini filaments pulling on the actin skeleton (Engler et al., 2006)[12]. Cells in mechanically active tissues also experience cyclic forces. Both types of forces can engage the same set of molecular sensors on the cell surface.

2.5.8 Focal adhesions

One of the key players in mechanosensation are focal adhesions (FA). FA connect extracellular matrix (ECM) proteins such as Collagen I or Fibronectin via integrins to intracellular actin filaments. Talin, which interacts with FA, recruits vinculin in a mechanosensitive manner. Vinculin binds to actin filaments, which are anchored to the nuclear membrane by the LINC complex (Parsons et al., 2010). This direct connection between the environment and the nuclear membrane allows the stiffness of the nuclear lamina, defined by A- and B-type lamin proteins (Swift et al., 2013), to correlate with the

[12] The interaction of myosin filaments with the actin cytoskeleton is one example of cell mechanosensation, in which myosin interacts with the adherens junctions of cells. However, as discussed in section 2.5.8, other structures including focal adhesions also contribute to the sensation of matrix stiffness. It should be noted that matrix stiffness is not the only environmental cue or force sensed by cells; the physical stimuli discussed earlier (e.g. brain expansion, mastication) also contribute to the mechanical environment.

stiffness of the surrounding matrix. In response to mechanosensation, stress fibers are established and can become stronger with increased tension in a process involving the Rho-ROCK signaling cascade (Geiger et al., 2009).

FA also trigger mechanosensitive cellular responses by linking integrin via paxillin to the FA kinase (FAK). FAK in turn can initiate multiple mechanosensitive signaling pathways, including ERK, JNK, Wnt/β-catenin, and Hippo pathways (reviewed in Humphrey et al., 2014). As a result, key transcription factors are differentially distributed between the cytosol and nucleus, which provides a direct means to regulate nuclear gene transcription. Amongst those are Yes-associated protein (YAP) and its transcriptional co-activator TAZ, which have a well-established role in osteoblast precursor cells (Kegelman et al., 2021).

2.5.9 Mechanosensitive channels

In addition to mechanosensitive adaptor proteins, mechanosensitive ion channels may similarly locate at focal adhesions and primarily convert mechanical stress into a cytoplasmic Ca^{2+} signal (Kobayashi & Sokabe, 2010). Many channels have been identified, including the earlier mentioned Polycystin 1/2, members of the transient receptor potential (TRP) channels (Kobayashi & Sokabe, 2010), and members of the Piezo family of mechanically activated cation channels (Ranade et al., 2014). The Ca^{2+} provided by activation of these mechanosensitive receptors is not only involved in the reorganization of the actin cytoskeleton; it also serves as a second messenger in various signaling pathways. Intracellular Ca^{2+} oscillations are furthermore mediators of durotaxis, a process that allows cells to seek out a substrate with appropriate stiffness during cell migration (Lo et al., 2000). Conditional deletion of *Piezo1* in mice impairs several axes of bone development which are dependent on osteoblast mechanical function (W. Sun et al., 2019).

2.5.10 Shaping and remembering the environment

Cells not only sense their surroundings, but actively shape them reciprocally. Mechanical and growth factor signals allow cells to change their micro-environment through expression of ECM proteins or ECM-modifying factors, such as matrix-metalloproteinases (MMPs). Cells also remember their environment; *in vitro* experiments have established that cells retain a mechanical memory, i.e. their cellular attachment machinery

(actomyosin, focal adhesions, nuclear YAP) connecting them to their previous substrate (Nasrollahi et al., 2017). How this ability impacts cell differentiation or matrix formation within a tissue with such rapidly changing properties as the patent suture needs to be addressed. When cells isolated from fused, ossified sutures were compared to cells from patent sutures, evidence for such a mechanical memory was identified (Barreto et al., 2017). On the other hand, a variety of genetic connective tissue disorders such as Ehlers-Danlos syndrome are caused by changes to ECM composition and/or structure. While these disorders affect tissue properties, such as increased elasticity, hypermobility, spine deformities, or lower bone mineral density (Basalom & Rauch, 2020), there have been no reports on suture-associated pathologies (Sonnesen et al., 2021).

ECM composition is not only important because of its structural properties. Many growth factors that are used *in vitro* for cell differentiation are semi-soluble *in vivo* and interact with the ECM to limit their spatial distribution. In addition to providing resting forces, the ECM also serves as a depository for growth factors, sequestering them for precise, local action. This includes many of the factors known to signal at the primary cilium or at its base (TGFβ, BMP, FGF, PDGF). Their release is dependent on mechanical engagement of the ECM as shown for TGFβ1 (Hinz, 2015), feeding back to regulate ECM components. Thus, the reciprocity between mechanical and chemical signaling is likely a combination of complex, interconnected relationships that influences much of suture cell biology.

2.6 Gene regulatory networks in suture mechanotransduction

2.6.1 Stem cells and suture patency

A key characteristic of a functional cranial suture is the preservation of suture patency, or maintenance of the unossified region separating cranial bones. This requires cellular coordination at several levels. It was recently shown that premature fusion of a suture in a mouse model for craniosynostosis can be prevented by re-introduction of normal progenitor cells by seeding mesenchymal stromal cells (M. Yu et al., 2021). This pool of stem cells and early progenitors must be maintained via self-renewal and must be responsive to differentiation toward bone-committed progenitor cells to sustain long-term function. Disruption of the osteogenic balance can shift a patent suture to craniosynostosis (Fig. 2.3), as is illustrated by premature fusion of the anterior frontal suture in mice

overexpressing *Bmpr1a* (Komatsu et al., 2013). Taken alongside the importance of *Bmpr1a* for self-renewal in human suture stem cells (Maruyama et al., 2021), one may hypothesize that dysregulation of the stem cell population by BMPs could lead to the observed obliteration of the cells populating the central suture mesenchyme. Another mechanism for maintenance of cells in a non-osteogenic state, enabling patency, is exclusion of β-catenin from the cell nucleus, accomplished by β-catenin target gene *Jagged* in sutures (Yen et al., 2010). Conversely, loss of Axin2, which leads to stabilization of β-catenin and constitutively active canonical Wnt signaling (Logan & Nusse, 2004), results in craniosynostosis in mice (Behr et al., 2013).

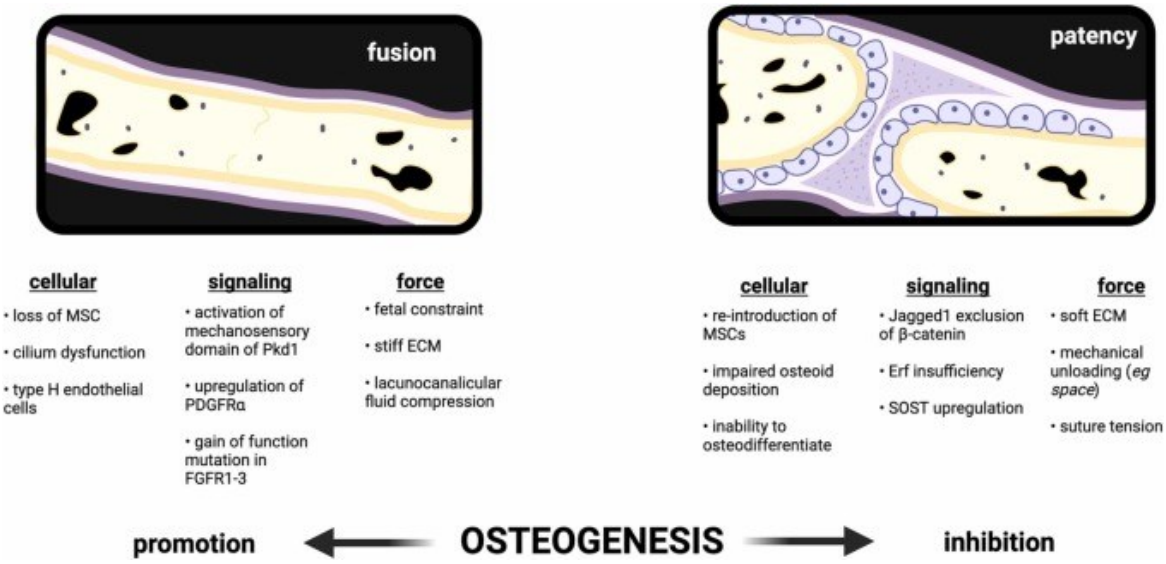

Figure 2.3 The balance between promotion and inhibition of osteogenesis in cranial sutures. Physiological and pathological instances of osteogenesis are dependent on common mechanisms. The stimuli listed here (categorized as cellular, signaling, or force) inhibit or promote osteogenesis, tipping the balance of osteogenesis to either side.

Studies continuously reveal additional hierarchical layers of regulation of this dynamic equilibrium. Several groups have demonstrated that the adipo-osteogenic balance can be tipped toward bone by priming MSCs for differentiation (Q. Chen et al., 2016; Przybyla et al., 2016). Misdirection of MSC commitment can range from a delay in osteogenic commitment as in ERF insufficiency, to inappropriate endochondral ossification as with constitutive Pdgfrα activation (He & Soriano, 2017; Vogiatzi et al., 2021). Mechanical forces also have key roles in lineage commitment of MSCs, with activity of signaling axes like ROCK/TAZ correlating with the fate of cells and extracellular matrix stiffness (Katoh et al., 2011; Li et al., 2020). The mechanotransduction

signaling partner of TAZ, YAP, also influences the adipo-osteogenic balance of MSC fate by promoting osteogenesis (Lorthongpanich et al., 2019). It is of interest to note that YAP/TAZ have been shown to set responsiveness of several signaling pathways (Aragona et al., 2013). Specifically, they form part of the β-catenin destruction complex, and thus control Wnt signal transduction (Azzolin et al., 2014). Appropriate cell lineage induction of stem cells is critical to suture patency and appropriate ossification. Several recent studies, summarized in Table 2.1, have revealed factors contributing to osteogenic differentiation in response to mechanical forces, ranging from limb loading to substrate stiffening. These signaling axes and cellular influences should be considered carefully in the context of suture biology.

Table 2.1 Summary of effects of mechanical stimuli on growth factor signaling and osteogenesis.

Type of force	Category of effect	Observations	Cell type	Reference
Limb loading	Bone formation / remodeling	↑ trabecular bone volume	*trabecular bone*	(Albiol et al., 2020)
		↑osteoblast proliferation	*osteoblasts*	(Zannit et al., 2020)
	Mechanotransduction	↑Piezo1	*osteoprogenitors*	(Deng et al., 2022)
	Signaling	Sost, Dkk1 expression varies diurnally, influencing loading effect	*cortical bone*	(Bouchard et al., 2022)
		↑Wnt1, Wnt7b ↓bone formation without Wnt secretion	*osteoblasts*	(Lawson et al., 2022)
		↑TGFß-1	*osteoprogenitors*	(Deng et al., 2022)
		Ngf/TrKa ↑ osteoblast differentiation with loading	*osteoblasts*	(Fioravanti et al., 2021)
Limb un-loading	Micro-RNAs	miR-138-5p targets MACF1 to inhibit differentiation	*osteoblasts*	(Z. Chen et al., 2021)
		silencing miRNA-132-3p ↑differentiation & osteogenesis	*limb bone tissue*	(Hu et al., 2020)
	Signaling	↑Leukemia Inhibitory Factor (LIF)	*BMMs*	(J. Du et al., 2020)
		Light OTM ↑Bcl-2	*PDL cells*	

Type of force	Category of effect	Observations	Cell type	Reference
Orthodontic tooth movement (OTM)	Bone formation / remodeling	Heavy OTM ↑Bax, ↓RANKL		(S. Kaya et al., 2020)
	Mechanotransduction	Piezo1 activation required for full Runx2, Sp7 function & RANKL/OPG ratio	*periodontal ligament (PDL) cells*	(Y. Jiang et al., 2021)
	Signaling	↑Scx on tension side via TGF-ß1-Smad3 signaling, inhibiting osteoblast differentiation	*PDL cells*	(Kawatsu et al., 2021)
		↓CXCL-14	*PDL cells*	(Ko et al., 2020)
Suture tension	Bone formation / remodeling	↑Runx2 Expansion of Gli1+ cells	*palatal suture cells*	(Huang et al., 2021)
	Signaling	CTGF required for pre-osteoblast aggregation	*sagittal suture pre-osteoblasts*	(W. Jiang et al., 2021)
Hydrogels with variable stiffness (*in vitro*)	Epigenetics	substrate stiffening ↑ histone acetylation, ↓HDACs via LINC complex	*human MSCs (hMSCs)*	(Killaars et al., 2020)
Mechanical stretch (altered plate micro-topography / bending *in vitro*)	Bone formation / remodeling	↓RANKL	*Saos-2 cells*	(Galea et al., 2020)
		↑osteogenesis via IP3R-mediated intracellular [Ca2+]	*MSCs*	(Huang et al., 2021)
		↑FOXO3 leading to ↑Ocn, Runx2, ß-catenin	*BMSCs*	(A. Jin et al., 2022)
		↑osteocyte-derived exosomes, promoting proliferation via miR-181b-5p/PTEN/AKT pathway	*human PDL (hPDL) stem cells* *MLO-Y4 cells*	(Lv et al., 2020)
	Cell cycle	↓Brd2	*Saos-2 cells*	(Galea et al., 2020)
		↓Cdkn1a in early/late osteoblasts	*BMSCs*	(Juran et al., 2021)
	Epigenetics	↓DMNT1/DNM13b	*MSCs*	(Carthew et al., 2021)
	Mechanotransduction	↑Yap	*mesenchymal stem cells (MSCs)*	(Carthew et al., 2021)

Type of force	Category of effect	Observations	Cell type	Reference
	Signaling	↑ROCK, TAZ translocation	*sagittal suture cells*	(W. Li et al., 2020)
		↓Sost	*Saos-2 cells*	(Galea et al., 2020))
		↑IL1-ß promoting osteochondrogenic differentiation via JNK/ERK	*tendon-derived stem cells (TDSCs)*	(Geng et al., 2020)
Orthodontic compressive force (in vitro)	Bone formation / remodeling	histamine ↑RANKL via H1R	*periodontal ligament fibroblasts (PDLF)*	(Groeger et al., 2020)
	Signaling	histamine ↑proinflammatory mediators via H1R	*periodontal ligament fibroblasts (PDLF)*	(Groeger et al., 2020)
Fluid shear stress	Signaling	↑LIF	*BMSCs*	(J. Du et al., 2020)
		Sost degradation by ↑lysosomal activation	*Ocy454 osteocytes*	(Gould et al., 2021)
			UMR106 osteosarcoma	
Pulsating fluid flow	Bone formation / remodeling	↑Fgf2, Runx2, Ocn, Dmp1, Col1a1 after flow cessation	*MC3T3-E1 cells*	(J. Jin et al., 2021)
	Signaling	↑nitric oxide in first hour of flow	*MC3T3-E1 cells*	(J. Jin et al., 2021)
Microgravity simulation (in vitro)	Micro-RNAs	↑miR-138-5p inhibiting differentiation	*MC3T3-E1 cells*	(Z. Chen et al., 2021)
		↑miRNA-132-3p inhibiting differentiation	*BMSCs*	(Hu et al., 2020)
	Signaling	↑LIF	*osteocytes*	(J. Du et al., 2020)

2.6.2 Osteoblast differentiation

Single-cell RNA sequencing of the developing coronal suture revealed an unexpected complexity of cell subsets forming the suture microarchitecture (Farmer et al., 2021). Farmer et al. identified several cell subsets representing the various stages of osteoblast differentiation. While the existence of gradual stages of osteoblast differentiation is unsurprising given the progressive nature of intramembranous ossification, the study also characterized the gene expression profiles of several subtypes of progenitor cells. Mapping cell subsets to anatomical locations revealed that most cell subsets are restricted to specific niches, albeit some of these niches showed a degree of spatial overlap. Each cell subset revealed discrete attributes according to its differentiation status. This finding is supported by previous literature describing variable expression of gene paralogues throughout osteoblast differentiation. For example, Fgfr2 is expressed by osteoprogenitors, but fellow Fgfr[13] paralogue Fgfr1 is expressed by more differentiated osteoblasts (Y. Xie et al., 2020). Other factors are suppressive of osteogenesis in a biphasic temporal pattern, as in Notch inhibition of early and late stages of osteoblastogenesis with a switch to induction of the intermediate stage (Regan & Long, 2013), indicating a difference in progenitor sensitivity or response to a Notch signaling cue. Notch signaling has additional roles in osteoclastogenesis, osteocyte differentiation, and mineralization, and has been reported to be regulated by shear stress in endothelial cells (Abuammah et al., 2018). Interestingly, this switch to inhibition of osteogenesis by Notch from enhancement can be induced with Bmp2 overexpression (Pakvasa et al., 2021). In the context of cranial sutures and the genetic milieu coming to light, the overlap of several signaling modalities with patterns such as these likely governs the complex nature of suture patency and fusion.

Other factors within the suture mesenchyme affect the ordered osteoblast differentiation, such as nerve-derived Fstl1, an inhibitor of Bmp/activins, acting to maintain patency by preventing terminal differentiation of osteoblasts and stimulating progenitor cell proliferation (Tower et al., 2021). Noggin, another Bmp antagonist, has similarly been identified in the mesenchyme of patent, unfused sutures and decreased phospho (p)Smad 2/4 activity is observed in regions where bone will form (Tholpady & Ogle, 2011; Warren et al., 2003). The discovery of differentially expressed genes between

[13] This gene name has been corrected to “Fgfr” from the published “Fgf”.

patent and fusing, and normal and craniosynostotic sutures using RNA sequencing technology is a rapidly expanding knowledge base which likely has yet to be utilized to its full potential.

2.6.3 Differentiation in response to mechanical force

The influence of mechanical force on cell differentiation is an intriguing axis to consider as sutures are dynamic, flexible regions supporting osteodifferentiation. For example, the effect of TGF-β signaling on MSC differentiation is influenced by cell-extrinsic differences in the extracellular matrix and other extracellular cues, in addition to cell-intrinsic factors (Rys et al., 2016). Factors like Bmp4 and Fgf2 are expressed by osteoprogenitors with stretching *in vitro*, and Bmp2 acts cooperatively with YAP/TAZ, perhaps mediating stretch-dependent responses (Wei et al., 2020; J. C. Yu et al., 2001). The modulation of TGF-β signaling by topographical cues is a clue to the multifaceted biophysical control of establishment and maintenance of cranial sutures (Vermeulen et al., 2020). How could the physical nature of anatomically distinct approximating bone fronts influence the differentiation or overarching signaling regulation of cells within the established suture?

It is known that the differentiation status of MSCs can guide their response to mechanical forces, evidenced by the increased sensitivity of undifferentiated MSCs to pressure when compared to their osteo-induced counterparts (J. Liu et al., 2009). This principle may be fundamental to the establishment of the suture's characteristic architecture and cellular distribution. A system central to mechanotransduction is YAP/TAZ, the nuclear localization of which is proportional to extracellular matrix stiffness and cell spreading (Romani et al., 2021). Manipulation of YAP/TAZ signaling can cause cells on a soft matrix to behave as they would on a hard substrate, and YAP depletion results in impairment of memory-dependent cell behaviors (Dupont et al., 2011; Nasrollahi et al., 2017). Generally, this axis is theorized to be directly regulated by the cytoskeleton, in addition to Hippo signaling.

The skull features 17 sutures, each of which is situated in a different strain environment based on bone shape, position relative to moving components of the skull, and architecture of the approximating bones. Even in early embryonic development, the effect of matrix stiffening on β-catenin accumulation is suggested to vary between tissue types (Astudillo, 2020). These different signaling environments could be due to intrinsic

genetic signatures and sensitivities intersecting with mechanical regulation of genes. Indeed, evidence of communication between signaling pathways and subpopulations of sutural cells is well represented in the literature. For example, the known role of Wnt signaling in osteoblast differentiation and osteocyte survival ties into its hypothesized role of balancing Fgf and Bmp signaling (Katsianou et al., 2016). Both Bmp and Fgf signaling facilitate intercellular communication, and disturbances in their signaling activities are associated with suture anomalies. This multi-level network of communication between cell populations and gene signaling pathways also overlaps with mechanosensation. For example, Bmp signaling is known to be regulated by mechanical cues, and MAPK signaling, downstream of Fgf, is regulated by mechanical stress. This induces remodeling of cytoskeletal proteins, feeding back into the mechanical environment of the suture (da Silva Madaleno et al., 2020; Kinoshita et al., 2020). Similarly, mechanotransduction inhibits the Wnt antagonist Sost, releasing Wnt signaling in terminally differentiated osteocytes (Manokawinchoke et al., 2017; X. Tu et al., 2012). The modulatory effects of mechanical stimuli on many signaling networks are yet unknown, but are a current topic of study.

2.7 Application of knowledge from other fields to cranial sutures

By virtue of the accessibility of manipulation of the cell environment in isolation, much of the mechanical influence on cell behavior has been found *in vitro*. For example, the role of the mechanosensory protein PC-1 in osteoblast differentiation was recently characterized using a craniosynostosis cell line (Katsianou et al., 2021). However, translation to tissue-level settings is often not straightforward. Cells *in vivo* do not exist in isolation or as a largely homogenous cell population in a petri dish. Many of the reciprocal interactions between populations described earlier in this review – and between other supporting tissues like the ECM, fibroblasts, vascularization, or nerves – are not represented *in vitro*. These missing components, however, play significant roles in determining the suture milieu that guides differentiation of MSCs.

The translation of *in vitro* stem cell cultures to cranial suture biology assumes that the starting population is the same between systems. Thus, a stem cell in a dish should behave similarly to an MSC in the suture if given the same cues. However, what are commonly known as “mesenchymal stem cells” or “mesenchymal stromal cells” are

actually a collection of cells. Some represent transcriptionally heterogeneous progenitor populations (Menon et al., 2021), while some might have evolved in a paralogous nature. There is evidence that suture niches contain multiple progenitor lineages that coexist with their differentiated counterparts heterogeneously within the suture niche (K. G. Chen et al., 2018). This is easiest to appreciate in sutures that are composed of a mixture of mesoderm and neural crest-derived cells, like the coronal and sagittal sutures.

It should also be noted that cells influence their surroundings, and inflexible synthetic culture environments do not allow this reciprocal interaction to occur. Efforts have been made in tissue regeneration to replicate the mechanical environment in culture using 3D systems in which properties like porosity, composition, and stiffness may be modulated (Vining & Mooney, 2017). Still, a more basic two-dimensional system is often preferable, as when simulating cyclic or static strains. 3D culture is conversely preferred for compressive or tensile loads. Several innovative methods have been used to tune mechanical force *in vitro*, such as fluid shear stress, acoustic waves, vibration, collagen-coated magnetic beads, or use of the microgravity-simulating clinostat. While these techniques are extremely valuable to tease apart the impact of mechanical stimulation on cell biology, it is not clear how representative they are of cell biology within a suture *in vivo*. Even suture explants, where anatomy is partially preserved, are missing several axes of strain.

In addition to physical influences on differentiation, one must consider crosstalk with other systems and extracellular components. Bone is an endocrine organ, both responding to systemic cues and secreting metabolically modulatory factors like osteokines. Examples are osteocalcin, the carboxylation status of which can modulate insulin sensitivity via the pancreas (Kirk et al., 2020), and Fgf-23, which regulates phosphorous excretion by the kidney when secreted by osteocytes (Y. Guo et al., 2018; Lu & Feng, 2011; Tresguerres et al., 2020). On the other hand, systemic factors also influence bone formation, such as growth hormone (GH), insulin-like growth factor-1 (IGF-1), leptin, or pro-inflammatory cytokines (Kirk et al., 2020). Several metabolic nodes interact with mechanochemical axes, as reviewed in Romani et al. (2021). For example, metabolism is partially regulated by nuclear translocation of YAP/TAZ, promoting glycolysis and autophagy. Consideration of the impact of hormones involved in bone

differentiation and strain response is mostly lacking in cranial suture biology. Interleukin (IL)− 11, a member of the IL-6 family, and its receptors that have important functions in tissue fibrosis and regulation of cancer stromal cells (P. Nguyen et al., 2019), have been associated with craniosynostosis (Kespohl et al., 2021). Similarly, IGF impacts the contractility and motility of osteoblasts, and itself is subject to modulation by tension (Al-Rekabi et al., 2016; Hirukawa et al., 2005).

The connection of cranial sutures to systemic networks is not surprising. As zones for intramembranous bone formation with high demands for nutrients and oxygen, sutures rely on vascularization. Thus, modulation of cell metabolism via the blood axis and endothelial cell metabolism has a meaningful influence on cranial suture biology (Rindone et al., 2021). Hemodynamic forces are known to influence the shape of vasculature, and suture tension acting on mechanosensitive fibroblast-like cells in the suture has been associated with their contribution to angiogenesis (G. Li et al., 2021). Conversely, the type H subtype of endothelial cells is linked with the presence of osteoprogenitor cells, and produces factors supporting osteogenesis (Kusumbe et al., 2014). Cerebral vein development also requires paracrine Bmp signaling from osteoprogenitor cells to the dura (Tischfield et al., 2017). Taken together, these observations highlight the reciprocal interaction between osteoprogenitors and angiogenesis, particularly in intersection with mechanical forces.

Many advances in our understanding of mechanosensation were made in non-bone-related fields. In the heart, critical components of the myocardium are myocardin-related transcription factors (MRTFs), which enable myocyte stretch-sensitivity. Through a dynamic actin mechanism in response to stretch, translocation of MRTF-A to the nucleus is triggered, driving smooth muscle cell differentiation (Finch-Edmondson & Sudol, 2016). MRTFs feed back to the cytoskeleton to reorganize and increase expression of actin proteins. Their downstream targets have been shown to be critical for cell spreading, adhesion, and response to stress fibers and focal adhesion plaques. Tissue fibrosis is another example: ECM stiffening with primary inflammation involves a phenotypic switch of vascular smooth muscle cells to osteoblast-like cells. In cancer, mechanotransduction mediators YAP and TAZ act in a fibrotic positive-feedback loop in treatment resistance, resulting in persistent cellular activation (Finch-Edmondson & Sudol, 2016). These

discoveries regarding tissue-level changes in response to mechanical stimuli inform our understanding of developmental mechanochemical mechanisms and the consequences of force on other stretch-sensitive structures, like craniofacial sutures.

The periodontal ligament (PDL), which connects the hard tissue of the tooth root to the surrounding bone, is another common application for mechanobiology. The response of bone to mechanical force is critical for Orthodontic Tooth Movement (OTM). Depending on the force applied, parts of the PDL experience tension that induces bone formation, with others experiencing compression that induces bone resorption. Mechanical differences translate into molecular differences that coordinate the different cellular responses. Key factors and associated signaling axes have been identified (Hliang et al., 2019; Odagaki et al., 2018; Takimoto et al., 2015). Given the anatomic similarities between sutures and the PDL, many of these signaling networks are observed in both tissues. Wnt-responsive Axin2+ cells in the PDL are especially responsive to mechanical force, which may be the same in sutures considering its expression in osteogenic fronts and the periosteum (H.-M. I. Yu et al., 2005). The association of expression of the Wnt-inhibitor Sost with compression, and the opposite reduction of Sost expression at the tension side (Odagaki et al., 2018) might also be paralogous in sutures. Piezo1 also mediates osteoblastic and osteoclastic functions on the tension side during OTM (Y. Jiang et al., 2021). Of interest, the plasticity of PDL stem cells in response to static mechanical strain has recently been shown to be modulated by the microenvironment inflammatory (Delgado-Ruiz et al., 2019; J. Liu et al., 2017) and a change in environment could also influence sutures. Thus, many findings concerning the mechanoregulation in the PDL are predicted to translate to cranial sutures, as tension forces are used to stimulate new appositional bone formation in both systems.

Outside of biological systems, *in silico* mathematical and computational models of cranial suture principles have substantially advanced our understanding of the overall dynamics of cell movement and responses to extracellular factors. A limitation of computational models, however, is the choice of assumptions that must be made to simplify the system enough for realistic modeling. Many studies have made efforts to fine-tune the suture theoretical framework by adding terms for elements like the “creep-relaxation transformation”, incorporating viscoelasticity of sutures into the equation (Romanyk et al.,

2014). Others opt to combine several levels of information, as in Khonsari et al.'s study combining biological information from histology and mathematical modeling with elements of evolution (Khonsari et al., 2013). The authors encourage consideration of the physics of cell movement in the viscoelastic suture, such as different migration velocities in relation to proximity to the bone surface. However, this study was limited by its inability to consider compression forces, which are part of the suture mechanoenvironment. Generally, computational models are best utilized to solve a specific physiologically relevant aspect of the complex system, such as interdigitation (Shibusawa et al., 2021). As the field progresses, however, it would be interesting to pursue more multidisciplinary collaborations linking biological evidence with theoretical frameworks, contextualized within mechanobiology as a whole.

2.8 Conclusions and outlook

Sutures are well-suited yet underutilized structures to model mechano-chemical signaling and its integration with bone growth, patency, interdigitation, and fusion. Cranial sutures in particular have proven to be a valid system to study how extracellular or extrinsic forces are integrated with cytoskeletal or intrinsic forces. The importance of mesenchymal stromal cells with stem/progenitor characteristics for maintenance of a functional, i.e. patent suture, is well established. The cellular composition of sutures is complex, maybe more complex than is sometimes appreciated. On the other hand, this is somewhat expected based on the rapidly expanding categorization of a variety of bone and cartilage progenitor cells in other anatomical locations, such as the growth plate in long bones (Chan et al., 2015, 2018).

Of the 17 sutures in the neonatal skull, over half connect facial bones. The majority of suture-related research has focused on cranial sutures, as cranial suture dysfunction is associated with craniosynostosis and leads to dramatic and often life-threatening manifestations. The cellular characteristics of cranial sutures differ from those of facial sutures while their mechanical behaviour appears to be similar (Herring, 2008). For example, facial sutures are not supported by the dura and, in contrast to most cranial sutures, do not fuse during the life-time. In addition, midfacial sutures experience significant proximal mechanical forces from mastication. Synostosis of midfacial sutures is observed in some craniofacial syndromes, but their etiology and contribution to facial

growth anomalies is not well investigated (M. M. Wang et al., 2021). It will be interesting to compare cellular composition and molecular regulation of facial sutures with their cranial counterparts.

Despite its prevalence in the literature, it must be noted that craniosynostosis is not the only consequence of suture dysfunction. The appearance of widened sutures as in cleidocranial dysplasia or the presence of supernumerary Wormian bones is also observed. Wormian bones are accessory skull bones that form *de novo* from ectopic or tertiary ossification centers. They are situated within sutures and have been observed to form within enlarged suture spaces. Their formation is associated with dural strain and their appearance has notably been described in skulls subject to mechanical stress induced by cultural skull deformation (O'Loughlin, 2004). Why and how these new ossification centers are induced is not well understood, though it has been speculated that their formation is a compensatory mechanism for extreme mechanical stress. Research into these interesting structures could shed light on the induction of ossification centers.

The field of osteogenic stem cell biology, while drawing on conclusions from many of the aforementioned model systems, finds a primary application in innovative bioengineering and regenerative therapies. A fundamental aim in these fields is to bring to light how a specific microenvironment can guide stem cells to regenerate missing or compromised tissues. A key consideration is the identification of biomaterial carriers that provide an appropriate biochemical and biophysical milieu. Biomaterials can be modified in countless ways, mainly to enhance osteoconductivity (A. E. Stanton et al., 2019; Yao et al., 2017). Knowledge from suture biology forewarns that bone formation is much more complex and highly integrated than reflected by current clinical practice, a feature that comes as no surprise given the hundreds of millions of years of developmental history molding this elegant system.

With the advent of space travel and the fact that unloading in space reduces bone mass, studies simulating microgravity and experimenting with mechanical force generation *in vitro* have grown more popular (Goodship et al., 1998). Specifically, the unloading of bone and muscle results in differential regulation of genes and proteins related to metabolism and protein synthesis, which would feed back to further compromise bone

quality (Herrmann et al., 2020). The integration of cellular metabolism into bone and mesenchymal stromal cell biology is expected to reveal more unknowns.

Moving forward, the integration of these various aspects will be required to truly understand suture biology (Fig. 2.4). Translating this knowledge into novel clinical or therapeutic applications will greatly benefit from a shift in engineering approaches. Within the context of sutures, this will not only concern the re-establishment of fused sutures to correct craniosynostosis as was recently demonstrated in a mouse model for craniosynostosis (M. Yu et al., 2021), but also the possibility of re-activating sutures that have lost their ability to grow. The latter would be of interest to certain orthognathic applications such as midfacial expansion after active growth has ceased. Despite vast progress in understanding what constitutes a suture and what is required for its continuous function, there is a great deal that is unknown regarding the intricate cell biological regulation that must integrate mechanical forces, cellular signaling, and cell differentiation. Further progress in suture research will benefit from purposeful integration of cell biology in addition to pathologic, clinical, and genetic views.

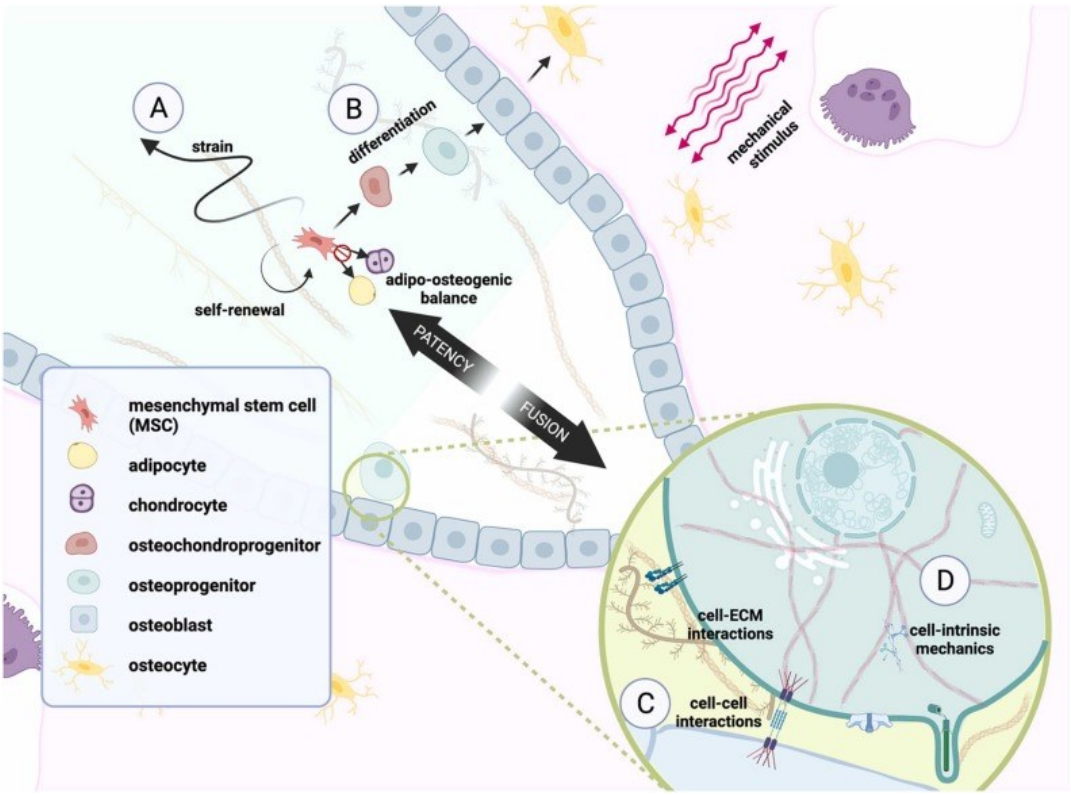

Figure 2.4. The mechanosensitive cranial suture milieu is an active zone of communication between cells and their environment as they perform their individual functions.
Many interconnected sub-structure processes can shift suture status between patency and fusion. Suture strain and other mechanical stimuli (A), for example, can influence mesenchymal stem cell (MSC) properties like self-renewal, maintenance of adipo-osteogenic balance, or osteogenic differentiation (B). Interactions between cells composing the suture are influenced by upstream mechanical cues, including secretion of signaling factors and physical contact between cells and with the extracellular matrix (C). As highlighted in the inset, cells additionally incorporate cell intrinsic forces in their perception of the mechanical environment (D).

CHAPTER 3

MATERIALS AND METHODS

3.1 Ethics, animal care, and general procedures

Animal experiments in Chapters 4 and 5 of this thesis were approved by the Research Ethics Office at the University of Alberta (Animal Care and Use Committee, AUP1149) in compliance with guidelines set by the Canadian Council of Animal Care. For experiments performed at the National Institutes of Health in Chapters 4 and 6, protocols were approved by the National Institute of Child Health and Human Development (NICHD) Animal Care and Use Committee (Animal Study Protocol #21-031). Mice were housed at the University of Alberta in Edmonton, Canada or the National Institutes of Health in Bethesda, U.S.A. (respectively) under controlled conditions with a regular light cycle and access to food and water *ad libitum*.

3.2 Animal models

All mice were of a C57Bl/6 *Mus musculus* genetic background (JAX stock #000664). All Cre recombinase constructs included mT/mG for lineage tracing with GFP (JAX stock #007576).

Mouse lines used in Chapter 4 were Bmp7:Wnt1-Cre:mT/mG (Zouvelou, Luder, et al., 2009; Zouvelou, Passa, et al., 2009), Bmp7:Wnt1-Cre2:mT/mG (Lewis et al., 2013), Bmp7:Col2Cre:mT/mG (Ovchinnikov et al., 2000), and wild type C57Bl/6. Control mice were Bmp7 fl/fl or wt/fl Wnt1-Cre^{neg} littermates. Previous data and from our group and my confirmatory experiments have shown that Bmp7 wt Wnt1-Cre^{pos} mice do not replicate the phenotype described in this chapter, indicating that Cre positivity is not sufficient to cause the phenotype described in this study.

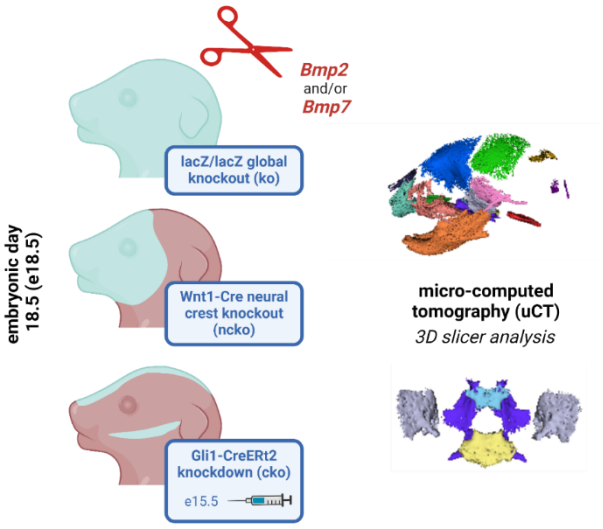

Figure 3.1 Chapter 5 mouse lines and methodology.
Bmp2 and/or *Bmp7* were deleted globally (lacZ/lacZ, ko) or conditionally in Wnt1-Cre+ cells (neural crest, ncko) and Gli1-CreERT2+ cells (osteoprogenitors, chondrocytes, cko).

For Chapter 5, the lines used were Bmp2:Gli1-CreERT2:mT/mG (Ahn & Joyner, 2004; Graf & Economides, 2008), Bmp7:Gli1-CreERT2:mT/mG, Bmp7:Rosa26-LacZ (JAX stock # 002073), and Bmp2:Wnt1-Cre:mT/mG, summarized in Figure 3.1. Gli1-CreERT2 mice were purchased from Jackson Laboratory (JAX stock #007913). Control mice for this chapter were Bmp2 or Bmp7 wt, wt/fl, or fl/fl Gli1-CreERT2^{neg} littermates and all mice were injected with Tamoxifen.

Mice used in Chapter 6 were of wild type background. Timed pregnancies were dated with day 0.5 indicating the plug date. All lines were backcrossed for at least 10 generations to C57Bl/6 mice. Genotyping of mice was performed from ear-notch or tissue biopsies with the primer combinations in Table 3.1.

Table 3.1 Primers used for PCR genotyping of mice.

Target	Primer type	Primer sequences
Bmp2	MAID 1169 (Bmp2) common reverse	5'-CAG AGG CAG TGG GAA AAA CAC C-3'
	MAID 1169 (Bmp2) target (-neo) forward	5'-CTG GGT GAT AAT AGG ACC TAG GAA G-3'
	MAID 1169 (Bmp2) knockout forward	5'-AGT GGC GTC ATT AGC ACT AAT CTT G-3'
	MAID 1169 (Bmp2) forward	5'-AAG GGC ACT GGA AAT CCA TCT C-3'
Bmp7	Bmp7 common reverse	5'-AAG CCA GCC TCG CTG ATT G-3'
	Bmp7 wild type forward	5'-GCG TGA GGG TCA GAG CTT ATG 3'
	Bmp7 floxed (-neo)	5'-GGT CAG CAT GGC CGA GGA AG-3'
	Bmp7 knockout forward	5'-TTT AGC CCC TCA GAC AGT CAC-3'
Cre	Twsg wild type forward	5'-ACT TTC TCC CCA CCC GTC TA-3'
	Twsg wild type reverse	5'-AAC AAC AAT GGC ACA ACC TAA T-3'
	Cre recombinase forward	5'-TTC CCG CAG AAC CTG AAG ATG-3'
	Cre recombinase reverse	5'- CCC CAG AAA TGC CAG ATT ACG -3'
mT/mG	gTom common	5'-CTC TGC TGC CTC CTG GCT TCT-3'

Target	Primer type	Primer sequences
	gTom wild type reverse	5’-CGA GGC GGA TCA CAA GCA ATA-3’
	gTom mutant reverse	5’-TCA ATG GGC GGG GGT CGT T-3’
LacZ	LacZ forward	5'-TGG TCG CTG GGG AAT GAA TC-3'
	LacZ reverse	5'-GCC AAA ATC ACC GCC GTA AG-3'
	Twsg wild type forward	5'-ACT TTC TCC CCA CCC GTC TA-3'
	Twsg wild type reverse	5'-AAC AAC AAT GGC ACA ACC TAA T-3'

3.3 Tamoxifen-mediated recombination

Embryonic and maternal effects of Tamoxifen have been previously reported (Ilchuk et al., 2022; Ved et al., 2019). For all of the studies in this thesis, I used Tamoxifen-injected genetic control littermates (negative for Cre allele) to identify recombination-based effects rather than broad consequences of treatment. It should be noted that based on my qualitative observations, bone mineral density in the skull and especially calvaria was reduced following Tamoxifen injection in all mice. However, this did not prevent analysis between littermates injected with Tamoxifen.

Tamoxifen was injected intraperitoneally in a biosafety cabinet at a dose of 10mg/kg for 4 consecutive days (Zhong et al., 2015); volume injected was determined on a case-by-case basis based on daily weight of the animal. Concentrations of working solution were selected as follows to minimize volume injected and ensure accuracy of measurement with 1mL syringes. The 20mg/mL stock solution was prepared from solid Tamoxifen (Sigma-Aldrich, 10540-29-1) in corn oil by shaking overnight at 37ºC (wrapped in foil). Once re-suspended, the Tamoxifen stock solution was stored at 4ºC. All handling of Tamoxifen was done in well-ventilated areas with proper PPE to protect against its potential cytotoxic effects. Mice undergoing Tamoxifen treatment or decontamination were kept in designated filter-top cages in isolation from other animals and monitored closely for co-morbidities. For embryonic inducible deletion using Gli1-CreERT2, dams were injected intraperitoneally with 20mg/mL Tamoxifen with a single dose using a 28-gauge needle at e15.5 for embryo collection at e18.5. For injection of postnatal mice (P5) and adults (P60),

mice were injected for 4 days with 1mg/mL or 2mg/mL working solution (respectively). P5 injection groups were collected at P21 for analysis. Adult mice were subjected to a 7-day washout period and analyzed 35 days later, with day 0 (d0) marking the end of decontamination. Animal welfare was tracked at the time of each injection using an Animal Health Score Sheet which logs criteria for termination according to a combination of Weight and Appearance/Posture scoring. Weight was scored as 0.0 if there was <10% daily weight loss, 0.1 for >10% weight loss, and 0.4 for >20% weight loss. Appearance/Posture was scored 0.0 if normal, 0.1 if the mouse had a slightly hunched posture or reduced activity, and 0.4 if hunching, slow or no movement, rough fur, or apparent distress were observed. The total score of these two measures corresponded to termination criteria, in which scores greater than or equal to 0.1 warrant close monitoring of the mouse (2x daily). If the score exceeded or equaled 0.4, the animal was euthanized.

3.4 Micro-computed tomography

All micro-computed tomography (μCT) scans were performed using a MiLabs UHT-μCT scanner (Milabs, Utrecht, the Netherlands) with the following parameters: 50 kV voltage, 0.24 mA current, 75ms exposure time, 1600 exposures per rotation. For live scans, mice were anaesthetized with isoflurane in a chamber, then transferred to the μCT scanning bed equipped with nose cone-delivery of isoflurane. Similar scanning parameters were used for *ex vivo* scans of PFA-fixed skulls. Borders for μCT scanning were selected in the MiLabs application based on preliminary x-ray preview and scans were reconstructed to contain the region of analysis at 25μm resolution prior to handling in 3D Slicer (www.slicer.org, Fedorov et al., 2012). Three dimensional reconstructions were used for anatomical comparison of skulls and representative orthogonal planes of sectioning.

For Chapter 5, embryos were collected and fixed at e18.5 for micro-computed tomography (μCT) to visualize hard tissue structures as previously described (Baddam, Biancardi, et al., 2021). CT scans were reconstructed at 25μm resolution and rendered in 3D Slicer for analysis (Fedorov et al., 2012). Semi-automatic segmentation was done in the Segment Editor module using the islands tool to split the reconstruction into segments greater than 50 voxels. Fine tuning of segmentation was done using the scissors tool.

3.5 CT morphometrics

For Chapter 4, I quantified the presence or absence of Wormian bones across P0, P7, P14, and P30 mice. These supernumerary inter-frontal bones are often found in wild type C57/BL6 mice. We noted that this bone disrupted the internasal suture and appeared larger in Bmp7 ncko mice (not quantified), so opted to count the frequency of its appearance in 3D reconstructions of CT scans. For each scan, the absence of a Wormian bone was scored as 0, and the presence as 1. I then visualized the relative proportions of total mice in each age group with stacked bar plots shown in Figure 4.1E.

To quantify the extent of interdigitation, also known as suture complexity, of the frontal-premaxillary suture in Bmp7 ncko mice, I collected 3 repeat measurements of 3D lengths in the Slicer Markups module on each side (left/L or right/R) for the total distance traveled by the suture (fpmx_a) (Curve tool) and the shortest distance between the first and last points of the suture (fpmx_b) (Line tool). For total distance, each point was placed at the furthest point of interdigitation for each period, as below. I then averaged each measurement per suture (recorded as avg_fpmx_a/b) and ascertained fpmx_complexity_L/R by dividing avg_fpmx_a by avg_fpmx_b. These measurements (recorded in mm) were collected for n=3 each of P14 Bmp7 ctrl (Bmp7 wt or wt/fl or fl/fl Wnt1-Cre^{neg}) and Bmp7 ncko (Bmp7 fl/fl Wnt1-Cre^{pos}) mice. I also approximated asymmetry between left and right suture complexity by dividing the two fpmx_complexity values, wherein a proportion of 1:1 (closest to 1.0) would indicate perfect symmetry between left and right sides, and smaller fractions (closer to 0) would indicate asymmetry. To visualize these metrics, I created a scatter plot of left and right fpmx_complexity values for both genotypes at P14 and box plots representing their standard deviation and average values. I visualized the fpmx_complexity_ratio score for symmetry with violin plots comparing the two genotypes. These plots are shown in Figure 4.1F.

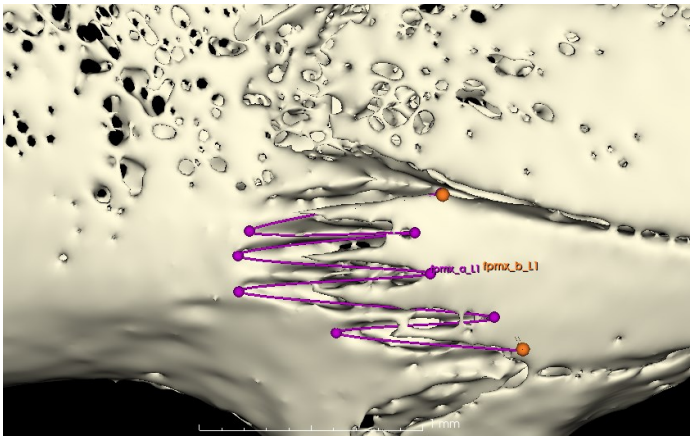

Figure 3.2 Suture interdigitation 3D measurement example. Top-down view of frontal-premaxillary suture reconstructed in 3D Slicer for landmarking. Purple curved lines measure length traveled by suture, while orange points indicate shortest distance. The ratio of purple length over orange length was used to calculate suture complexity.

Preliminary morphometric mesh comparison of P14 Bmp7 ctrl and ncko CT scans in Figure 4.1B,C was done in collaboration with Dr. B. Hallgrimsson's lab. Briefly, the two skulls were compared on the basis of extracted surface meshes, which could be mapped to each other as previously described to predict regions of cranial dimensionality (Roth, Baddam, et al., 2021). Results were visualized as heatmaps using Morpho (Schlager, 2017).

Nasal bone trabeculation in Bmp Gli1-CreERT2 mice for Chapter 5 was quantified in ImageJ. Coronal cross-sections through the nasal bones, captured in 3D Slicer at 2-3 depths, were loaded into ImageJ and converted to 8 bit image format (Figure 3.3). The rectangle tool was used to capture the nasal bone cross-section spanning from the left to right lateral pre-maxillary/nasal bone sutures, and including the most endocranial point of the nasal bones. This cropped field of view was thresholded to binarize the bone and negative space (and therefore separating the trabeculae). Area of trabeculae was recorded

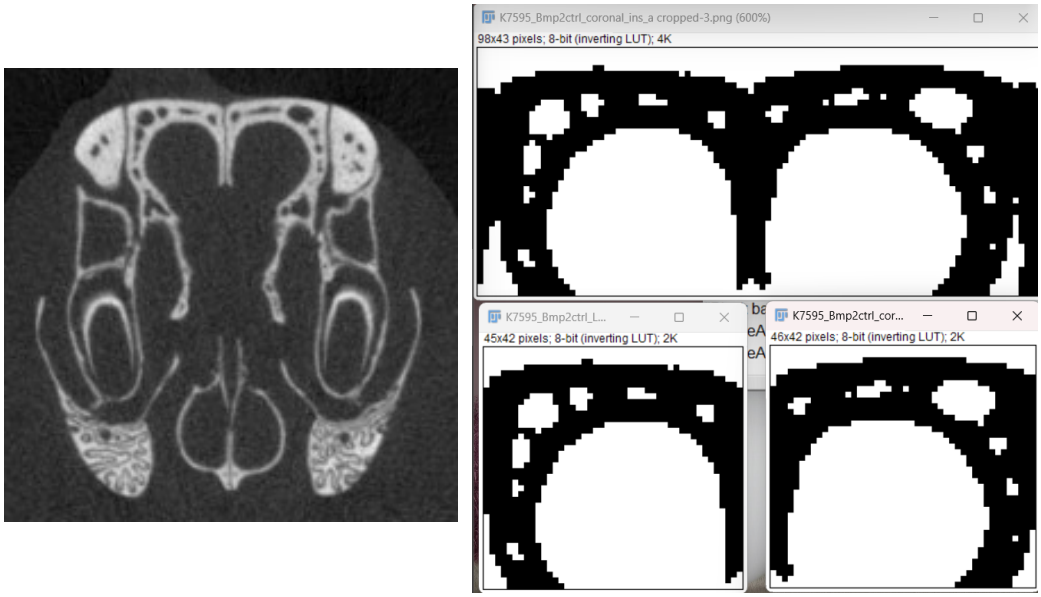

Figure 3.3 Binarization of nasal bone cross-sections from CT scans for ImageJ trabecular analysis.
Left panel: Un-adjusted CT scan coronal cross-section through nasal bones (image captured in 3D Slicer). Right panels: Binarized and cropped nasal bones in ImageJ, where black pixels indicate mineralized tissue and white islands of pixels are trabeculae within the bone.

using the Analyze Particles tool, excluding edges and enabling bare outlines to check accuracy of segmentation. Area for each trabecula was recorded. Total bone area was captured by inverting the cropped images, unchecking the "exclude on edges" menu option, and recording the area output.

I also developed a method to score the cranial base synchondrosis fusion phenotype observed in Bmp2 and Bmp7 cko mice. The framework was based loosely on a four-stage characterization of human synchondroses that scored fusion in stages from 0 (unfused) to 3 (complete fusion), with intermediate scores 1 and 2 indicating endocranial or ectocranial fusion (Franklin & Flavel, 2014). In my analysis, I defined stages as follows:

Stage		***Description***
1	Unfused	Normal, unfused appearance (completely open).
2	Fusing	Bridging of the endocranial or ectocranial margin; not fully fused.
3	Fused	Single, fused bone. May bear evidence of a "fusion scar", but cartilage/synchondrosis is not evident.

For the postnatal injection groups, I analyzed 10 Bmp2 or Bmp7 ctrl mice (Bmp2/7 fl/fl:Gli1-CreERT2^{neg}, Tamoxifen-injected; 6 female, 4 male), 6 Bmp2 cko mice (Bmp2

fl/fl:Gli1-CreERT2^{pos}, Tamoxifen-injected; 4 female, 2 male), and 3 Bmp7 cko mice (Bmp7 fl/fl:Gli1-CreERT2^{pos}, Tamoxifen-injected; 2 female, 1 male). Adult groups included 15 Bmp2 or Bmp7 ctrl mice (7 female, 8 male), 6 Bmp2 cko mice (3 female, 3 male), and 9 Bmp7 cko mice (5 female, 4 male). CT scans were reconstructed in 3D Slicer using the Segment Editor Tool, and a parasagittal orthogonal slice was positioned using the Reformat module. Scrolling through the entire width of the synchondroses, I assigned scores of 1-3 for each mouse. These scores were visualized with stacked barplots of frequency for each score and group, split by synchondrosis (ISS or SOS).

The visualization of embryonic cranial base CT phenotypes in Figure 5.4 of Chapter 5 was built from four categories of binary observations corresponding to phenotypes I discuss: absence of the presphenoid bone (missing_presph), likely cleft palate (cleft), fragmented basisphenoid bone (frag_basisph), and a hole or notch in the basisphenoid bone (basisph_notch). The goal of the visualization was to see if the different genotypes (ctrl, Bmp2 ncko, Bmp7 ncko, Bmp7 cko, Bmp7 ko, Bmp2hetBmp7hetncko, Bmp2hetBmp7flncko, Bmp2flBmp7hetncko) clustered according to these metrics. With 4 categories of scoring, 8 genotypes, and several measurements for each group, I chose to use Uniform Manifold Approximation and Projection (UMAP) to plot the results in high dimensions, and project into a low-dimensional (2D) space. For each category, I logged the mouse's ID, genotype, and 0 or 1 for each category indicating presence or absence of the given phenotype. I generated this plot in R by loading the data from my data collection spreadsheet into R and applying UMAP. The four binary phenotype columns were concatenated into a single string with the get_combinations() function so that I would be able to identify unique combinations of the phenotypes per observation. These scores are ultimately plotted using UMAP on the plot to fit UMAP1 and UMAP2 dimensions for lower-dimensional embedding.

3.6 Tissue processing

For tissue collection at the University of Alberta, mice were euthanized with Euthanyl Sodium Pentobarbital injection (200mg/kg, DIN #00141704) and pre-fixed via 4% PFA cardiac perfusion (4% PFA w/v, 0.04M NaOH, 10% 10X PBS). Skinned heads were further fixed for 24 hours on a rotator at room temperature in 4% PFA. At the National Institutes of Health, mice were sacrificed by CO_2 inhalation and cervical dislocation. Tissue was

fixed using 10% neutral buffered formalin. After CT scanning, heads were decalcified with 0.5M EDTA, pH 7.4 for 1-30 days, depending on extent of mineralization. Adult heads were dissected with a fresh razor blade for deeper EDTA penetration. After sufficient decalcification, tissue was pre-soaked in 50% ethanol and processed for paraffin embedding in tissue cassettes using a benchtop Leica TP1020 or cabinet HistoCore tissue processor according to the following program: 70% EtOH (1hr), 95% EtOH (1hr), 2X 100% EtOH (1hr each), 3X xylene (1hr each), 2X paraffin (1hr each, with vacuum). Cassettes were then transferred to a 60-65ºC paraffin bath (Fisherbrand Histoplast LP, Cat No. 22900702) for embedding at the Leica EG1160 paraffin embedding station. Blocks were cooled at 4ºC prior to sectioning.

3.7 Histology

Paraffin blocks were sectioned using a manual American Optical Corporation microtome or semi-automated Leica HistoCore Autocut at 5-10µm thickness onto Superfrost™ Plus charged glass slides (Fisher Scientific, #12-550-15). For all histological stains, slides were deparaffinized and rehydrated as described in Appendix A (Roth, Puttagunta, et al., 2022). Briefly, wax was melted at 60ºC and slides were treated with a series of xylene and graded EtOH washes to water. For hematoxylin and eosin staining, nuclei were stained with Mayer's hematoxylin (Fisher, #SH30-500D), bluing reagent (Richard-Allan Scientific, Cat No. 7301), and clarifier (Richard-Allan Scientific, Cat No. 7402). Tissue was counterstained with eosin (1% Eosin Y w/v in 60% EtOH), dehydrated, and coverslipped with toluene-based mounting medium. For tartrate-resistant acid phosphatase (TRAP) staining, slides were incubated in TRAP staining buffer (800µg/mL Fast Red Violet LB Salt, 0.02g/mL Naphthol AS-MX Phosphate, 40µL/mL 2-Ethoxyethanol in lab-made TRAP Basic Incubation Medium, pH 5.0) at 37ºC. When the violet osteoclast stain had developed sufficiently, slides were counterstained with 0.02% Fast Green, dehydrated, and coverslipped. For orcein stain, slides were incubated at 56ºC in orcein solution (1g/mL orcein in 70% EtOH, 1% hydrochloric acid) until red stain had deposited on elastic fibers, then differentiated in 1% acid alcohol until brown. Tissue was counterstained with 1% methylene blue (1% w/v methylene blue, 2% w/v citric acid in 95% EtOH) until nuclei and chondrocytes were dark blue, then dehydrated and mounted. For pentachrome staining, slides were treated with 6% nitric acid, then dipped in toluidine blue (0.5g in 100mL

ddH_2O, pH 1-1.5) and incubated in picrosirius red solution (0.5% w/v Sirius Direct Red in aqueous picric acid) with agitation for 10 min or until bone was stained red, then dehydrated and mounted.

Brightfield microscopy was captured using an Olympus IX73 microscope equipped with a DP80 camera (U of A School of Dentistry), a Hamamatsu Nanozoomer slide scanner (CPPFD), or a Zeiss Axioscan.Z1 slide scanner with a Hitachi sCMOS Orca Flash 4.0 camera as single planes (U of A Cell Imaging Core). Images were adjusted using the respective software from each microscope, ImageJ (Schindelin et al., 2012), or Adobe Suite software.

3.8 Immunofluorescence and in situ hybridization

Indirect immunofluorescence for protein detection was performed following deparaffinization and rehydration as in histological stains. Slides were then washed in 1X TBST (5mM TBST, 0.0025% Triton, pH 7.6) and submerged in 1X PBS (0.8% NaCl, 0.02% KCl, 0.144% Na_2HPO_4, 0.024% KH_2PO_4). Tissues with dense cartilage matrix, such as the cranial base, were pretreated with an enzymatic proteinase K antigen retrieval period at 37ºC. Antigen retrieval with boiling sodium citrate was used for all other tissue. Slides were then incubated for 30 minutes at room temperature with a 10% blocking solution of goat or donkey serum in 1X TBST (according to secondary antibody host). Blocking solution was replaced with 20-50µL appropriately diluted primary antibodies (information in Table 3.2) and incubated in a humid chamber at 4ºC overnight. On the following day, slides were washed in 1X TBST and submerged in 1X PBS prior to secondary antibody application (details in Table 3.2). Working in the dark, slides were incubated at room temperature for two hours, then washed again in 1X TBST and 1X PBS. Nuclei were counterstained with DAPI (Molecular Probes, Cat No. D-1306) for 15 minutes at room temperature. Slides were washed as before and mounted with aqueous lab-made DABCO-Mowiol and allowed to dry overnight before imaging.

Table 3.2 Reagents and resources.

REAGENT or RESOURCE	SOURCE	IDENTIFIER
Antibodies for immunofluorescent detection (dilution)		
BD Pharmingen™ Rat Anti-Mouse CD44 (1:200-400)	BD Biosciences	553133
Fibromodulin Monoclonal antibody (1:400)	Proteintech	60108-1-Ig
Non-phospho (Active) β-Catenin (Ser45) (D2U8Y) XP® Rabbit mAb (1:100-200)	Cell Signaling Technology	19807S
PCNA Antibody (PC10) (1:200)	Santa Cruz Biotechnology	sc-56

Piezo1 (extracellular domain) Polyclonal antibody (1:200)	Proteintech	15939-1-AP
Phospho-SMAD1 (Ser463/465)/ SMAD5 (Ser463/465)/ SMAD9 (Ser465/467) (D5B10) Rabbit mAb (1:200)	Cell Signaling Technology	13820S
ROCK2(middle) Polyclonal antibody (1:100/200)	Proteintech	21645-1-AP
Probes for RNAscope *in situ* hybridization		
RNAscope™ Probe-Mm-Sparc-C2	Advanced Cell Diagnostics	466781-C2
RNAscope™ Probe-Mm-Alpl-C4	Advanced Cell Diagnostics	441161-C4
RNAscope™ Probe-Mm-Dmp1-C3	Advanced Cell Diagnostics	441171-C3
RNAscope™ Probe-Mm-Ctsk	Advanced Cell Diagnostics	464071
RNAscope™ Probe-Mm-Six2-C3	Advanced Cell Diagnostics	500011-C3
RNAscope™ Probe-Mm-Bmp7	Advanced Cell Diagnostics	407901
RNAscope™ Probe-Mm-Runx2-C2	Advanced Cell Diagnostics	414021-C2
RNAscope™ Probe-Mm-Sost-C4	Advanced Cell Diagnostics	410031-C4
Additional immunofluorescent / RNAscope reagents		
10X 50mM TBST 0.025% Triton, pH 7.6	Labmade	N/A
10X PBS, pH 7.4	Labmade	N/A
DAPI	Molecular Probes	D-1306
2.5% DABCO-Mowiol aqueous mounting medium	Labmade	N/A
RNAscope™ Probe Diluent	Advanced Cell Diagnostics	300041
RNAscope™ Multiplex Fluorescent Reagent Kit v2	Advanced Cell Diagnostics	323100
Custom Bone Pretreatment Reagent	Advanced Cell Diagnostics	300040
RNAscope™ 4-plex Ancillary Kit for Multiplex Fluorescent Kit v2	Advanced Cell Diagnostics	32310
Antibody Diluent/Block	Akoya Biosciences	ARD1001EA
Secondary antibodies / probe detection		
Donkey anti-Rabbit IgG (H+L) Highly Cross-Adsorbed Secondary Antibody, Alexa Fluor™ 647	Invitrogen	A-31573
Donkey Anti-Rabbit IgG H&L (Alexa Fluor® 647)	Abcam	ab150075
Opal™ 520 Reagent Pack	Akoya Biosciences	FP1487001KT
Opal™ 690 Reagent Pack	Akoya Biosciences	FP1497001KT
Opal™ 780 Reagent Pack	Akoya Biosciences	FP1501001KT

ACD Manual RNAscope assays for one- to four-plex *in situ* hybridization were performed as previously described (Piña et al., 2023), using the probes designated in the key resources table above. Briefly, paraffin slides were baked at 60ºC for 30 minutes and deparaffinized/rehydrated as previously described. All slides were pretreated with Custom Bone Pretreatment Reagent for complex tissues (Advanced Cell Diagnostics, Cat No. 300041) at 40ºC for 30 minutes, followed by hydrogen peroxide incubation for 10 minutes at room temperature. Target probes were diluted in a C1:C2:C3:C4 ratio at 50:1:1:1 as suggested (details in Table 3.2). For probe panels that did not include a C1 component, probe diluent was used in its place. Sections were incubated with 20-50µL probe mix at 40ºC for two hours in a humid chamber, then washed with 1X Wash Buffer and incubated in 5X SSC overnight. Slides were washed 1ith 1X Wash Buffer between each step for the remainder of the experiment. On the second day, RNAscope Multiplex FL v2 Amp reagents 1 to 3 were applied sequentially at 40ºC for 30 minutes, 30 minutes, and 15 minutes (respectively). Slides were washed with 1X Wash Buffer prior to developing channels. Development step was dependent on the probe panel and desired fluorophore

combination, but generally involved 1) application of the appropriate Multiplex FL v2 HRP reagent (15 min, 40ºC), 2) addition of the desired fluorophore (details in Table 3.1), and 3) blocking with Multiplex FL v2 HRP Blocker (15 min, 40ºC). Of note, there is a different protocol for this step when using the Polaris 780 antibody and it must be the final channel developed. Briefly, the appropriate Multiplex FL v2 HRP for the desired channel was added for 15 minutes (40ºC), then replaced with diluted TSA-Dig (30 min, room temperature). Sections were treated with Multiplex FL v2 HRP Blocker (15 min, 40ºC) and the diluted Polaris 780 antibody was added to sections for 30 minutes at room temperature. Following channel development, slides were counterstained with DAPI and coverslipped with Prolong Gold Antifade Mountant (Invitrogen, Cat No. P36930). Slides were dried overnight at room temperature, with long term storage at 4ºC.

Images of fluorescent slides were taken with 10X or 20X objectives on one of the following four microscopes: Olympus IX73 microscope (cellSens Dimension software), Zeiss AxioImager M2 fluorescence microscope with an ORCA-Flash LT sCMOS Camera (ZEN software), Zeiss Axioscan.Z1 slide scanner with a Hitachi sCMOS Orca Flash 4.0 camera (ZEN software), or Leica THUNDER deconvolution widefield microscope equipped with a Leica K8 Monochrome sCMOS camera (LAS X software, ImageJ). Most images were captured as single plane files, except for Z-stacks in 4.7G which were imaged using the Leica Thunder microscope. Images in Chapter 5 were captured with the Zeiss slide scanner using Z-stack acquisition. Only a single focal plane was extracted for analysis.

3.9 Image analysis

Histology and fluorescent staining were interpreted semi-quantitatively in ImageJ (Schindelin et al., 2012) as follows:

3.9.1 Chapter 4

Internasal suture deviation, shown in Figure 4.2, was scored at postnatal days 7 and 14 using coronal FFPE stained sections. Images of sutures were loaded into ImageJ for two calculations: the straightness of the internasal suture (ins.angle) and the angle of the endocranial internasal suture axis relative to the superior nasal septum axis (suture.septum.angle). For ins.angle, three points were placed along the superior, middle, and endocranial internasal suture in the central suture mesenchyme, and the angle was

recorded. For suture.septum.angle, points were placed at the middle and endocranial central points of the internasal suture and one point at the superior central margin of the nasal septum. Each measurement was repeated three times on the same section, with at least 3 sections analyzed per biological replicate by two raters. Three or more biological replicates were analyzed per age and genotype. Scatter plots were generated in RStudio using ggplot.

The density of the suture mesenchyme cells makes counting individual cells challenging. To overcome this limitation, relative measurements of stain compared with the total length of measurement were used. To approximate coverage of osteogenic cells

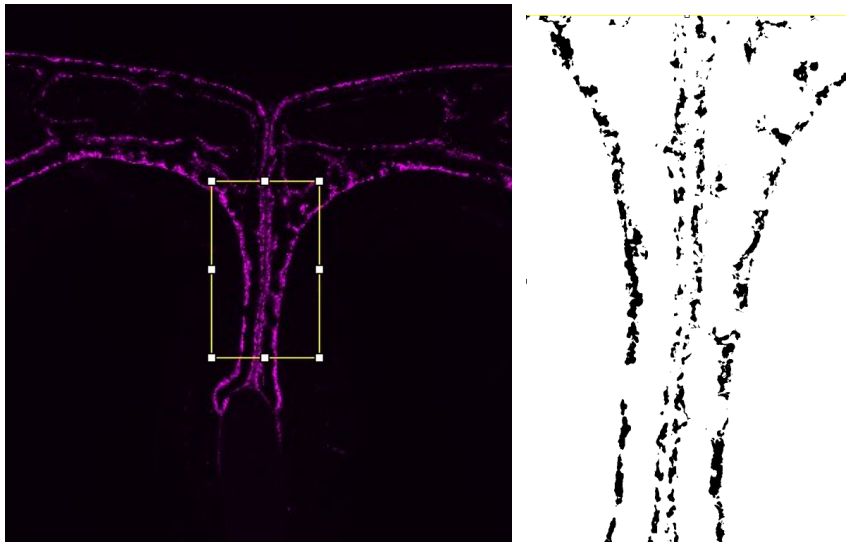

Figure 3.4 Region of interest and binarization example of internasal suture used to calculate coverage of bone by osteogenic cells.
Left panel: Isolated fluorescent image of *Alpl* RNAscope stain in coronal plane of internasal suture. Yellow rectangle indicates the region of interest, which encompasses the endocranial to middle internasal suture. Right panel: Binary image from which proportion of black (*Alpl* positive) pixels was calculated.

over the internasal suture bone surface, I analyzed 1-4 images from 3 Bmp7 ctrl and 3 Bmp7 ncko mice stained for *Alpl* with RNAscope. First, I cropped the coronal section in ImageJ from the bottom of the nasal bone trabeculae to the region of the intracranial internasal suture where the mesenchyme changes in uniformity (in control mice) (Figure 3.3). Then, I applied a binary thresholding mask using Image>Adjust>Threshold and set the scale to highlight *Alpl* positive cells. This yielded a black and white binary image which could be analyzed for simple presence or absence of stain (Figure 3.4). On the thresholded image, I drew a segmented line down the center of the outermost suture positivity (black in this binarization) along the entire vertical field of view. The Gray Values along the line

were extracted using Analyze>Plot Profile and Data>Copy All Data, which I pasted into an Excel spreadsheet separately for each side of the suture. I averaged gray values for each side and then calculated the relative proportion of each. The alpl_ratio scores were then plotted in R for violin plot visualization (Figure 4.3).

To quantify osteoclast infiltration, I used a similar approach on Ctsk immunofluorescent images and a modified technique on brightfield TRAP-stained images. For brightfield, first I loaded images into ImageJ and cropped matching areas of the suture. Then, I split the color channels and closed all windows except the one in which the violet stain was best differentiated. I duplicated this image and applied the threshold settings described above (with "Dark Background" unchecked for brightfield). I again used the segmented line tool to trace the bone-lining cells inside the internasal suture on the un-thresholded image, then copied the selection over to the thresholded image (Figure 3.5). As before, I used the Plot Profile function to determine gray values for each pixel or point along the line, averaged the values, and then calculated a ratio (Ctsk_ratio). Unlike the images in the RNAscope analysis, the TRAP and Ctsk IF images were collected over several years using different microscopes. Thus, the file formats vary. Absolute values collected were not directly comparable without translation of the scale of the images. The ratio calculation method overcomes this limitation by producing relative values that are directly comparable without further transformation.

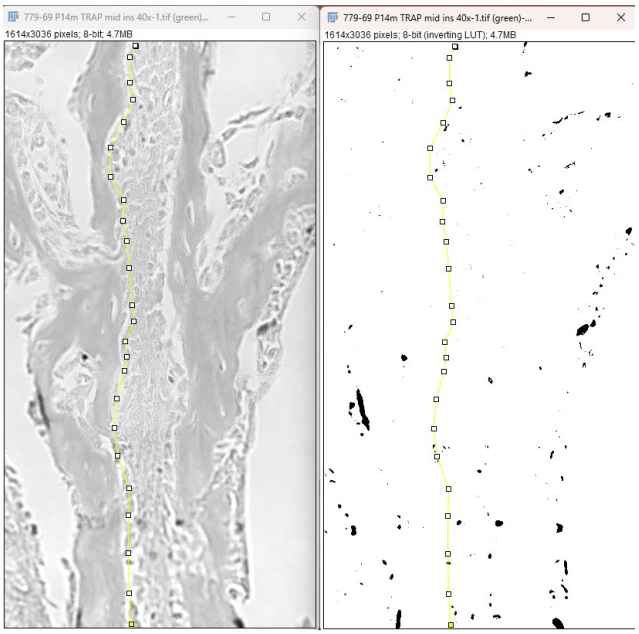

Figure 3.5 Histological image analysis for coverage of bone with TRAP^{pos} cells in ImageJ.
Left panel: Green channel of RGB image of TRAP stain, where violet-stained TRAP^{pos} cells appear darker than Fast Green counterstained tissue. A yellow segmented line was drawn along the inner surface of the nasal bones facing the internasal suture. Right panel: Binary version of image in left panel with segmented line copied over. The proportion of black pixels along the line was recorded for each side.

In normal sutures, there should be very few TRAP^{pos} cells, though occasionally a few cells do stain even if osteoclasts are not present. My Alpl_ratio calculation method was therefore problematic as the appearance of these rare cells skewed the values significantly, with the infiltration of a single cell translating to severe asymmetry. Thus, I modified the calculation so that the proportion of the line drawn with Gray_Values above 0 was accounted for rather than the overall mean. With a threshold of 1, I counted the number of points above the threshold and divided by the total number of measurements with the following Microsoft Excel formula: = COUNTIF (*Gray_Value_range*, ">1") / COUNTA (*Gray_Value_range*). The same approach was used for immunofluorescent staining quantification for Ctsk.

For osteocyte quantification in the P0 nasal bones, I loaded my Leica or Zeiss microscope images into QuPath and used the "Send region to ImageJ" tool to import the files. I selected the endocranial nasal bones with a square selection tool of 500-1000px^2. Using the Brightness & Contrast tool, I adjusted the maximum levels for each channel so that the brightest pixels were not oversaturated, keeping the detail of the cells. Then, working in Composite mode from the Channels tool, I used the brush tool to mark nuclei expressing *Dmp1* (magenta) or *Sost* (white) (Figure 3.6). I also added cyan dots to cells which co-expressed *Runx2*. Due to the compact nature of the internasal suture and nasal bone-lining cells, it is challenging to identify which cells are inside the bone or in the lining

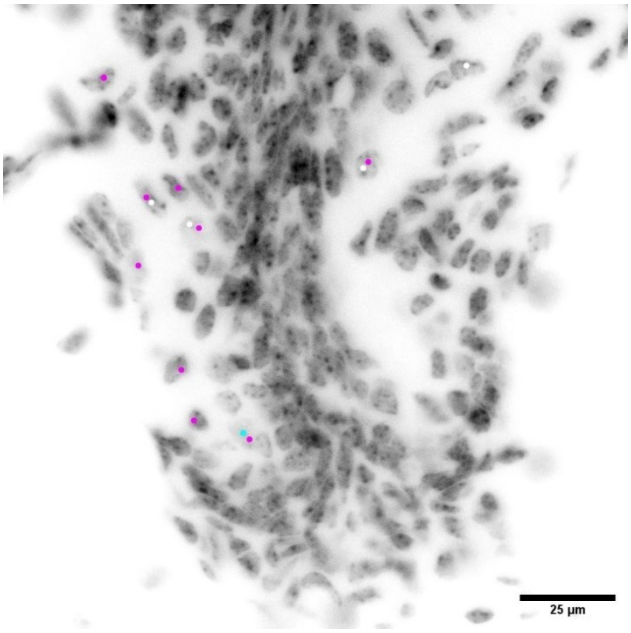

Figure 3.6 Example from newborn internasal suture of labeled osteocytes based on RNAscope *Runx2/Dmp1/Sost* multiplex experiment.
DAPI nuclear counterstain is visualized as an inverse projection of greyscale pseudocoloring in this image. I used the brush tool in ImageJ to add colored dots to nuclei determined to be positive for *Dmp1* (magenta) or *Sost* (white) in the composite image to aid with counting and documentation. For cells also expressing *Runx2* (in addition to the other osteocyte markers), I added a cyan dot. The proportions of each combination of colored dots were calculated for left and right sides in all mice.

compartment. This method was focused on cells that were only positive for *Dmp1* or *Sost*. I manually counted the cells in the bone on each side and used the combinations of *Dmp1* and *Sost* positivity to approximate osteocyte maturity with a weighted index of maturity (oct_mat). For this, I assigned a weight of 1 to presumed early-stage osteocytes which were *Dmp1* positive only, a weight of 2 for mid-stage *Dmp1/Sost* double positive cells, and a weight of 3 for late-stage *Sost* single positive cells. I calculated this index for each side (left or right) with the following formula:

$$oct\_mat_L = (1 \cdot Dmp1_L) + (2 \cdot Dmp1\_Sost_L) + (3 \cdot Sost_L)$$

Then, I divided the oct_mat measurements from each side to identify osteocyte maturation index symmetry between left and right nasal bones (asymm_oct_mat). I visualized the data with a violin plot of asymm_oct_mat values between Bmp7 ctrl and Bmp7 ncko groups, wherein 1.0 indicated perfect symmetry between scores on either side, and 0 indicated asymmetry. I used the Wilcoxon rank-sum test (Mann-Whitney U) to compare central tendencies without assuming normality and calculated the effect size for the data.

To quantify my qualitative observations of *Bmp7* asymmetry in the P0 internasal suture abutment, I cropped images of the endocranial tips of control nasal bones using the ImageJ selection tool (150px^2). For each of three mice, I recorded the percent coverage of DAPI^{pos} pixels in the field of view (DAPI_L/R) and *Bmp7*^{pos} pixels (Bmp7_L/R). This measurement was done after conversion of the images into 8bit format and binarization with the Threshold tool. I accounted for cell density by dividing the Bmp7_L/R value by DAPI_L/R and recorded this output as poscells_L/R, which could then be further divided between sides to approximate symmetry. I also recorded an un-normalized ratio by dividing Bmp7_L and Bmp7_R. Data was visualized with boxplot script in R to compare Bmp7 (un-normalized) symmetry with DAPI symmetry, with additional Wilcoxon rank-sum test, pictured in Figure 4.7F.

3.9.2 Chapter 5

For osteocyte quantification in adult Gli1-CreERT2 experimental groups in Figure 5.2, images were captured using the Zeiss Slidescanner and the whole internasal suture with bordering nasal bones was imported into ImageJ. The optimal plane of focus was selected from Z-stack projection and isolated for further analysis. Nuclei expressing *Dmp1* (magenta) or *Sost* (white) were marked using the brush tool. The osteocyte scoring process

was similar to the methodology described for Chapter 4., though without *Runx2* quantification. Asymmetry in osteocyte maturation (asymm_oct_mat) between the left and right nasal bones was calculated by dividing the oct_mat measurements from each side. This data was visualized using violin plots to compare asymm_oct_mat values between Bmp7 control (ctrl) and Bmp7 neural crest knockout (ncko) groups, where a value of 1.0 indicated perfect symmetry and 0 indicated asymmetry. The Wilcoxon rank-sum test (Mann-Whitney U) was used to compare central tendencies without assuming normality, and the effect size for the data was calculated. Total osteocyte presence was also evaluated by counting the total number of nuclei (DAPI-positive cells) and visualized using scatter plots with accompanying box plots. The data was grouped by genotype, and the Wilcoxon rank-sum test was applied to compare the groups. Osteocyte maturation was quantified as described in Chapter 4, with cells positive for *Dmp1*, *Dmp1/Sost*, and *Sost* counted, and the proportions normalized to DAPI counts were calculated. These proportions were visualized using a stacked bar plot to illustrate the distribution of osteocyte maturation markers across genotypes.

Chondrocyte hypertrophy in Figure 5.3 was approximated with ColX immunofluorescent experiment .czi image files. Images were loaded in Zeiss Zen Blue software, adjusted, and cropped to the spheno-occipital synchondrosis (SOS). Each file was then loaded into ImageJ, split into separate images with “Stack to Images”, and thresholded for binary assessment with auto settings. The percent area for each binary mask was calculated with the Measure tool and recorded for DAPI and ColX in a spreadsheet, which was then processed in R for visualization and statistical analysis.

3.10 Spatial transcriptomic assays

Freshly cut 5-10µm-thick paraffin sections were used for both 10X Genomics Visium and Xenium spatial transcriptomic assays. Multiple sections were placed within a defined fiducial frame (11mm^2 for Visium, 12mm by 24mm for Xenium) and baked briefly at 56ºC. Standard protocols for each assay were followed, with high resolution brightfield imaging at their conclusion. Both Visium and Xenium spatial transcriptomics systems enable spatially resolved gene expression analysis, however each has its strengths. Visium assays typically capture 2-10 cells in each barcode and involve whole-transcriptome sequencing. The Xenium system allows for sub-cellular detection of individual mRNA transcripts. At

the time of adoption, however, the assay only allowed a 350-gene list for custom probe panel design.

The Xenium experiment was one slide containing three regions of wild type coronal craniofacial sections: Region 5, 6, and 7. Region 5 contained two P0 anterior planes of sectioning (P0a,b) and one anterior e15.5 section (e15.5a). Region 6 contained one middle P0 section (P0c), one torn P0 section that was not analyzed (P0d), one anterior e17.5 section (e17.5a), and one middle e17.5 section (e17.5b). Region 7 contained two posterior e15.5 sections (e15.5b,e), one middle e15.5 section (e15.5c), and one anterior e15.5 section (e15.5d). For the study in this thesis, only the middle region e15.5 was analyzed (section e15.5c).

3.11 RNA sequencing

For Chapter 4 single nucleus RNA sequencing (snRNA-seq), internasal sutures were dissected from postnatal day 4 (P4) wild type mice provided by Dr. E. Mezey (3F, 3M littermates) into 1.5mL Eppendorf tubes and snap frozen on dry ice as depicted in Figure 3.7. Briefly, mice were euthanized with CO_2 overdose and decapitation. Skin, hair, and extra tissue were removed and the outer surface of the skull was gently scraped with a fresh razor blade. Using a razor blade, the rostral end of the nasal bone was severed at its transition to the cartilaginous nasal tip, exposing the sinus cavity. Fine point scissors were used to cut just below the nasal bone surface from anterior to posterior to release the nasal bones from the nasal septum. Then, the nasal bones were each cut down their central anterior-posterior axes back to the frontonasal suture to remove the lateral margins. The internasal suture block was then flipped upward and removed for collection with a single cut just anterior to the frontonasal suture. Snap frozen tissue was stored at -80ºC until digestion. For Chapter 6 single-cell RNA sequencing (scRNA-seq), mid-palatal sutures were dissected with surrounding palate tissue from embryonic day 15.5 (e15.5) or P1 littermates and snap frozen. Tissue handling and RNA sequencing were performed at the NICHD Molecular Genomics Core. Cellranger output files were then used for further downstream computational analysis. All analysis in this thesis was done using single technical replicate datasets.

Figure 3.7 Dissection of internasal suture for RNAseq.
The rostral cartilaginous portion of the nose was removed using a sharp razor blade, then nasal bones were bisected in the rostral to caudal direction with small surgical scissors. A single cut was also made in this direction through the superior border of the nasal septum to release the nasal bones. The resultant tissue block, containing the internasal suture, was flipped upward and collected with a final cut rostral to the frontonasal suture.

Nuclei were dissociated for snRNA-seq according to the 10X Genomics protocol for "Nuclei Isolation from Complex Tissues for Single Cell Multiome ATAC and Gene Expression Sequencing" (10X Genomics protocol CG000375), then sequenced on the Illumina NovaSeq 600 sequencer at the NICHD Molecular Genomics Core using the 10X Genomics Chromium System. For scRNA-seq done at the NIH, standard 10X Genomic operating procedures were followed. Cellranger output files were then used for further downstream computational analysis. In addition to RNA sequencing data that we generated, I also made use of online Facebase scRNA-seq repositories, specifically for frontal sutures from the Holmes group (Holmes et al., 2017; Samuels et al., 2020).

For scRNA-seq at the University of Alberta shown in Chapter 5, we followed the Parse Biosciences Evercode WT v2.2.1 protocol for cell suspension, fixation, barcoding, and library generation on primary tissue dissected from Bmp2 ctrl and ncko cranial base. Tissue was digested and processed for single-cell suspension according to Parse Biosciences standard protocols. Briefly, tissue was manually broken down into small pieces and incubated in collagenase type II enzymatic solution (13.33µL 3% collagenase type II, 200µL DMEM, 5µL 20X BSA) at 37ºC, 350RPM for up to 2 hours. Digested tissue was diluted in warm DMEM with 10% FBS, 1% Pen/Strep, and 1% L-glutamine. Cells were filtered through a 40µm strainer and centrifuged for 10min at 4ºC, 200xg. Supernatant was replaced with 1mL complete DMEM and resuspended. After single-cell suspension, up to 4 million cells were used for fixation. Cells were centrifuged 10 min at 4ºC, 200xg and supernatant was replaced with cold Cell Prefixation Buffer. Cells were resuspended and

filtered through a 40µm strainer, then sequentially treated with Cell Fixation Solution, Cell Permeabilization Solution, and Cell Neutralization Buffer. After 10min centrifugation at 4ºC and 200xg, the supernatant was replaced with cold Cell Buffer and cells were resuspended and filtered through a 40µm strainer. These cells were used for Parse Biosciences Evercode barcoding, library preparation, and sequencing by Mike Wong at the University of Alberta Advanced Cell Exploration Core and by Tara Stach at the University of British Columbia sequencing core. Sequencing was done in two stages on an Illumina sequencer, with 8 billion reads each for a total of 100k cells across all libraries and a second "top-up" round for a total of 16 billion reads.

3.12 Computational analysis

All computational analysis was done in the R programming environment, mainly using the Seurat v4 and 5 (Hao et al., 2021, 2024). Other packages used for pre-processing and visualization included PopsicleR (Grandi et al., 2022), Nebulosa (Alquicira-Hernandez & Powell, 2021), Giotto (Dries et al., 2021), SCpubr (Blanco-Carmona, 2022), and singlecellHayStack(Vandenbon & Diez, 2023). Up to date code is located at github.com/dmartaroth. Code is written with reproducibility in mind using the here() package to define file architecture and in-code export of figure panels. Custom themes, packages, functions, and directories are defined in separate .R files within the 'docs' directory for each project or major stream of analysis. For GO term analysis, I utilized a combination of the GO::TermFinder (Boyle et al., 2004) web tool with export to REVIGO (Supek et al., 2011). Annotation was done manually based on marker genes from the literature. A description of the computational analysis is organized below by chapter, as mixed methods and techniques were used for each. Chapter 4 utilized 10X Genomics single-nucleus RNA sequencing and Visium spatial transcriptomics, Chapter 5 utilized Parse Biosciences single-cell RNA sequencing only, and Chapter 6 included 10X Genomics single-cell RNA sequencing and Visium/Xenium spatial transcriptomic platforms in tandem.

3.12.1 Chapter 4: snRNA-seq, Visium

The Visium analysis in Figure 4.4 was done in the R coding environment. Two samples, WT1 and WT2, were loaded, normalized, and assessed for predicted gene expression. I subsetted endocranial and ectocranial gems (barcodes) from each section with a

combination of spatial and gene expression criteria. These subsets, designated “endo” for endocranial and “ecto” for ectocranial, were used for comparative analysis of gene expression trends between the regions. Following segmentation of these gems, I used the SpatialFeaturePlot() function in Seurat to visualize *Runx2*, *Cd200, Col2a1,* and *Sost* spatial expression. Violin plots of known osteogenesis-related genes were generated with the Stacked_VlnPlot() function. I extracted markers for the different regions (endo vs ecto) with FindAllMarkers(), and visualized the results in a heatmap, spatial feature plot, and violin plot. For Gene Ontology analysis, I used the ReviGO web tool (Supek et al., 2011).

Single-nucleus RNA sequencing data pre-processing was initially conducted using the PopsicleR() package; some scripts have been updated for compatibility with Seurat v4 changes in documentation. In the updated scripts, raw data was imported with the Read10X() function. Basic quality control, detailed in my FIG6_01_import-snrnaseq-process.R script, was applied based on violin plot examination with the following parameters:

- 200 < nFeature_RNA < 4000
- nCount_RNA > 200
- percent.mito < 0.15

Data was then normalized and scaled followed by variable feature identification and dimensionality reduction with PCA. To visualize the data, I applied UMAP reduction and selected the optimal clustering resolution iteratively. For further analysis and annotation, I set the resolution parameter to 0.1. Doublet detection and filtering was performed using DoubletFinder(). I then manually annotated cell types for each cluster based on the literature and previously identified markers. This process was aided by extraction of top markers for each cluster to predict possible cell populations.

The annotated RDS object was further subsetted to investigate expression profiles of cells expressing *Bmp7*. First, I assigned labels to barcodes where *Bmp7* expression was greater than zero (pos_cells) and exactly zero (neg_cells) in a new metadata column. Then, the data was split according to this variable. I used FindAllMarkers() to identify marker genes associated with *Bmp7*-positive cells with a log.fc.threshold of 0.25 (positive changes only). These results were saved to a .csv file for further analysis and visualized with

heatmap plotting. Finally, I plotted GO Terms from this list of top genes with the ReviGO web tool. Scripts for this chapter are backed up to Github in the Bmp7-ins repository.

3.12.2 Chapter 5: scRNA-seq

For Chapter 5, the cellRanger output was filtered using the Seurat v5 package in R. Each dataset was imported as a Seurat object (CTRL_1: 3,322 cells total, median 5,256 genes/cell; CTRL_2: 3,774 cells total, median 7,360 genes/cell; NCKO_1: 5,435 cells total, median 4,356 genes/cell; NCKO_2: 7,486 cells total, mean 2,746 genes/cell (after filtering)). Control datasets were integrated separately from mutant datasets, then both groups were integrated using Seurat canonical correlation analysis (CCA) integration for further analysis. The merged integrated Seurat object was clustered at two resolutions (low: 0.1, high: 0.3) and annotated manually according to the expression of known marker genes from the literature. At 0.3 resolution, the following clusters were identified: chondrogenic (chondro.1-3), ciliated, epithelial (epith), immune (imm.1-2), mesenchymal (mes.1-4), mitotic (mito.1-2), neural (neu.1-6), and vascular (vasc.1-2). Additional packages used for plot generation are detailed in complete code, available at github.com/dmartaroth in the parse-seq repository.

3.12.3 Chapter 6: scRNA-seq, Visium, Xenium

10X Xenium analyzer outputs were fully analyzed in RStudio. I did not use the Xenium Explorer browser for this study due to its incompatibility with downstream in-depth analyses. The raw data contained a cell feature matrix, experiment.xenium file, images of the H&E stained slide, spreadsheet of features included in my custom xenium panel, coordinates for cell and nucleus boundaries, transcript detection information, and spatial localization details for detected cells. In script 01_import-xenium-regions_save-gobject.R, each of these components was loaded and appended with metadata for the features (ensemble_ID, feat_name, feat_type) using the Giotto R package, which was utilized for most of the following analysis. Transcript-level data was loaded and filtered by Phred score, which is an indication of the precision of base calling during the sequencing. The Phred filtering threshold was set to include values greater than or equal to 20, as suggested in the Giotto processing vignette. Loaded data was previewed for expression of transcript with distinct expression patterns. Polygon data was loaded and a subcellular Giotto object

was generated with the createGiottoObjectSubcellular() function, then saved for future analysis as an .Rds file.

Sections within each region were subsetted and processed in script 02_subset-regions_process.R. For this chapter, the region 7 Giotto object (gobject) was loaded and interactively subsetted to the e15.5c section using a looping script I wrote to fine-tune coordinate selection. E15.5c was bounded by the following coordinates: x_min = 5150, x_max = 5800, y_min = 3150, y_max = 3500. The subset metadata was stored in a new gobject and feature metadata was appended. Data was then filtered to include cells with expression greater than 1, features detected in at least 3 cells, and cells with at least 5 features each. I then added gene and cell statistics to the gobject with the addStatistics() function using 'raw' expression values. Data was normalized according to the cell spatial unit and scale factor of 5000 and Highly Variable Features were calculated for the dataset. I ran a PCA reduction on the gobject using the cell spatial unit and scaled expression values, then ran tSNE and UMAP reductions using dimensions 1:10. For Xenium data, I used Leiden clustering instead of default Seurat clusters or Louvain clustering. First, I used the createNearestNetwork() function for dimensions 1:10 and used a k value of 10, then applied doLeidenCluster() on the gobject with a resolution of 0.25 and 100 iterations. This clustering resolution was determined visually by repeating the analysis across several resolutions. 0.25 provided distinct clusters with clear separation both spatially and in the UMAP visualization (Figure 3.8). In particular, the identification of the mineralizing bone (leiden_clus 6), advancing bone front (leiden_clus 2), and midline mesenchyme (leiden_clus 4) were well resolved. The epithelial layers (leiden_clus 3 and 8) were distinct. The filtered and clustered gobject was saved for further analysis.

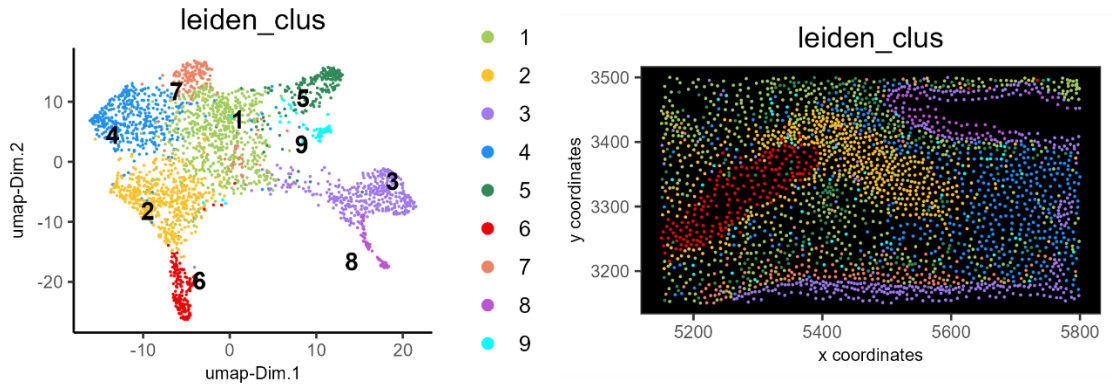

Figure 3.8 UMAP and spatial mapping of Leiden clusters for e15.5 palatal shelf Xenium experiment.
Left panel: UMAP Giotto dimPlot of Leiden clusters (leiden_clus) for wild type e15.5 left palatal shelf. Clusters are color coded as indicated in numbered legend on the right side of the plot and superimposed labels. Right panel: Spatial plot of cells belonging to each defined leiden cluster. Color code is maintained between plots. Plots were generated with the Giotto package in the R coding environment.

Clusters were annotated in script 03_annotate-clusters_save-annotated-gobject.R. I used a combination of cluster heatmaps, dendrograms, and cluster marker identification to predict the identity of the clusters. To find top markers, I used findScranMarkers_one_vs_all with a p-value threshold of 0.01 and log fold change (logFC) minimum threshold of 0.25, based on the Leiden clusters. I then examined the top 10 markers with comparison against the literature and other annotations. I also considered the top marker for each cluster in a spatial context, using my knowledge of the morphology of the palate to inform annotation (Figure 3.9).

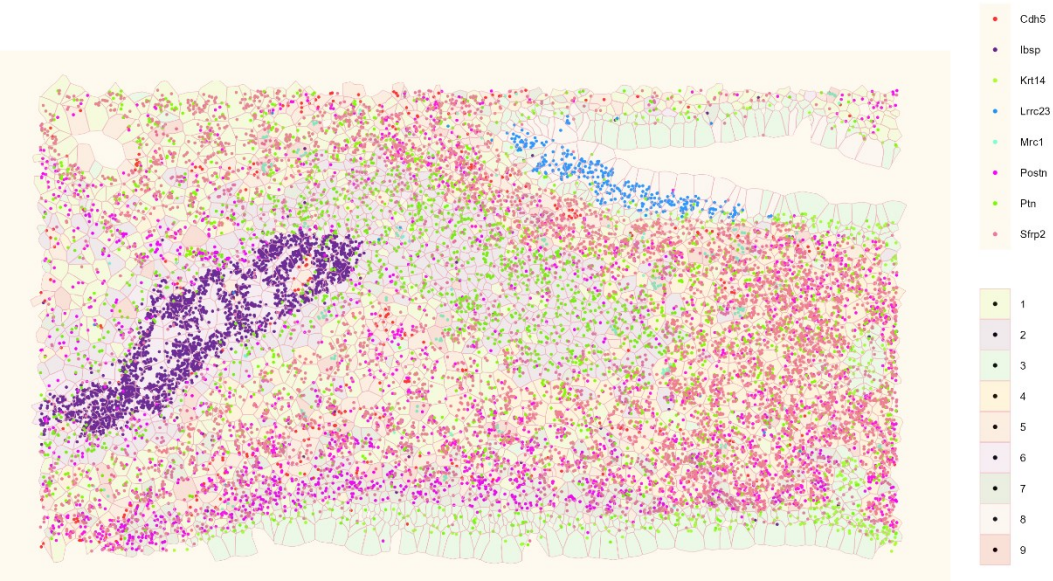

Figure 3.9 Giotto SpatPlot of transcript localization of top markers for each Leiden cluster at e15.5.
UMAP Giotto spatial plot (SpatPlot) of top1 marker gene for each Leiden cluster (leiden_clus) for wild type e15.5 left palatal shelf. Clusters are color coded as indicated in numbered legend on the right side of the plot. Cell shape and size was predicted with the Giotto package workflow. Transcripts are listed in the upper section of the legend, including: *Cdh5, Ibsp, Krt14, Lrrc23, Mrc1, Postn, Ptn,* and *Sfrp2*.

I annotated the clusters broadly as epithelial (epith.1-2), mesenchymal (mes.1-5), osteogenic (osteo), and vascular (vasc) for the left palatal shelf subset using the annotateGiotto() function and saved the gobject. Annotation is shown in Figure 3.10.

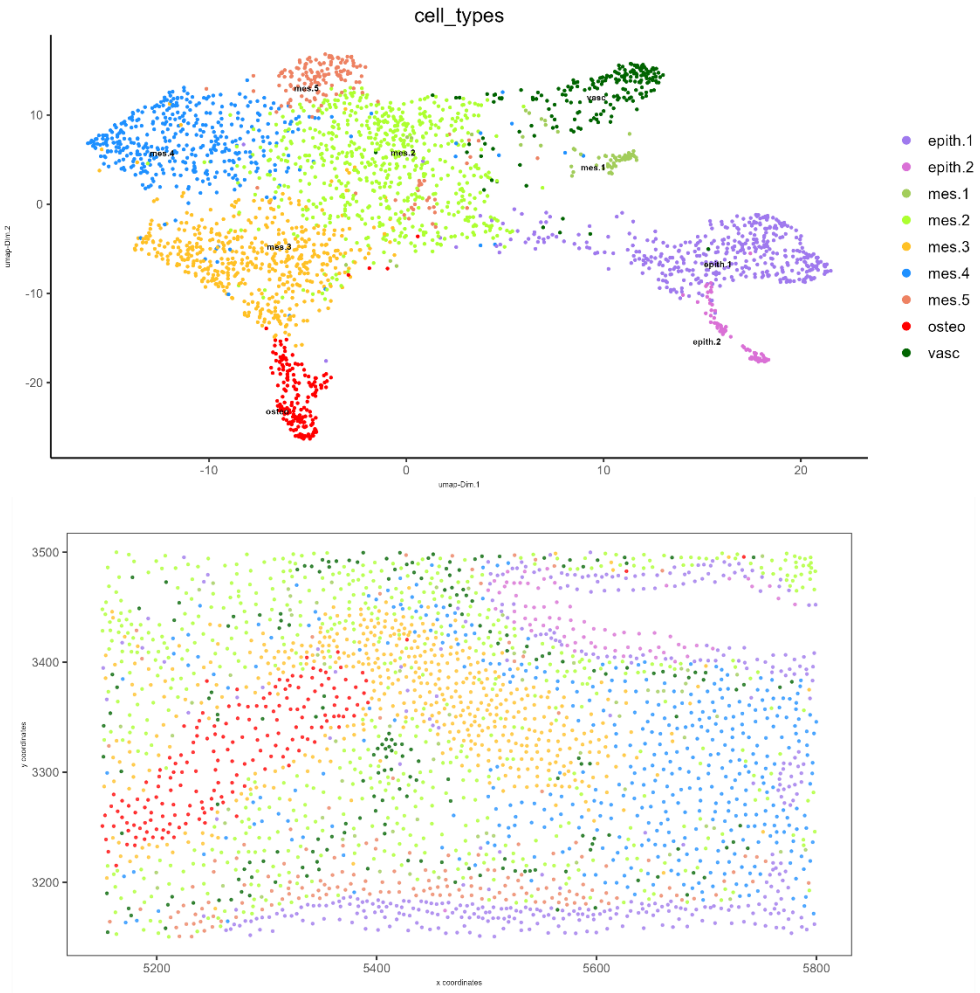

Figure 3.10 Giotto SpatDimPlot() with cell type annotations.
Top panel: UMAP Giotto dimPlot with Leiden clusters annotated by cell type for wild type e15.5 left palatal shelf. Clusters are color coded as indicated in annotated legend on the right side of the UMAP plot and superimposed labels. Lower panel: Spatial plot of cells belonging to each annotated cluster. Color code is maintained between plots.

In Figure 6.2, I leveraged the additional single-cell RNA-seq (scRNA-seq) dataset for the whole palate at e15.5 (generated in the D'Souza lab) for comparison with the Xenium data and Facebase-deposited scRNA-seq from the Holmes lab. At the time of analysis, mid-palatal suture scRNA-seq pre-processing was done using the PopsicleR package with Seurat v4. This package is not currently compatible with Seurat v5 due to differences in file nomenclature (ie slots vs layers); thus, 01_import-E15mps_preprocess-PopsicleR.R must be run with the Seurat v4 environment. The remaining analysis was done after the update to Seurat v5 using the output .Rds file. This import script involved the generation of preprocessing quality control plots using the PrePlots() function to determine

appropriate filtering thresholds (Figure 3.11), including only genes expressed in at least 0.1% of cells (default) and cells with at least 200 genes.

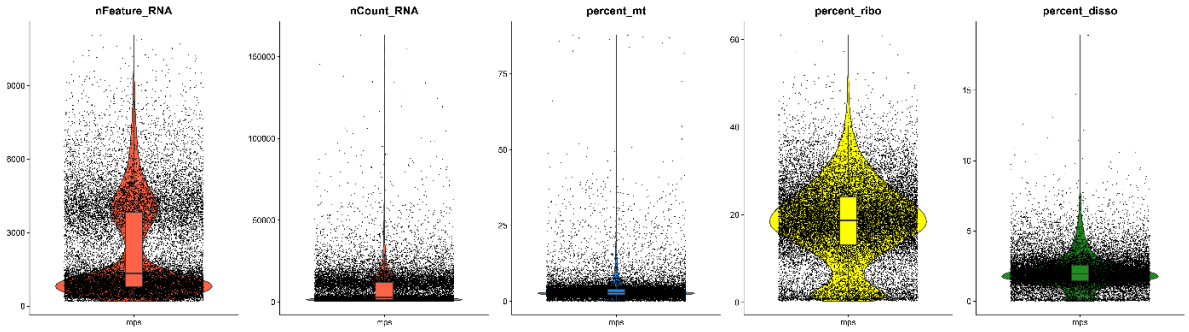

Figure 3.11 Violin plots for e15 scRNA-seq palate dataset used for quality control. From left to right, the violin plots (generated with the PopsicleR pre-processing package in R) depict nFeature_RNA, nCount_RNA, percent_met, percent_ribo, and percent_disso for the dataset. Thresholds for further filtering were predicted from the distribution of barcodes in this visualization.

On visual examination of the QC violin plots, I filtered the dataset using FilterPlots() with a minimum of 200 genes detected per cell and a maximum of 8000, at least 200 molecules detected per cell with a maximum of 30000, upper limit of mitochondrial reads at 30%, maximum ribosomal reads at 50%, and maximum percent dissociation of 7. I then used scrublet implementation with the CalculateDoublets() function to view predicted doublets in the dataset, beginning with an examination of the doublet histogram (Figure 3.12). For doublet removal, I set the threshold accordingly at 0.39.

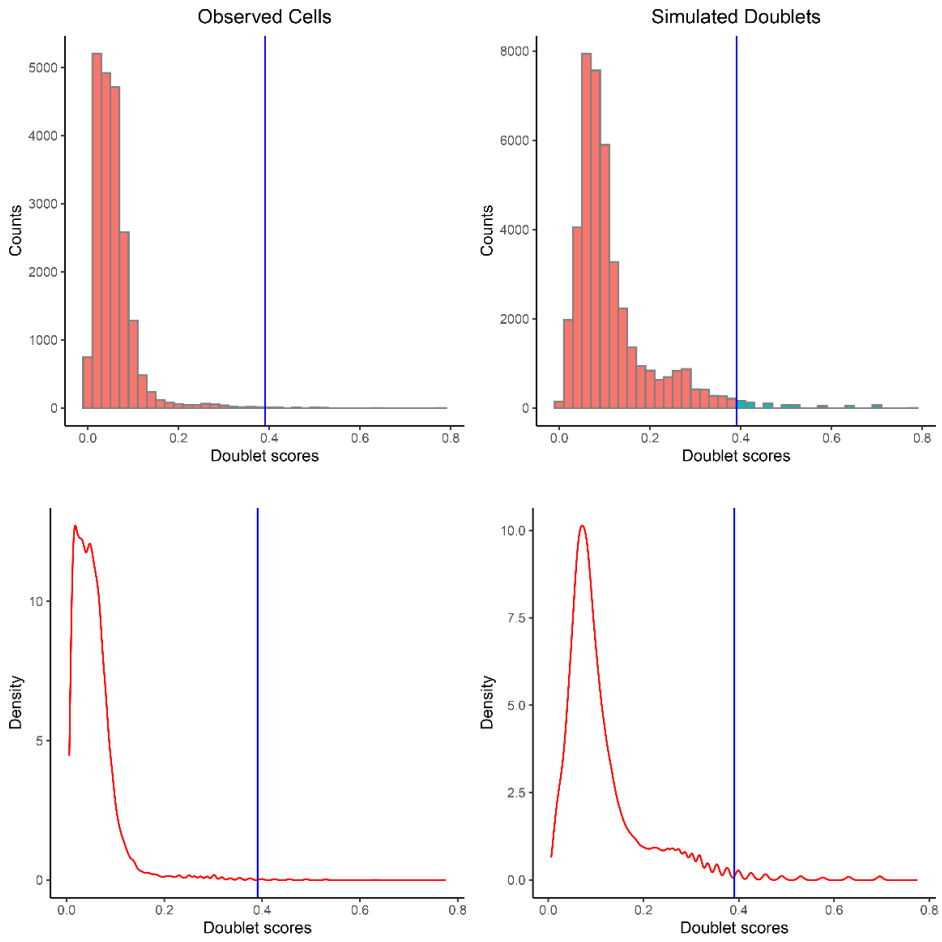

Figure 3.12 Doublet score detection histograms used for visual determination of threshold for filtering.
Plots generated with PopsicleR() package in R.

The dataset was then normalized with 2000 variable genes to be investigated after normalization, and cell cycle effects were regressed out based on S phase and G2M phase scores using the ApplyRegression() function. I performed clustering with several resolutions and finally chose 0.4 cluster resolution for UMAP visualization, which yielded 15 Seurat clusters (Figure 3.13). The pre-processed dataset was then saved as an .Rds object for further analysis.

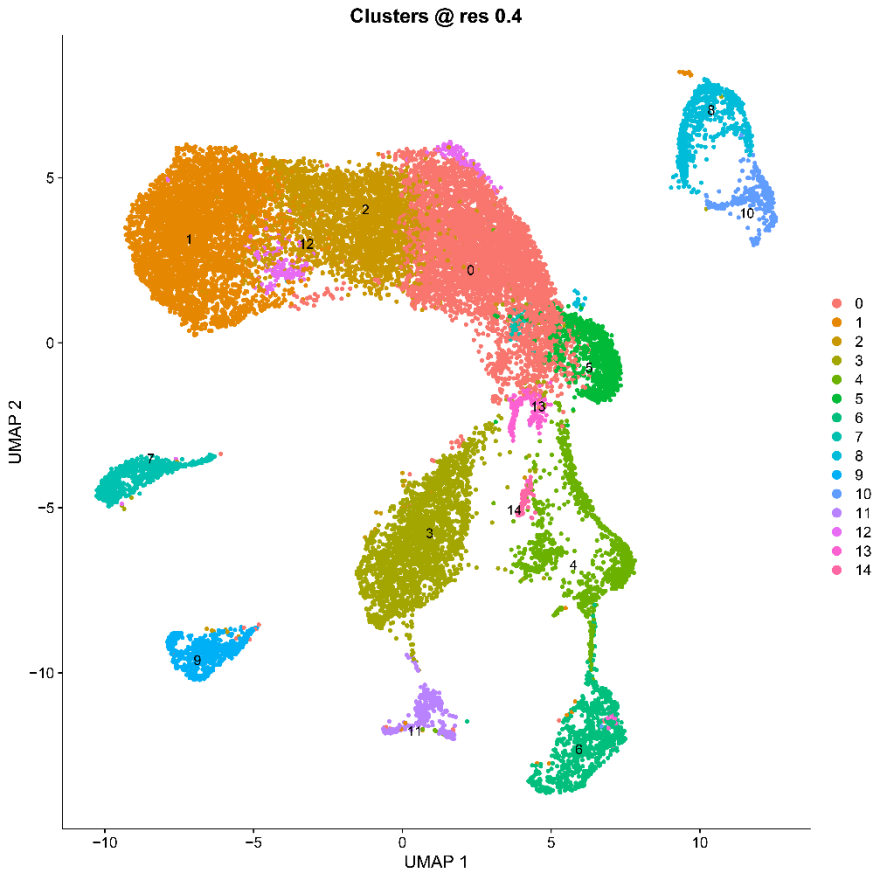

Figure 3.13 UMAP of e15 palate scRNA-seq Seurat clusters at 0.4 clustering resolution.

The clustered object was loaded for annotation in 02_annotate_save-Rds.R. First, the top markers for each cluster were calculated using the FindAllMarkers() Seurat function, only returning positive markers that are detected in 0.25% of cells with at least a 1-fold difference in expression between clusters, on a log-scale. The method used for this detection was MAST, which uses a hurdle model and the MAST package to identify differentially expressed genes between clusters. I chose my cluster annotations based on DotPlot visualization of top3 markers, exported top50 markers, and DotPlot visualization of known marker genes for cell types composing the palate (osteochondroprogenitors, osteoblasts, osteocytes, osteoclasts, endothelial cells, and neural cells, to name a few). I then releveled the data with the following cluster identities: mesenchymal (mes.1-3), ciliated (cilia), epithelial (epith), muscle (musc), neuronal (neu.1-5), and vascular (vasc) (Figure 3.14).

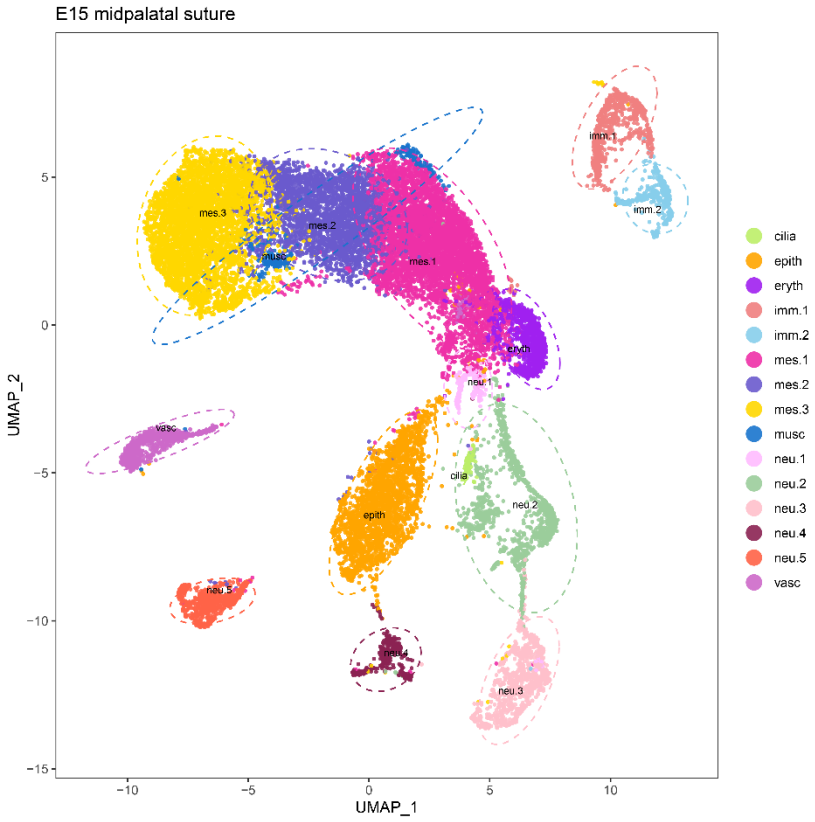

Figure 3.14 Annotated dittoSeq UMAP for e15 palate scRNA-seq. Clusters were annotated based on cell type and Seurat clustering at 0.4 resolution. The clusters are: cilia (ciliated cells), epith (epithelial cells), eryth (erythrocytes), imm.1-2 (immune cells), mes.1-3 (mesenchymal cells), musc (muscle), neu.1-5 (neural), and vasc (vascular cells).

For Figure 6.3, I used the preprocessed and subsetted left palatal shelf e15.5 Xenium Giotto object to perform spatial correlation analysis as generally outlined in Giotto package documentation, described in my 04_spatial_correlation.R script. After importing the annotated e15.5c section gobject, I utilized the Delaunay triangulation method to generate a spatial neural network based on the left palatal shelf. This network connects the cells in the assay based on their physical distance, Delaunay triangulation, a defined maximum distance between cells, and a defined number of neighbors. I selected a minimum kNN k value of 6 and a maximum Delaunay distance of 12 based on visual interpretation of the output of the plotStatDelaunayNetwork() function (Figure 3.15). The Delaunay triangulation network is visualized *in situ* in Figure 6.3A.

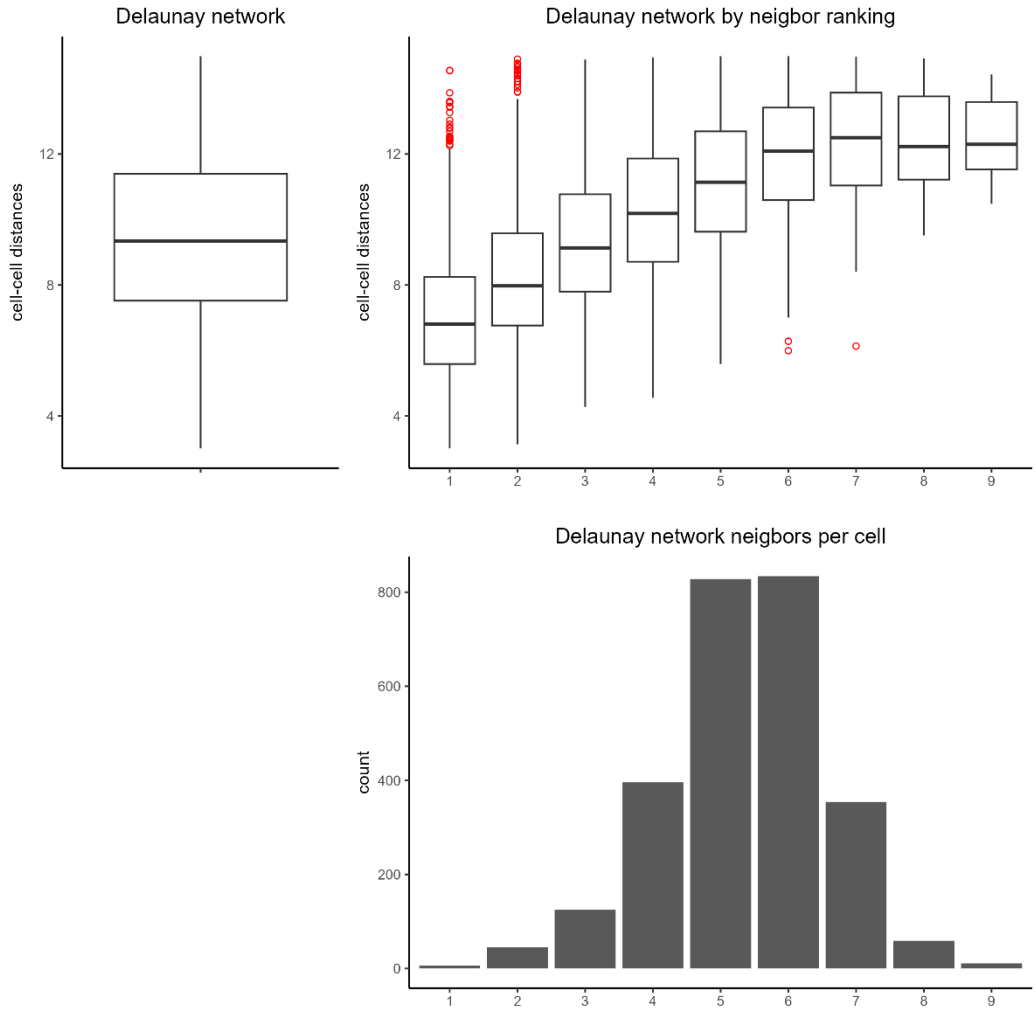

Figure 3.15 Delaunay network plots for e15.5 Xenium left palatal shelf used for parameter definition.

To identify spatially correlated features in the Xenium sample, I used Giotto's binSpect() function, which is a method for binary spatial extraction of genes with similar expression patterns. For this analysis, I used the rank percentile parameter for gene binarization in each cell for the calculation of a contingency table based on the edges of neighboring cells. I then identified spatially correlated features with detectSpatialCorFeats() and performed clustering with clusterSpatialCorFeats(). These results were visualized in a heatmap (Figure 6.3D) and spatially (Figure 6.3E). The cell-cell interaction barplot and spatial visualizations in Figure 6.3B-C were generated following cellProximityEnrichment() computation, which uses the Delaunay spatial network and cluster annotations to calculate cell Proximity scores based on the ratio between observed and expected cell-cell interaction frequencies. The expected frequency

was determined by the function as the average of 1000 spatial network simulations in which cell type labels are reshuffled repeatedly along each node of the Delaunay network. This computational approach to infer cell-cell interaction enrichment was plotted with cellProximityBarplot() with a minimum of 3 interactions between both original and simulated groups, with fill indicating the type of interaction (hetero: between different cell types; homo: between two cells of the same annotation). Three interactions of interest (select_mes.2/3/4) were plotted with spatPlot() in a spatial context alongside non-interacting cells from the same cluster (other_mes.2/3/4).

Figure 6.5 contains analysis of the midline mesenchyme based on whole-transcriptome low-resolution spatial transcriptomics with Visium of the wild type e15.5 palate. Data import and initial processing were performed with script 01_import-visium-findmarkers_save.R. Briefly, the output files from the Visium analyzer were imported into R with the Load10X_Spatial() Seurat function and visualized according to nCount_Spatial data. The entire slide was normalized with NormalizeData() using the "RC" normalization method and a scale factor of 10000, then tissue coordinates were appended. In this figure, I identified features that were biased toward midline mesenchyme expression using region 1 on the slide. This slide also included a second palate section (region 2) and tissue from a separate project (which was

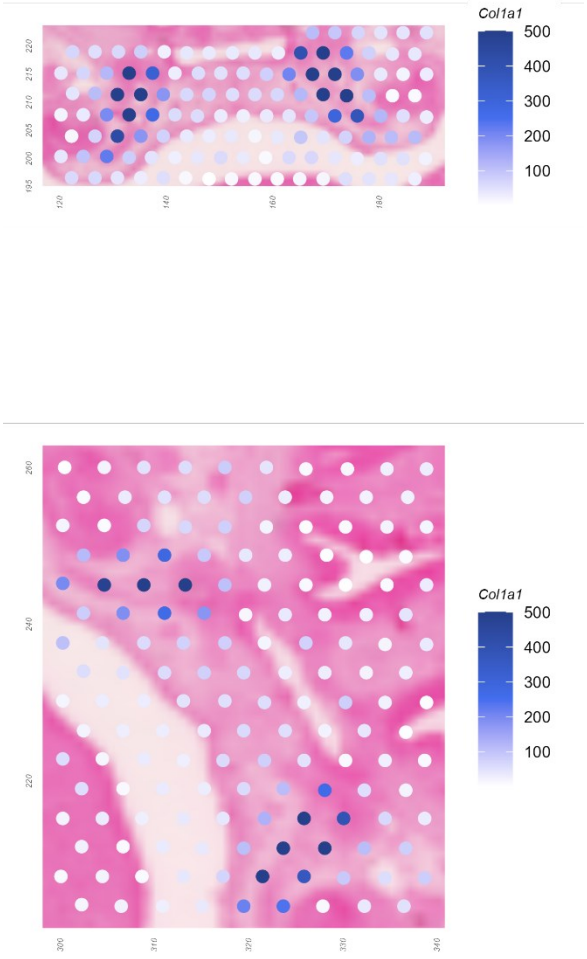

Figure 3.16 Visium *Col1a1* spatial gene expression plots for two e15.5 biological replicates.

excluded from the outputted data). I subsetted both regions 1 and 2 and visualized *Col1a1* expression as a control between sections (Figure 3.16). Further analysis was performed using region 1. I used Seurat functionality to scale data, find variable features, run PCA, find neighbors, and cluster the subsetted region based on the original Louvain shared nearest neighbor (SNN) clustering algorithm at 2.5 resolution. UMAP was run on dimensions 1:30 followed by cluster marker identification with FindAllMarkers() (thresh.use = 0.25, min.pct = 0.1, min.diff.pct = 0.05), with the addition of percentage differences to the DE data.frame output. Before analyzing marker genes, I filtered them based on the minimum average log_2FC and average expression. From this list, I extracted the top 50 markers per cluster arranged by descending average log_2FC. These results were exported to a .csv document for input into my custom function (generate_spatial_feature_plots()) which automated visualization of the top n genes per list as spatial feature plots, which I used to generate plots for the top 40 genes in cluster 3 (midline mesenchyme). I selected two examples from the 40 generated plots for inclusion in Figure 6.5 with specific enrichment of the gene in the midline mesenchyme across several barcodes ("gems"), *Sfrp2* and *Tnn*, though it should be noted that they were chosen as representative genes amongst several informative targets with midline enrichment.

To test my hypothesis that midline mesenchyme-enriched genes from the palate would be expressed by a subset of mesenchymal cells in cranial sutures, I analyzed scRNA-seq frontal suture datasets across four ages of mice (e16, e18, P10, P28) from Greg Holmes' group, which were deposited for open access on Facebase. I began by downloading the datasets from the repository (DOI: 10.25550/1WW8): 1-P588 (e16a), 1-P58A (e16b), 1-C3QM (e18a), 1-8DVP (e18b), 2-55HC (P10a), 2-55HE (P10b), 2-55H2 (P28). For each sample, I loaded the data using Seurat functionality including only genes expressed in at least 3 cells, which should have with at least 200 features each. Preprocessing of this data was done similarly to other RNA-seq analyses in this thesis, detailed in 01_import-fs-data.R. Filtering was performed based on visual assessment of QC metrics using the subset function with the following parameters:

- e16a: 200 < nFeature_RNA < 10000, 200 < nCount_RNA < 100000, mito < 0.15
- e16b: 200 < nFeature_RNA < 2000, 200 < nCount_RNA < 50000, mito < 0.4
- e18a: 200 < nFeature_RNA < 6000, 200 < nCount_RNA < 40000, mito < 0.15

- e18b: 200 < nFeature_RNA < 7500, 200 < nCount_RNA < 100000, mito < 0.2
- P10a: 200 < nFeature_RNA < 5000, 200 < nCount_RNA < 40000, mito < 0.1
- P10b: 200 < nFeature_RNA < 6000, 200 < nCount_RNA < 30000, mito < 0.08
- P28: 200 < nFeature_RNA < 5000, 200 < nCount_RNA < 45000, mito < 0.2

Filtered objects were saved for further analysis. For e16, e18, and P10, I merged the two replicates for each age and normalized for scaling and dimensional reduction as previously described. Layers were then integrated with Seurat's IntegrateLayers() functionality using the CCA integration method. After rejoining the layers of the Seurat object, I performed clustering at several resolutions, comparing the results with the clustree() package and visual inspection of the UMAP. Final resolutions for each plot were: 0.15 (e16), 0.08 (e18), 0.08 (P10), and 0.1 (P28). Each integrated dataset was clustered separately as described previously utilizing a combination of visual examination of feature plots for known marker genes and exported top marker lists, documented in 02_clustering.R. The top 50 markers were identified with FindAllMarkers() and exported to .csv. For this analysis, I annotated clusters as either mesenchymal (mes) or non-mesenchymal (other). The e16 dataset clustered into 6 clusters (2 mes, 4 other), e18 had 10 clusters (4 mes, 6 other), P10 had 12 clusters (1 mes, 11 other), and P28 had 13 clusters (1 mes, 12 other). Annotated files were saved for import into 05_joint-densities_cranial-sutures.R. Each integrated dataset with "mes" or "other" labels was plotted with Seurat FeaturePlot() joint density functionality to visualize co-expression of the two example midline mesenchyme-enriched genes (*Sfrp2, Tnn*). Individual expression of each gene was red or green, with co-expression indicated with yellow (seen in Figure 6.5).

The comparison of sutures in Figure 6.2 made use of the e15 mid-palatal suture scRNA-seq, e18 frontal suture scRNA-seq, and e15.5 Xenium palate datasets for cross-analysis. Summarized in 03_mps-fs-comparison.R, I identified top markers for Xenium clusters with the scan method and generated dot plots with these hits for each dataset. I also visualized expression of genes associated with craniosynostosis (*Efnb1, Fgfr1, Fgfr2, Fgfr3, Twist1*) using heatmaps.

3.13 Statistical analysis

For the mouse phenotyping studies done in Chapters 4 and 5, we could not assume normality of the data due to the small sample size (3-5 mice per group) and variability of phenotype. Therefore, statistical analysis was generally performed using non-parametric methods which do not require assumptions about data distribution. Significance and effect size for two-group comparisons were calculated using the Wilcoxon rank-sum test (aka Mann-Whitney U test). I considered a p-value below 0.05 to be statistically significant across all tests. Importantly, some aspects of this thesis – in particular Chapter 5 – were conducted as pilot studies for further research and thus do not meet minimum requirements for quantitative comparison due to limited sample size. The experiments in which biological triplicate was not collected are indicated in the corresponding figures and accompanying descriptions. For analyses in which statistical significance was not observed, but p-value magnitude suggested a possible trend, I also conducted an effect size calculation with the Common Language Effect Size (CLES) test. This metric is the probability that a randomly selected value from one group is greater than one selected from another group. Given the small sample sizes in these studies, this combination of tests enabled closer examination of data to predict trends.

Wormian/interfrontal bone frequency was recorded as a binary presence (1) or absence (0). Thus tests for normality were not applicable. For each age group, I assessed distribution of counts in contingency tables to decide between Chi-squared testing (if expected frequency of all cells was at least 5) and Fisher's exact test (if any cell had expected frequency <5). This analysis utilized Fisher's exact test due to the small sample size.

Two raters scored internasal suture deviation (internally and relative to the nasal septum) for Figure 4.2 according to two measurements: ins.angle and suture.septum.angle. For analysis, I first assessed normality of the data prior to testing using the Shapiro-Wilk test. The data were normally distributed ($p > 0.05$), thus I opted to use parametric statistical tests. T-tests were used to compare the means between groups, and ANOVA was conducted to assess the effects of genotype, age, and their interaction on the measurements. To evaluate reliability of the measurements amongst the raters, I used Intraclass Correlation Coefficients (ICCs) both within rater groups and between. ICC testing for the measurements indicated excellent agreement among raters, with values ranging from 0.783

to 0.989. Post-hoc analysis using Tukey's HSD test was performed to identify specific group differences.

The semi-quantitative techniques in the phenotyping sections of this thesis were done using histomorphometric assessments, such as counting cells in a TRAP-stained section or *Dmp1*+ nuclei in RNAscope. This technique is highly dependent on tissue quality and integrity after fixation, sectioning, and staining. Therefore, only sections where artifacts did not distort or disrupt the region of interest were assessed. I also did not draw quantitative conclusions regarding stain intensity, as histological staining can be highly variable due to decalcification time, fixation, time spent in blocks before sectioning, sectioning thickness, etc. Further considerations for histological staining are detailed in Appendix A.

For statistical comparison of staining ratios between genotypes, as in Figure 4.3 for *Alpl* coverage and *Ctsk* positivity, I used a combination of non-parametric tests. The Wilcoxon Rank-Sum test was used to compare the distribution of alpl_ratio or ctsk_ratio between genotypes without assuming normality. I also observed a greater spread of values in Bmp7 ncko groups, so applied the Fligner-Killeen test to compare the variances of these ratios between genotypes as well.

To analyze the differences in nasal bone trabeculation between genotypes in Chapter 5, I performed a series of statistical tests suited to the characteristics of the data. Given the small sample sizes and the potential for non-normal distributions, I chose non-parametric tests, which do not assume a normal distribution of the data. First, I conducted the Kruskal-Wallis test to compare the average trabecular area (avg_trab) across the three genotypes (Bmp7 ctrl, Bmp2 cko, and Bmp7 cko). The Kruskal-Wallis test is an extension of the Mann-Whitney U test and is appropriate for comparing more than two groups when the data are not normally distributed. I included a portion of code to conditionally run additional post-hoc testing if the Kruskal-Wallis test showed a significant result. I then performed post-hoc pairwise comparisons using Dunn's test with Bonferroni correction.

Statistical analysis for sequencing analysis is detailed separately in section 3.11 Computational analysis.

3.14 Sex- and gender-based analysis

The potential influence of sexual dimorphism on the physiological processes investigated in this thesis is an important consideration. For example, estrogen is a potent regulator of osteogenesis and bone health (Andrew et al., 2022). Mice reach sexual maturity around 35 days of age, at which point sex hormones become major contributors to the skeletal physiology. The research in Chapter 4, parts of Chapter 5, and all of Chapter 6 was done using early postnatal and embryonic mice, and thus the results are less likely to be dependent on difference in sex. Nevertheless, there may be interplay with X-linked genes or other sex-dependent factors beyond the differing levels of sex hormones. Experimental cohorts were of mixed sex groups, including sequencing experiments where female and male pups were pooled (described in methodology of each experiment). We recorded sex for all postnatal mice to confirm that there was not a difference between effects and survival between sexes. However, due to small sample size for experimental animals, we did not reach a sufficient sample size of n >3 per sex for each age and genotype and thus cannot exclude possibility of sex-related effects. Empirically, I did not observe a phenotypic difference.

For the Bmp7 internasal suture study in Chapter 4, I tested the assumption that male and female mice were equally distributed for each age by conducting a binomial statistical test on my observed frequency of sexes per age (not stratified by genotype). The null hypothesis was that the sex ratio, between males and females, would be 1:1. For P7, P14, and P30 mice, the results indicated no significant deviation from the expected ratio in any age group (not stratified by genotype) (Figure 3.17). Specifically, for P7 the ratio was 4 males to 12 females ($p = 0.0768$), at P14 the ratio was 25 males to 15 females ($p = 0.154$), and at P30, the ratio was 60 males to 52 females ($p = 0.509$). In all cases, the p-values were above the significance threshold of 0.05, indicating no significant difference from the expected 1:1 ratio.

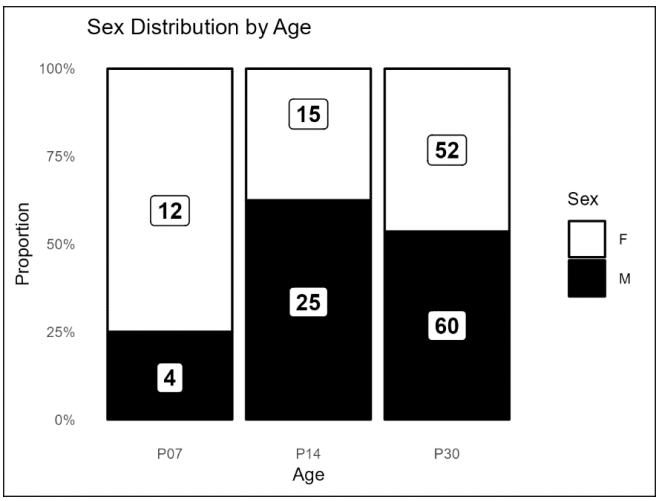

Figure 3.17 Sex distribution by age. Proportion of males and females within each age group (P7, P14, P30) in Chapter 4 Bmp7 internasal suture study. Labels on bars indicate sample size for each sex and age. A binomial test was performed to assess whether the sex ratios deviated significantly from the expected 1:1 ratio. The results indicated no significant deviations in any age group (P07: p = 0.0768, P14: p = 0.154, P30: p = 0.509).

In the adult Gli1-CreERT2 experiments in Chapter 5, sex hormones were a more acutely relevant consideration as these mice were 2 months and older during the experiment. I generated a second version of Figure 5.3D stratified by sex to inspect the data for sex differences (Figure 3.18). Robust statistical analysis was not possible due to small sample size in some groups, but in general I found that there was no significant effect of sex on ISS or SOS frequency across all groups (p = 1.0 for all). Thus I continued my analysis without stratifying for sex; though did not exclude the possibility of an effect definitively.

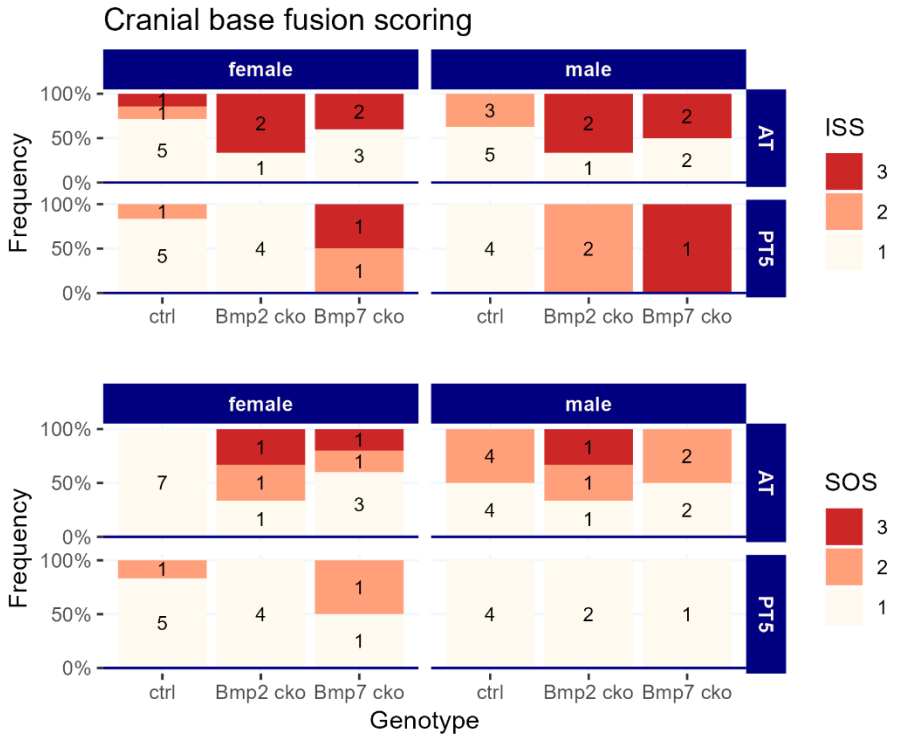

Figure 3.18 Stacked bar plot showing the frequency of ISS and SOS scores by genotype and age group stratified by sex.
AT: Adult injection group. PT: Postnatal injection group. ISS: Intersphenoidal synchondrosis. SOS: Spheno-occipital synchondrosis.

CHAPTER 4
REGULATION OF SYMMETRIC INTERNASAL SUTURE ARCHITECTURE BY *BONE MORPHOGENETIC PROTEIN 7*

Most craniofacial research is focused on the calvarial sutures, with little attention to the midface. With 27 sutures found in this region and midface hypoplasia reported as a common facial difference amongst patients with craniofacial disorders, this oversight is unjustified. The internasal suture, which converges with the frontal and frontonasal sutures at the nasion, is very rarely described at any meaningful resolution. There is also currently no robust method for quantification of suture morphometrics beyond linear measurements and simple calculations. The midface hypoplasia exhibited by Bmp7 neural crest knockout mice, reported by our group in 2021 (Baddam, Biancardi, et al., 2021)*, has not been fully explained. The literature surrounding Bone Morphogenetic Proteins is also incomplete, with a tendency to group the family members together according to their presumed homogeneous function.*

In this chapter, I first characterize the midfacial suture phenotype in Bmp7 neural crest knockout (Bmp7 ncko) mice using micro-computed tomography, suture morphometric quantification, and histological analysis. The wild type internasal suture transcriptome was profiled using single-cell RNA sequencing and whole-transcriptome Visium spatial RNA sequencing, contextualizing Bmp signaling. These techniques were then leveraged to identify forces at play in the Bmp7 ncko internasal suture phenotype and to draw conclusions about normal Bmp function and internasal suture biology. The Bmp7 ncko midfacial phenotype is a valuable example of a subtle change to suture biology which is barely evident at birth and magnifies to a highly detrimental physiological effect over early postnatal development. Unlike craniosynostosis-focused studies, this work explores perturbations to an intact craniofacial suture and their effects over time. In this case, the internasal suture is canonically "patent", but not developing normally.

This study presented a new multiomic characterization of the internasal suture from transcriptome to physiology and morphology at high resolution – a system which we anticipate will be an excellent platform for suture development studies beyond craniosynostosis given its clear stratification of cell layers and high surface area. These results contextualize the Bone Morphogenetic Protein family within the internasal suture

at transcriptomic and proteomic resolution, challenging indiscriminate consideration of genes like Bmp7, Bmp5, and Bmp4. This chapter lays a foundation for further Bmp study and understanding of functional growth of patent sutures, which is built upon in Chapter 5.

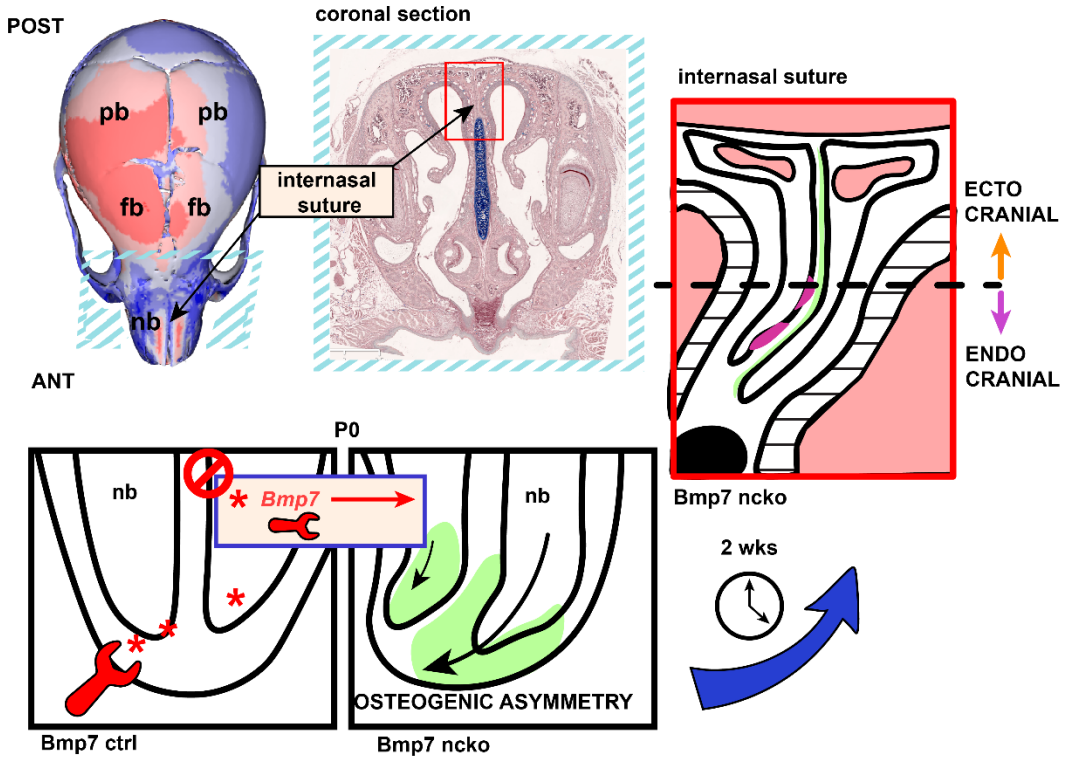

4.1 Summary

Midfacial growth occurs at midline structures (cranial base, nasal cartilage) or mirrored symmetrical growth zones (sutures). The mechanoregulatory properties of sutures bring into question the mechanisms by which symmetrical growth is sustained in the face of potentially asymmetric mechanical forces induced by suckling or mastication. Here, we study malformation of midfacial sutures in a genetic mouse model of neural crest cell *Bmp7* deletion. Loss of *Bmp7* results in midface hypoplasia and midfacial suture asymmetries which appear to worsen over the first two weeks of postnatal development. Close examination of the signaling milieu in the internasal suture through multi-omic characterization revealed a complex and tightly regulated suture microenvironment, in which Bmp7 is required to maintain growth symmetry. Bmp7 is asymmetrically expressed endocranially and in its absence permanent midline deviation manifests. This study

identifies novel roles for *Bmp7* in suture morphogenesis and function where it is required for maintenance of symmetry in a unique system of intramembranous ossification.

4.2 Introduction

In early life, the midface undergoes rapid multi-dimensional changes and growth that involve cranial base elongation, nasal cartilage growth, and bone formation along midfacial sutures. The relative contribution of different growth sites to overall craniofacial growth is still under debate (Baldwin et al., 2023; Katsube et al., 2019; Twigg & Wilkie, 2015) and understanding of how these different structures adapt to dynamic and changing mechanical conditions to respond with straight and symmetric growth has not been addressed. Sutures are critical biomechanical osteogenic centers between bones of the skull with the ability to tune osteogenesis and remodeling in response to physical stimuli (Herring, 2008; Roth, Souter, et al., 2022). The resident stem cell niche and osteogenic front in a patent or unfused suture enable integration of key developmental regulators with osteogenesis in a bidirectional growth zone (Bok et al., 2023; Calandrelli et al., 2021). Cranial sutures in the calvarial vault are well-studied due to their involvement in craniosynostosis, a congenital condition in which premature fusion of cranial sutures prevents normal brain development.

Current treatment for craniosynostosis involves surgical resection of the fused suture, which may be augmented with biomaterial replacement therapy to prevent re-synostosis (Buchanan et al., 2017; J. C. Lee & Volpicelli, 2017; E. Stanton et al., 2022; Tiberio, Cacciotti, et al., 2021). Thus, there has been a concerted effort to unravel the roles of stem cells (Bok et al., 2023; Menon et al., 2021; M. Yu et al., 2021), genetic factors (Alamer et al., 2021; Justice et al., 2012; Twigg & Wilkie, 2015), extracellular matrix (Carinci et al., 2000; Stamper et al., 2011), and biomechanics (Barreto et al., 2017; Moazen et al., 2022; Oppenheimer et al., 2009) in a craniosynostotic setting.

There is comparatively little study of non-obliterative suture pathology in which suture function is altered but not destroyed by premature ossification, and even less of facial sutures (M. M. Wang et al., 2021). The midface is home to a high concentration of complex, symmetrical sutures that reflect the multifactorial mechanical loading experienced by this region, maintaining midfacial growth. However, not all extrinsic forces are symmetrical. The mechanisms by which symmetry of mechanosensory structures like the sutures is maintained in the presence of uneven forces have not been explored. To this

end, we characterized the early postnatal development of suture asymmetry in a mouse model of neural crest-specific *Bmp7* deletion (Bmp7 ncko).

Bmp7 is associated with several types of progenitors and broadly with osteogenic fate (F. Chen et al., 2019; Segklia et al., 2012; B. Shen et al., 2010; Tomita et al., 2013; H. Zhang et al., 2021). Its precise role in osteogenesis *in vivo* has not been explained, though cell culture experiments implicate mechanical regulation and osteogenic commitment (F. Chen et al., 2019; Santos et al., 2011; Z. Wang & Guo, 2013), two core principles in suture remodeling. The *BMP7* locus has been reported as a risk factor for non-syndromic metopic craniosynostosis (Justice et al., 2012). Interestingly, patients with *BMP7* variants have craniofacial and skeletal anomalies including midfacial hypoplasia (Wyatt et al., 2010), a craniofacial feature which is shared amongst many syndromes involving craniosynostosis (M. M. Wang et al., 2021). Our group has previously characterized that Bmp7 ncko mice have midfacial hypoplasia with physiological consequences including deviated nasal septum and associated breathing difficulties with an impact on lifespan (Baddam, Biancardi, et al., 2021).

In the absence of Bmp7, we observed nasal bone anomalies preceding nasal septum deviation. Macroscopically, the effects on midfacial sutures appeared to worsen over time alongside midfacial hypoplasia. Here we sought to elucidate the control of suture morphogenesis and osteodifferentiation by *Bmp7* through multiomic analysis focusing on the internasal suture, which is relatively understudied among abutting midfacial sutures. This suture presents a valuable readout for osteogenic disruption, however, due to the symmetrical abutment of the nasal bones on either side of the suture with the superior border of the nasal septum. As a result, asymmetrical growth is evidenced by midline deviation or a change in abutment to the nasal cartilage. We observed postnatal internasal suture development in both normal and *Bmp7*-deficient contexts from birth to 2 weeks of age, at which point the internasal suture deviation was prominent in severely affected mice. Histomorphometric changes to cell populations composing the internasal suture and eventual architectural changes suggested an asymmetrical disruption to key functional suture niches, particularly in the endocranial portion of the nasal bones. We found that the endocranial and ectocranial axes of the internasal suture have broad transcriptomic differences and represent a presently unexplored dynamic of midfacial morphogenesis.

Finally, we observed a stochastic, asymmetric expression pattern of *Bmp7* in control mice at the endocranial tip of the nasal bones – a potential regulatory feature disturbed in Bmp7 ncko mice. This study addresses gaps in understanding of regulation and growth of midfacial sutures and non-obliterative suture pathology in skeletal hypoplasia and provides novel insights into the maturation and maintenance of sutures and how facial symmetry might be maintained during midfacial growth.

4.3 Results

4.3.1 Loss of Bmp7 *from neural crest cells causes disruption to midfacial sutures correlated to severity of midface hypoplasia*

Conditional deletion of *Bmp7* from neural crest cells using *Wnt1-Cre* or *Wnt1-Cre2* (Baddam, Biancardi, et al., 2021; Danielian et al., 1998; Lewis et al., 2013; Zouvelou, Passa, et al., 2009; Zurowski et al., 2018) (Bmp7 ncko) results in clear midface hypoplasia by one month of age (Fig.4.1A). This midfacial insufficiency develops over time, with quantifiable morphometric changes observed as early as P14 (Fig.4.1B,F). Morphometric comparison of Bmp7 ctrl and ncko skulls at P30 showed that mutant mice had shorter and wider skulls than controls, with expansion of the control midface especially around the midfacial sutures (Fig.4.1C). The midface contains numerous sutures separating the paired frontal bones, nasal bones, and pre-maxilla (Fig.4.1D). In the absence of *Bmp7* we observed morphological changes to several of these sutures, such as asymmetric and periodically inconsistent interdigitation of the frontal-premaxillary suture, irregular margins of the frontonasal suture, and a frequent large supernumerary Wormian bone that appeared to disrupt the frontonasal and internasal sutures at their anterior margin. Statistical analysis revealed no significant differences in the presence of Wormian bones between genotypes at ages P0 (n=12), P07 (n=11), and P14 (n=10) using Fisher's exact test, all with p-values of 1.00. However, a significant difference was observed at age P30 (n=18), where Bmp7 ncko mice showed a significantly higher frequency of persistent Wormian bones ($p = 0.004$, using Fisher's exact test). Frontal-premaxillary suture complexity was compared between the Bmp7 ctrl and Bmp7 ncko genotypes using the Wilcoxon rank-sum test. The test results indicated a p-value of 0.05927 ($W = 39$), suggesting that there is no statistically significant difference in suture complexity between the two genotypes at the 0.05 significance level. However, the p-value indicates a trend towards a difference.

Additionally, the Common Language Effect Size (CLES) was calculated to be 0.8125. With an 81.25% probability that a randomly selected suture complexity value from the Bmp7 ncko group will be greater than a randomly selected value from Bmp7 ctrl genotype, further measurements to increase sample size may reveal a difference in suture complexity. The distinct skull shape of *Bmp7* deletion in Wnt1-Cre mice was also observed in *Bmp7* Wnt1-Cre2 mice. *Bmp7:*Col2-Cre mice (laboratory observations, not shown) did not develop midface hypoplasia or midface suture anomalies, indicating that cartilage-specific deletion is not sufficient to recapitulate this phenotype. These data show that midfacial suture anomalies in Bmp7 ncko mice develop over time and involve the frontal, frontonasal, frontal-premaxillary, and nasal sutures.

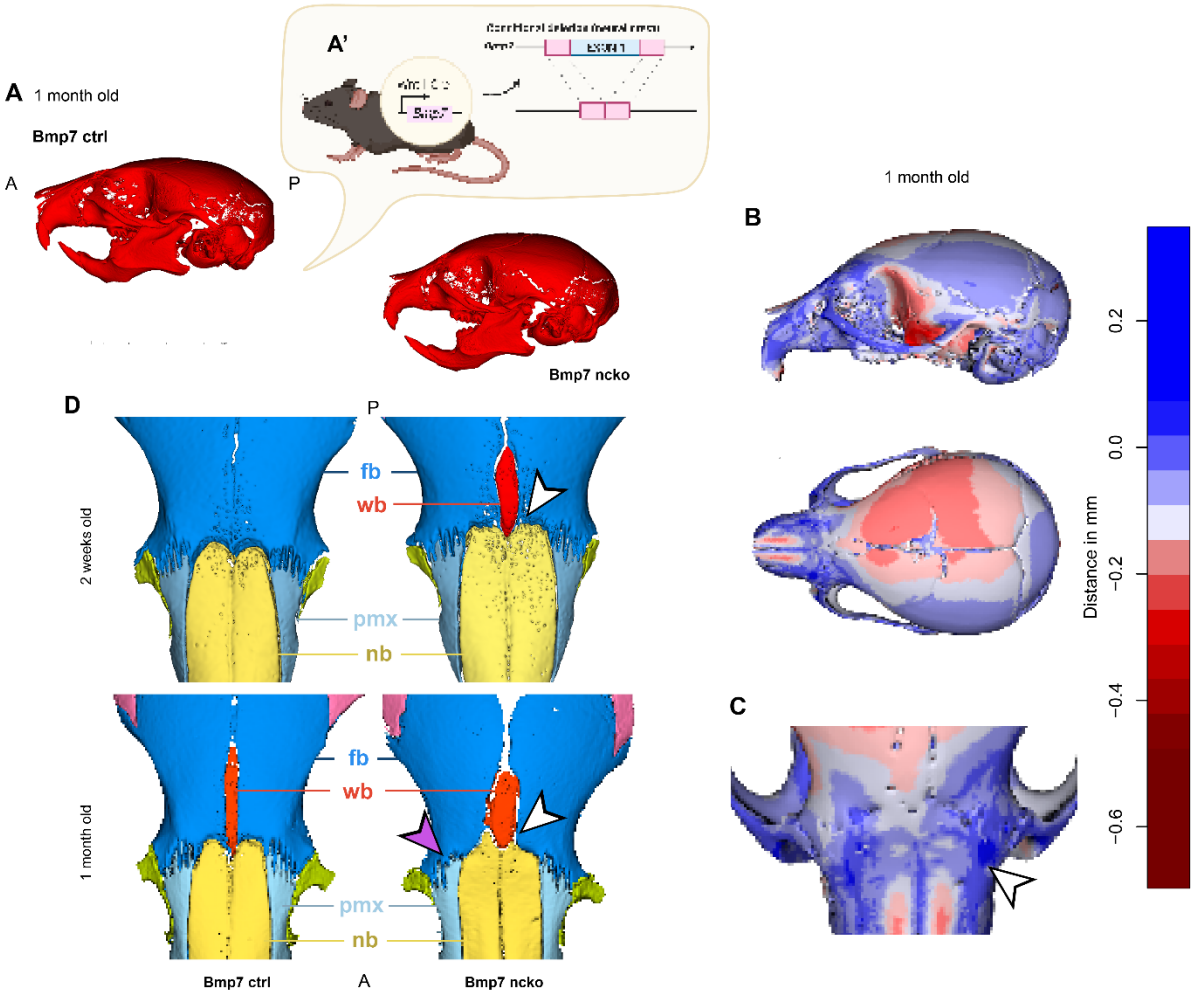
A
1 month old
Bmp7 ctrl
A
P
A'
Bmp7 ncko
B
1 month old
Distance in mm
0.2
0.0
−0.2
−0.4
−0.6
C
D
P
2 weeks old
fb
wb
pmx
nb
1 month old
fb
wb
pmx
nb
Bmp7 ctrl
A
Bmp7 ncko

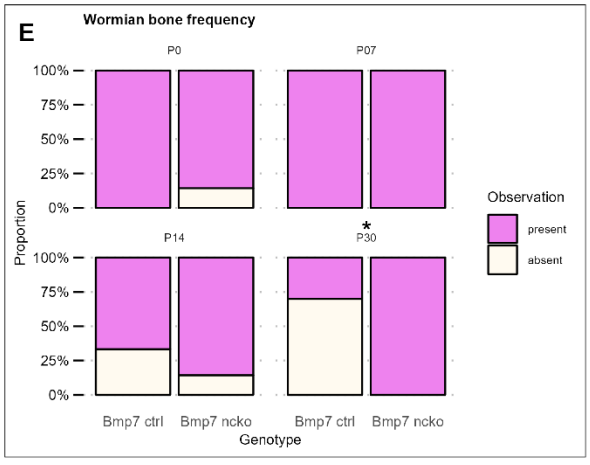
E
Wormian bone frequency
P0
P07
P14
P30
100%
75%
50%
25%
0%
Proportion
*
Observation
present
absent
Bmp7 ctrl
Bmp7 ncko
Bmp7 ctrl
Bmp7 ncko
Genotype

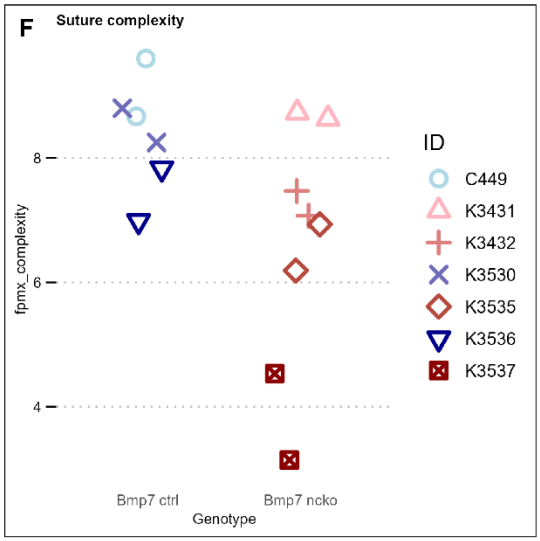
F
Suture complexity
fpmx_complexity
8
6
4
ID
C449
K3431
K3432
K3530
K3535
K3536
K3537
Bmp7 ctrl
Bmp7 ncko
Genotype

Figure 4.1 Development of midface hypoplasia and correlated midfacial suture anomalies in Bmp7 ncko mice.
(A) Micro-computed tomography (μCT) scan reconstructions of postnatal day 30 (P30) skulls from control (Bmp7 ctrl) and Bmp7 neural crest-specific knockout mice (Bmp7 ncko). Skulls were scanned with the following parameters: 50 kV voltage; 0.24 mA current; 75 ms exposure time and reconstructed at 25μm voxel resolution. 3D rendering created using open-source 3D Slicer software. (B) Heatmap of differences between P30 Bmp7 ctrl and ncko surface meshes built from micro-CT scans. Red color represents expansion of the Bmp7 ncko mesh, while blue represents comparative expansion of the Bmp7 ctrl condition. (C) Cropped midfacial mesh comparing Bmp7 ctrl and Bmp7 ncko. White arrow points to frontal-premaxillary suture region. (D) μCT reconstructions of postnatal day 14 (P14) (top panel) and P30 (bottom) midfacial sutures in Bmp7 ctrl and ncko mice from a superior view. Anterior (A) and posterior (P) directions are annotated. Bones are pseudocolored according to identity (fb: frontal bone; wb: Wormian bone; pmx: premaxilla; nb: nasal bone). (E) Relative proportions of presence or absence of a supernumerary Wormian interfrontal bone across P0, P07, P14, and P30 cohorts. Sample sizes for each genotype and age group are as follows: P0 (Bmp7 ctrl = 5, Bmp7 ncko = 7), P07 (Bmp7 ctrl = 8, Bmp7 ncko = 3), P14 (Bmp7 ctrl = 3, Bmp7 ncko = 7), and P30 (Bmp7 ctrl = 10, Bmp7 ncko = 8). Fisher's exact test was used for all age groups, p = 1.000 (n.s.) for P0, P07, and P14, and p = 0.004* for P30. (F) Suture complexity measurements split by genotype in P14 mice. Blue icons are Bmp7 ctrl mice, with separate points for left and right sides. Red icons are Bmp7 ncko mice. The figure legend refers to animal ID numbers, with each icon representing a different animal/biological replicate. 3 mice were measured for each genotype. Suture complexity was not significantly different between groups (p = 0.05927, CLES = 0.8125).

4.3.2 Architecture of the internasal suture changes in Bmp7^{ncko} mice

The internasal suture is an abutting intramembranous growth site which separates the two nasal bones along the antero-posterior axis and forms a symmetrical connection to the nasal septum at its most inferior border that is maintained during rapid midfacial growth between P7 to P14 (Fig. 4.2A). In Bmp7 ncko mice, the internasal suture variably deviates from the midline with no observed directional tendency. Deviation is noted as early as P7 (Fig. 4.2B). This bony asymmetry magnifies over time, with the most severely affected mice losing the close abutment of the nasal bones and suture to the nasal septum cartilage. Angular quantification of internasal suture straightness (ins.angle) and relative position of the internasal suture midline to the nasal septum cartilage (suture.septum.angle) demonstrate a relationship between the measures at P14. The observed ins.angle trend shows that internasal suture deviation is independent of the reported nasal cartilage anomaly as its occurrence precedes it (Fig. 4.2C). Genotype has significant effects on both ins.angle ($F(1,15) = 6.724$, $p = 0.0204$) and suture.septum.angle ($F(1,15) = 13.878$, $p = 0.00203$). Age and genotype-age interactions were not significant. The suture.septum.angle measure was significantly different between Bmp7 ctrl and ncko mice overall ($p = 0.002031$), between 2-week-old Bmp7 ncko and 1-week-old ctrl mice ($p = 0.0291024$), and

between 2-week-old mice of both genotypes (p = 0.0219707), suggesting that the relative position of the internasal suture to the nasal septum is more sensitive to the combination of genotype and age. The development of the internasal suture deviation is a gradual process involving the surrounding bone, indicating the involvement of bone remodeling.

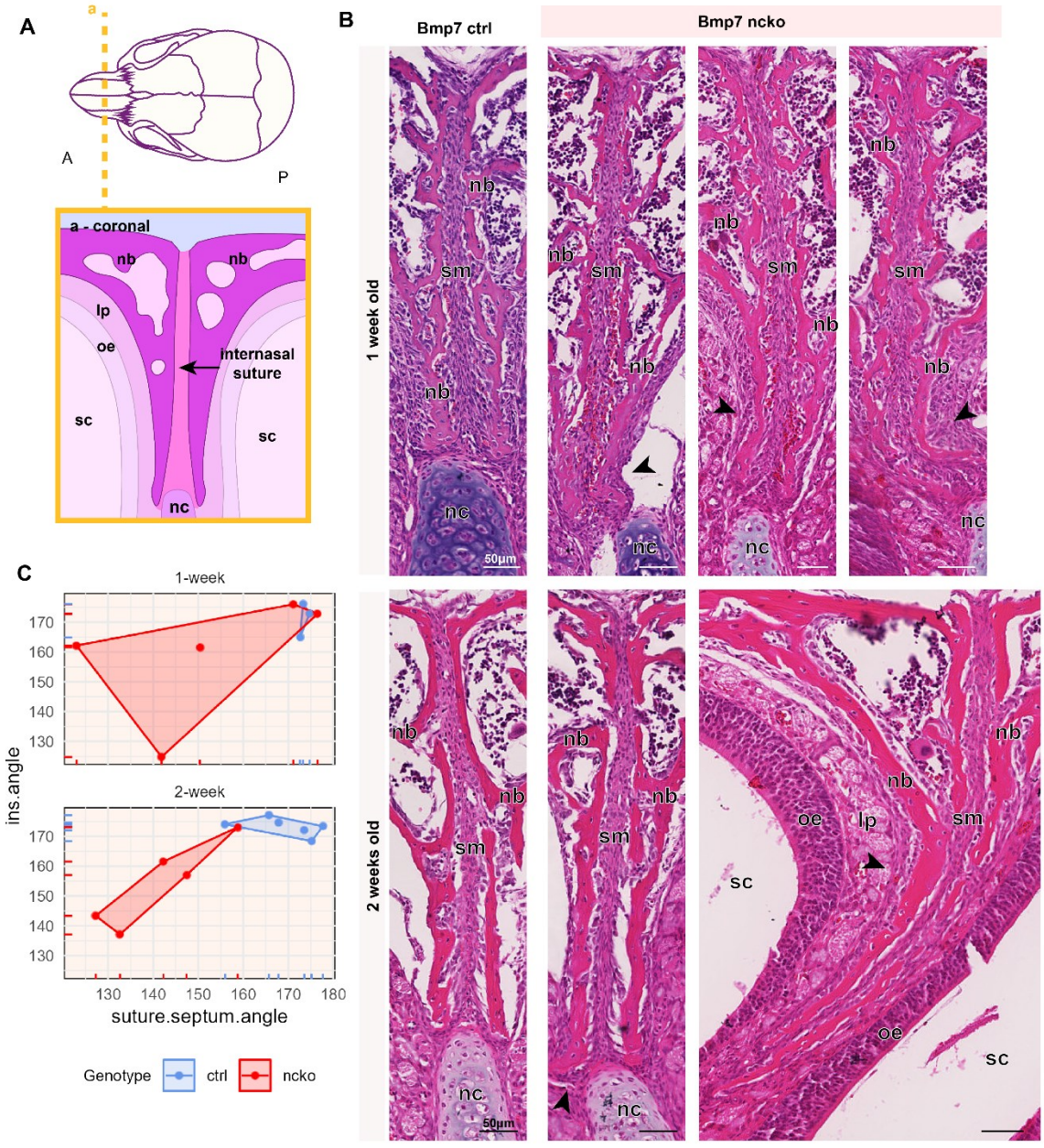

Figure 4.2 Internasal suture architecture changes from one to two weeks of age.
(A) Diagram of internasal suture anatomy through coronal plane. Yellow dotted line indicates plane of sectioning for internasal suture histology in all figures. (B) Hematoxylin & eosin stained coronal internasal suture sections at 7 days postnatal (P7) and 14 days (P14) for Bmp7 ctrl and Bmp7 ncko mice. Multiple representative sections shown for Bmp7 ncko cohort to highlight the variable phenotype between mice. Black arrowheads indicate deviation of the nasal bone(s) from the midline in ncko mice. (C) Scatterplots of the relationship between internasal suture internal

angle of deviation (y-axis) and the angle of the internasal suture relative to the nasal septum (x-axis) at P7 (top panel) and P14 (bottom panel). Blue points represent individual Bmp7 ctrl measurements (2 raters for ≥ 3 mice, with 3 measurements each across several sections), and red points represent Bmp7 ncko measurements. Convex hulls illustrate the boundary of data points for each group, filled with a color corresponding to genotype. P7: n=3 (ctrl) or 5 (ncko); P14: n=7 (ctrl) or 6 (ncko). ANOVA results revealed significant effects of genotype on ins.angle ($p = 0.0204$) and suture.septum.angle ($p = 0.00203$), with no significant effect of age or genotype-age interaction for ins.angle, but significant interactions for suture.septum.angle. Tukey's HSD post-hoc tests identified specific genotype differences in ins.angle ($p = 0.0204$) and suture.septum.angle ($p < 0.05$). Notably, significant interactions were observed between ncko:2-week vs. ctrl:1-week ($p = 0.0291$) and ncko:2-week vs. ctrl:2-week ($p = 0.0220$) for suture.septum.angle. nb: nasal bone; sc: sinus cavity; nc: nasal cartilage; sm: suture mesenchyme; oe: olfactory epithelium; lp: lamina propria

4.3.3 Aberrant bone remodeling in the Bmp7^{ncko} suture corresponds with unilateral loss of osteoblasts

Like other cranial sutures, the internasal suture has a characteristic composition of osteogenic bone-lining osteoblasts flanking a mixed suture mesenchyme, with a general differentiation trend from the midline towards either side. Absence of *Bmp7* did not appear to interfere with the overall process of osteoblast differentiation, as both Bmp7 ctrl and ncko sutures have some degree of expression of *Alpl* (pre-osteoblasts), *Sparc* (osteoblasts), and *Dmp1* (osteocytes) (Fig. 4.3A,B). However, the clearly defined osteoblasts seen on both sides of the Bmp7 ctrl suture in Fig. 4.3A,C are absent unilaterally from the Bmp7 ncko bone-lining suture compartment, and remaining osteoblast-like cells appear flattened and are difficult to distinguish from other mesenchymal cells (Fig. 4.3D). We quantified this difference by measuring proportional coverage of *Alpl*^{pos} cells between left and right sides of the internasal suture (alpl_ratio), and found that Bmp7 ncko sutures had greater variation in alpl_ratio than controls ($\chi^2 = 6.6239$, $p = 0.01006$) but no significant difference in central tendencies in this small sample cohort ($W = 21$, $p = 0.6991$, n = 2-3 mice). Interestingly, the qualitative reduction in *Sparc*+ osteoblasts at 2 weeks is accompanied by an asymmetric accumulation of bone-resorbing *Ctsk*+ osteoclasts within the same suture compartment (Fig. 4.3E-F). The Wilcoxon rank-sum test, used to compare the central tendencies of Ctsk_ratio between the two genotypes, yielded a p-value of 0.0636 ($W = 9$). This result suggests a trend towards a difference in Ctsk_ratio between the genotypes, though it is not statistically significant at the conventional 0.05 threshold, likely due to the reduced sample size (2 Bmp7 ctrl, 3 Bmp7 ncko). The Fligner-Killeen test for homogeneity of variances indicated no significant difference in variances of Ctsk_ratio between genotypes ($\chi^2 = 2.2893$, $p = 0.1303$). While *Ctsk*+/TRAP+ osteoclasts are occasionally

observed in the normal internasal suture mesenchyme at this age, they do not clearly line the mesenchyme-facing nasal bone surface as observed in Bmp7 ncko sutures. Further replicates must be done to draw statistically significant conclusions. However, these findings were qualitatively consistent between Cathepsin K RNAscope *in situ* hybridization, immunofluorescent experiments, and TRAP histological staining.

Evidence of asymmetric active bone remodeling can be found at P7 with low levels of mesenchymal *Ctsk* and TRAP-positivity already evident (Fig. 4.3G). At this age, Bmp7 ncko mice have comparably subtle but observable qualitative disturbances to osteogenic niches that do not broadly prevent osteoblastic differentiation from *Six2* positive progenitors to *Alpl*- or *Sparc*-expressing osteoblasts (Fig 4.3I-K).

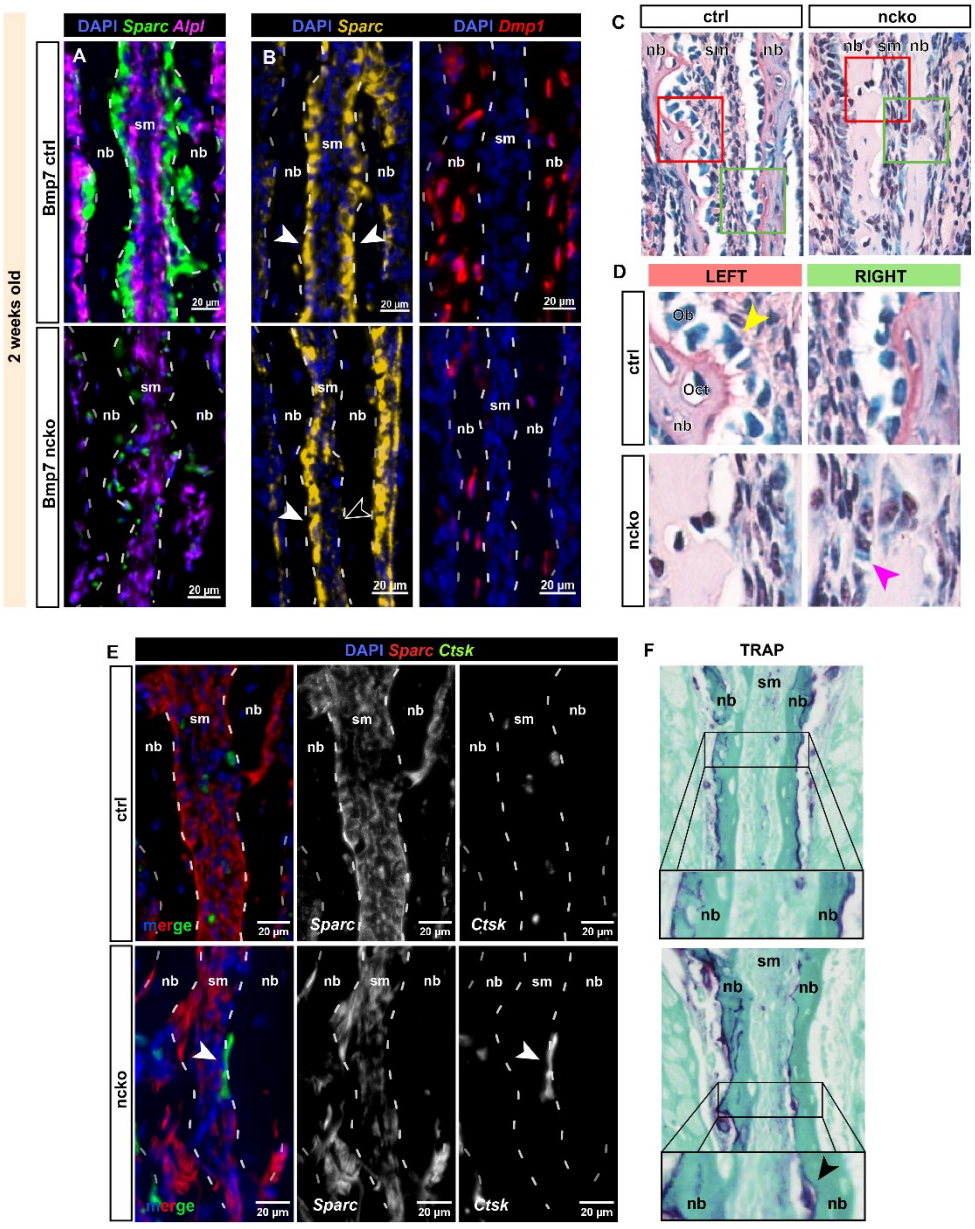
2 weeks old
Bmp7 ctrl
Bmp7 ncko
A
DAPI Sparc Alpl
B
DAPI Sparc
DAPI Dmp1
sm
nb
20 μm
C
ctrl
ncko
D
LEFT
RIGHT
Ob
Oct
E
DAPI Sparc Ctsk
merge
Sparc
Ctsk
F
TRAP

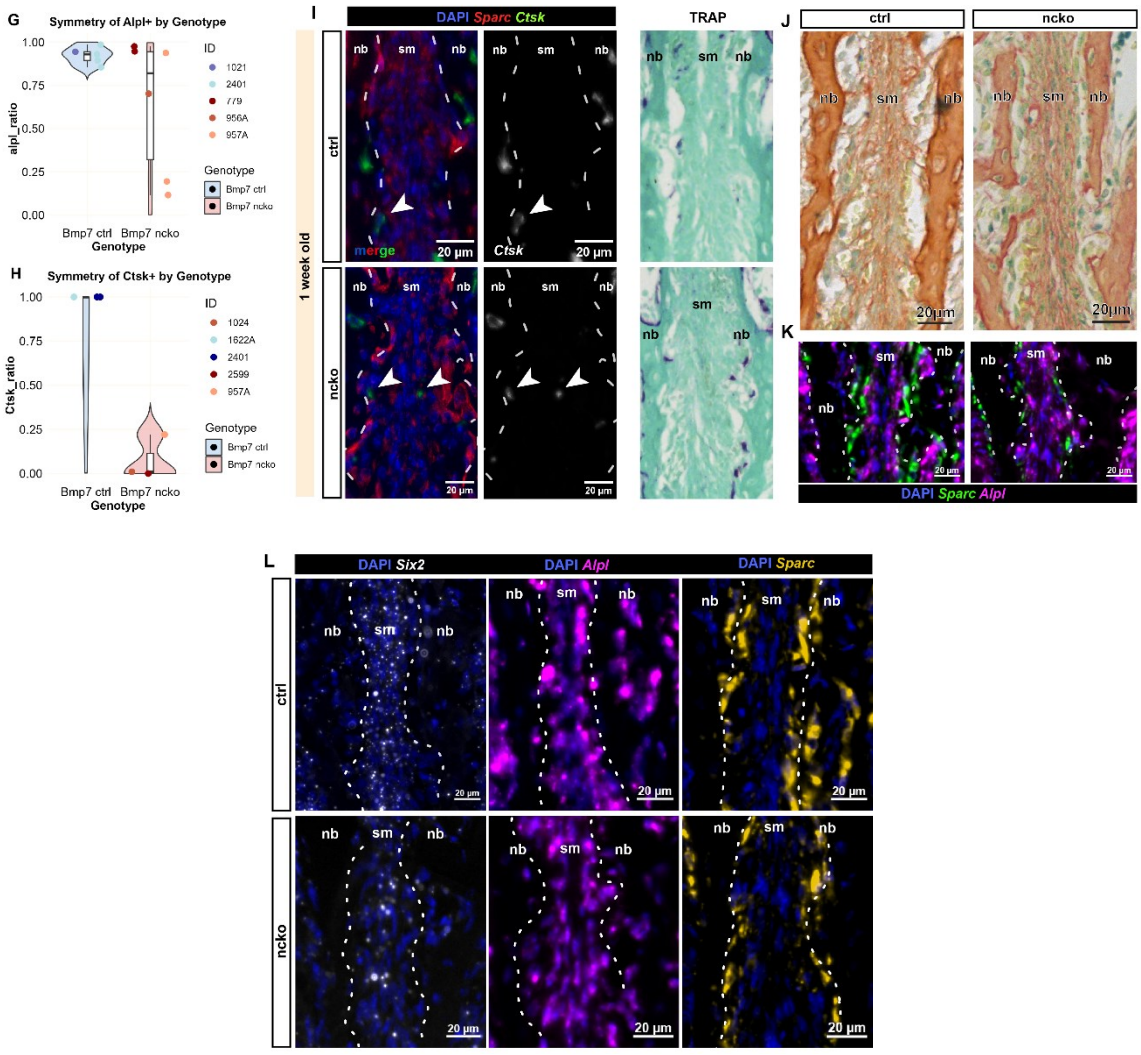

Figure 4.3 Bmp7 ncko mice have asymmetric bone remodeling, but osteodifferentiation is not prevented.

(A) RNAscope in situ hybridization (ISH) of Bmp7 control (ctrl) and neural crest knockout (ncko) 2 week old (P14) coronal internasal suture paraffin sections with probes targeting *Sparc* (green pseudocolor, osteoblasts) and *Alpl* (violet, pre-osteoblasts). Images are cropped to comparable regions mid-internasal suture. DAPI nuclear counterstain is blue. Nasal bone margins are indicated with white dotted lines. (B) ISH for osteoblasts (*Sparc*, yellow) and immature osteocytes (*Dmp1*). White arrowhead highlights maximal Sparc expression in presumptive osteoblast layer. Hollow arrowhead in Bmp7 ncko represents unilateral absence of *Sparc* positivity. (C,D) Orcein stain at comparable internasal suture regions with methylene blue counterstain. Red and green boxes in (C) denote region magnified in (D). Yellow and violet arrows indicate morphologically typical and abnormal osteoblasts (respectively). Ob: osteoblast; Oct: osteocyte; nb: nasal bone. (E) ISH co-staining for *Sparc* (osteoblasts) and *Ctsk* (osteoclasts). White arrowhead indicates large *Ctsk* positive osteoclast lining the mesenchymal surface of the right nasal bone in Bmp7 ncko. Merged image is pseudocolored with blue for DAPI nuclear counterstain, red for *Sparc*, and green for *Ctsk*. Individual channels are shown in greyscale with dotted lines indicating nasal bone margins. (F) Tartrate-resistance Acid Phosphatase (TRAP) stain of comparable mid-internasal suture sections in P14 ctrl (top) and ncko (bottom) mice. Violet chromogenic stain predominantly indicates bone-resorbing osteoclast activity (highlighted with black arrow in ncko), with Fast green counterstain for context. Mesenchymal regions bounded by a black rectangle are magnified at the bottom of each image. (G) Plot of asymmetry scores for *Alpl* positivity from RNAscope lining the suture edge of the nasal bones. Scores closer to 1.0 indicate

equivalent coverage between the left and right sides; 0 score reflects absence of stain on one side of the suture. Control values are plotted with blue icons and accompanying violin plot. Mutant mice are red. IDs indicated in the figure legend are coded to individual animals and their identification numbers. n = 2 Bmp7 ctrl, 3 Bmp7 ncko. Wilcoxon rank-sum test showed no significant difference in central tendencies (W= 19, p = 0.5368), but the Fligner-Killeen test confirmed a significant difference in variances (χ^2 = 6.6239, p = 0.01006). (H) Visualization of similar assessment as in G, but counting Ctsk positivity in immunofluorescent experiments instead to approximate symmetry of osteoclast infiltration. The Wilcoxon rank-sum test showed a trend towards a difference in central tendencies of Ctsk_ratio between genotypes (W = 9, p = 0.0636). Each point represents an individual measurement, with shape corresponding to ID of biological replicates (2 Bmp7 ctrl, 3 Bmp7 ncko). (I) ISH co-staining for *Sparc* (osteoblasts) and *Ctsk* (osteoclasts) in the P7 internasal suture. White arrowhead indicates *Ctsk* positive osteoclasts or pre-osteoclasts. Merged image is pseudocolored with blue for DAPI nuclear counterstain, red for *Sparc*, and green for *Ctsk*. *Ctsk* stain is isolated in greyscale, with dotted lines indicating suture mesenchyme margins. TRAP stained P7 internasal suture showing positivity within the suture mesenchyme, with some osteoclasts lining the nasal bone surface in Bmp7 ncko mice (bottom panel). (J) Pentachrome histological stain of region of internasal suture captured in subsequent ISH panels at P7 in ctrl (left) and ncko (right) mice. (K) ISH targeting Sparc (green) and Alpl (violet) in P7 Bmp7 ctrl and ncko mice. Blue DAPI counterstain. (L) ISH targeting progenitor cells (*Six2*, white), pre-osteoblasts (*Alpl*, violet), and osteoblasts (*Sparc*, yellow) at P7 in Bmp7 ctrl (top panels) and ncko (bottom panels) mice. nb: nasal bone; sm: suture mesenchyme

4.3.4 The internasal suture has discrete endocranial and ectocranial compartments

Picrosirius red positive collagen fibers align in bundles along the length of the internasal suture, providing the mesenchyme with extracellular support while maintaining flexibility. The inflection point of deviation in Bmp7 ncko mice is marked by a change in collagen fiber orientation, leading us to hypothesize that there is an endocranial-ectocranial axis of signaling in the internasal suture in addition to known lateral osteogenesis (Fig. 4.4A-B). We define the endocranial internasal suture compartment, where Bmp7 ncko deviation is most apparent, as proximal to the nasal septum cartilage (Fig. 4.4C).

To test our hypothesis of spatially distinct signaling environments in the internasal suture, we employed Visium CytAssist spatial transcriptomics (10X Genomics) for P3 wild type mice to query the whole transcriptome at a 3-10 cell resolution (Fig. 4.4D). The Visium platform proved to be a useful tool to examine regional multi-cell population trends. As an illustration, osteogenic genes (*Runx2, Cd200*) can be detected in the expected regions of the internasal suture, maximally in bone. Similarly, chondrogenic genes (ie *Col2a1*) are found mainly in Visium 'gems', or barcoded regions, overlying cartilage (Fig. 4.4E). We selected endocranial and ectocranial gems from 3 postnatal day 3 (P3) internasal suture Visium experiments (10 endocranial gems, 11 ectocranial gems total) for differential gene expression analysis (Fig. 4.4F). Querying core osteogenic genes (Fig. 4.4G), we confirmed that bone formation is overall not significantly different between endo- and

ectocranial gems (Fig. 4.4H). We then generated biased gene lists for each group using the FindAllMarkers function in Seurat to identify differences between the endocranial and ectocranial transcriptomes (Fig. 4.4I) (Hao et al., 2021). Several themes of internasal suture biology emerged from this approach as visualized with GO::TermFinder mapping (Fig. 4.4J) (Boyle et al., 2004). Molecular function GO terms associated with genes more highly represented in endocranial gems indicate an important role for extracellular matrix composition and interactions in this region, especially in the context of tensile strength, as well as calcium-dependent protein binding. In the case of genes such as *Col9a1* or *Mgp*, spatial visualization suggests that proximity to highly expressing chondrocytes (whether artifact or paracrine relationships) could be responsible for the designation. However, genes such as *Hmox1* and *Gpha2* are less clearly associated with neighboring structures and have endocranially-focused localization (Fig. 4.4K). Thus, the local signaling environment in the endocranial internasal suture compartment was of particular interest to investigate at a higher resolution.

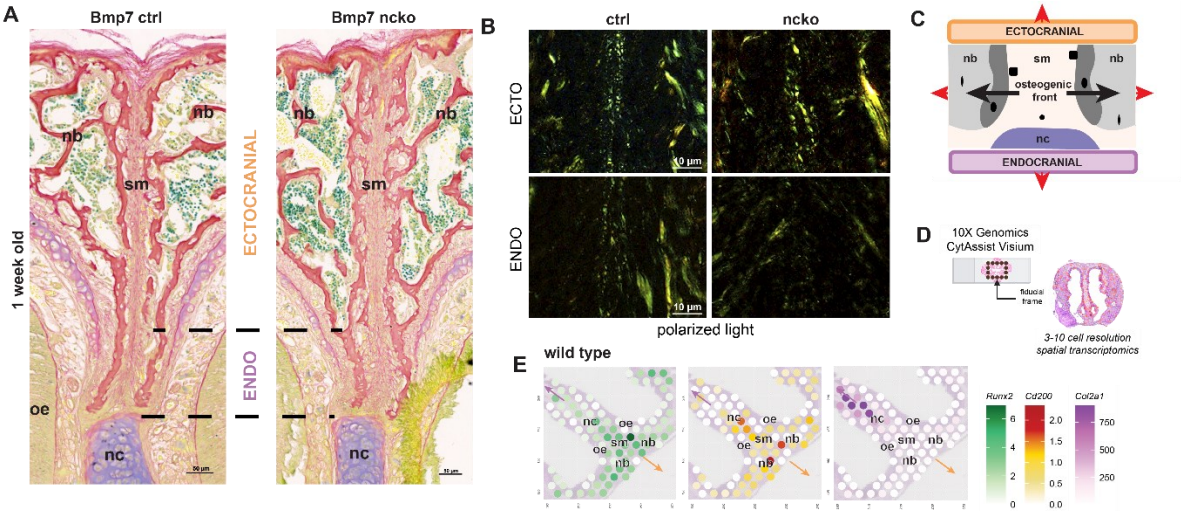

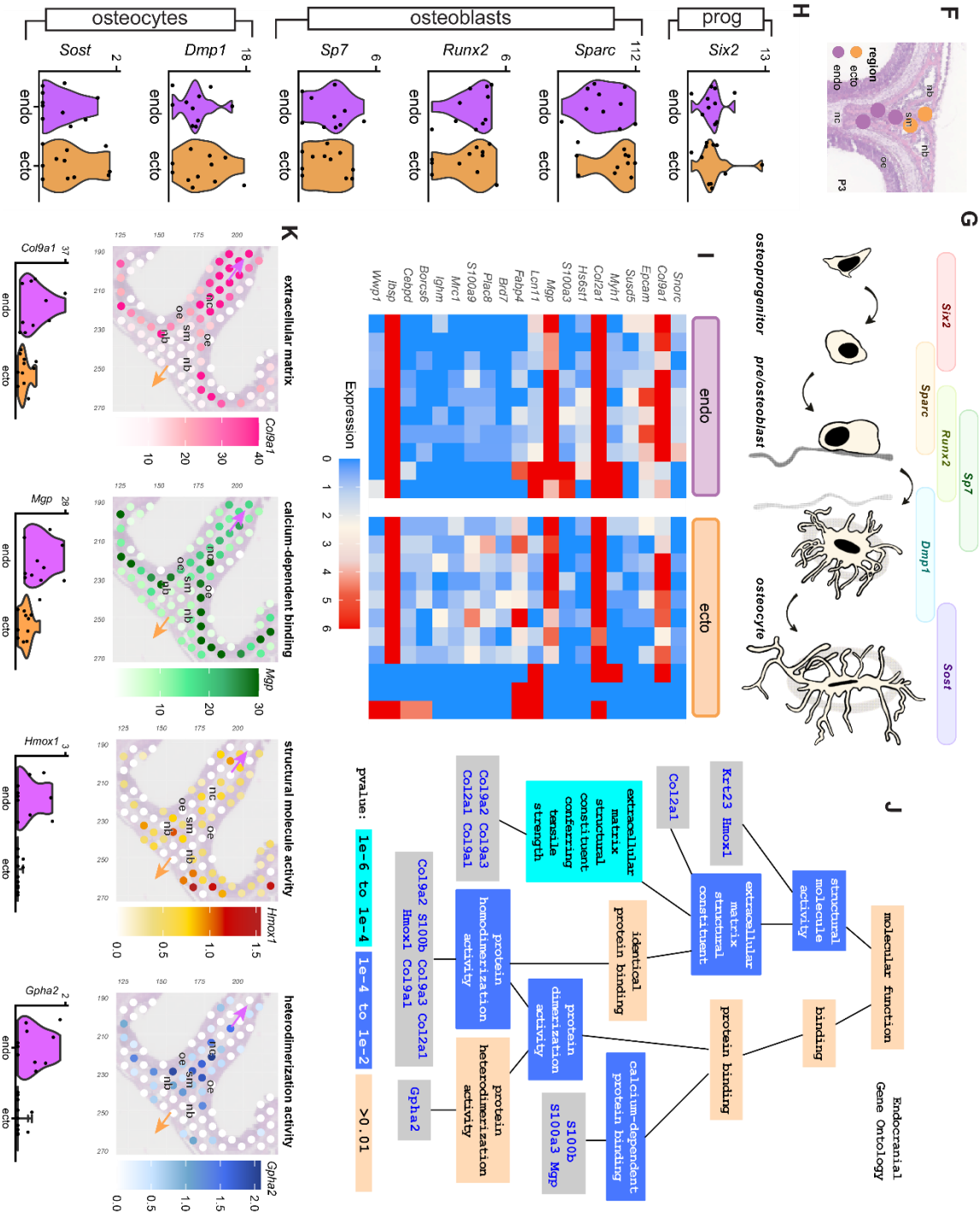

Figure 4.4 Transcriptomic definition of endocranial and ectocranial domains of the wild type internasal suture at postnatal day 3.

(A) Pentachrome histological stain (2 weeks old) annotated with endocranial and ectocranial domains of the internasal suture according to the mesenchymal collagen fiber organization, stained red. Dashed lines border the distinct nasal cartilage-proximal ("endocranial") region. Red: pan-collagen stain; purple: cartilage; green: red blood cells; yellow: background tissue. (B) Darkfield polarized light images of pentachrome stained slides from panel (A), revealing organization of collagen fibers. Images were taken at 40X magnification, and cropped to representative ectocranial

and endocranial regions of the internasal suture. (C) Graphic representation of internasal suture-nasal septum abutment. Black ellipses represent progenitors, osteoblasts, and osteocytes lining and residing in nasal bones (unmineralized: dark grey, mineralized: light grey). We define the endocranial compartment of the internasal suture as proximal to the nasal cartilage (nc). Red arrows emphasize the multidimensionality of this 3D complex, with differentiation dynamics spanning not only laterally (left/right), but also previously undefined endo/ectocranial compartments (up/down). (D) Graphic representation of 10X Genomics Visium CytAssist technology used to explore endo- and ectocranial aspects broadly. Tissue is mounted on a slide within the fiducial frame, which assigns "gems" or barcodes to the overlying tissue at approximately 3-10 cell resolution for whole-transcriptome RNA sequencing. (E) Visium expression of known osteogenic (*Runx2, Cd200*) and chondrogenic (*Col2a1*) genes in the P3 internasal suture region, confirming assay reliability but revealing limitations of resolution. Purple arrow: endocranial direction; orange arrow: ectocranial direction, as defined in (C). (F) Representative internasal suture section showing gems selected to capture endocranial (purple) and ectocranial (orange) compartments at P3 from 3 sections, for a total of 10 endocranial (endo) and 11 ectocranial (ecto) gems. (G) Diagram of osteogenic differentiation and selected genes expressed by progenitors, osteoblasts, and osteocytes corresponding to panel (H). (H) Violin plots of gene counts from each region representing progenitors (Six2), pre-osteoblasts *(Sparc, Runx2),* osteoblasts (*Sp7*), and osteocytes (*Dmp1, Sost*). There is no significant difference between these osteogenic domains in a wild type P3 animal at this resolution. (I) Heatmap of biased genes in each compartment overall. Each column represents a single "gem" barcode, which encapsulates several cells. Blue color indicates an absence of transcripts detected, while red signifies maximum relative expression. Top10 genes plotted were identified using the FindMarkers function in Seurat with the Poisson statistical method. (J) Gene Ontology (GO) View Tree of top30 biased genes from endocranial P3 gems, generated with Princeton GO::TermFinder (Boyle 2004). Term nodes are filled according to p-value, with connections drawn based on direct annotation of genes with GO term(s). Results with p-value above 0.01 are excluded from the graph. (K) Selected genes from panel I/J shown spatially on Visium sections (relative to cropped field of view) and in violin plots with relative counts for endo- and ectocranial domains. All Visium data presentation and processing was performed using Seurat in RStudio. nb: nasal bone; sm: internasal suture mesenchyme; nc: nasal cartilage; oe: olfactory epithelium.

4.3.5 Local loss of symmetry in individual Bmp7 ncko suture compartments gradually gives rise to endocranial internasal suture deviation

We define the nasal septum-internasal suture abutment as the junction between the paired nasal bones and the nasal septum cartilage (Fig 4.5A). Normally, the suture mesenchyme interfaces with the upper-most nasal septum margin directly, flanked on either side by the nasal bones with a central blood vessel, the dorsal nasal vein. However, this abutment is typically offset in Bmp7 ncko P14 mice with the most severe phenotypes exhibiting significant expansion of the mesenchyme, characterized by a gap between the endocranial aspect of the nasal bones and the formerly adjacent nasal cartilage (Fig 4.5B).

Given the gradual, endocranially-focused nature of Bmp7 ncko internasal suture deviation, we chose to examine the abutment of the internasal suture with the nasal septum cartilage at a higher resolution for local molecular changes at the ages prior to observed major bone remodeling. Examining the P7 internasal suture abutment, we observed qualitative protein-level structural- and matrix-related asymmetries indicating local

restructuring of the environment. In neighboring sections, we observed shifted domains of Fibromodulin (Fmod) and Cd44 from control midline symmetry, corresponding to the degree of curvature in Bmp7 ncko mice (Fig 4.5C). In Bmp7 ctrl mice, the punctate Fmod stain is mainly concentrated in the center of the internasal suture mesenchyme, flanked on either side by Cd44. This inverse relationship is maintained in Bmp 7 ncko mice, however lacks the clear lateral stratification expected for the internasal suture. Instead, patches spanning the entire mesenchyme width are either Fmod or Cd44 positive, concentrated around the point of deviation endocranially. Interestingly, a similarly curved stream of Pcna+ proliferating cells follows this trajectory. In Bmp7 ctrl mice, proliferating cells are less common in the most central Fmod+ mesenchymal domain.

Considering the subtle but substantial differences at the abutment by P7, we predicted that similar patterns of expression may already be present shortly after birth (P0), when the nasal bones are mineralized sufficiently to form the boundaries of the internasal suture on either side of the suture mesenchyme, which contains the dorsal nasal vein (Fig 4.5D). Indeed, we found that several axes of suture biology appeared disturbed (Fig 4.5E). Piezo1 and Rock2, which participate in the mechanoregulatory cascade, show asymmetry in Bmp7 ncko mice, which have laterally asymmetric clustering of positive cells ahead of or within the inferior tip of the nasal bones. Expression of these proteins is symmetrical in control mice (Fig 4.5F). Cd44, a cell surface-anchored protein which plays diverse roles in growth factor sequestration, cell metabolism, and extracellular matrix composition, is typically highest surrounding the outer border of the nasal bones. This distribution is perturbed in mutant mice, with less clear boundaries and a broader expression domain spanning the mesenchyme. Together, these results indicate local, highly specific molecular and structural changes during early internasal suture establishment.

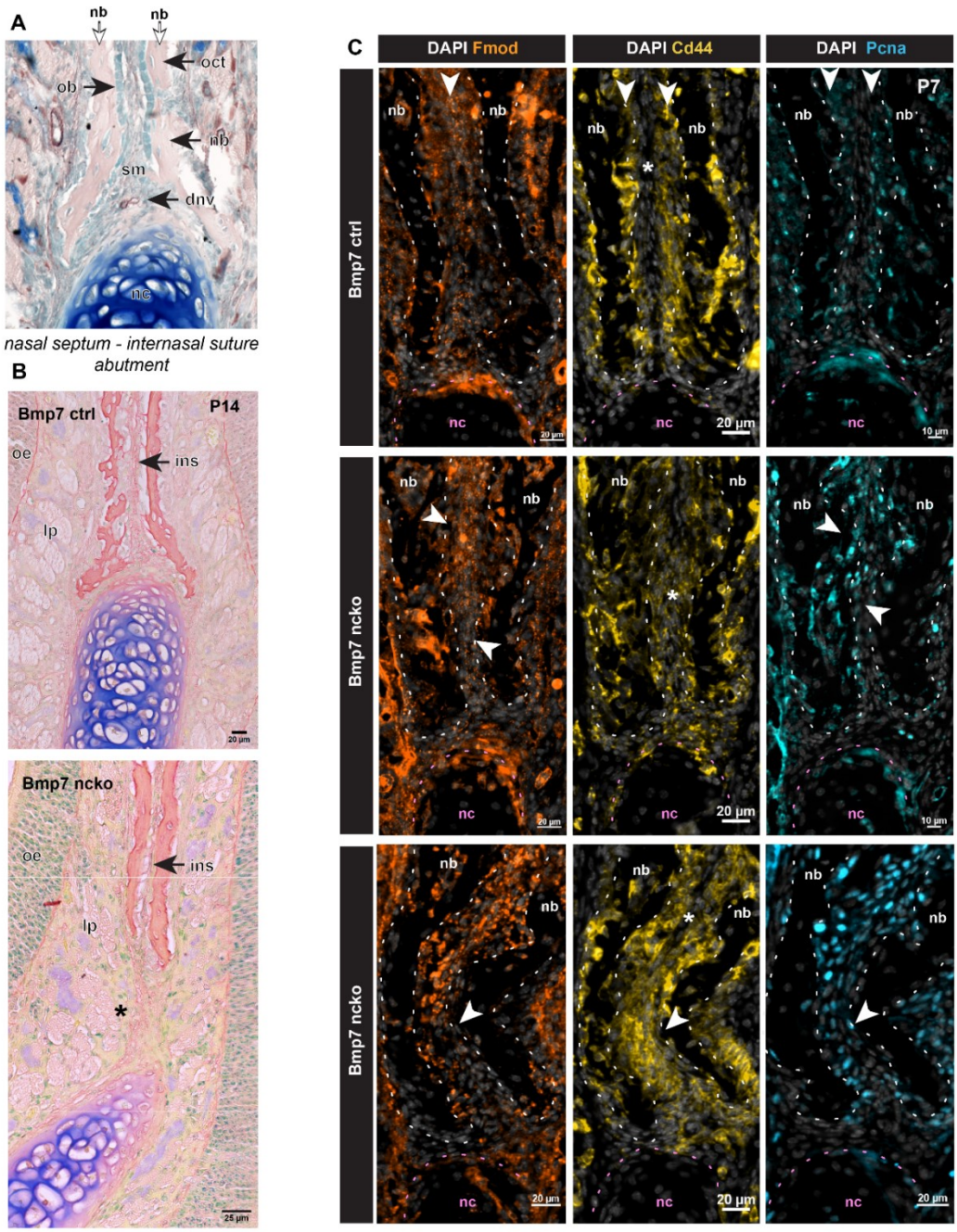
A
nb
nb
oct
ob
nb
sm
dnv
nc
nasal septum - internasal suture abutment
B
Bmp7 ctrl
P14
oe
ins
lp
20 µm
Bmp7 ncko
oe
ins
lp
*
25 µm
C
DAPI Fmod
DAPI Cd44
DAPI Pcna
P7
Bmp7 ctrl
Bmp7 ncko
Bmp7 ncko
nb
nc
*
20 µm
10 µm

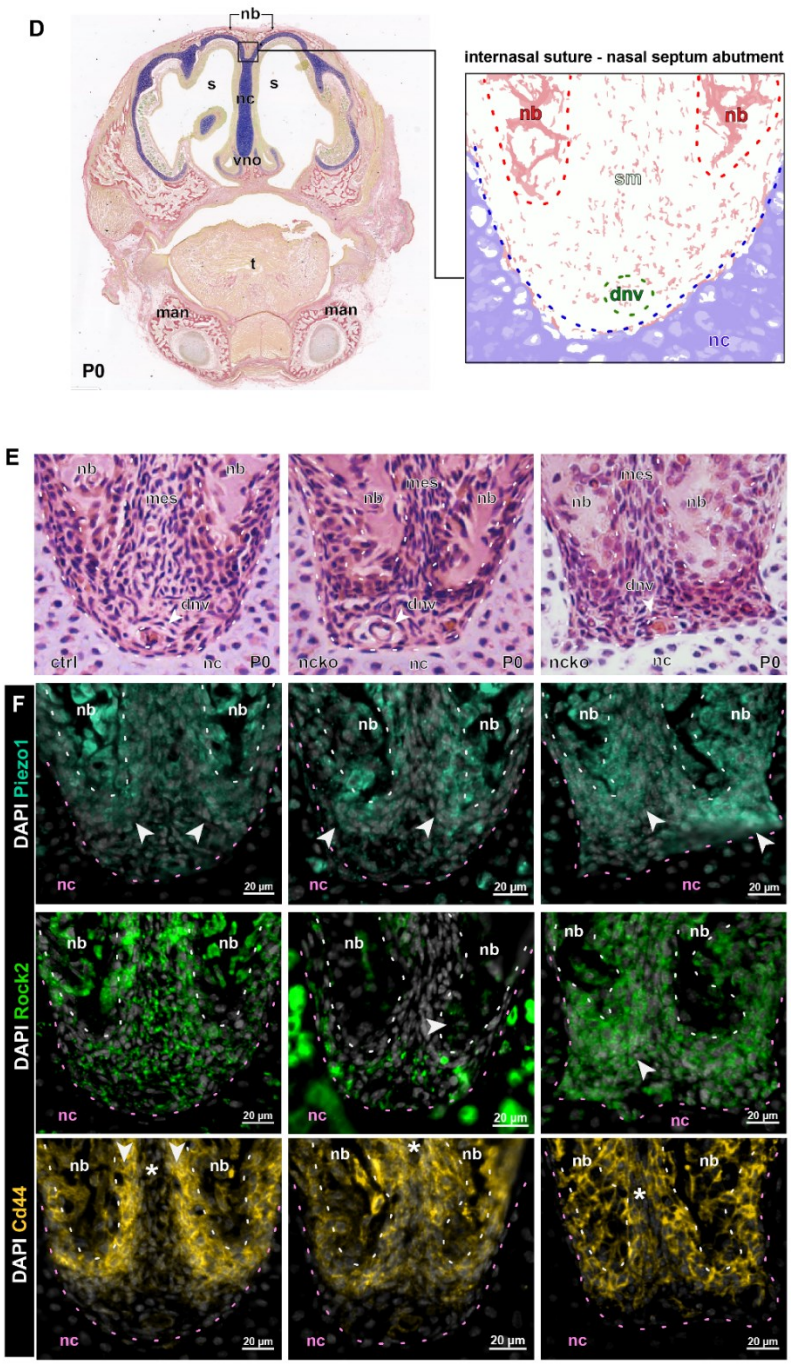

Figure 4.5 Local asymmetry in the Bmp7 nasal septum – internasal suture abutment.
(A) Orcein and methylene blue histological stain demonstrating expected anatomy of the abutment between the nasal septum and internasal suture in the coronal plane at 2 weeks (P14). Elastic fibers are stained reddish-brown and proteoglycans are dark blue. Other cells can be distinguished morphologically, including cuboidal bone-lining light blue osteoblasts and osteocytes within lacunae in nasal bones. The elastic dorsal nasal vein (dnv) is evident within the most endocranial mesenchyme of the internasal suture, at the abutment with the nasal septum cartilage (dark blue). (B) Modified pentachrome histological stain of nasal septum-internasal suture abutment at P14. The internasal suture (ins) is flanked on either side by nasal bones, which are situated within the lamina propria (lp) and olfactory epithelium (oe). Expanded region

between the nasal bones and nasal septum cartilage is indicated with an asterisk (*). (C) Immunofluorescent staining of the internasal suture abutment in P7 mice (top row: control, lower rows: ncko) for Fibromodulin (orange), Cd44 (yellow), and Pcna (blue) in neighboring paraffin sections. DAPI nuclear counterstain is light grey. Arrows and asterisks indicate regions of disruption to suture in each image. Mesenchymal Fibromodulin (Fmod) is central in Bmp7 ctrl mice (white arrowhead), but follows a curved trajectory in the Bmp7 ncko ins. Cd44 is similarly disrupted, with control positivity along the inside surface of nasal bones (white arrowheads) and central mesenchymal negativity (*) but patchy, discontinuous patterns in Bmp7 ncko sections. Highest mesenchymal Cd44 is seen in Bmp7 ncko sections in the region of deviation corresponding to notable Fmod absence (white arrowhead). Proliferating Pcna+ cells follow a similarly skewed trajectory in Bmp7 ncko mice, with a stream of positive cells in regions of unusual Fmod and Cd44 expression (white arrowheads). (D) Pentachrome histological stain of neonatatal (P0) coronal head section. Internasal suture – nasal septum abutment is indicated in left panel by black rectangle, expanded in graphic representation on right. In this early stage of internasal suture establishment, the nasal cartilage (nc) forms a continuous U-shape below the entire internasal suture (ins) and nasal bone (nb) complex. (E) Hematoxylin and eosin staining for Bmp7 ctrl (left panel) and Bmp7 ncko (right panels) internasal suture abutment. (F) Immunofluorescent staining for Piezo1 (turquoise), Rock2 (green), and Cd44 (yellow) in neighboring sections to histological sections in (E). Piezo1 and Rock2, indicative of mechanoregulatory activity, are asymmetrically distributed in Bmp7 ncko sections as early as P0, highlighted with white arrowheads. Bmp7 ncko sections show a preferential positivity of cells within one endocranial nasal bone tip, with contralateral increase in the opposite endocranial osteogenic condensation. As in P7 sections, Cd44 is less clearly defined (white arrowheads lining bone, asterisk of negative central mesenchyme) and trends toward a mesenchymal distribution. nb: nasal bone; sm: suture mesenchyme; ins: internasal suture; nc: nasal cartilage; ob: presumptive osteoblast; oct: presumptive osteocyte; dnv: dorsal nasal vein; lp: lamina propria; oe: olfactory epithelium; s: sinus; man: mandible; t: tongue

4.3.6 Bmp7 is expressed by early progenitor and pre-osteoblast populations in the internasal suture

To define the transcriptomic landscape in which *Bmp7*+ cells reside at a biologically relevant resolution, we performed single-nucleus RNA sequencing of actively transcribing cells from internasal sutures dissected from P4 wild type mice. Tissues included minimal nasal bone from either side of the internasal suture and a small amount of the superior nasal septum margin. Skin was removed and the surface periosteum was debrided prior to sample collection (Fig. 4.6A). We filtered the snRNA-seq output using the Seurat v3 (Stuart et al., 2019) and PopsicleR (Grandi et al., 2022) R packages and obtained 1026 cells (median of 1654 genes per cell). We identified 12 cell clusters through unsupervised graph clustering, which we predicted to belong to the following categories: mesenchymal progenitors (mes.prog.1-3), osteogenic (osteog.1-5), chondrogenic (chondro), hematopoietic (hemato), vascular (vasc), or olfactory epithelium (olf.epith) (Fig. 4.6B). Cluster annotations were assigned based on previously reported marker genes and highly expressed genes in each cluster (Fig. 4.6C). *Bmp7* is most highly expressed in focal subclusters within early

progenitor (mes.prog.1) and early osteoblast (osteog.2) populations, with some expression in chondrogenic and late osteogenic cells (Fig. 4.6D). Notably, less than 4% of cells in positive clusters express the gene highly, indicating restricted localization of *Bmp7*+ cells. The top genes expressed by *Bmp7*+ cells were broadly associated with energy metabolism and extracellular matrix composition according to molecular function gene ontology term grouping with REVIGO (Fig. 4.6E-F).

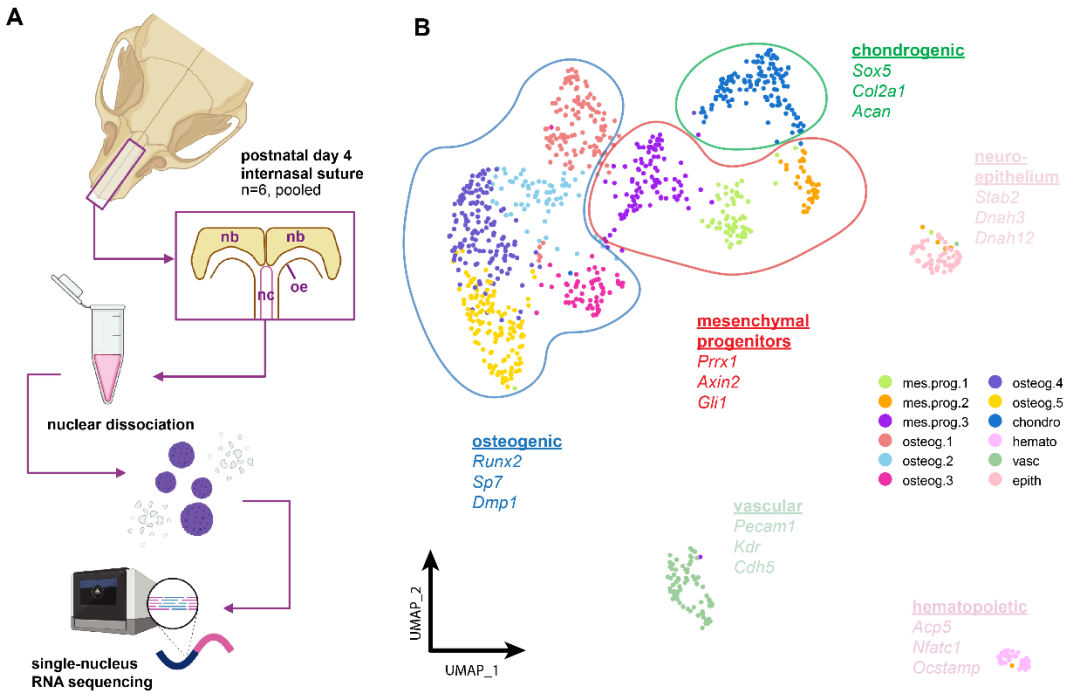

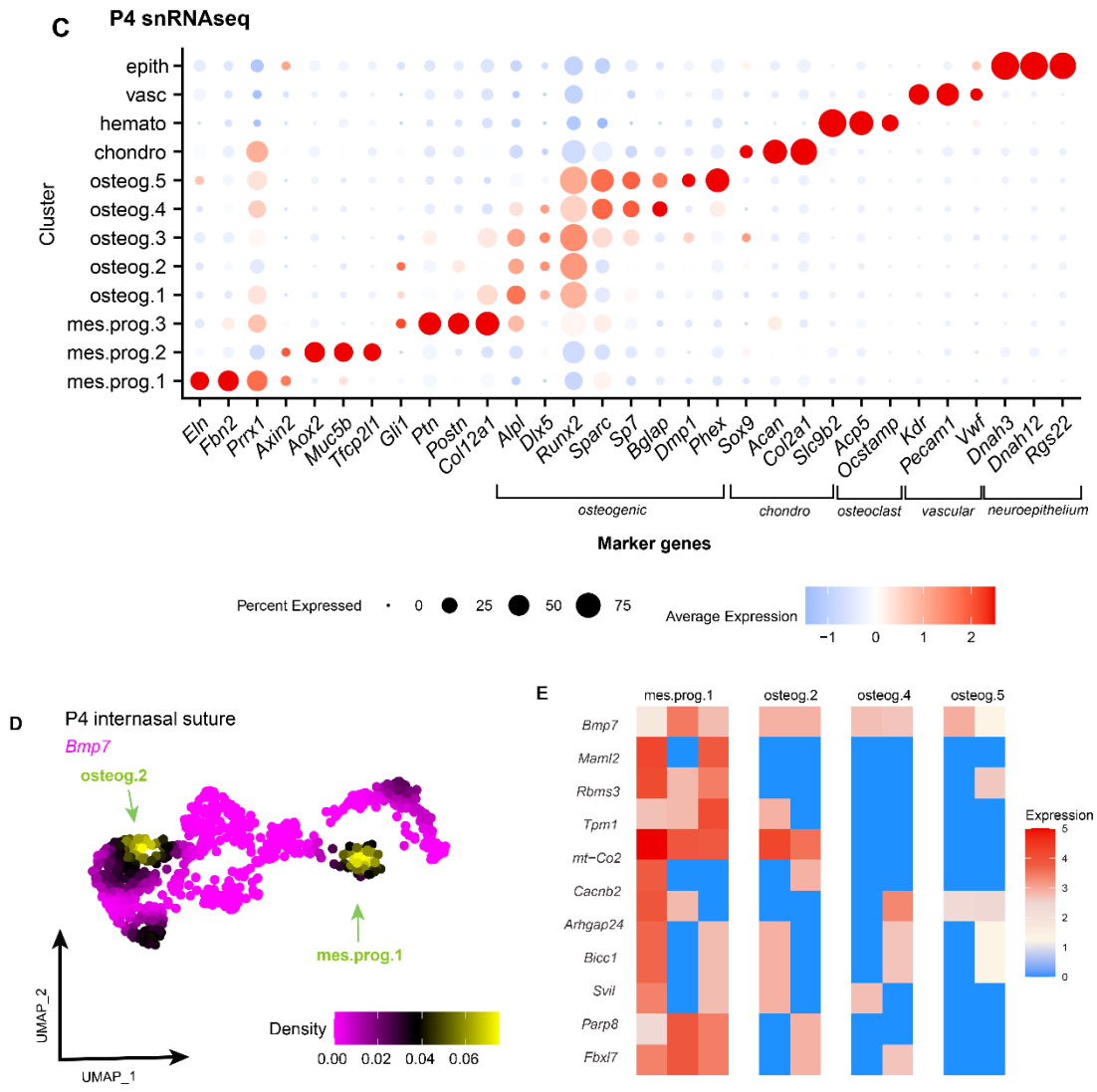
C
P4 snRNAseq
epith
vasc
hemato
chondro
osteog.5
osteog.4
osteog.3
osteog.2
osteog.1
mes.prog.3
mes.prog.2
mes.prog.1
Cluster
Eln
Fbn2
Prrx1
Axin2
Aox2
Muc5b
Tfcp2l1
Gli1
Ptn
Postn
Col12a1
Alpl
Dlx5
Runx2
Sparc
Sp7
Bglap
Dmp1
Phex
Sox9
Acan
Col2a1
Slc9b2
Acp5
Ocstamp
Kdr
Pecam1
Vwf
Dnah3
Dnah12
Rgs22
osteogenic
chondro
osteoclast
vascular
neuroepithelium
Marker genes
Percent Expressed
0
25
50
75
Average Expression
−1
0
1
2
D
P4 internasal suture
Bmp7
osteog.2
mes.prog.1
UMAP_2
UMAP_1
Density
0.00
0.02
0.04
0.06
E
mes.prog.1
osteog.2
osteog.4
osteog.5
Bmp7
Maml2
Rbms3
Tpm1
mt−Co2
Cacnb2
Arhgap24
Bicc1
Svil
Parp8
Fbxl7
Expression
5
4
3
2
1
0

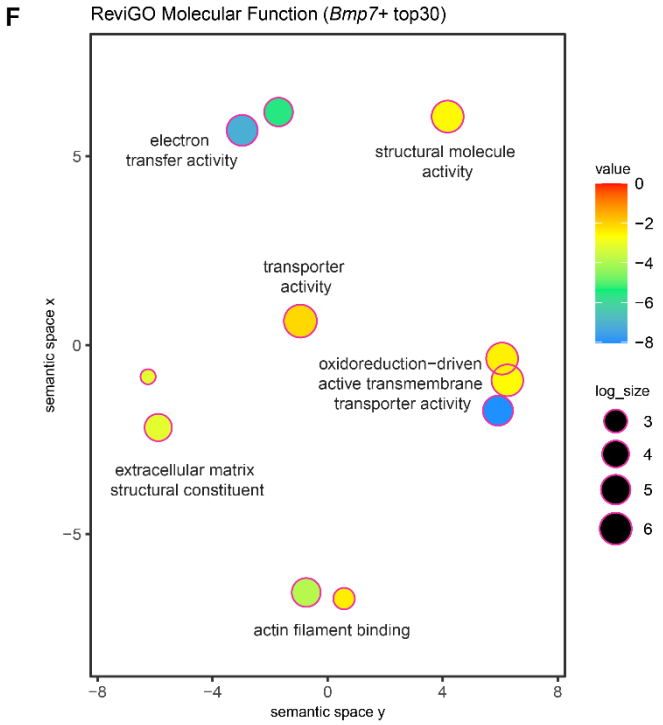

Figure 4.6 *Bmp7* is expressed in osteogenic snRNA-seq clusters of wild type internasal suture. (A) Graphic representation of single-nucleus RNA sequencing (snRNA-seq) workflow. Briefly, the internasal suture and adjacent nasal bone (nb), nasal cartilage (nc), and olfactory epithelium (oe) margins were dissected from 3 male and 3 female 4-day-old wild type mice (P4). Nuclei were dissociated and processed for sequencing using the 10X Genomics Chromium system. (B) Uniform Manifold Approximation and Projection (UMAP) highlighting osteogenic, chondrogenic, mesenchymal progenitor, olfactory epithelium, vascular, and hematopoietic clusters, with indicative genes listed below each category. (C) Dot Plot representing expression of selected genes used to assign cluster identities. (D) Nebulosa density plot of Bmp7 expression in mesenchymal clusters. Highest density of cells expressing Bmp7 is colored yellow, with absence of expression in magenta. Top two concentrations of Bmp7+ cells are highlighted with green arrows (mes.prog.1, osteog.2). (E) Heatmap of top10 genes identified with FindAllMarkers function across all cells expressing Bmp7. Non-mesenchymal clusters are excluded from this heatmap, but not from biased gene identification. (F) REVIGO scatterplot of semantic similarity between Gene Ontology terms associated with top30 biased genes in Bmp7+ cells after redundancy reduction. Log.size represents the frequency of the annotated GO term in the Molecular Function database. GO Term list generated using Princeton GO::TermFinder.

4.3.7 Bmp7 *is expressed asymmetrically within the internasal suture-nasal septum abutment of control mice*

The mounting evidence for asymmetric effects of *Bmp7* deletion, especially endocranially, led us to examine *Bmp7* expression at the leading edge of the nasal bones in this region. *In situ* hybridization at P0 revealed that *Bmp7* was mainly expressed in the olfactory epithelium and along the borders of the *Alpl*+ osteogenic front (Fig. 4.7A,B). Its bone-associated expression appeared to be concentrated along the endocranial top of the nasal bones (Fig. 4.7C-D). Interestingly, *Bmp7* expression appeared qualitatively asymmetric between the paired nasal bones. In the example shown, more *Bmp7* positive cells were observed within the left nasal bone and in the most proximal mesenchymal condensation but reaching more endocranially and laterally from the right bone (Fig. 4.7E). However, quantification of *Bmp7* positivity and its symmetry between three Bmp7 ctrl mice did not indicate a statistically significant asymmetry ($p = 0.1$). Nevertheless, the mean and median

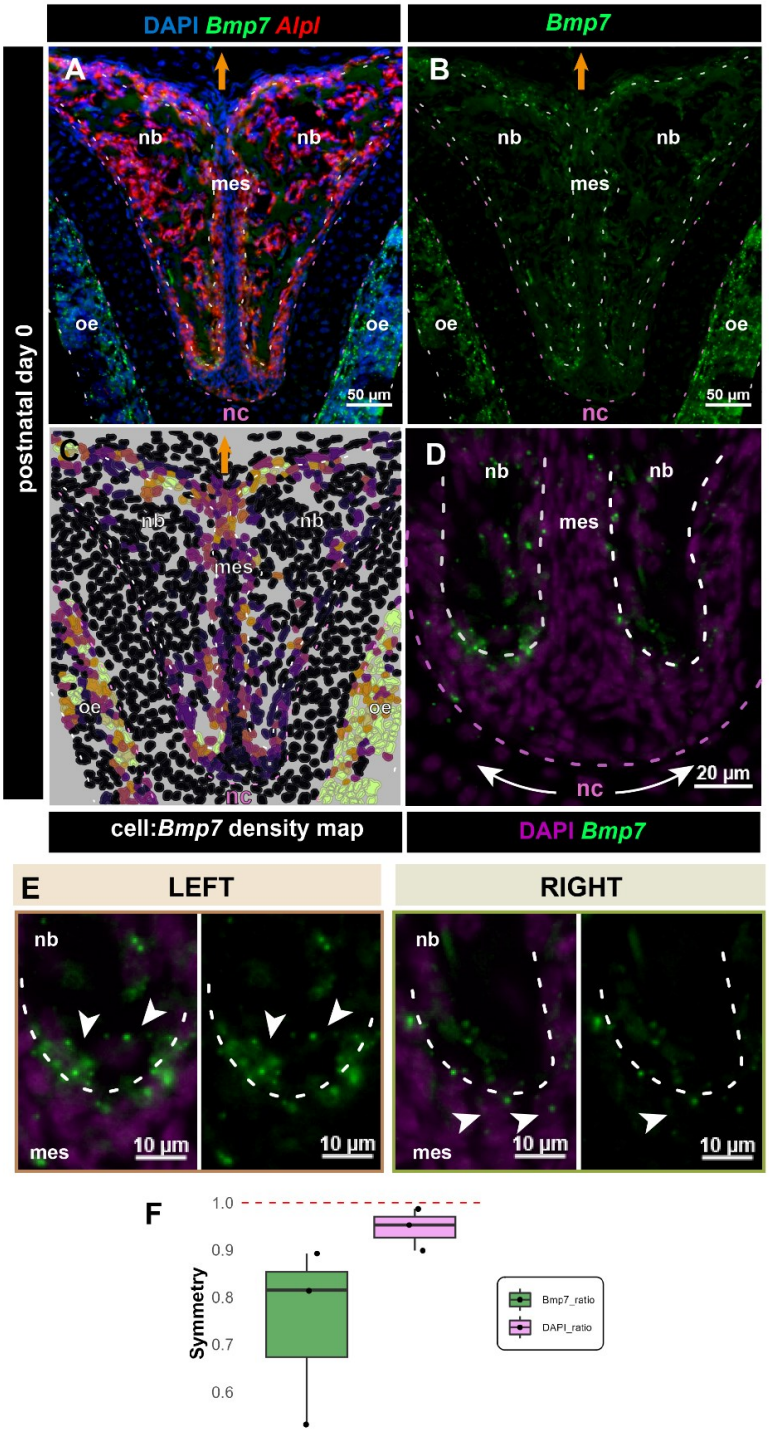
DAPI Bmp7 Alpl
Bmp7
A
B
nb
nb
mes
oe
oe
nc
50 μm
postnatal day 0
C
D
20 μm
cell:Bmp7 density map
DAPI Bmp7
E
LEFT
RIGHT
10 μm
F
Symmetry
1.0
0.9
0.8
0.7
0.6
Bmp7_ratio
DAPI_ratio

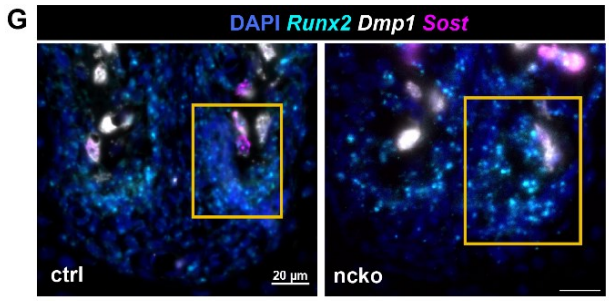
G
DAPI Runx2 Dmp1 Sost
ctrl
20 µm
ncko

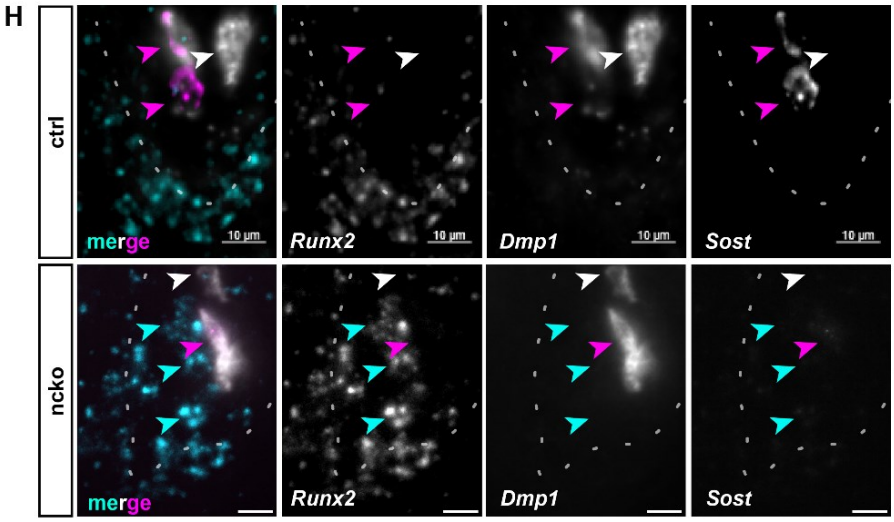
H
ctrl
merge
10 µm
Runx2
Dmp1
Sost
ncko

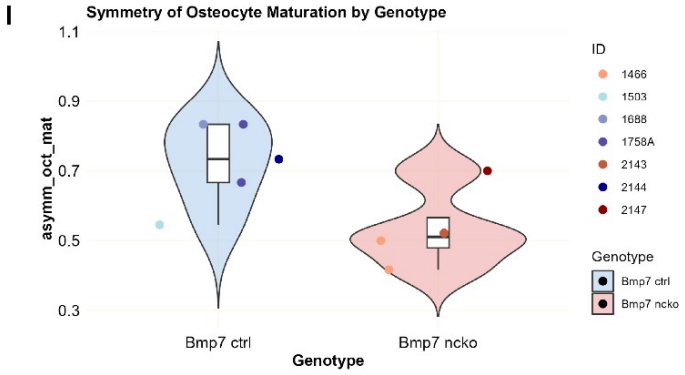
I
Symmetry of Osteocyte Maturation by Genotype
asymm_oct_mat
1.1
0.9
0.7
0.5
0.3
Bmp7 ctrl
Bmp7 ncko
Genotype
ID
1466
1503
1688
1758A
2143
2144
2147
Genotype
Bmp7 ctrl
Bmp7 ncko

Figure 4.7 Asymmetric Bmp7 expression along the endocranial surface of the nasal bones birth.

(A,B) RNAscope in situ hybridization (ISH) of probes for *Bmp7* (green) and *Alpl* (pre-osteoblasts, red) in postnatal day 0 Bmp7 ctrl mice. Single-channel *Bmp7* expression shown in (B). (C) Density map of relative *Bmp7* stain brightness assigned to automatically segmented cells using QuPath (Bankhead 2017), depicting brightest regions of expression in the oral epithelium (oe) and endocranial tip of nasal bones (nb), with lower but notable expression lining the internasal suture mesenchymal surface of the nasal bones. (D) Magnified view of the *Bmp7* expression in the abutment between the internasal suture and nasal septum cartilage. Green: *Bmp7* positivity; violet: DAPI nuclear counterstain. (E) Cropped left and right nasal bone surfaces from panel (D), with white arrows highlighting expression of *Bmp7* in the nasal bone (nb) or endocranial mesenchyme (mes). (F) Box plot comparing the symmetry of Bmp7 and DAPI ratios. The mean and median Bmp7 ratio were both below 1 (mean = 0.746, median = 0.815), while the mean and median DAPI ratio were close to 1 (mean = 0.946, median = 0.953). The Fligner-Killeen test showed no significant difference in variances (chi-squared = 1.0421, p = 0.3073), and the Wilcoxon rank-sum test revealed no significant difference betweenthe Bmp7 and DAPI ratios (W = 0, p = 0.1). 3 Bmp7 ctrl mice were analyzed. (G) ISH for *Runx2* (light blue, pre-osteoblasts), *Dmp1* (white, maturing osteocytes), and *Sost* (violet, mature osteocytes) in the P0 abutment. Yellow rectangle indicates region of magnification in panel (H). (H) Magnified region indicated with yellow rectangle in G, split by channel and presented in greyscale. White dotted outline marks predicted nasal bone edge. Pink arrowheads show *Dmp1*+/*Sost*+ cells, white indicate *Dmp1*+ only, and turquoise indicate *Runx2*+ only. Neonatal Bmp7 ncko mice have a unilateral zone of *Runx2* positivity within the endocranial nasal bone, with less clear progression of differentiation from osteoblast to maturing osteocyte. (I) Violin plot comparing the asymmetry of osteocyte maturation index (asymm_oct_mat) between Bmp7 ctrl and Bmp7 ncko groups. The Wilcoxon rank-sum test showed no significant difference between groups (W = 18, p = 0.06506) with Common Language Effect Size of 0.9. n = 4 Bmp7 ctrl, 3 Bmp7 ncko.

Bmp7 ratio were both below 1 (mean = 0.746, median = 0.815), indicating asymmetry, whereas the mean and median DAPI ratio were close to 1 (mean = 0.946, median = 0.953), suggesting near symmetry. The standard deviation for the Bmp7 ratio (0.190) was higher than that for the DAPI ratio (0.0446), indicating greater variability in the Bmp7 ratio. This qualitative trend toward asymmetry supports a potentially corrective role for *Bmp7*, eliminated with genetic deficiency as in the Bmp7

ncko mouse. If so, the response is variable and highly specific, as suggested by the variable Bmp7 ncko phenotype observed and rare nature of *Bmp7*+ cells (Fig. 4.6D, 4.7E).

The organization of *Bmp7* expression around the osteogenic leading edge and gradual bony deviation in Bmp7 ncko mice led us to consider osteogenesis within the internasal suture abutment with respect to local cellular differentiation. Despite (or, as a result of) asymmetric *Bmp7* expression, Bmp7 ctrl mice had a clearly defined and symmetrical stratification of osteogenic cells across the endocranial nasal bone leading edge. A layer of *Runx2*+ cells encapsulated the nasal bone within the osteogenic mesenchymal condensation, as described in other sutures (X. Qin et al., 2019) (Fig. 4.7F). Within the developing nasal bone, morphologically distinct osteocytes were either

Dmp1+/*Sost*- (immature) or *Dmp1*+/*Sost*+ (maturing) (Fig. 4.7G). These cells may have had some *Runx2* positivity. Bmp7 ncko sutures, however, were considerably less organized. Across 3 Bmp7 ncko mice, we observed clustered or single-cell triple positivity on one side, with *Runx2* continuity into the nasal bone (compared with 4 Bmp7 ctrl mice). These indicators of osteogenic status (*Runx2, Dmp1, Sost*) appeared lopsided between paired nasal bones in Bmp7 ncko mice, but matched in Bmp7 ctrl mice. Comparison of osteocyte maturity scores and their symmetry revealed that, in mice, there was no significant difference between scores ($W = 18$, $p = 0.06506$). However, Common Language Effect Size (CL) was calculated to be 0.9, indicating a high likelihood (90% probability) that Bmp7 ctrl bones have higher symmetry of osteocyte maturation than a randomly selected measurement from Bmp7 ncko.

4.4 Discussion

The patterning of the craniofacial complex is generally very robust, with major gross congenital asymmetry mainly limited to severe disruption to central developmental gene regulatory networks. Comparatively little is understood about agents of postnatal maintenance of symmetry. There are seemingly endless combinations of extrinsic forces which a newborn may encounter, and it is unlikely that all are applied to the skull evenly. Yet, asymmetry of mechanoresponsive elements like the cranial sutures is disproportionately rare. Thus, there must be a robust network of counter-regulation to balance uneven external pressure. This study utilized a genetic mouse model of neural crest cell-specific *Bmp7* deletion with internasal suture asymmetry to explain craniofacial suture contribution to midface deficiency. The *Bmp7* neural crest cell-specific knockout (Bmp7 ncko) mouse provided an informative example of postnatal craniofacial suture disruption which magnified to detrimental physiological effect, without synostosis. In the context of midfacial hypoplasia, this presented a pre-clinical model to understand the intricacies of facial suture functional growth and impacts at a whole-system scale. We observed correlation between facial suture disruption and midface hypoplasia severity in Bmp7 ncko mice. Through morphometric, histological, and multi-omic analysis of the internasal suture, we concluded that these macroscopic changes were downstream effects of disrupted molecular determinants of suture symmetry. In this setting, small changes to the suture

microenvironment are magnified via physiological processes like bone remodeling, which contribute to a whole-organism effect (Baddam, Biancardi, et al., 2021).

4.4.1 Asymmetric expression of **Bmp7** *is necessary for symmetrical nasal bone extension*

Loss of *Bmp7* did not interfere with initiation of osteogenesis or bone formation, but it seemed to prevent cells from responding or performing functions normally, and initiated cascades that manifested as severe architectural and physiological consequences. In Bmp7 ncko mice, these included nasal bone deviation, obliteration of osteoblasts, nasal septum deviation (Baddam, Young, et al., 2021), and midface hypoplasia (Baddam, Biancardi, et al., 2021) which we hypothesize are due to disruption of balance required for symmetry. Despite the bone-specific role implied by its name, Bmp7 has several non-osteogenic functions throughout the body. For example, its expression in cancer is associated with the inhibition of EMT-related genes, a process which is known to be closely interwoven with biomechanical changes and compressive stress (Cai et al., 2022; Ying et al., 2015). Our data supports a role for Bmp7 as a response element with substantial impact on the osteogenic system, given its highly restricted spatiotemporal expression and the dramatic effects that its loss had on facial symmetry. We also observed strong, specific expression of *Bmp7* in the olfactory epithelium of wild type mice, a structure which is primarily derived from the non-neural crest olfactory placode and is thus unaffected directly by Bmp7 ncko (Suzuki & Osumi, 2015). While our study does not preclude Bmp7-related changes in earlier development, the internasal suture only becomes defined around birth, which is when we observed *Bmp7* localization at the internasal suture-nasal septum abutment. At this age, suckling could provide a mechanical input necessitating a balancing response from cells, an event which has been connected to sutures regarding timing of metopic suture closure and mid-palatal suture changes (W. Du et al., 2021; Haravu et al., 2023; J. Li et al., 2016). This function could be fulfilled by direct transcriptional regulation or through epistatic processes.

4.4.2 Family of hypotheses: Bmp7 and asymmetry

We propose a family of hypotheses based on our data to explain internasal suture deviation without Bmp7. One possibility is that there are two slightly different genetic programs, one

of which involves *Bmp7*, which balance nasal bone osteogenesis through independent mechanisms (Fig. 4.8A). Both would likely act in the same gene regulatory network and result in the same osteogenic outcome to facilitate symmetrical midfacial growth. The loss of one such balancing factor would cause asymmetry if not compensated for, though this theoretical predetermined patterning program would likely result in predictable deviation direction or severity, which is not supported by our data. Also, *Bmp7* was not constitutively active in Bmp7 ctrl sutures though it was mainly expressed unilaterally. We did not identify any genes which share the *Bmp7* pattern contralaterally, though do not exclude this possibility.

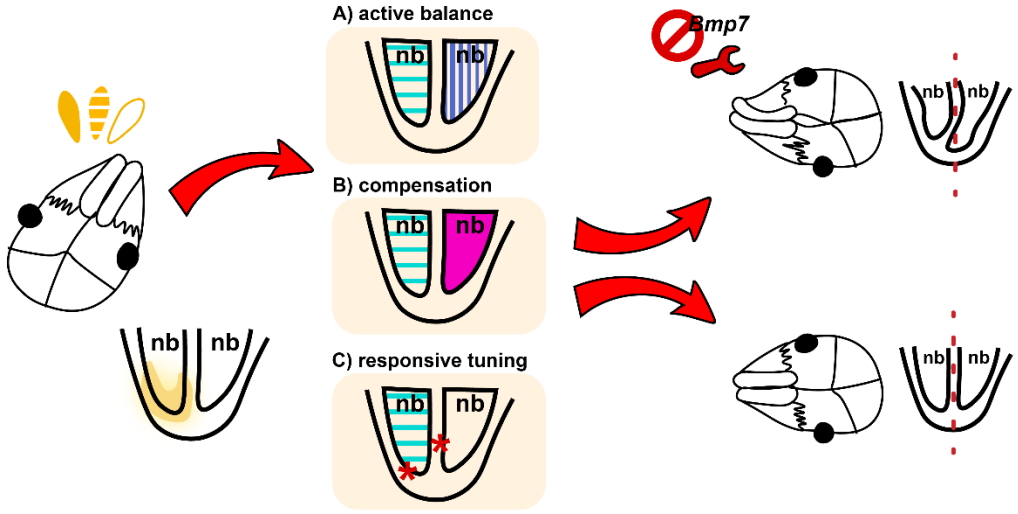

Figure 4.8 Family of hypotheses for Bmp7 function.
(A) Two slightly different genetic programs, one of which involves Bmp7, balance nasal bone osteogenesis through independent mechanisms ("active balance"). (B) Constitutive expression of a compensatory gene which balances Bmp7 and whose induction causes pathology in the absence of Bmp7 ("compensation"). (C) Bmp7 expression has a mechanoresponsive role in osteogenesis to facilitate correction of or resistance to postnatal asymmetric forces ("responsive tuning"). nb: nasal bone. Yellow fill represents extrinsic force applying asymmetric pressure to the skull. Asterisk represents hypothetical Bmp7 expression.

A related alternate hypothesis involves the constitutive expression of a compensatory gene which balances Bmp7 and whose induction causes pathology in the absence of *Bmp7* (Fig. 4.8B). We did observe disturbed osteogenesis unilaterally in P0 Bmp7 ncko mice which is not necessarily directly downstream of *Bmp7,* though its asymmetric expression suggests that it is involved. We do not have evidence to support or disprove this hypothesis so cannot exclude it. High resolution spatial transcriptomic analysis or Laser Capture Microdissection of the endocranial internasal suture in Bmp7 ctrl

and ncko conditions could identify up-regulated genes in the opposite compartment to this end as done in Holmes et al 2020 for calvarial suture mesenchyme, which we were unable to address sufficiently in this study (Holmes et al., 2020).

Another hypothesis is that *Bmp7* expression has a mechanoresponsive role in osteogenesis to facilitate correction of or resistance to postnatal asymmetric forces (Fig. 4.8C). The asymmetric expression of Piezo1/Rock2 in Bmp7 ncko mice indicates some involvement of Bmp7 with mechanoregulation. Our observations of its skewed and rare spatiotemporal expression pattern (snRNA-seq, RNAscope) and varying severity/direction of deviation point to a stochastic response mechanism. We posit that *Bmp7* is expressed as a result of normal asymmetric forces and fulfills a regulatory measure to maintain symmetry in the growing abutment. *Bmp7* could plausibly tune the rate of osteogenesis, inhibit another factor, or feed into another gene regulatory network that indirectly affects osteogenesis. Our data does not, however, support a critical role for *Bmp7* in osteogenesis in general. We propose that an indirect regulatory mechanism involving *Bmp7* is a likely element of internasal suture symmetrical development and maintenance. Beyond the scope of our study, this hypothesis could be tested by quantifying *Bmp7* induction upon mechanical stimulation. Previous studies have shown that *Bmp7* is in fact upregulated *in vitro* when mechanically loaded (Santos et al., 2011; Z. Wang & Guo, 2013). Deletion of *Bmp7* from Yap/Taz-expressing cells could be informative to develop this concept further. Interestingly, *Bmp7* expression is not asymmetric across the entire craniofacial complex in our mice; it may be specific to the internasal suture environment or require a high threshold of mechanical stimulation. This hypothesis does not exclude the possibility that the Bmp7 ncko phenotype at P14 could be due to magnification of bone overgrowth and remodeling changing the mechanical environment in the midface.

4.4.3 The internasal suture as a model of intramembranous ossification

The unique anatomy of the internasal suture amongst other sutures makes it a useful model for study of intramembranous bone formation. The long, abutting dorsoventral surface of the nasal bones flanking the internasal suture provides sufficient surface area to examine osteogenic cell organization and behavior. This suture is also isolated anatomically from the *dura mater* of the brain, a complicating source of signaling in the cranial vault (Farmer et al., 2021; Gagan et al., 2007; H.-J. Kim et al., 1998; S. Li et al., 2007; Opperman et al.,

1995). Traditionally, endo- and ectocranial directions in the sutures are in reference to proximity to the dura. We present cellular evidence of ecto- vs. endocranial suture patterning in a viscerocranial suture.

The endocranially stratified asymmetry observed in the Bmp7 ncko internasal suture highlights an unexplored aspect of suture patterning and development beyond synostosis or facial clefting. We observed an overall theme of actin assembly and the extracellular environment in the endocranial internasal suture domain with mutant asymmetry resulting in altered Piezo1/Rock2 expression as early as P0, suggesting mechanoregulatory contribution to the phenotype (J. M. Collins et al., 2023). By P7, when structural asymmetry was developing, we observed anomalies in the matrix including Fibromodulin expression and collagen fibers in picrosirius red staining. We hypothesize that these early effects in Bmp7 ncko mice magnified to result in a major deviation and consequently bone remodeling by P14.

4.4.4 Abnormalities in midfacial sutures prohibit sufficient advancement of the midface

There are 27 facial sutures, yet their contribution to midfacial growth is still undervalued (M. M. Wang et al., 2021, 2022). There is a correlation between cranial suture pathology and midface deficiency of hypoplasia (MFH), but insufficient functional evidence acknowledging shared mechanisms (Calandrelli et al., 2023; Katzen & McCarthy, 2000; Layton et al., 2023). Premature fusion of the sutures is frequently involved. In this study, we observed correlation of suture malformation with the severity of MFH, though notably in the absence of synostosis. Harnessing the intrinsic growth potential of facial sutures for treatment of MFH is a promising therapeutic avenue and is less traumatic than the surgical midfacial advancement techniques like Le Fort osteotomy (Cedars et al., 1999; Fariña et al., 2018; Hariri et al., 2011; B. Kim et al., 2020). However, appreciation of the biological mechanisms of suture growth in altered genetic and mechanical contexts is critical for the success of novel therapies. For example, the long-term outcomes of distraction osteogenesis, like trans-sutural distraction osteogenesis (TSDO), are dependent on the intrinsic osteogenic capacity of the targeted suture at the time of distraction as well as the axes and magnitude of tension applied (Ross, 1987; Scolozzi, 2008). To this end, it may be prudent to consider the practical use of sutures as indicators of compromised

intramembranous ossification that may impact success of potential clinical interventions. In the case of the Bmp7 ncko mouse, distraction osteogenesis may not be a viable therapeutic intervention due to compromised mechanoregulation of osteoblast function. Distraction osteogenesis for midface advancement was ineffective in the Yucatan minipig model of midface hypoplasia when compared with other pigs – a sign of prohibitive intrinsic biology in congenital hypoplasia (Herring et al., 2024). Other groups have identified correlation between midface hypoplasia and suture anomalies in mice, which may reveal additional insights into suture contribution to midfacial growth upon histochemical characterization (B. Kim et al., 2020; B.-S. Kim et al., 2021; D. K. Nelson & Williams, 2004).

Congenital pathological fusion of cranial sutures in craniosynostosis has been tremendously informative for genetic determinants of osteoblast behavior and suture fusion. This study presented an example of non-obliterative suture pathology and midface hypoplasia which begins subtly and worsens over time, with characterization of the sub-structural effect of *Bmp7* loss in the internasal suture. While lateral asymmetry of the skull was not evident in CT scans, a cross-section of the nasal cavity revealed an internal nasal bone asymmetry that precedes nasal septum deviation. Our data suggests that initial asymmetry arises due to disturbed osteogenic balance at the internasal suture-nasal septum abutment, but we did not rule out potential combinatorial effects of other morphologically irregular features of midfacial sutures identified in Figure 1, like interdigitation of the frontal-premaxillary suture. Furthermore, we previously identified biochemical changes to the nasal septum cartilage in Bmp7 ncko mice around the point of deviation (Baddam, Young, et al., 2021). The present study did not address potential structural instability arising from nasal septum chondrocyte status, especially in light of its delayed deviation. This etiology is particularly relevant for human health as personalized medicine and predictors of pathology are further developed, moving toward a more clear picture of spectra of facial variation and their correlation with successful craniofacial interventions (Aponte et al., 2021; Hallgrimsson et al., 2014; Kuehle et al., 2023; Matthews et al., 2018; Yankee et al., 2023; J.-N. Zhang et al., 2023).

4.4.5 Limitations of this study

Bmp7 was only deleted from neural crest cells (NCC) in our mouse model. While NCC have been reported to give rise to the majority of the anterior craniofacial complex, they are not the sole contributor to this system, nor has their interaction with cell types of other embryonic origins been fully characterized *in vivo* (Barrallo-Gimeno & Nieto, 2006; Doro et al., 2019, 2024; Dupin et al., 2006; Etchevers et al., 2019; Knight & Schilling, 2006; Roth, Bayona, et al., 2021; Snider & Mishina, 2014; T. Wu et al., 2017). The internasal suture signaling milieu most likely also bears contributions from NCC-independent structures like nerves or vasculature, potentially including facilitation of osteodifferentiation by perivascular cells (J. M. Collins et al., 2023; Y. Liang et al., 2016; Tower et al., 2021; Xu et al., 2021). *Bmp7* has a reported relationship with stem cell migration and angiogenesis (C. Liang et al., 2022; Tischfield et al., 2017), so this may be an interesting avenue for further study. Conditional deletion from suture stem cells may help to further separate neural crest-specific effects from those impacting mechanosensitive osteoprogenitors (Huang et al., 2021; A.-Q. Liu et al., 2020; Y. Shi et al., 2017).

CHAPTER 5

BMP2 AND BMP7 ARE INDEPENDENT MODULATORS OF BONE FORMATION AT CRANIOFACIAL GROWTH ZONES

Two of the canonically osteogenic Bone Morphogenetic Proteins, Bmp2 and Bmp7, are often unjustifiably interchanged in experimental systems. I had observed overall distinct effects of Bmp7 deletion on structures not impacted by Bmp2 deletion in Wnt1-Cre neural crest models, and hypothesized that their individual roles may be more clear in a suture-targeted system. For this, I used the Gli1-CreERT2 system to induce Bmp2 or Bmp7 recombination embryonically, in early postnatal development, and in adulthood to answer whether specific deletion of each from Gli1+ suture "stem" cells resulted in the same phenotype.

5.1 Introduction

The fields of craniofacial reconstruction and tissue regeneration have been rapidly evolving toward innovative, permanent solutions alongside our growing understanding of molecular underpinnings of pathology and cell behavior. As new developments unfold, it is increasingly important to examine dogmas that underly the premise of current clinical practice and future therapeutics. One such topic is bone regeneration involving the use of the Bone Morphogenetic Protein (Bmp) family for critical size defect repair (G. Chen et al., 2012; Chenard et al., 2012; Sheikh et al., 2015; Zhu et al., 2022). Both Bmp2 and Bmp7 are considered to be potent inducers of osteogenesis and were developed into osteogenic therapeutics – though only rhBMP-2 is currently in use and often for off-label applications (BMP-2 Evaluation in Surgery for Tibial Trauma (BESTT) Study Group et al., 2002; Friedlaender et al., 2001; Ong et al., 2010; Poon et al., 2016; *Scanlon v. Medtronic Sofamor Danek USA Inc.*, 2014; Sheikh et al., 2015). The quality of bone formed with supraphysiologically high doses of rhBMP-2 is still not optimal and requires further development despite its current use (Pan et al., 2017; Zara et al., 2011).

Our research on Bmps in murine craniofacial development, alongside that of other groups (Baddam, Biancardi, et al., 2021; Y. Guo et al., 2018; D. O. Wagner et al., 2010), has revealed that the relationships of Bmp2 and Bmp7 with craniofacial osteogenesis and each other are still incompletely understood (H.-S. Kim et al., 2019). In this study we set out to investigate how deletion of *Bmp2* and *Bmp7* independently affect

osteochondrodifferentiation within two craniofacial growth zones, the intramembranous sutures and the endochondral cranial base (Long, 2012). While they are located in opposite domains of the skull, these growth zones share several features including maintenance of progenitors, long-term bidirectional osteogenic deposition, mechanical loading, and contribution to midfacial growth (Fig. 5.1) (Rosenberg et al., 1997).

Through multimodal techniques including micro-computed tomography, protein and mRNA fluorescence, and single-cell RNA sequencing, we demonstrate that Bmp2 and Bmp7 are not redundant but serve different and specific roles in cranial base development.

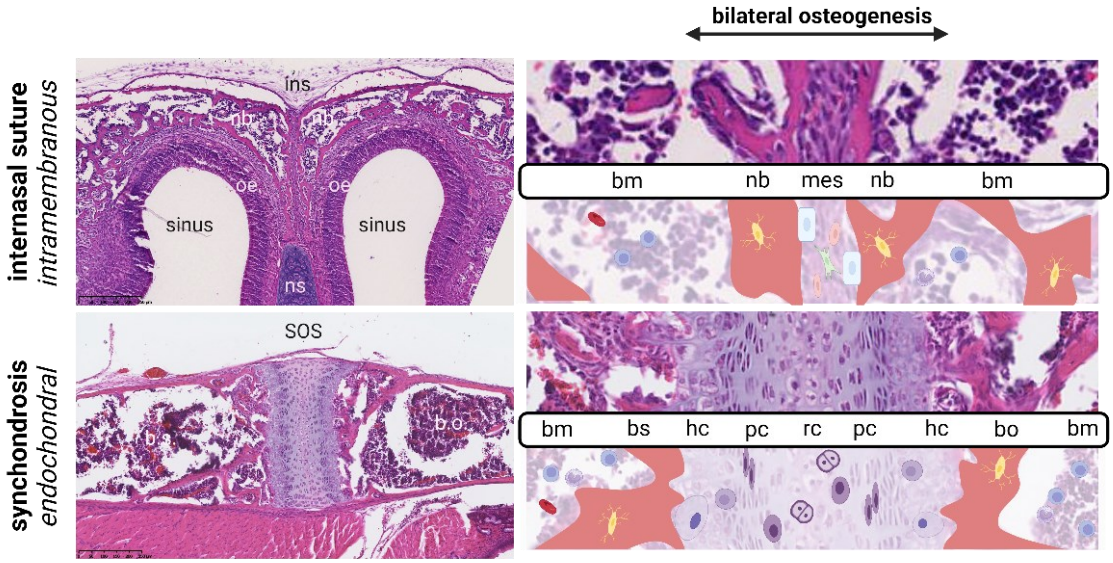

Figure 5.1 Cranial sutures and cranial base synchondroses are examples of bilateral osteogenic growth zones in the craniofacial complex.
Red illustration highlights bone matrix, with yellow osteocytes embedded within. Bone-lining osteoblasts are light blue, fibroblasts are green, and MSCs are pale red. Bone marrow cells are blue or light purple, with red disc-like red blood cells. Chondrocytes are visually represented in purple. Internasal suture coronal section is from a P14 mouse. The sagittal synchondrosis section is from a P21 mouse. ins: internasal suture, oe: olfactory epithelium, ns: nasal septum, SOS: spheno-occipital synchondrosis, bs: basisphenoid bone, bo: basioccipital bone, mes: mesenchyme, nb: nasal bone, bm: bone marrow, rc: resting chondrocytes, pc: proliferative chondrocytes, hc: hypertrophic chondrocytes.

5.2 Results

5.2.1 Conditional deletion of Bmp7 from Gli1^{pos} progenitors, but not Bmp2, impacts trabecular bone remodeling

Bmp2 or *Bmp7* were conditionally deleted from Gli1-CreERT2^{pos} cells (Bmp2 or Bmp7 cko) in adult mice via Tamoxifen induction (Fig. 5.1A). Mice were injected at 2 months of age, left to decontaminate for 7 days, and CT scanned on days 0 and d35 of the experiment wherein d0 is 7 days after the final injection of 2-month-old mice and collected for

histological assessment at d35. Thus, the ages of the mice at d0 and d35 correspond to 2 months + 10 days and 4.5 months, respectively. While Bmp2 cko nasal bones and the intervening suture were histologically comparable to controls, the trabeculae within the Bmp7 cko nasal bones were smaller in diameter though overall nasal bone morphology appeared unchanged (Fig. 5.2B,C). Quantitative analysis of nasal bone trabeculation revealed a significant difference in the average trabecular area (avg_trab) between the genotypes ($\chi^2 = 8.5354$, df = 2, p = 0.01401), as determined by the Kruskal-Wallis test. Post-hoc analysis using Dunn's test with Bonferroni correction indicated a significant difference between the Bmp7 cko and control groups (p.adj = 0.01568772). The average trabecular area was smallest in the Bmp7 cko mice (mean = 0.550 px, sd = 0.120), compared to Bmp2 cko mice (mean = 0.700 pixels, sd = 0.100) and control mice (mean = 0.722 px, sd = 0.122). The endocranial surface of the nasal bone contacting the nasal septum in Bmp7 cko mice stained TRAP positive, indicating ongoing bone resorption by osteoclasts (Fig. 5.2D). Similarly, the endocranial portion of the nasal bones flanking the internasal suture was thicker in width and the internasal suture – nasal septum abutment was asymmetric (Fig. 5.2E), reminiscent of early effects of Bmp7 neural crest knockout (Bmp7 ncko, Chapter 4). Notably, there was no remodeling along the straight ectocranial internasal suture-bone interface, unlike the asymmetric remodeling we have observed in postnatal Bmp7 ncko mice. The Bmp2 cko nasal bones appeared to have smaller medial nasal bone trabeculae in some mice, but sutures looked more normal overall and trabecular area was not significantly different (Fig. 5.2D,E).

We next assessed the appearance of mature *Sost*-positive osteocytes within the cranial bones. Interestingly, the number of mature osteocytes within the nasal bone itself (*Sost*^{pos}) differed between control, Bmp2 cko, and Bmp7 cko skulls (Fig. 5.2E,F). The mean proportions of *Sost*^{pos} cells relative to total DAPI-positive nuclei were 37.0% in control, 39.3% in Bmp2 cko, and 7.29% in Bmp7 cko mice. The Kruskal-Wallis test revealed a significant difference in Sost proportions between genotypes ($\chi^2 = 6.6273$, p = 0.03638). Pairwise comparisons indicated that the difference between Bmp7 cko and control groups approached significance (p = 0.2), suggesting a notable reduction in mature osteocytes in Bmp7 cko mice. Although there was a slight increase in *Dmp1*^{pos} immature osteocytes in Bmp2 cko mice (mean = 4.06%) and Bmp7 cko mice (mean = 2.44%) compared to controls

(mean = 1.45%), the differences were not statistically significant (χ^2 = 0.61172, p = 0.7365). Endocranially, we observed asymmetric *Dmp1*^{pos} expression lining the internasal suture – bone interface in Bmp7 cko mice (Fig. 5.2G). Moreover, the total number of nuclei (DAPI-positive) was higher in both Bmp2 cko and Bmp7 cko mice compared to controls. The mean DAPI counts were 73.5 for control, 106 for Bmp2 cko, and 103 for Bmp7 cko. However, the Kruskal-Wallis test did not show a statistically significant difference in total DAPI counts between the genotypes (χ^2 = 3.4636, p = 0.177).

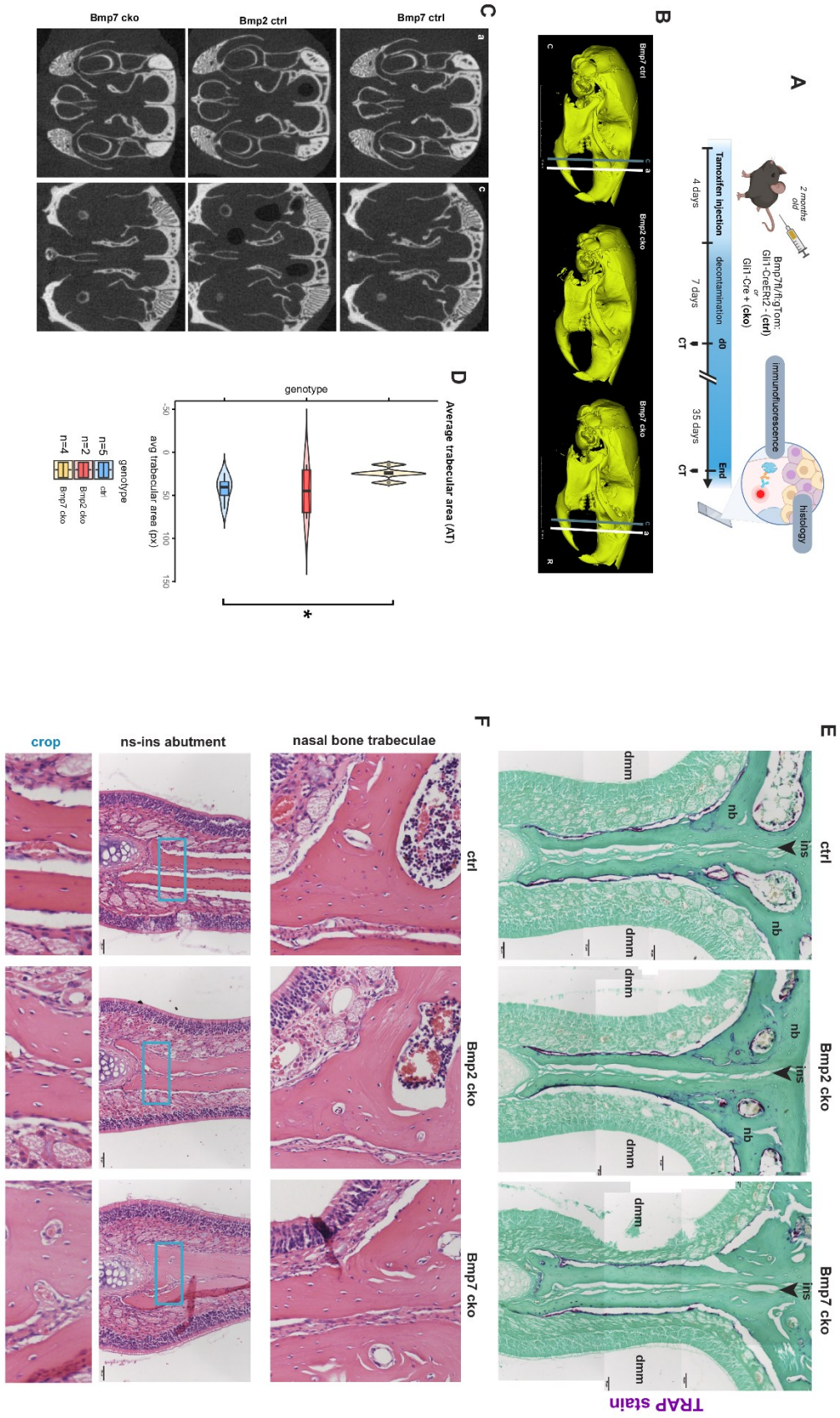
A
2 months old
Bmp7fl/fl;tdTom;
Gli1-CreERt2 -(ctrl)
or
Gli1-Cre+ (cko)
Tamoxifen injection
4 days
decontamination
7 days
d0
CT
End
35 days
CT
immunofluorescence
histology
B
Bmp7 ctrl
Bmp2 cko
Bmp7 cko
C
Bmp7 cko
Bmp2 ctrl
Bmp7 ctrl
D
Average trabecular area (AT)
genotype
avg trabecular area (px)
genotype
ctrl
Bmp2 cko
Bmp7 cko
n=5
n=2
n=4
*
E
ctrl
Bmp2 cko
Bmp7 cko
ins
nb
dmm
TRAP stain
F
nasal bone trabeculae
ns-ins abutment
crop

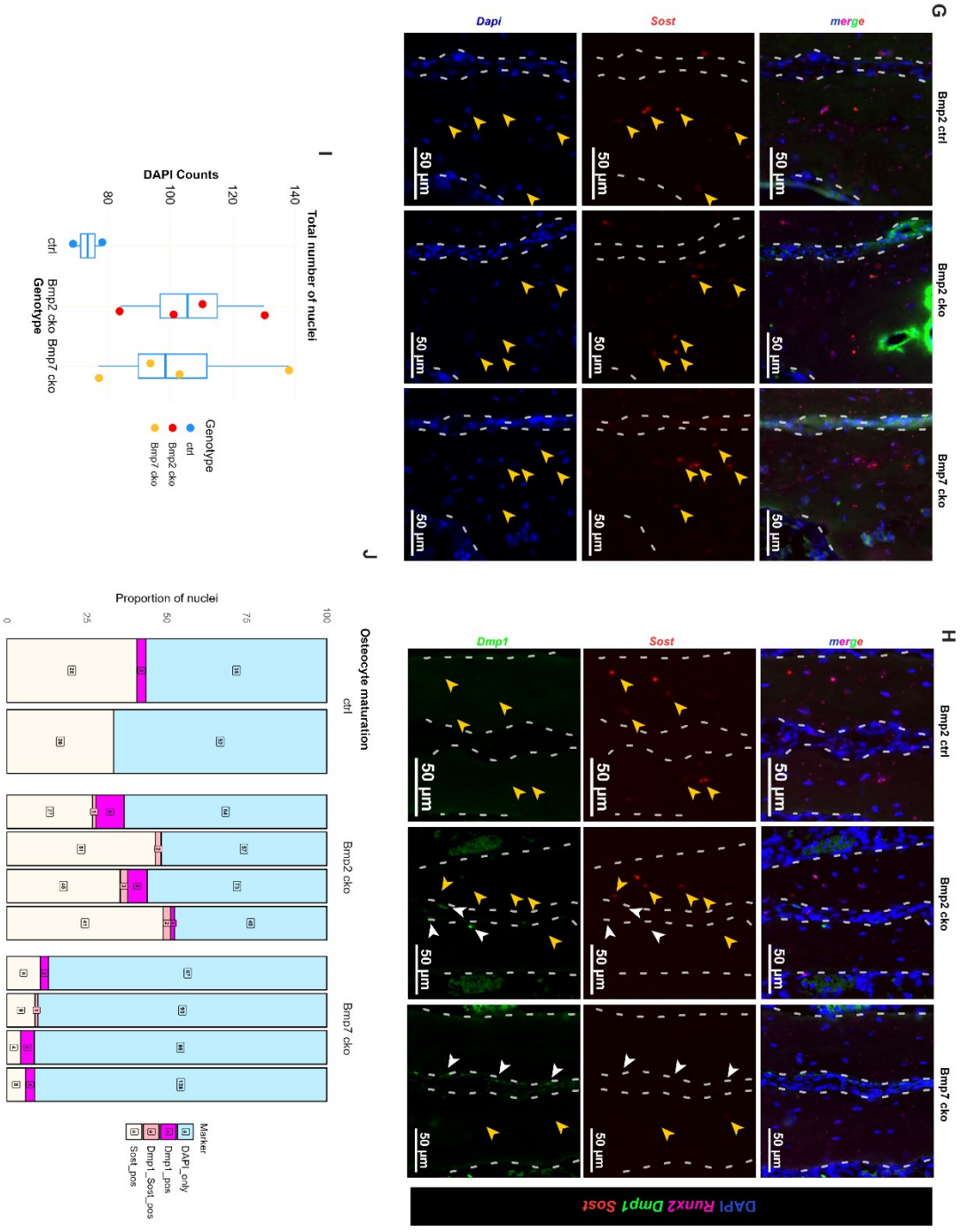

Figure 5.2 Deletion of Bone Morphogenetic Proteins 2 and 7 has independent effects on trabecular bone.

Adult mice were injected for Gli1-CreERt2-mediated recombination as shown in (A). After 35 days, heads were CT scanned and reconstructed using 3D Slicer (B,C). R indicates rostral direction, C caudal. White and blue lines indicate cross sections a and c represented in panel C. (D) Violin plot comparing the average trabecular area (avg_trab) between genotypes. The Kruskal-Wallis test showed a significant difference between groups (chi-squared = 8.5354, df = 2, p = 0.01401). Post-hoc Dunn's test revealed a significant difference between Bmp7 cko and ctrl groups (p.adj = 0.01568772). 2-3 measurements collected per side (paired nasal

bones) for 4 ctrl mice and 3 Bmp2 and Bmp7 cko biological replicates each. (E) Tartrate-resistant acid phosphatase (TRAP) stain for osteoclast enzymatic activity in 7-10um FFPE coronal sections through the nasal bones (nb) and ins. (F) Hematoxylin and eosin (H&E) staining of the internasal suture, with magnification on the endocranial border of the nasal bone trabeculae (top), nasal septum – internasal suture abutment (middle), and a cropped region indicated in blue from the endocranial nasal bones (bottom). (G-H) RNAscope *in situ* hybridization for *Dmp1, Sost, and Runx2* showed that mature osteocytes within the nasal bone (*Sost*^{pos}) were present in different amounts between control, Bmp2 cko, and Bmp7 cko skulls. The region of interest selected in panel (G) is comparable to the histology selected in E for nasal bone trabeculae, and H corresponds to the area of the cropped endocranial nasal bones. Yellow arrows point to *Sost*^{pos} cells, and white arrowheads point to *Dmp1*^{pos} cells. Exposure of RNAscope images was adjusted for representative images according to region of focus due to fluorescent edge effect and autofluorescence from PFA-fixed bone. White dotted lines indicate bone edges. (I) Box plot with individual points showing total nuclei (DAPI counts) in nasal bones for each genotype. The mean DAPI counts were 73.5 (control), 106 (Bmp2 cko), and 103 (Bmp7 cko), indicating a higher density of cells in Bmp2 and Bmp7 cko mice. The Kruskal-Wallis test did not show a statistically significant difference in total DAPI counts between genotypes ($\chi^2 = 3.4636$, $p = 0.177$). (J) Stacked bar plot showing the proportions of Dmp1, Dmp1/Sost, and Sost positive cells relative to total DAPI positive nuclei in nasal bones across different genotypes. The Kruskal-Wallis test revealed a significant difference in Sost proportions between genotypes ($\chi^2 = 6.6273$, $p = 0.03638$). Pairwise comparisons suggested a notable reduction in Sost positivity in Bmp7 cko mice compared to controls ($p = 0.2$). The mean proportions of Sost-positive cells were 37.0% (control), 39.3% (Bmp2 cko), and 7.29% (Bmp7 cko).

5.2.2 Bmp2: or Bmp7:Gli1-CreERt2 conditional knockout disrupts synchondroses by different mechanisms

To follow up our observations regarding bone remodeling in adult cohorts, we next sought to examine if and how loss of *Bmp2* or *Bmp7* from Gli1+ cells would affect growth during a period of rapid midfacial expansion and calvarial growth. We hypothesized that early postnatal injection of tamoxifen (P5) would lead to profound cranial suture malformation in Bmp2 and Bmp7 mutants (Fig. 5.3A). Surprisingly, the sutures were not synostosed or grossly deviated at this age. In contrast, both Bmp2: and Bmp7:Gli1CreERT2 mutants, when injected at P5 and collected at P21, had notable cranial base malformations. In both mutant strains, the intersphenoidal synchondrosis (ISS) was variably affected, with the most severe samples showing a ventral bony bridging of the synchondrosis that enclosed or obliterated the ISS (Fig. 5.3B), seen also in adult cohorts following tamoxifen injection. This was confirmed by Fisher's Exact Test for ISS showing significant differences among genotypes in both postnatal (PT) and adult (AT) age groups (PT, $p = 0.004721$; AT, $p = 0.02279$), with pairwise comparisons indicating significant differences between control and Bmp7 cko in both PT and AT groups. The Bmp2 cko mice also showed altered cranial base morphology, but these changes were less pronounced compared to Bmp7 cko mice and were not statistically significant in pairwise comparisons for ISS or SOS.

Beyond differences in bone formation and mineralization a common vertical outgrowth of the intersphenoidal synchondrosis (ISS) was often seen in both Bmp2 cko and Bmp7 cko mice (Fig. 5.3C). Notably, the distinctive and organized layers of differentiating chondrocytes were altered in different ways between Bmp2 cko and Bmp7 cko mice. Control mice had clear distinction of oblong resting chondrocytes in the midline of the ISS and progressive swelling in size toward the bone tidemark. Bmp2 cko mice had vertically compressed cells in the midline with an abundance of intervening extracellular matrix, and an abrupt boundary between cartilage in bone without clear signs of chondrocyte hypertrophy. Bmp7 cko mice, however, had more normal resting chondrocytes with more lateral compression. In contrast to the Bmp2 cko ISS, Bmp7 cko had more hypertrophic chondrocytes than the control upon histological assessment. It should be noted that these phenotypes were variable in severity and frequency. Examination of lineage-traced GFP^{pos} cells in sagittal cranial base sections of the spheno-occipital synchondrosis (SOS) further supported our hypothesis that loss of *Bmp2* and *Bmp7* affected chondrocyte maturation differently. GFP^{pos} cells spanned the entire Bmp7 cko synchondroses 13 days after the last Tamoxifen injection. In contrast, GFP^{pos} cells were comparably less represented in the Bmp2 cko pre-/hypertrophic chondrocyte compartment. (Fig. 5.3D). A similar pattern of GFP^{pos} cells was noted in Bmp2 cko mice after a shorter chase (collected on day 4 of injection). As this indicated a specific role for Bmp2 in chondrocyte hypertrophy and/or transdifferentiation to osteoblasts, we determined expression of these two growth factors. Indeed, *Bmp2* and *Bmp7* show discrete expression patterns in the P21 cranial base. We noted clear *Bmp2* mRNA expression in hypertrophic chondrocytes of control and Bmp7 cko mice (Fig. 5.3E). Chondrocyte hypertrophy, detected with ColX IF staining, was nearly completely abolished in Bmp2 cko mice with a reduced proportion in Bmp7 cko mice ANOVA $p < 0.001$) (Fig. 5.3E-F). Post-hoc analysis indicated significant differences in ColX positivity between Bmp2 cko and control ($p < 0.001$), and between Bmp7 cko and control ($p = 0.002$). Additionally, Bmp2 cko mice had a significantly lower proportion of ColX positivity compared to Bmp7 cko mice ($p = 0.011$). Effect sizes further supported these findings, with substantial differences observed: Cohen's d for Bmp2 cko vs. control was -11.79, for Bmp7 cko vs. control was -3.95, and for Bmp2 cko vs. Bmp7 cko was -2.60. In Bmp2 cko mice, the RNAscope assay, which targets mutant and functional *Bmp2*

mRNA, revealed absence from the hypertrophic zone and an increase of either type of mRNA in the medial SOS.

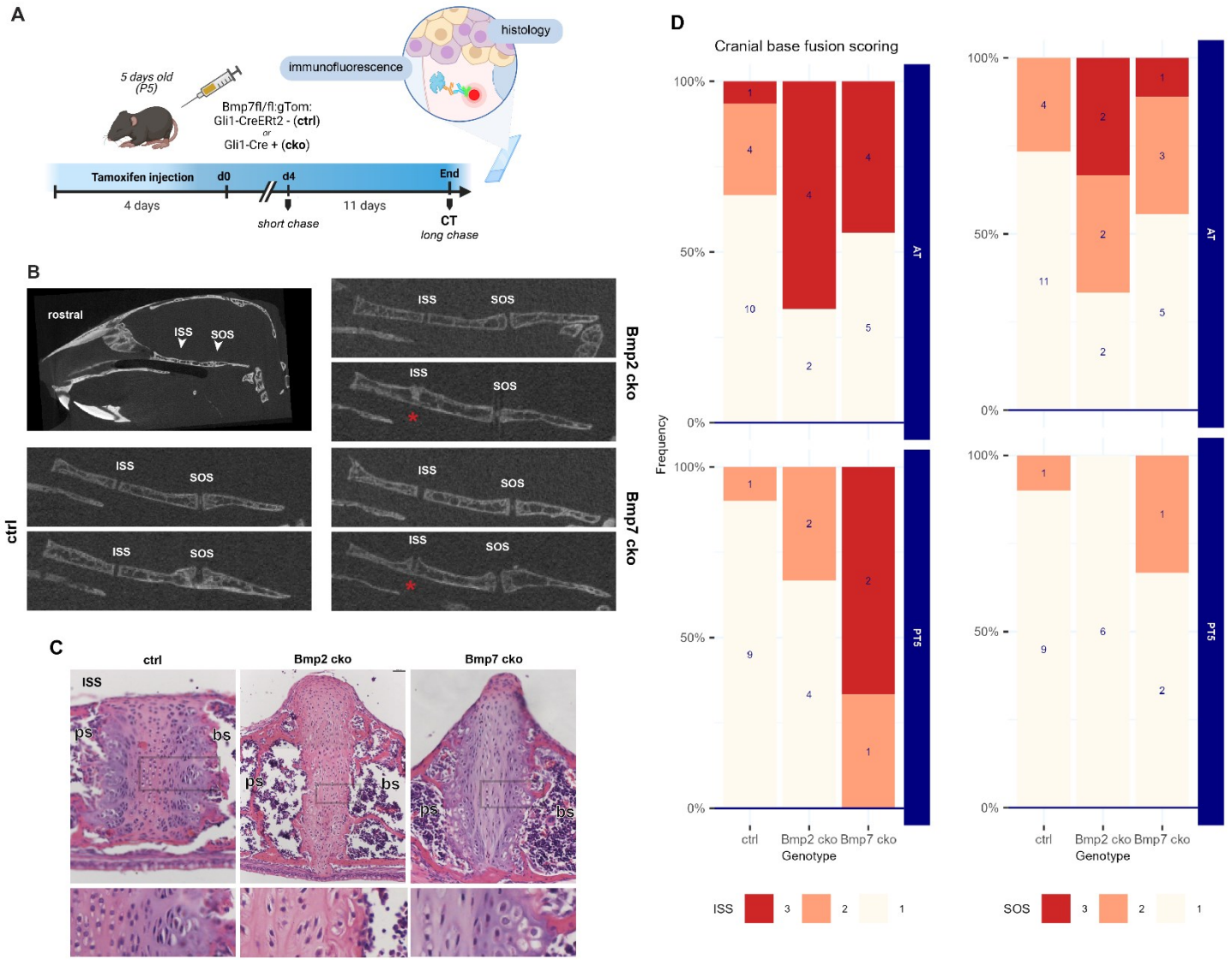
A
5 days old (P5)
Bmp7fl/fl:gTom:
Gli1-CreERt2 - (ctrl)
or
Gli1-Cre + (cko)
immunofluorescence
histology
Tamoxifen injection
d0
d4
End
4 days
11 days
short chase
CT
long chase
B
rostral
ISS
SOS
ctrl
Bmp2 cko
Bmp7 cko
C
ctrl
Bmp2 cko
Bmp7 cko
ISS
ps
bs
D
Cranial base fusion scoring
Frequency
100%
50%
0%
AT
PT5
ctrl
Bmp2 cko
Bmp7 cko
Genotype
ISS
SOS
3
2
1

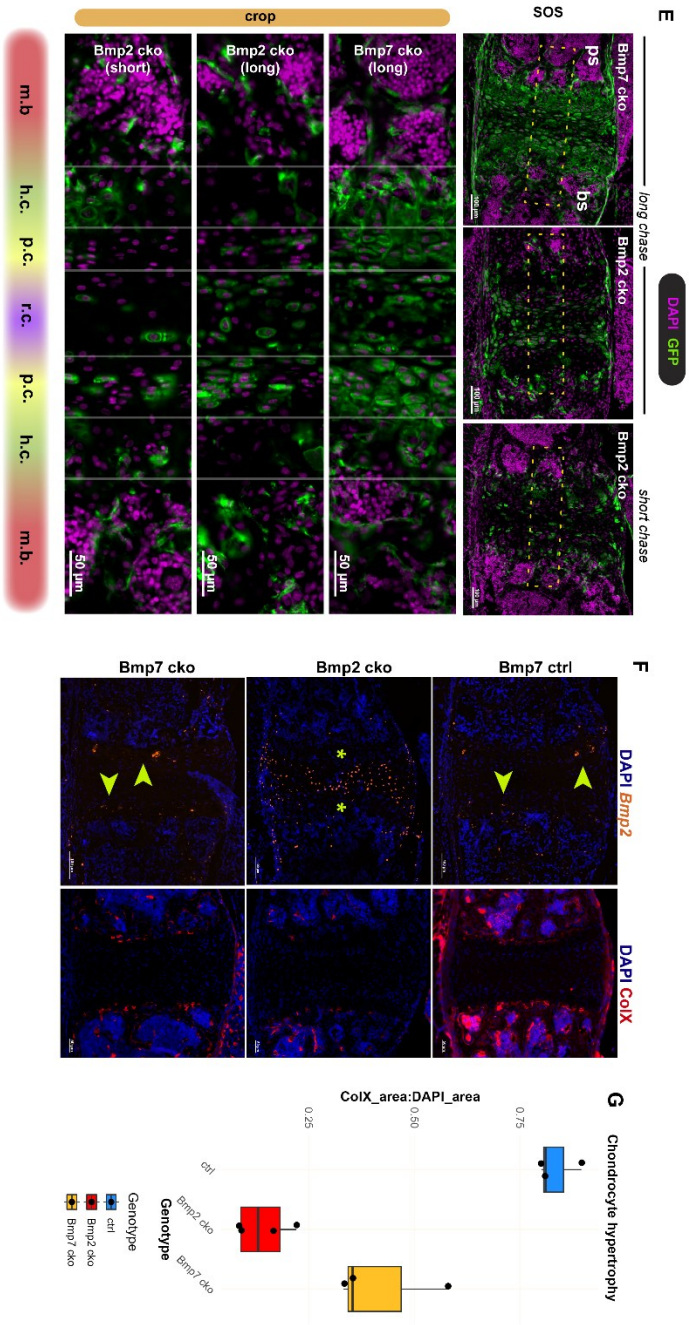

Figure 5.3 The cranial base synchondroses model Bmp2 and Bmp7 roles in endochondral ossification.

(A) Postnatal injection of mice at 5 days, with analysis at P21 or P8 (short chase lineage tracing). (B) uCT parasagittal sections through mineralized tissue of ctrl, Bmp2 cko, and Bmp7 cko mice. ISS: intersphenoidal synchondrosis, SOS: spheno-occipital synchondrosis. Red asterisk shows severe ISS phenotype in some mice of both cko genotypes. (C) Hematoxylin and eosin (H&E) histological staining of the ISS. Crop in lower panel indicated in overview with grey rectangle. (D) Stacked bar plot showing the frequency of ISS and SOS scores by genotype and age group.

The Fisher's exact test indicated significant differences in ISS scores between genotypes for both postnatal (PT) ($p = 0.0047$) and adult (AT) ($p = 0.0228$) groups, specifically between ctrl and Bmp7 cko. No significant differences were observed for SOS scores (PT: $p = 1$; AT: $p = 0.2107$). Sample size: PT - 20 ctrl, 9 Bmp2 cko, 5 Bmp7 cko; AT - 15 ctrl, 6 Bmp2 cko, 9 Bmp7 cko. (E) GFP lineage tracing of Bmp7 cko long chase and Bmp2 cko short and long chase SOS. Yellow dotted crop highlights stages of differentiation in synchondrosis. r.c.: resting cells, p.c.: pre-hypertrophic chondrocytes, h.c.: hypertrophic chondrocytes, m.b.: mineralized bone and bone marrow. Note absence of green stain in p.c. and h.c. zones of Bmp2 cko mice. (F) Left column: RNAscope localization of *Bmp2* transcript in the SOS. *Note: this does not necessarily reveal functional Bmp2, only presence of transcript which is not lost in Bmp2 cko.* Right column: IF stain for ColX, marking chondrocyte hypertrophy (and its severe reduction in Bmp2 cko mice). (G) Box plot comparing the proportion of ColX positive area to DAPI positive area across genotypes. Bmp2 cko mice showed a significantly reduced proportion of ColX positivity compared to controls ($p < 0.001$, Cohen's $d = -11.79$). Bmp7 cko mice also exhibited a reduced proportion of ColX positivity compared to controls ($p = 0.002$, Cohen's $d = -3.95$), with a significant difference observed between Bmp2 cko and Bmp7 cko ($p = 0.011$, Cohen's $d = -2.60$). Sample size: 15 ctrl, 6 Bmp2 cko, 9 Bmp7 cko.

5.2.3 Bmp2 and Bmp7 have spatiotemporally diverging roles in endochondral ossification.

Bmp2 and *Bmp7* are both expressed in and around the developing cranial base, however, their expression is only partially overlapping (Fig. 5.4A). Examining the entire region between ISS cartilage and the region that will undergo endochondral ossification to form the basisphenoid bone (b.s.) at embryonic day 14.5 (e14.5), most of the cells which express *Bmp7* also express *Bmp2,* though some cells are exclusively *Bmp2*^{pos}. The double-positive cells appear to be periosteal or perichondral cells. Over time, however, the expression pattern of these two Bmps diverge such that at e18.5 *Bmp7* expression is mainly observed in the chondrocytes of the ISS, while *Bmp2* is most highly expressed in the enlarging pre-hypertrophic chondrocytes that will contribute to the future basisphenoid bone (Fig. 5.4B). There are still a few regions where *Bmp2* and *Bmp7* are co-expressed, especially along the edges of the cartilage in the perichondrium.

In line with expectations from the expression data, deletion of Bmp2 from neural crest cells (Bmp2 ncko) resulted in a cranial base discontinuity at the region where chondrocyte hypertrophy distinguishes the caudal end of the ISS from the rostral part of the basisphenoid bone. This is evident at e18.5 (Fig. 5.4C). Furthermore, deletion of *Bmp2* and *Bmp7* in various combinations of zygosity using several conditions (global knockout via lacZ/lacZ, Wnt1-Cre-mediated neural crest knockout, Gli1-CreErt2 Tamoxifen-mediated e15.5 knockdown) generated a broad range of distinct sphenoid bone morphologies by e18.5 (Fig. 5.4D,E). This includes a reduced size or loss of the

presphenoid element (100% in Bmp7 k/o, 50% in Bmp7 cko, 75% in Bmp2 ncko), a caudal notch in the basisphenoid bone (57.14% in Bmp7 k/o, 40% in Bmp7 ncko), fragmentation or complete loss of the basisphenoid bone (75% in Bmp2 ncko, 100% in Bmp2/7 double ncko), and shape changes to the wings of the sphenoid and alisphenoid. These observations argue for absence of or minimal redundancy between *Bmp2* and *Bmp7* within the context of cranial base development (Kruskal-Wallis for UMAP1, $p = 0.0034$; UMAP2, $p = 0.0039$).

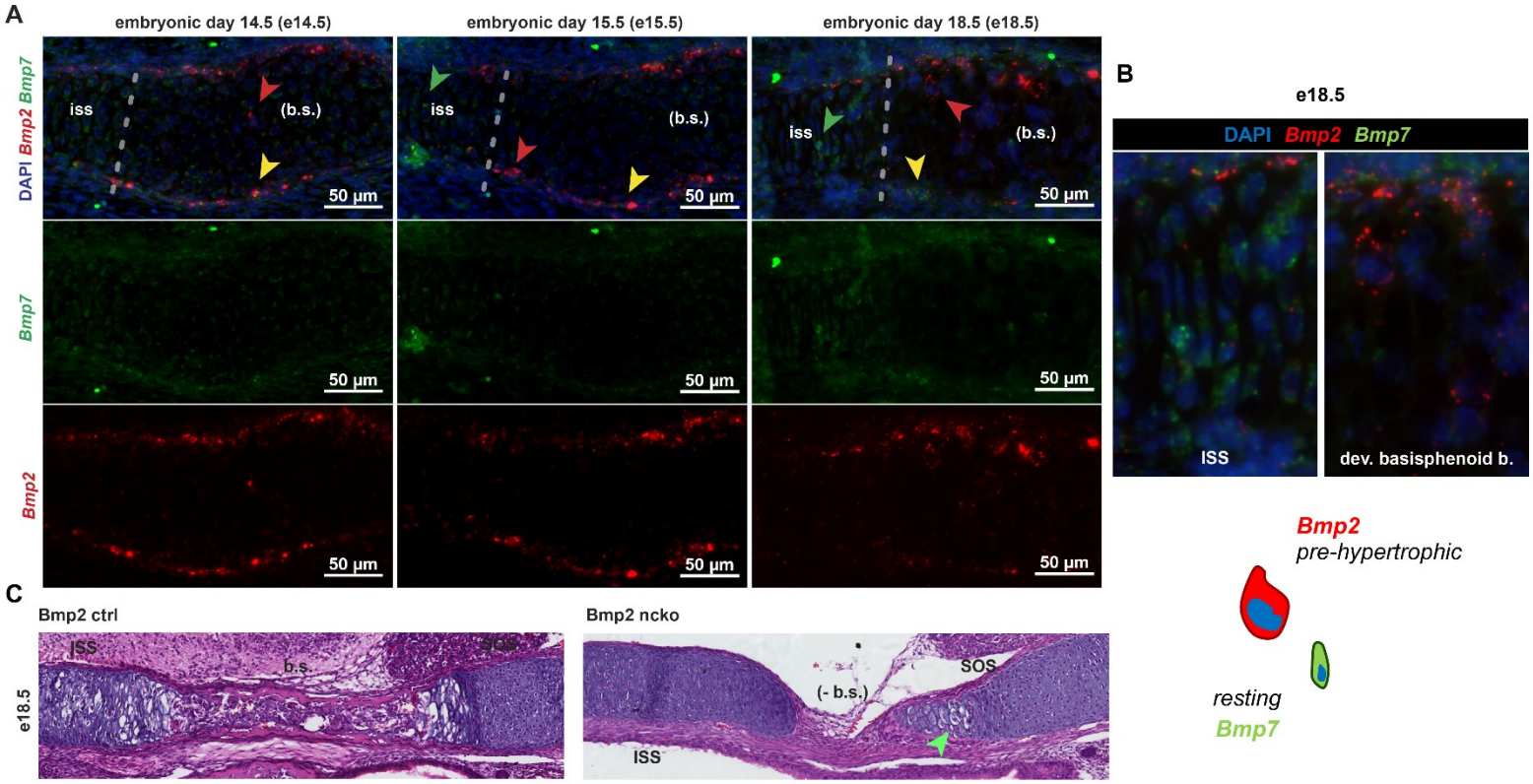
A
embryonic day 14.5 (e14.5)
embryonic day 15.5 (e15.5)
embryonic day 18.5 (e18.5)
DAPI Bmp2 Bmp7
Bmp7
Bmp2
iss
(b.s.)
50 µm
B
e18.5
DAPI Bmp2 Bmp7
ISS
dev. basisphenoid b.
Bmp2
pre-hypertrophic
resting
Bmp7
C
Bmp2 ctrl
Bmp2 ncko
e18.5
ISS
b.s.
SOS
(- b.s.)

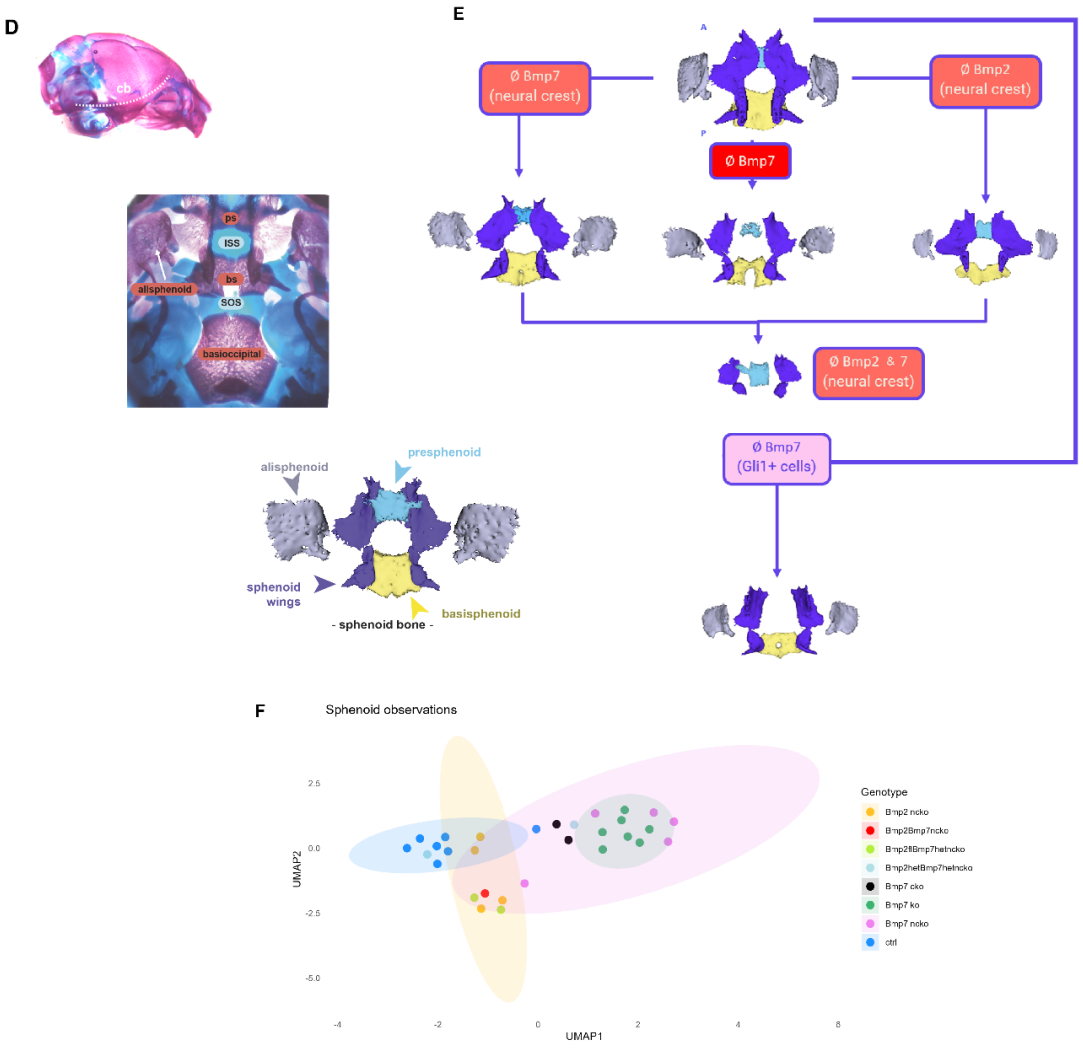

Figure 5.4 Embryonic conditional deletion of Bmps impacts sphenoid morphology.
(A) RNAscope for *Bmp2* (red) and *Bmp7* (green) in the transition between the ISS and developing basisphenoid bone. Green arrows indicate cells that express *Bmp7*, red arrows for *Bmp2*, and yellow arrows indicate cells expressing both genes. As development progresses and hypertrophy is initiated, the domains of Bmp2 and Bmp7 begin to segregate into pre-hypertrophic and resting chondrocytes (respectively) (magnified in (B)). (C) Bmp2 neural crest-specific (Bmp2 ncko) deletion variably causes basisphenoid bone fragmentation or insufficiency. Hematoxylin and eosin stain of e18.5 parasagittal sections. (D) Skeletal preparation of e18.5 skull and cranial base showing mineralized bone (red/purple) and cartilage (blue), from the presphenoid bone (ps, rostral) to the basioccipital bone (caudal). Bottom panel: µCT scan reconstruction of wild type sphenoid bone. This structurally and developmentally complex bone can be segmented manually into its components: presphenoid, basisphenoid, alisphenoid, and the sphenoid wings. (E) Sphenoid bone morphological changes under conditional/global conditions shown in Fig. 5.2. Ø indicates allele targeted (*Bmp2*, *Bmp7*, or both), with condition in parentheses (neural crest, Gli1). (F) UMAP plot showing clustering of cranial base phenotypes. The genotypes with the most pronounced basisphenoid abnormalities include Bmp2 ncko (75% missing presphenoid, 75% fragmented basisphenoid), Bmp7 k/o (100% basisphenoid notch), and Bmp2/7 double ncko (100% fragmented basisphenoid). The Kruskal-Wallis test indicated significant clustering differences (UMAP1: $p = 0.0034$, UMAP2: $p = 0.0039$). Sample sizes: Bmp2 ncko (4), Bmp2Bmp7ncko (1), Bmp2flBmp7hetncko (2), Bmp2hetBmp7hetncko (2),

Bmp7 cko (2), Bmp7 ko (7), Bmp7 ncko (5), ctrl (7). Ellipses were only drawn for conditions with 3 or more measurements.

5.2.4 Loss of Bmp2 from neural crest cells impairs chondrocyte hypertrophy in the ISS

To begin unraveling the underlying mechanisms of chondrocyte hypertrophy as it relates to *Bmp2* specifically, we performed a pilot single-cell RNA sequencing Parse Biosciences Evercode experiment on the ISS of Bmp2 ctrl and ncko mice at e18.5 (Fig. 5.5A). For this project, we dissected a margin of the sphenoid bone with the intersphenoidal cartilage (as pictured in Fig. 5.5B,C). The resultant dataset clustered as expected when analyzed with the Seurat v5 R package, with distinct chondrogenic and osteogenic clusters at 0.3 resolution in addition to neural (neu.1-6), vascular (vasc.1-2), epithelial, ciliated, and immune (imm.1-2) clusters (Fig. 5.5D). Two mitotically enriched clusters were also identified (mito.1-2), each bearing characteristic traits of chondrogenesis or osteogenesis. Clusters chondro.1-3 and mito.1 contained maturing and differentiating chondrocytes (Fig. 5.5E).

Initial analysis was focused on chondrocyte maturation and hypertrophy in response to our *in vivo* findings (Fig. 5.5F). Cluster chondro.3 appeared to resemble hypertrophic chondrocytes most closely, and when examining known markers of hypertrophy such as *Col10a1* and *Mmp13*, we found that Bmp2 ncko cells had less high-expressing cells, and fewer chondro.3 cells overall (Fig. 5.5F). Interestingly, Bmp expression was affected by Bmp2 ncko in the ISS, with less hypertrophic expression of *Bmp3* and *Bmp4* and a shift in *Bmp6* toward higher expression in the chondro.3 cluster away from chondro.2 (Fig. 5.5G). *Bmp7* was somewhat increased in chondro.3.

We then used the singlecellHaystack R package to identify biased gene lists between Bmp2 ctrl and ncko conditions in osteochondrogenic clusters, and projected them onto the UMAP with SCpubr (Fig. 5.5H). Many of the top genes identified were involved in cell adhesion, attachment, and spreading, including *Ptn, Postn, Cacna1g,* and *Svil* (Fig. 5.5H-I). We observed differences in expression of these genes to varying extents in different chondrogenic clusters, especially in the immature chondrocyte chondro.2 cluster.

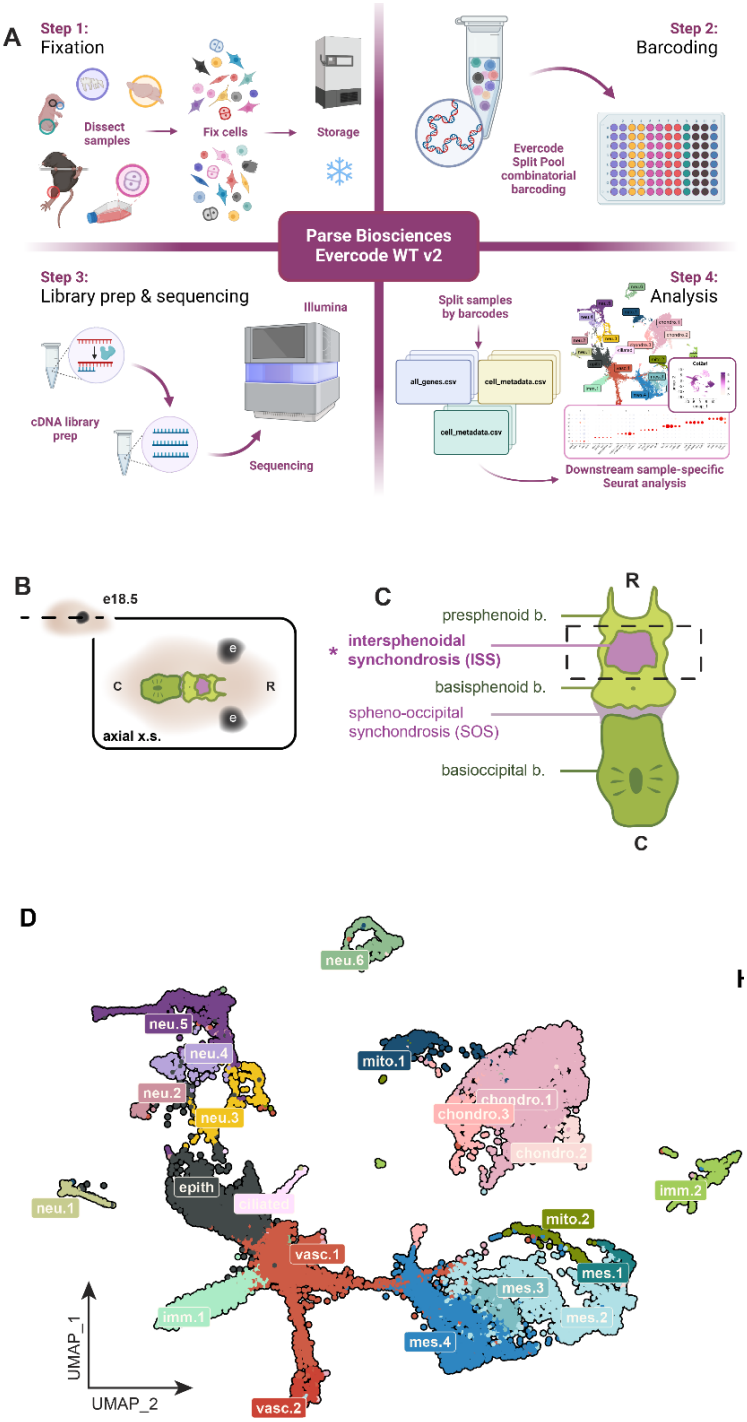
A
Step 1:
Fixation
Dissect samples
Fix cells
Storage
Step 2:
Barcoding
Evercode Split Pool combinatorial barcoding
Parse Biosciences Evercode WT v2
Step 3:
Library prep & sequencing
Illumina
cDNA library prep
Sequencing
Step 4:
Analysis
Split samples by barcodes
all_genes.csv
cell_metadata.csv
cell_metadata.csv
Downstream sample-specific Seurat analysis
B
e18.5
e
C
R
e
axial x.s.
C
presphenoid b.
*
intersphenoidal synchondrosis (ISS)
basisphenoid b.
spheno-occipital synchondrosis (SOS)
basioccipital b.
R
C
D
neu.6
neu.5
neu.4
neu.2
neu.3
neu.1
epith
ciliated
vasc.1
vasc.2
imm.1
mito.1
chondro.1
chondro.3
chondro.2
imm.2
mito.2
mes.1
mes.3
mes.2
mes.4
UMAP_1
UMAP_2

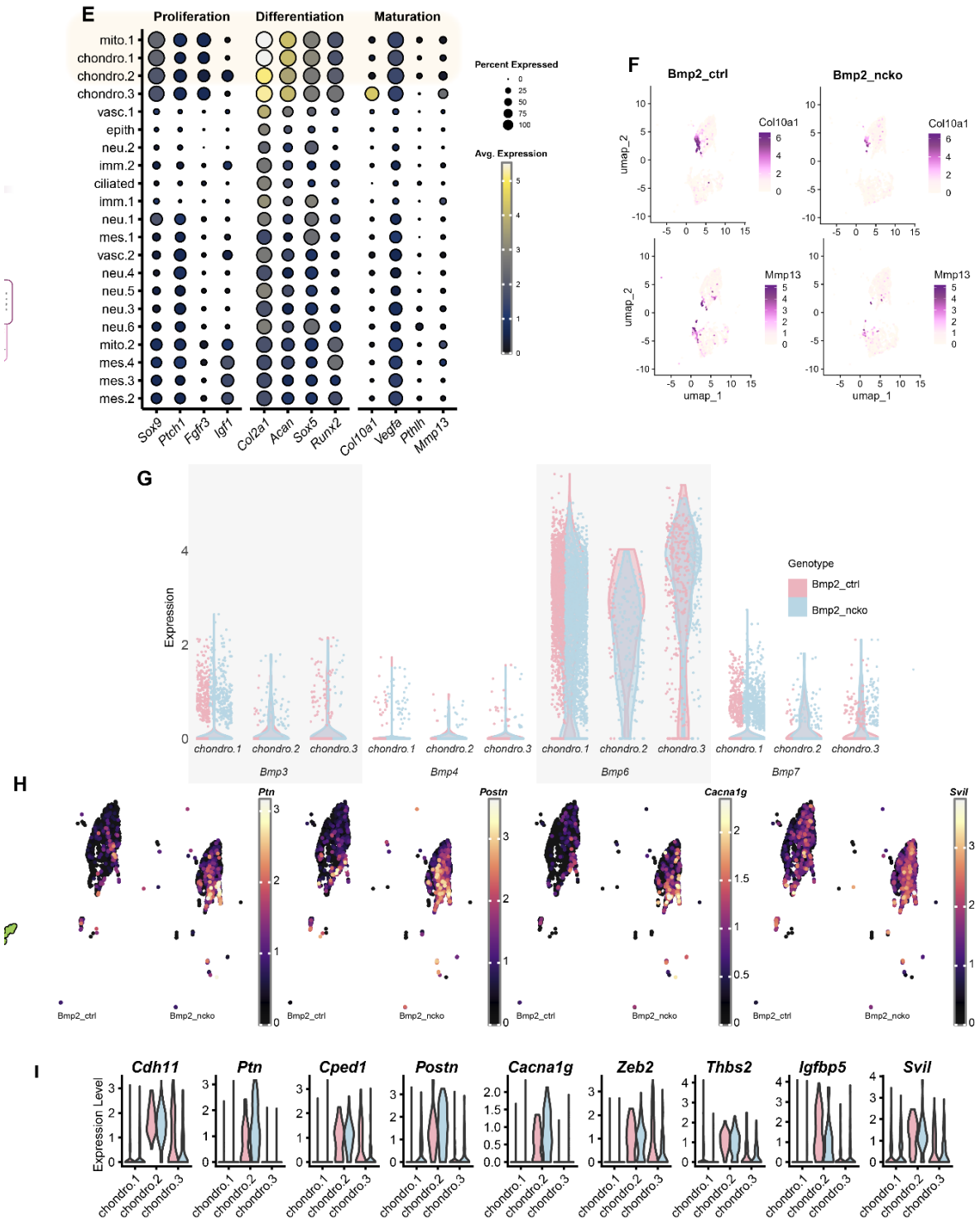
E
Proliferation
Differentiation
Maturation
mito.1
chondro.1
chondro.2
chondro.3
vasc.1
epith
neu.2
imm.2
ciliated
imm.1
neu.1
mes.1
vasc.2
neu.4
neu.5
neu.3
neu.6
mito.2
mes.4
mes.3
mes.2
Sox9
Ptch1
Fgfr3
Igf1
Col2a1
Acan
Sox5
Runx2
Col10a1
Vegfa
Pthlh
Mmp13
Percent Expressed
Avg. Expression
F
Bmp2_ctrl
Bmp2_ncko
Col10a1
Mmp13
umap_1
umap_2
G
Expression
Genotype
Bmp2_ctrl
Bmp2_ncko
chondro.1
chondro.2
chondro.3
Bmp3
Bmp4
Bmp6
Bmp7
H
Ptn
Postn
Cacna1g
Svil
Bmp2_ctrl
Bmp2_ncko
I
Cdh11
Ptn
Cped1
Postn
Cacna1g
Zeb2
Thbs2
Igfbp5
Svil
Expression Level
chondro.1
chondro.2
chondro.3

Figure 5.5 Bmp2 neural crest knockout synchondroses have impaired chondrocyte maturation, Bmp signaling, and cell adhesion at a transcriptomic level.
(A) Parse Biosciences single-cell RNA sequencing workflow. The intersphenoidal synchondrosis (ISS) was dissected from e18.5 Bmp2 ctrl and ncko mice for sequencing using the Parse Bioscience Evercode WT v2 kit. Briefly, samples of equivalent genotype were pooled, cells were digested and fixed, and processed using the split pool combinatorial barcoding process. After sequencing, samples were split by barcodes and analyzed further using the Seurat v5 package. (B,C) Region of dissection for sequencing shown in axial cross-section diagram, indicated by dashed rectangle. (D) SCpubr UMAP projection showing annotated chondrogenic clusters (pink, chondro.1-3) and mesenchymal/osteogenic clusters (blue, mes.1-4). E) SCpubr dot plot of chondrocyte marker gene expression in all annotated clusters, indicating that cluster chondro.3 contains most hypertrophic chondrocytes. F) Integrated Bmp2 ctrl and ncko samples show reduction in hypertrophic chondrocyte *Col10a1* transcript in mutant mice. G) Violin plots showing Bmp 3/4/6/7 expression in chondrogenic clusters (chondro.1-3). H) ScPubr feature plots of selected biased genes involved in cell attachment and spreading (*Ptprd, Postn, Cacna1g, Svil*) between osteochondrogenic clusters, identified with singlecellHaystack package. I) Violin plot visualization of chondrogenic cluster expression of cell attachment genes in top25 gene list from singlecellHaystack. Pink violins represent Bmp2 ctrl samples; blue violins represent Bmp2 ncko.

5.3 Discussion

This work specifically focused on two Bmps known to interact with the osteochondrodifferentiation pathway (Kawai et al., 2006; Sheikh et al., 2015; D. O. Wagner et al., 2010). We demonstrated independent roles for *Bmp2* and *Bmp7* in both intramembranous bone maintenance and endochondral development of the cranial base *in vivo*, targeting suture progenitor cells and chondrocytes through *Gli1* expression (a Hedgehog (Hh) signaling intermediate). Through craniofacial characterization and single-cell RNA sequencing of mouse genetic models of Bmp deficiency, we studied expression patterns and the molecular and structural effects of their loss.

The unusual morphology of the sphenoid bone that we observed varied depending on the Bmp deleted (*Bmp2* or *7*) and the Cre drivers identifying the target cell type (global knockout, Wnt1-Cre, e15.5 Gli1-CreERT2). We hypothesize that these discrete shapes are at least in part related to the spatiotemporally diverging expression patterns of *Bmp2* and *Bmp7* observed in Fig. 5.5 in the developing cranial base, around e15.5 to e18.5. In this window, *Bmp2* is expressed separately from *Bmp7* in pre-hypertrophic chondrocytes. *Bmp7* expression remains highest in the resting zone of the ISS. A simple explanation for the impact of *Bmp2* deficiency on cranial base growth is its clear role in chondrocyte hypertrophy, supported by our RNA sequencing data of reduced hypertrophic markers in the Bmp2 ncko synchondrosis (Fig. 5.5). However, we did not rule out secondary effects

of the palatal clefting seen in Bmp7 ncko, Bmp7 ko, and Bmp2 ncko mice. Further insight may be gleaned from careful consideration of the timing and sequence of developmental and cellular processes involved in cranial base maturation, described in detail in McBratney-Owen et al., 2008.

The murine cranial base forms from a cartilaginous template which ossifies in caudal to rostral stages, beginning with the basioccipital bone around e14.5 (Kawasaki & Richtsmeier, 2017). The basisphenoid and presphenoid elements begin ossifying from the hypophyseal and trabecular cartilages around e15.5 and e17.5, respectively. At the time of *Bmp2* and *7* divergence, which we place starting around e15.5, several major changes occur corresponding to the mutant sphenoid bone morphological features described. At e15, the acrochordal cartilage forms a continuous bar at the rostral border of the basicranial fenestrae, which coincides with the location of the basisphenoid notch, hole, and depression in e18.5 Bmp7-mutant mice. Unlike bony fenestrae in the mature skull, these interruptions in the cartilage are not channels for nerves or blood vessels and disappear over time. The acrochordal cartilage also corresponds to the NCC-mesodermal interface with the hypophyseal cartilage. The entire endocranium is continuous at e16.

The contribution of neural crest- or mesoderm-derived cells to the cranial base is dynamic, with complex cellular behavior causing shifting proportions of the progeny of each. A possible cause for the variation in severity of the basisphenoid notch in Bmp7 mutant mice could be explained by the keyhole-shaped ectodermal invagination of Rathke's pouch at the same region, hypothesized to contain mesenchyme not derived from NCC (McBratney-Owen et al., 2008). This results in a NCC-mesoderm boundary in the SOS with a rostral mesoderm projection along the dorsum. In this study we observed that, in NCC-targeted *Bmp7* deletion, mice had a shallow impression on the dorsum of the caudal basisphenoid bone. In contrast, global Bmp7 deletion caused a cleft in the bone of this region. While we were unable to observe global Bmp2 knockout due to early embryonic lethality, we did note that deletion from NCC affected the margins and continuity of the entire basisphenoid bone and presphenoid bone, and not specifically the region of Rathke's pouch invagination. Furthermore, while the hypophyseal cartilage giving rise to the basisphenoid bone is neural crest-derived, parts of the bone itself contain a mix of NCC- and mesoderm-derived osteoblasts and periosteal cells by e17.5. By other

mechanisms, the presphenoid bone also has mixed embryonic origin through the fusion of NCC-derived orbital and trabecular cartilages with mesodermal hypochiasmatic cartilage.

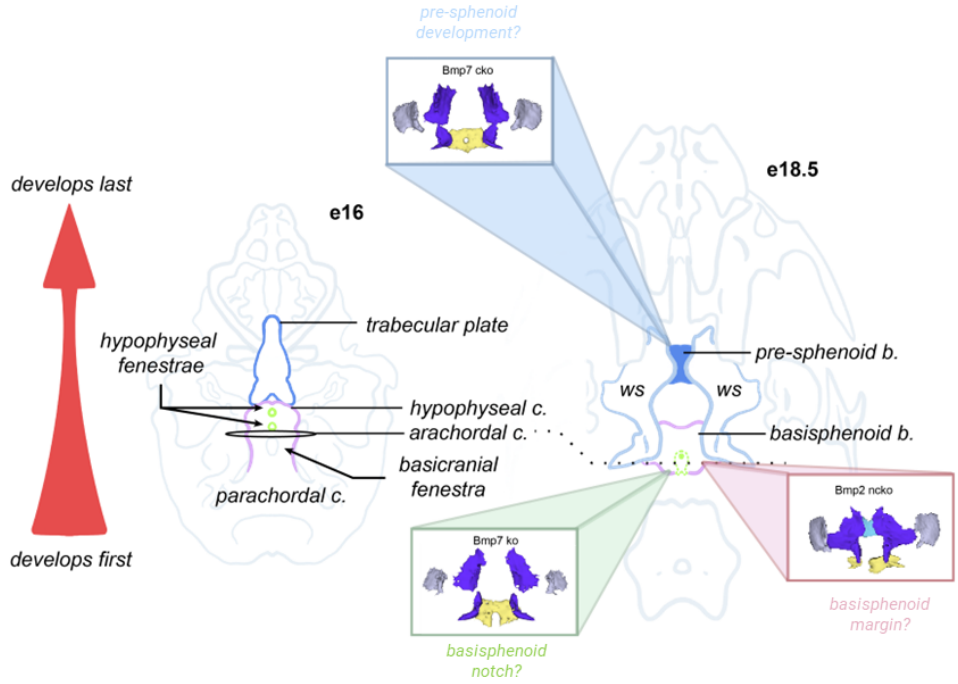

Figure 5.6 Summary of Bmp mutant phenotypes and embryonic development of the cranial base.
Illustration of elements composing the embryonic day 16 (e16) and e18.5 cranial base. The red arrow indicates the general direction of development over time. In general, the rostral end (top of panel) develops after the caudal region (bottom). Main components are labeled with lines and circles. c.: cartilage; b.: bone; ws: wings of the sphenoid bone. Cut out zooms are of the ventral sphenoid bone in three conditional Bmp mutant mice: Bmp7 cko (Bmp7:Gli1-CreERT2), Bmp7 ko (Bmp7 global knockout), and Bmp2 ncko (Bmp2 neural crest knockout).

By birth, the anterior part of the skull is recognizably NCC-derived, with some mesodermal contribution evident through histological analysis. We hypothesize that the combination of mesoderm and NCC contribution to the rostral part of the basisphenoid bone and SOS is related to the Bmp7 sphenoid phenotypes we described (Figure 5.6). The abrupt interface between NCC- and mesoderm-derived periosteum/perichondrium is of particular interest in the case of Bmp2 and 7, as this is the main region in which we observed co-expression over late cranial base development. McBratney-Owens et al. speculate that mesoderm-derived osteoblasts may arise from a non-NCC source via blood vessels or adjacent periosteum. Several cell types have demonstrated unique interaction

kinetics with NCC as opposed to tissue of other embryonic origins, such as the enhanced movement of angioblasts through NCC or differing osteogenic potential (Galea et al., 2021; Yoshida et al., 2008). Interestingly, by P10 the entire SOS has lost its NCC contribution (McBratney-Owen et al., 2008). The known behavioral differences of and interactions between NCC and mesodermal cells could further magnify time- or tissue-specific deletion (Doro et al., 2024; Gonzalez Malagon et al., 2019; Merrill et al., 2006).

This study was the first *in vivo* demonstration of the effects of loss of embryonic and postnatal *Bmp2* and *Bmp7* expression on the cranial base. However, previous studies have shown their effects on osteochondrogenesis *in vitro* and in other organ systems (G. Chen et al., 2012; Dudley & Robertson, 1997; Y. Guo et al., 2018; Malik et al., 2020; Shu et al., 2011). Both Bmps are widely associated with experimental and clinical osteogenesis but have not been characterized systematically across craniofacial development together. Bmp2 and Bmp7 may signal through different receptors and belong to different "classes" based on sequence homology (Yang et al., 2014). Their relationship with each other has mainly been centered around the concept of heterodimerization, which involves the formation of hybrid protein complexes between Bmp2 and 7 and their downstream effects on signaling pathways (Y. Guo et al., 2018; H.-S. Kim et al., 2019). Our data does not support a primarily heterodimeric role for Bmp2 and 7 in craniofacial ossification in craniofacial development due to the variable phenotype between mutant mouse lines. However, there are more complex ways in which both Bmps may theoretically interact with each other, osteogenesis, and other gene regulatory networks that are comparatively less well explored in the cranial base (Fuentealba et al., 2007; Manzari-Tavakoli et al., 2022; R. Zhang et al., 2013; Y. Zhang et al., 2022). It should be noted that we observed an element of stochasticity in the degree of cranial base malformation. This could be attributed to the unaddressed complexity of Bmp signaling, incomplete progenitor targeting, palatal development, or some combination involving phenotype attenuation (Andrade et al., 2024; Merkuri & Fish, 2019; Song & Palmiter, 2018; S. Yu et al., 2021). Both Bmp2 and 7 regulate Sox9, which is required for initial mesenchymal condensation prior to cartilage formation (Healy et al., 1999; Nifuji & Noda, 1999), but other major developmental regulators are induced by one or the other gene (Knippenberg et al., 2006; Nifuji & Noda, 1999; R. N. Wang et al., 2014). Comparison of results from previous studies localizing

Bmp2-6 in the developing cranial base to our *Bmp2* and *Bmp7* expression experiments suggests that multiple Bmps, including *Bmp3* and *Bmp4*, may be coexpressed in the periosteum with *Bmp2* and *7* (Kettunen et al., 2006). Similarly, expression of *Bmp2* and *Bmp6* appear to overlap in later stages of chondrocyte hypertrophy. Our scRNA-seq results support a relationship between Bmp2 and some of these other Bmps given the altered expression of Bmp3, 4, and 6 in Bmp2 ncko ISS samples (Fig. 5.5). These relationships have still not been characterized at a functional level in the cranial base, though developmental studies hint at possible mechanisms for their interaction (Daluiski et al., 2001; Lorda-Diez et al., 2014). *Gli1* expression identifies periosteal progenitors in long bones used for fracture repair (Xia et al., 2020), which complicates the assumption that Gli1-CreERT2 deletion specifically affects "suture stem cells" (Zhao et al., 2015). Perivascular cells involved in the remodeling of vasculature also express *Gli1*, a process that is important during the transition from avascular cartilage to highly vascularized bone in endochondral ossification (A. H. Baker & Péault, 2016). Clearly our understanding of Gli1+ cell contribution to the cranial base, sutures, and bone as well as Bmp2/7 dynamics concerning osteogenesis have far to go.

The implications of the nuanced spatiotemporal dynamic described in this study, especially with respect to *Bmp2* and chondrocyte hypertrophy, cannot be understated in the context of oromaxillofacial reconstruction and the potential for off-target effects (Friedlaender et al., 2001; James et al., 2016; Poon et al., 2016). The primary goal of craniofacial regenerative medicine is often to return functional or aesthetic form to the face, which may require extensive tissue grafting or synthetic scaffold implantation in the case of critical-sized defects. The long-term integration and success of any particular method, however, is highly dependent on the quality of the tissue formed. In orthopedic replacement of joint surfaces, for example, the biomechanical properties of the newly formed cartilage are critical for the success of the intervention. Amongst the three well-described types of cartilage (hyaline, elastic, and fibrocartilage), each has different osteogenic potential and resistance to forces (Naujoks et al., 2008). *In vitro* work has shown that Bmp2 promotes the formation of fibrocartilage with ossification potential, unlike Bmp7 which encourages a non-osteogenic hyaline-type cartilage, each of which has different biomechanical competence (Caron et al., 2013). Even under osteogenic conditions, the complex

heterogeneous environment of the skull could alter clinical outcomes further, increasing chances of adverse effects (Baek & Song, 2006; Borgiani et al., 2021; Novak et al., 2023). For example, inflammation can variably oppose chondrogenesis *or* initiate differentiation of cartilage precursors to bone, depending on the environment – a known side effect of rhBMP-2 application (Alblowi et al., 2009; Gerstenfeld et al., 2003; V. Nguyen et al., 2017). Interestingly, high doses of rhBMP-7 are associated with lower inflammatory response than rhBMP-2 (K.-B. Lee et al., 2012), though it is not a viable or approved clinical intervention after reports of adverse effects (Friedlaender et al., 2001). We feel that these differences in physiological *Bmp2* and *Bmp7* could influence clinical and experimental *in vitro* use further, challenging indiscriminate use of recombinant Bmp proteins for general osteogenesis at high doses, and specifically in the craniofacial complex (Panos et al., 2023).

CHAPTER 6

MESENCHYMAL EXPRESSION OF TENDON-ASSOCIATED GENES PRECEDES OSTEOGENESIS IN MID-PALATAL SUTURE ESTABLISHMENT

Despite decades of cranial suture research, the mechanisms governing suture patency are still not understood. Determination of spatiotemporal suture establishment and the biological processes at play in this complex event are even more unclear. The maintenance, mechanisms of maturation, and patency of the mid-palatal suture are critical to the success of orthodontic and orthognathic surgical treatments. Yet, biology is only minimally taken into consideration in cases of maxillary insufficiency, therapeutic optimization, or timing of interventions. The mid-palatal suture is still treated at large as a macroscopic fissure in the skull.

In this chapter, I approached the mid-palatal suture as I would other (more thoroughly characterized) cranial sutures, with the goal of observing mechanisms of suture establishment. This suture had not been examined through this lens at the time. To this end, I investigated the wild type mid-palatal suture according to defined cranial suture identifiers (cell type, composition, behavior) with histology, RNAscope, scRNA-seq, and spatial transcriptomics. This study showed that the mid-palatal suture models cranial suture establishment and shares basic composition of cell types and ECM according to gene expression. A discrete nonosteogenic mesenchymal population was uncovered in the midline of the mid-palatal suture with a tendon-like mesenchymal cluster separating it from the advancing palatine process of the maxilla. I discuss the implications of tendon-like cells in the palate and contextualize my findings within cranial suture biology and patency. At the time of thesis submission, this manuscript was available on bioRxiv as a pre-print.

6.1 Summary

Orthodontic maxillary expansion relies on intrinsic mid-palatal suture mechanobiology to induce guided osteogenesis, yet the establishment of the mid-palatal suture within the continuous secondary palate and the causes of maxillary insufficiency remain poorly understood. In contrast, advances in cranial suture research hold promise to improve surgical repair of prematurely fused cranial sutures in craniosynostosis to potentially restore the obliterated signaling environment and ensure continual success of the intervention. We hypothesized that mid-palatal suture establishment is governed by shared principles with calvarial sutures and involves the functional linkage between expanding primary ossification centres with the midline mesenchyme. We characterized the establishment of the mid-palatal suture from late embryonic to early postnatal timepoints. Suture establishment was visualized using histological techniques and multimodal

transcriptomics. We identified that mid-palatal suture formation depends on a spatiotemporally controlled signaling milieu in which tendon-associated genes play a significant role. We mapped relationships between extracellular matrix-encoding gene expression, tenocyte markers, and novel suture patency candidate genes. We identified similar expression patterns in FaceBase-deposited scRNA-seq datasets from cranial sutures. These findings demonstrate shared biological principles for suture establishment, providing further avenues for future development and understanding of maxillofacial interventions.

6.2 Introduction

Management of transverse maxillary deficiency is highly dependent upon the intrinsic regenerative capacity of the mid-palatal suture, a fibrous joint connecting the palatine bones. Most commonly, force is applied to the maxilla through orthodontic appliances to expand the palate through techniques such as rapid maxillary expansion (RME), miniscrew-assisted rapid palatal expansion (MARPE), or surgically assisted maxillary expansion (SARME) if the suture is highly interdigitated (N. Kaya et al., 2023). These tools for orthodontic manipulation of the mid-palatal suture are rapidly evolving, but our understanding of the underlying biology is still incomplete. Cranial sutures are comparatively well-studied with respect to osteoblast and mesenchymal stromal cell behavior under different conditions and bear significant resemblance to the biomechanical and osteogenic properties of the mid-palatal suture.

The mechanisms enabling developmental establishment of both types of sutures are still under debate. Historically, development of the palatal shelves is well studied from the perspective of patterning, elevation, elongation, and mesenchyme fusion. However, this level of molecular understanding is incomplete beyond the point of mesenchymal tissue fusion wherein the epithelial seam degrades or transitions to mesenchyme. While the former body of knowledge has been pivotal in understanding the etiology of cleft lip and/or palate (CL/P) incidence and prevention, the latter is required to address long-term maxillary insufficiency in patients having undergone CL/P repair and complications following routine maxillary expansion (Diah et al., 2007; Gurel et al., 2010; Liberton et al., 2020; Williams et al., 2012; Ye et al., 2015). A similar challenge exists in the field of craniosynostosis management, the premature obliteration of cranial sutures by bone (E.

Stanton et al., 2022). Current treatment begins with excision of the fused suture, with ongoing innovation to prevent re-synostosis. The longevity of CL/P and craniosynostosis repair both depend on eventual establishment of a functional, patent suture with intact mechanosensory, osteogenic, and regenerative capacity. Thus, there is an unmet need for robust understanding of the fundamental principles involved in suture establishment for innovation in both calvarial and palatal clinical intervention.

This study aimed to close the gaps between our incomplete understanding of mid-palatal suture establishment and known cranial suture dynamics. With a toolkit of powerful genomic analyses, including *in situ* hybridization, single-cell RNA sequencing (scRNA-seq), and spatial transcriptomics of the palate (10X Genomics Visium, Xenium), we characterized the mid-palatal suture according to cranial suture definitions regarding cellular composition and expression of craniosynostosis risk genes. We then identified a core transcriptomic pattern involved in mid-palatal suture establishment composed of stratified expression of tendon-related genes, Wnt signaling, and extracellular matrix modulators. We confirmed cranial suture expression of these genes using publicly available scRNA-seq datasets (Holmes et al., 2017; Samuels et al., 2020). Our analysis also identified candidates for maintaining suture patency in the midline mesenchyme of early mid-palatal sutures. This study links molecular understanding of cranial suture biology with that of the mid-palatal suture, drawing connections to support further innovation in craniofacial research and suture-based clinical interventions.

6.3 Results

6.3.1 The mid-palatal suture models craniofacial suture establishment

The palate is a continuous structure separating the oral and nasal cavities (Fig. 6.1A). Following fusion of the mesenchymal compartments of the palatal shelves around embryonic day 15 (e15) (Bush & Jiang, 2012; Lan & Jiang, 2022; Piña et al., 2023), the consequent stages of palate development involve expansion of the palatine process of the maxilla towards the midline (Fig. 6.1B). By postnatal day 0 (P0), closely approximated bone fronts flank the region which will give rise to the mid-palatal suture. The mid-palatal suture undergoes additional chondrogenic changes by P3, which are beyond the scope of this paper (J. Li et al., 2015, 2016). Based on spatial analysis of cell heterogeneity at e15.5, the palatal shelf is composed of distinct cell populations, including mesenchyme,

osteoprogenitors (*Cd200, Alpl*), epithelium (*Krt14*), and vasculature (*Pecam1*) (Fig. 6.1C-E). The presence of midline mesenchyme separating bone and a bilateral ossification front is a common feature between cranial sutures and the mid-palatal suture, warranting further exploration.

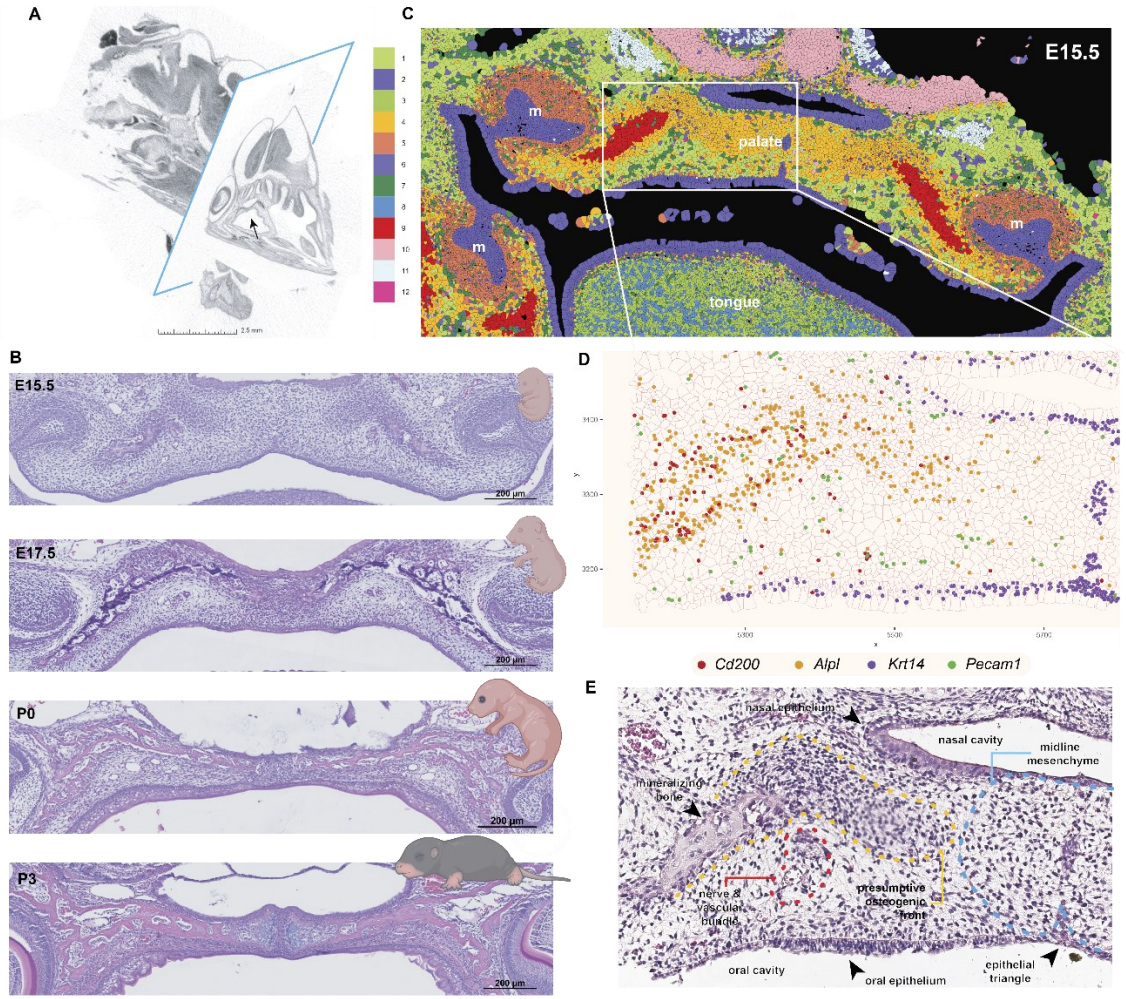

Figure 6.1 The mid-palatal suture models craniofacial suture establishment.
(A) Micro-computed tomography reconstruction of iodine-contrasted mouse head at postnatal day 1. 3D image is sliced cross-sectionally in the axial, coronal (blue rectangle), and sagittal planes. Black arrow indicates palatal shelf. Voxel size = 10µm. (B) Hematoxylin and eosin-stained 5-10um thick paraffin sections through the coronal plane of the mid-palatal suture at ages e15.5, e17.5, P0, and P3. (C) 10X Xenium Giotto spatial in situ plot from e15.5 coronal section with cell polygons colored by Leiden clustering algorithm. (D) Spatial plot of transcripts for *Cd200* (osteoblasts), *Alpl* (pre-osteoblasts and progenitors), *Krt14* (epithelium), and *Pecam1* (vasculature). (E) Annotated H&E of Xenium section in C,D.. m: molar; mb: mineralizing palatine process of the maxilla; nc: nasal cavity; ns: nasal septum; oc: oral cavity

6.3.2 Basic cranial suture composition is consistent with that of the mid-palatal suture

The early (e17.5) mid-palatal suture mesenchyme is flanked by osteogenic fronts, exemplified by a sequential distribution of pre-osteoblasts (*Runx2*), osteoblasts (*Sp7*), and osteocytes (*Dmp1*) similar to cranial sutures (Fig. 6.2A and B). However, the mid-palatal suture lies between epithelial layers separating the nasal and oral cavities. The frontal suture is only bordered by epithelium ectocranially, with the dura mater in direct contact on its endocranial side. When characterized at the single cell transcriptomic level, e15.5 mid-palatal suture cells clustered into similar cell type groupings in UMAP space as the e18 frontal suture (Fig. 6.2C-F). The Xenium spatial transcriptomic platform allows for spatial contextualization of clustering beyond what is traditionally possible with scRNA-seq datasets, which I used to contextualize identified cell types on e15.5 histological sections of the palate (Fig. 6.2D). The top 3 genes identified in each cluster of the e15.5 Xenium mid-palatal suture dataset were also observed in comparable cell clusters from the e15.5 mid-palatal suture and e18 frontal suture scRNA-seq datasets, with similar marker genes for frontal suture mesenchyme as in palate mesenchymal clusters in both scRNA-seq and spatial transcriptomic data (Fig. 6.2G-I). For example, *Itm2a*, *Col1a1*, and *Col12a1* were mapped to similar mesenchymal clusters in all three datasets. This established feasibility of cross-analysis of cluster components between the mid-palatal suture and cranial suture for further interpretation.

Genes commonly associated with craniosynostosis (premature fusion of the cranial sutures) such as *Efnb1*, *Fgfr1*, *Fgfr2*, and *Twist1* were found in mesenchymal clusters in the mid-palatal suture e15.5 scRNA-seq dataset, with highest expression in mesenchymal cluster 3 (mes.3) (Fig. 6.2J). A similar mesenchymal expression was observed in the e18 frontal suture scRNA-seq dataset (Fig. 6.2K). *Fgfr3* was infrequently expressed in both datasets but followed the same general mesenchymal association. Mapping these craniosynostosis-related genes back to the e15.5 Xenium mid-palatal shelf revealed that *Fgfr1*, *Fgfr2,* and *Twist1* were expressed along the expanding osteogenic front (“mes. 3” cluster) and in the ciliated nasal epithelium (“cilia” cluster) (Fig. 6.2L).

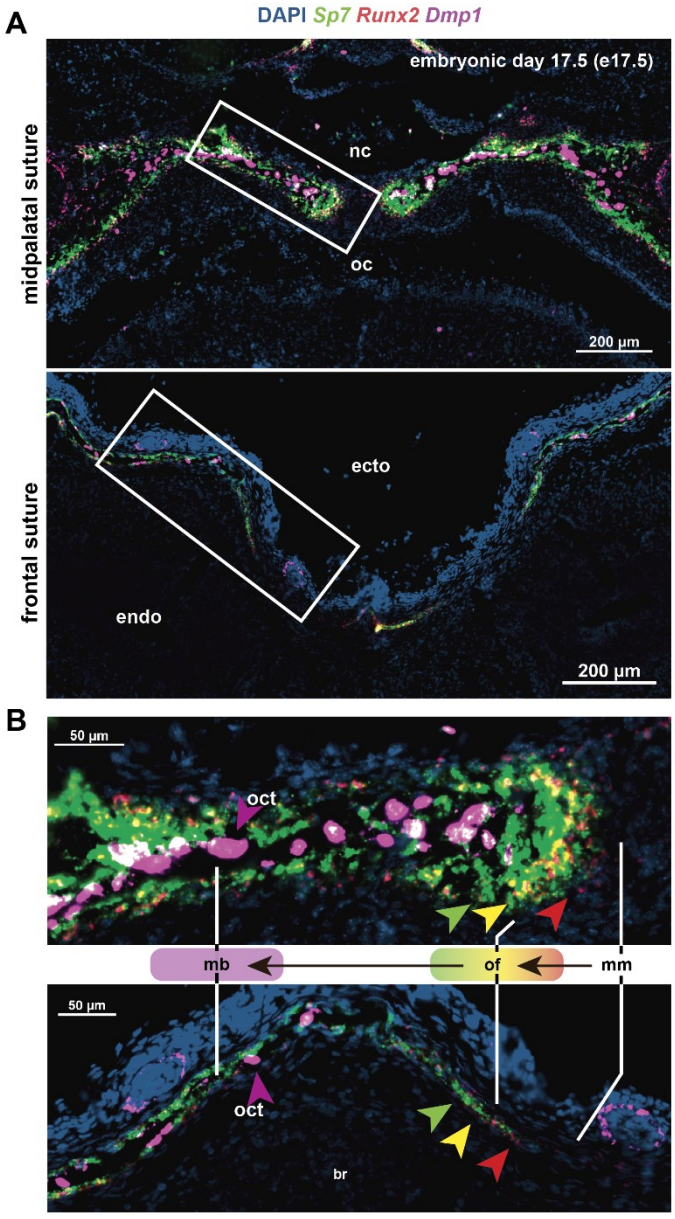
A
DAPI Sp7 Runx2 Dmp1
embryonic day 17.5 (e17.5)
midpalatal suture
nc
oc
200 µm
frontal suture
ecto
endo
200 µm
B
50 µm
oct
mb
of
mm
50 µm
oct
br

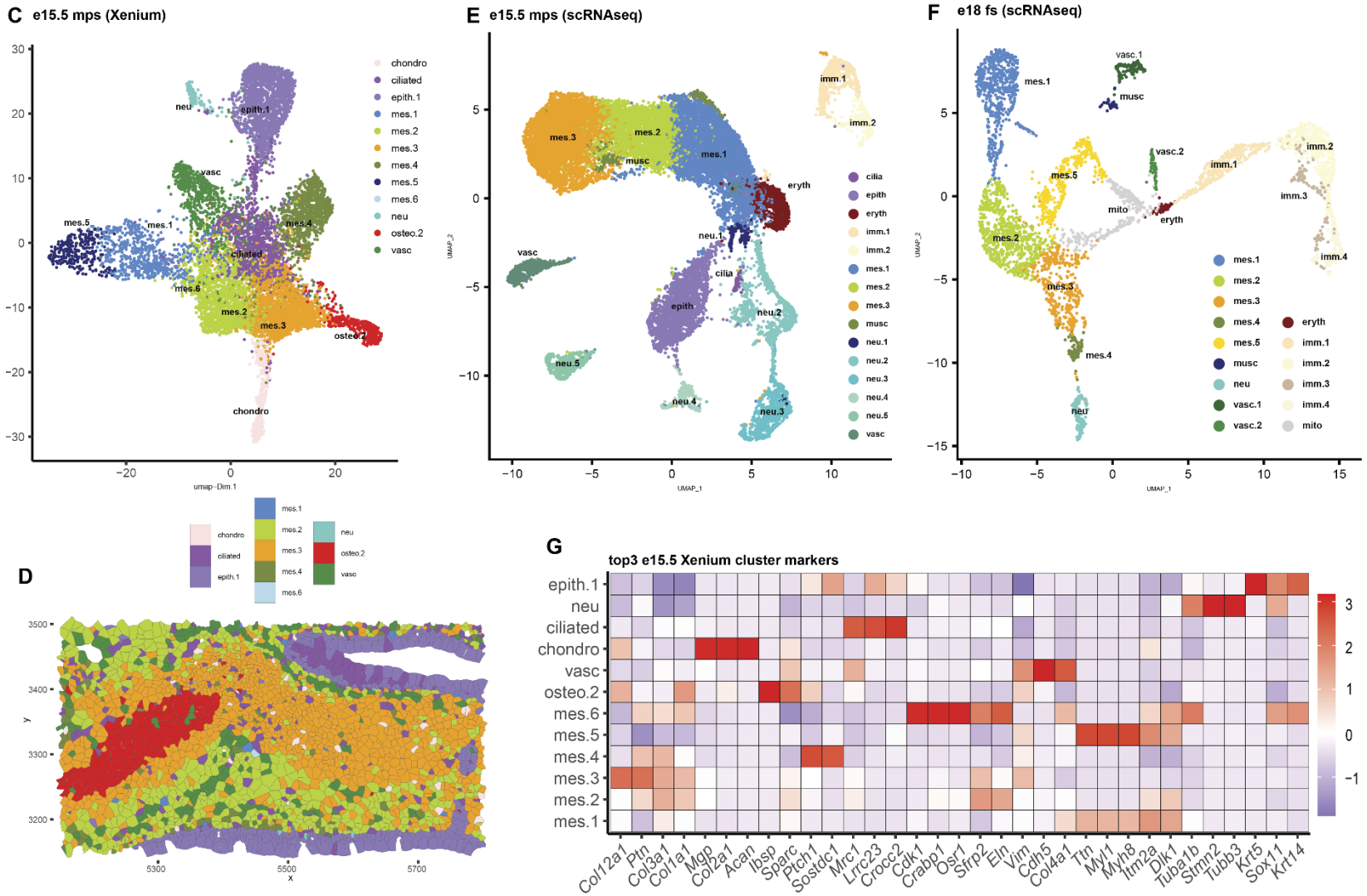
C
e15.5 mps (Xenium)
chondro
ciliated
epith.1
mes.1
mes.2
mes.3
mes.4
mes.5
mes.6
neu
osteo.2
vasc
umap−Dim.1
E
e15.5 mps (scRNAseq)
cilia
epith
eryth
imm.1
imm.2
musc
neu.1
neu.2
neu.3
neu.4
neu.5
UMAP_1
UMAP_2
F
e18 fs (scRNAseq)
vasc.1
vasc.2
mito
D
x
y
G
top3 e15.5 Xenium cluster markers
Col12a1
Ptn
Col9a1
Col1a1
Mgp
Col2a1
Acan
Ibsp
Sparc
Ptch1
Sostdc1
Mrc1
Lrrc23
Crocc2
Cdk1
Crabp1
Osr1
Strp2
Eln
Vim
Cdh5
Col4a1
Ttn
Myl1
Myh8
Itm2a
Dlk1
Tuba1b
Strmn2
Tubb3
Krt5
Sox11
Krt14

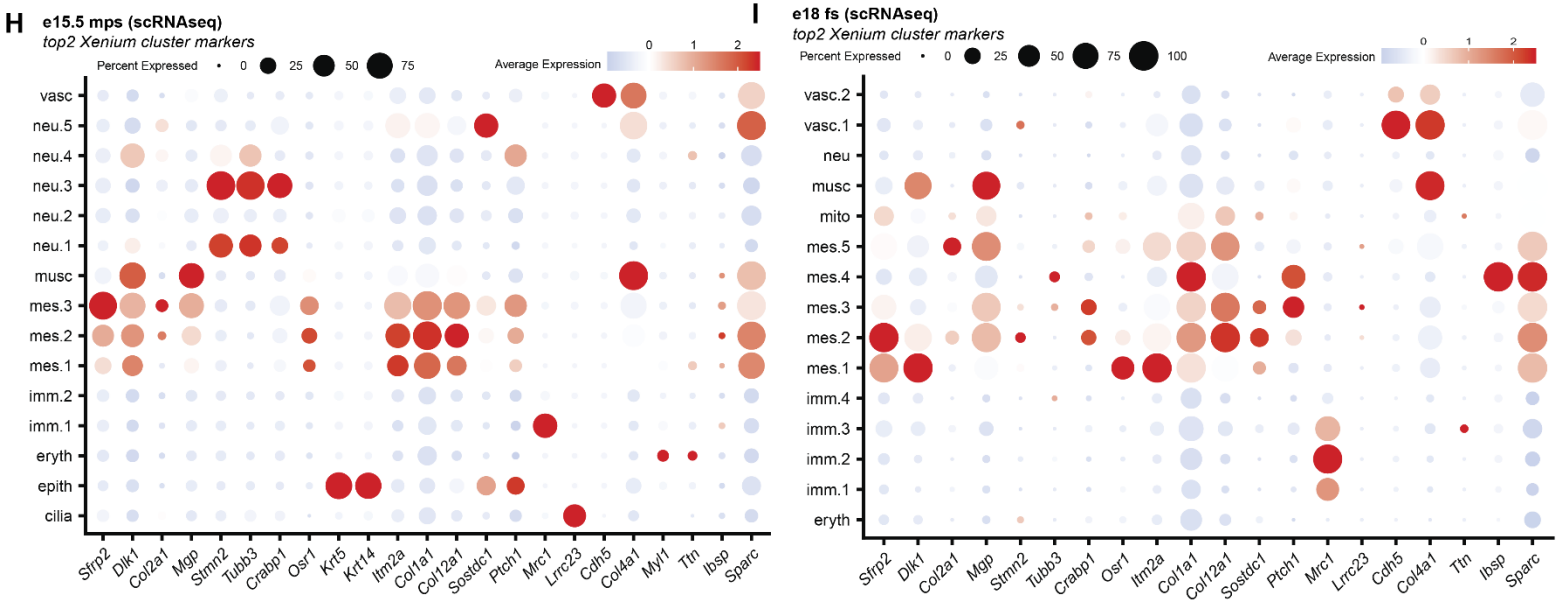
H
e15.5 mps (scRNAseq)
top2 Xenium cluster markers
Percent Expressed
0
25
50
75
Average Expression
0
1
2
vasc
neu.5
neu.4
neu.3
neu.2
neu.1
musc
mes.3
mes.2
mes.1
imm.2
imm.1
eryth
epith
cilia
Sfrp2
Dlk1
Col2a1
Mgp
Stmn2
Tubb3
Crabp1
Osr1
Krt5
Krt14
Itm2a
Col1a1
Col12a1
Sostdc1
Ptch1
Mrc1
Lrrc23
Cdh5
Col4a1
Myl1
Ttn
Ibsp
Sparc
I
e18 fs (scRNAseq)
top2 Xenium cluster markers
Percent Expressed
0
25
50
75
100
Average Expression
0
1
2
vasc.2
vasc.1
neu
musc
mito
mes.5
mes.4
mes.3
mes.2
mes.1
imm.4
imm.3
imm.2
imm.1
eryth
Sfrp2
Dlk1
Col2a1
Mgp
Stmn2
Tubb3
Crabp1
Osr1
Itm2a
Col1a1
Col12a1
Sostdc1
Ptch1
Mrc1
Lrrc23
Cdh5
Col4a1
Ttn
Ibsp
Sparc

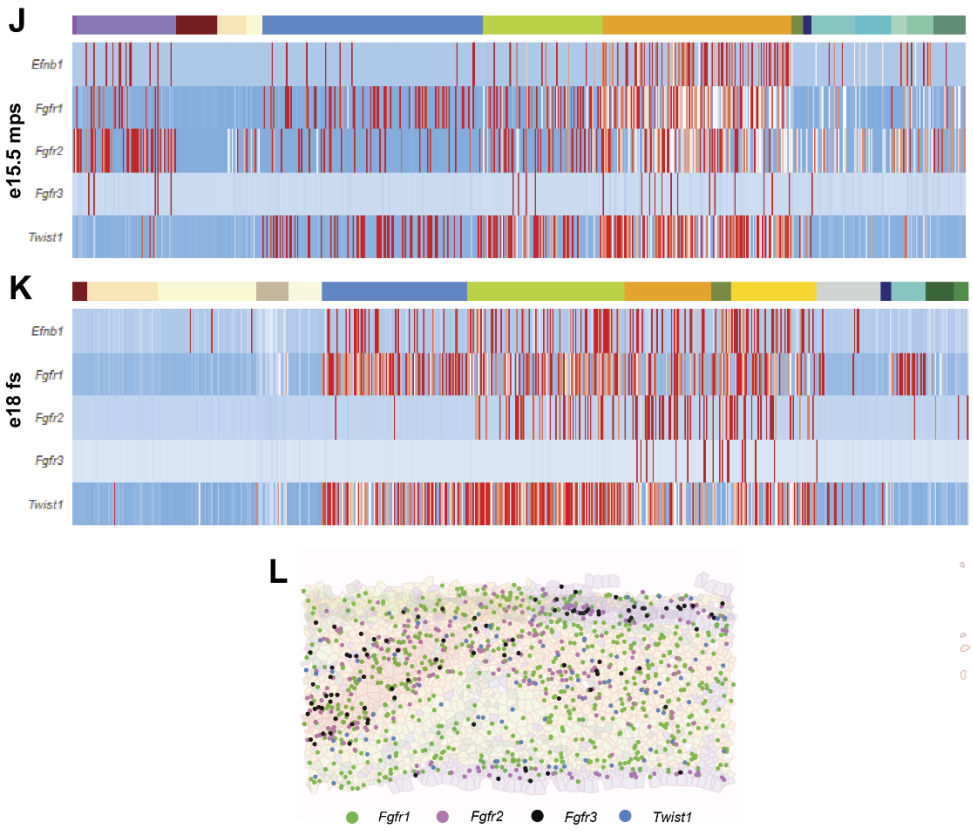

Figure 6.2 Basic cranial suture composition is consistent with that of the mid-palatal suture. (A) RNAscope mRNA detection of osteogenic markers in the mid-palatal suture and frontal suture. (B) Magnified region from white box in A, highlighting the gradient of osteogenic differentiation from mesenchyme to bone in both structures. nc: nasal cavity; oc: oral cavity; ecto: ectocranial; endo: endocranial; oct: osteocyte; br: brain. (C) Xenium spatial transcriptomic UMAP of E15.5 palate using Giotto analysis pipeline. Leiden clusters annotated based on top gene markers and spatial localization. chondro: chondrogenic; epith: epithelial; mes: mesenchymal; neu: neural; osteo: osteogenic; vasc: vascular. (D) Giotto spatial projection of left E15.5 palatal shelf, with polygons labeled according to annotated Leiden clusters (as in C). (E) E15.5 palate (mps) single-cell RNA sequencing (scRNA-seq) UMAP projection. Seurat clusters annotated based on top genes identified with the FindMarkers function. epith: epithelial; eryth: erythrocytes; imm: immune; mes: mesenchymal; musc: muscle; neu: neural; vasc: vascular. (F) E16 frontal suture (fs) scRNA-seq UMAP projection. Dataset downloaded from FaceBase courtesy of Holmes et al. Seurat clusters annotated based on top genes identified as in E. (G) Heatmap of top 3 gene markers in each E15.5 Xenium Leiden cluster. mes: mesenchymal; musc: muscle; neu: neural; vasc: vascular; eryth: erythrocytes; imm: immune; mito: mitochondrial. (H) Heatmap of expression of top 2 marker genes from E15.5 Xenium clusters in E15.5 mps scRNA-seq dataset. (I) Heatmap of top 2 marker genes as in H, according to their expression in E18 fs scRNA-seq dataset. (J,K) Heatmaps of expression of genes frequently associated with craniosynostosis in E15.5 mps scRNA-seq clusters (J) and e18 fs scRNA-seq clusters (K). Highest expression in both datasets for all genes appears to be focused around mesenchymal clusters, with the addition of epithelial expression in the E15.5 mps scRNA-seq dataset. (L) Spatial expression Giotto plot (spatplot) of four craniosynostosis-associated genes on the left E15.5 palatal shelf, with *Fgfr1* in green, *Fgfr2* in purple, *Fgfr3* in black, and *Twist1* in blue. Polygons are colored according to Leiden clustering. Each point is a detected transcript for the coded gene.

6.3.3 The palate osteogenic front is preceded by a gradient of spatially correlated genes

With the knowledge that, by birth, the palate midline would closely resemble a patent, approximated suture, we sought to identify the transitional gradients or guiding forces already at play in the palate mesenchyme. To this end, we used bioinformatic techniques to interpret complex relationships between clusters, their localization, and gene expression. First, we generated a Delaunay-triangulated network of correlation for the e15.5 palatal shelf (Fig. 6.3A). Using the Delaunay network and the Giotto package's cell proximity enrichment algorithm, we generated scores for cell proximity and interactions between annotated Seurat clusters, plotted in Fig. 6.3B**.** Focusing on interactions between different mesenchymal clusters, we identified that three of the highest inter-group interactions were between mes.2—mes.4, mes.2—mes.3, and mes.3—mes.4, indicating spatial relationships between the different transcriptionally distinct mesenchymal clusters (Fig. 6.3C). We then identified six spatially correlated "meta-feats" using the binSpect rank method to draw connections beyond individual gene cluster to cluster comparison (Fig. 6.3D). This method uses lists of genes to computationally identify correlated patterns of expression and overall trends. Each of the identified clusters mapped back to the original tissue in unique patterns, though some general categories were evident, such as epithelial localization of patterns 1 and 3 (Fig. 6.3E). Pattern 5 identified a mesenchymal gradient away from pattern 4, with maximal meta-feat expression in the midline mesenchyme. This pattern representing a group of spatially correlated meta-feats connecting bone with midline was particularly interesting to us as it might offer clues to explain how the advancing osteogenic front and "patent" suture midline mesenchyme interact, both of which are central to successful suture establishment.

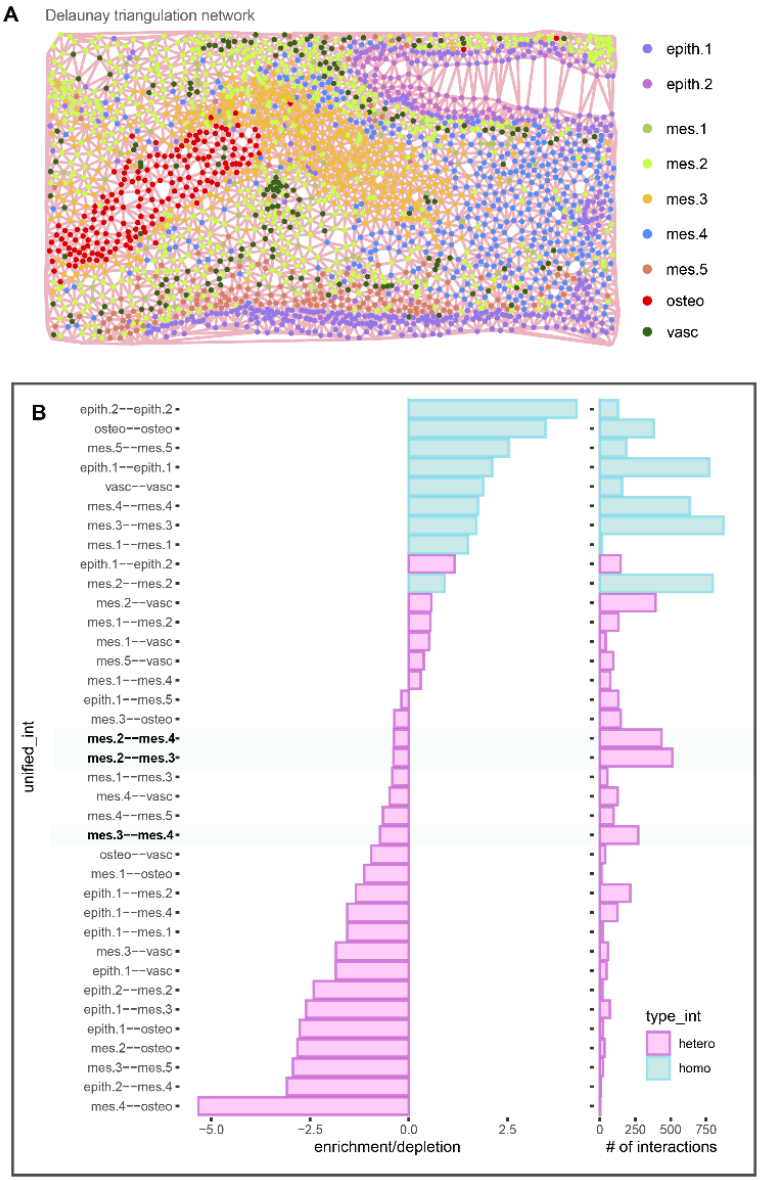
A
Delaunay triangulation network
epith.1
epith.2
mes.1
mes.2
mes.3
mes.4
mes.5
osteo
vasc
B
unified_int
epith.2--epith.2
osteo--osteo
mes.5--mes.5
epith.1--epith.1
vasc--vasc
mes.4--mes.4
mes.3--mes.3
mes.1--mes.1
epith.1--epith.2
mes.2--mes.2
mes.2--vasc
mes.1--mes.2
mes.1--vasc
mes.5--vasc
mes.1--mes.4
epith.1--mes.5
mes.3--osteo
mes.2--mes.4
mes.2--mes.3
mes.1--mes.3
mes.4--vasc
mes.4--mes.5
mes.3--mes.4
osteo--vasc
mes.1--osteo
epith.1--mes.2
epith.1--mes.4
epith.1--mes.1
mes.3--vasc
epith.1--vasc
epith.2--mes.2
epith.1--mes.3
epith.1--osteo
mes.2--osteo
mes.3--mes.5
epith.2--mes.4
mes.4--osteo
−5.0
−2.5
0.0
2.5
enrichment/depletion
0
250
500
750
# of interactions
type_int
hetero
homo

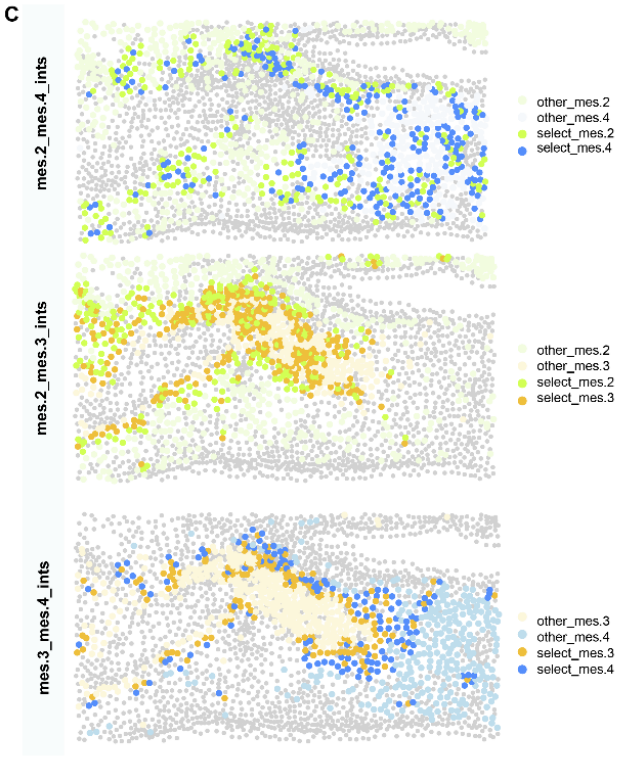
C
mes.2_mes.4_ints
other_mes.2
other_mes.4
select_mes.2
select_mes.4
mes.2_mes.3_ints
other_mes.2
other_mes.3
select_mes.2
select_mes.3
mes.3_mes.4_ints
other_mes.3
other_mes.4
select_mes.3
select_mes.4

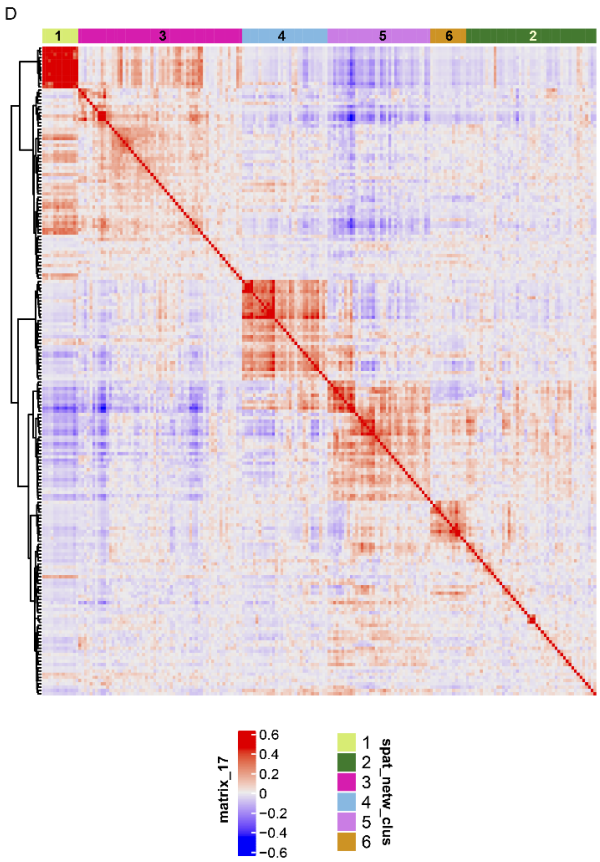
D
1
3
4
5
6
2
matrix_17
0.6
0.4
0.2
0
−0.2
−0.4
−0.6
spat_netw_clus
1
2
3
4
5
6

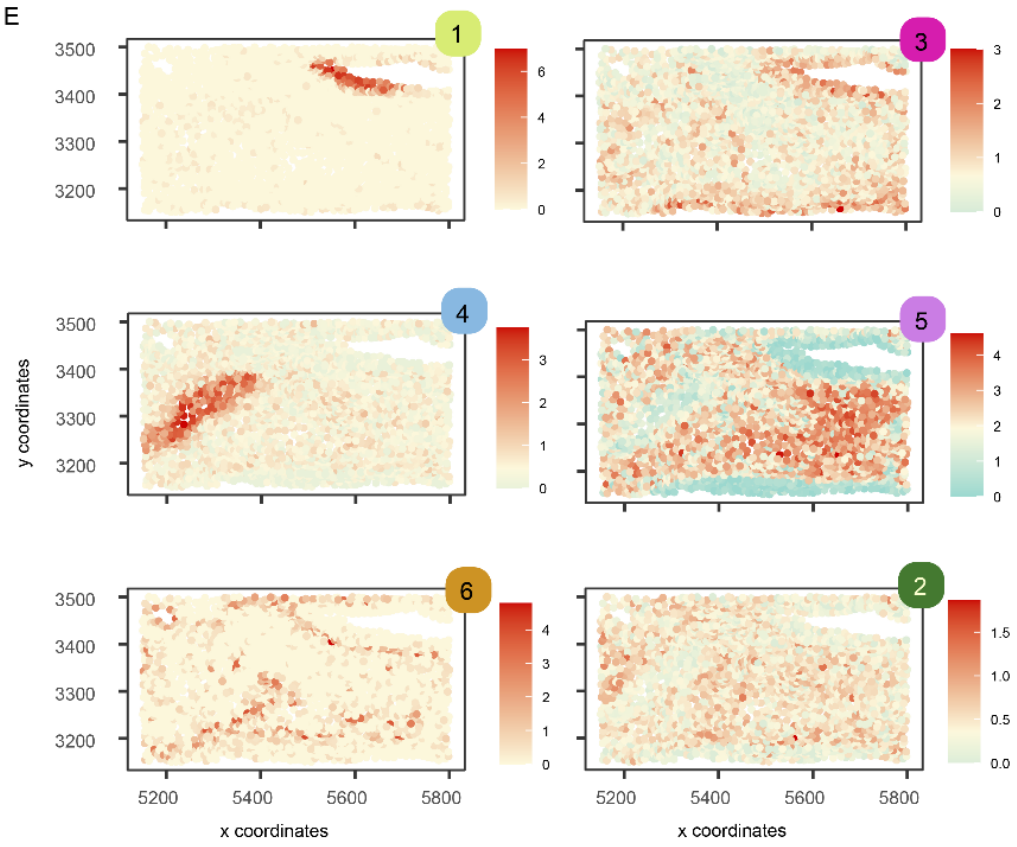

Figure 6.3 The midline-approaching osteogenic front in the palate is preceded by mesenchyme with a gradient of spatially correlated genes.
(A) Delaunay network of correlation between clusters in E15.5 left palatal shelf Xenium experiment. Pink lines indicate edges between nodes of the undirected graph output by Delaunay triangulation. (B) Cell Proximity Barplot of enrichment or depletion and number of interactions between different annotated clusters at e15.5 (e.g. mes.2—mes.3 indicates spatially correlated interaction between cluster mes.2 and cluster mes.3). Bars are colored according to intra-cluster (homo) or intercluster (hetero) interaction type. Bolded interactions are featured in panel (C). (C) Visualization of interacting cells in mes.2—mes.4, mes.2—mes.3, and mes.3—mes.4 interactions. (D) Heatmap of clusters generated from spatial co-expression analysis using binSpect rank method. Six spatially correlated patterns of expression were identified. (E) Spatial expression of six "metafeats" identified in panel (D).

6.3.4 Tendon-associated genes are expressed between the midline mesenchyme and palate osteogenic center

At e15.5, a band of stromal cells bridging the mineralizing bone (*Dmp1*+) with the palate midline and its epithelial remnants (*Krt14*+) expressed tendon-associated genes, like *Mkx* and *Chodl* (Fig. 6.4A). Other tendon- or ligament-related genes identified in cranial suture mesenchyme (Farmer et al., 2021; Holmes et al., 2020) were also enriched in Pattern 5, including *Col3a1, Lum, Six2,* and *Mkx* (Fig. 6.4B). These genes mainly encode

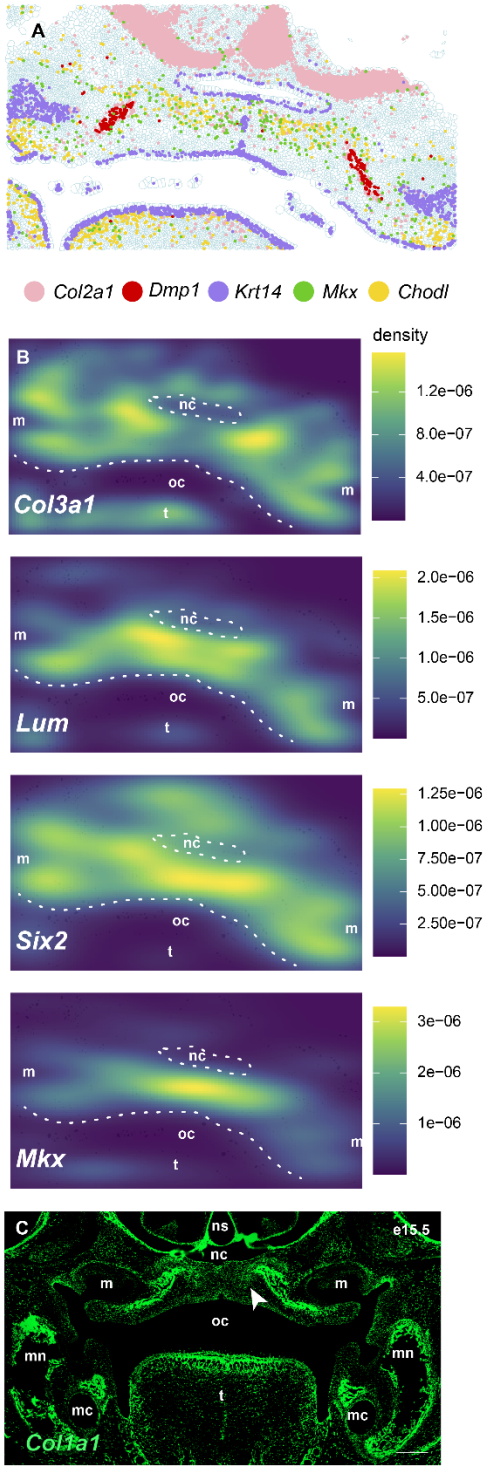

proteoglycans composing the extracellular matrix in tendons (*Col3a1, Lum, Mkx)*, though *Six2* is also expressed by osteochondroprogenitor cells. The condensed mesenchyme (henceforth referred to as "tenocyte-like cells", or TLC) was enriched for *Col1a1* based on RNAscope *in situ* hybridization, marking the mesenchyme medial to the mineralizing bone (Fig. 6.4C).

Figure 6.4 Establishment of the mid-palatal suture involves gradiated expression of tendon- and extracellular matrix-associated genes between the midline mesenchyme and osteogenic center.
(A) Giotto spatial transcript plot contextualizing *Mkx* and *Chodl* in the e15.5 palate, with *Col2a1* mainly marking chondrocytes, *Dmp1* marking the mineralizing palatine process of the maxilla, and *Krt14* marking epithelium. (B) Giotto spatial density plots of known tenocyte markers in Xenium dataset: *Col3a1*, *Lum, Six2, Mkx.* Scale indicates density of expression, with dark blue denoting zero and yellow as maximal density for each gene. (C) RNAscope *in situ* hybridization of *Col1a1* in the e15.5 coronal palate. White arrowhead indicates *Col1a1* concentration medial to mineralizing bone.

6.3.5 Midline mesenchyme marker genes become more restricted in expression over developmental time in the mid-palatal suture and cranial sutures

The e15.5 midline mesenchyme was histologically identifiable as condensed mesenchyme surrounding the formerly continuous midline epithelial seam (MES) (Fig. 6.5A). Even at low resolution, the midline mesenchyme clustered into distinct transcriptional identities when compared with other palatal populations (cluster 4) with Visium whole-transcriptome analysis (Fig. 6.5B). Genes that were spatially enriched in the palate midline, such as *Sfrp2* and *Tnn*, were also co-expressed in frontal suture scRNA-seq mesenchymal clusters from e16 to P28 (Fig. 6.5C,D). Wnt signaling has been associated with regulation of tissue differentiation in response to biomechanical stress (Byun et al., 2014; Robinson et al., 2006; X. Wu et al., 2020). To query Wnt signaling in the context of biomechanically active suture development, we localized Wnt receptor-encoding *Lrp6* and Wnt modulator/osteocyte marker *Dkk1* in the developing craniofacial complex at e17.5 and P3 (Fig. 6.5E). In coronal planes of sectioning, we observed midline mesenchyme expression of *Lrp6* in all visible sutures, including the mid-palatal suture. From e17.5 to P3, expression grew more restricted to a thin, central region of the suture mesenchyme – away from *Dkk1-positive* osteogenic cells. The intensity of RNAscope staining suggested that abutting sutures had more focally arranged *Lrp6*+ cells than the overlapping frontal suture.

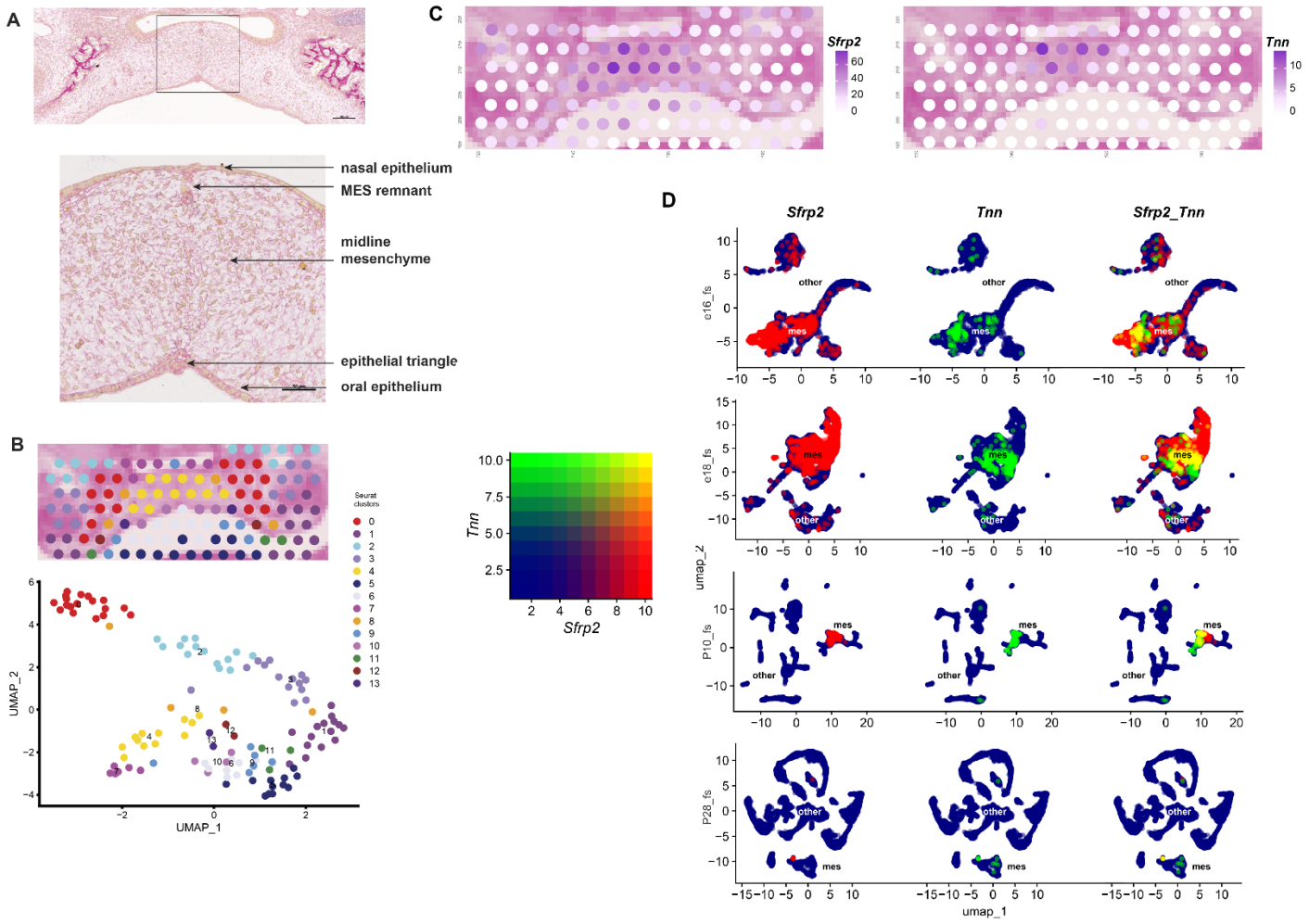
A
nasal epithelium
MES remnant
midline
mesenchyme
epithelial triangle
oral epithelium
B
Seurat clusters
0
1
2
3
4
5
6
7
8
9
10
11
12
13
UMAP_2
UMAP_1
Tnn
Sfrp2
C
Sfrp2
Tnn
D
Sfrp2
Tnn
Sfrp2_Tnn
e16_fs
e18_fs
P10_fs
P28_fs
umap_2
umap_1
other
mes

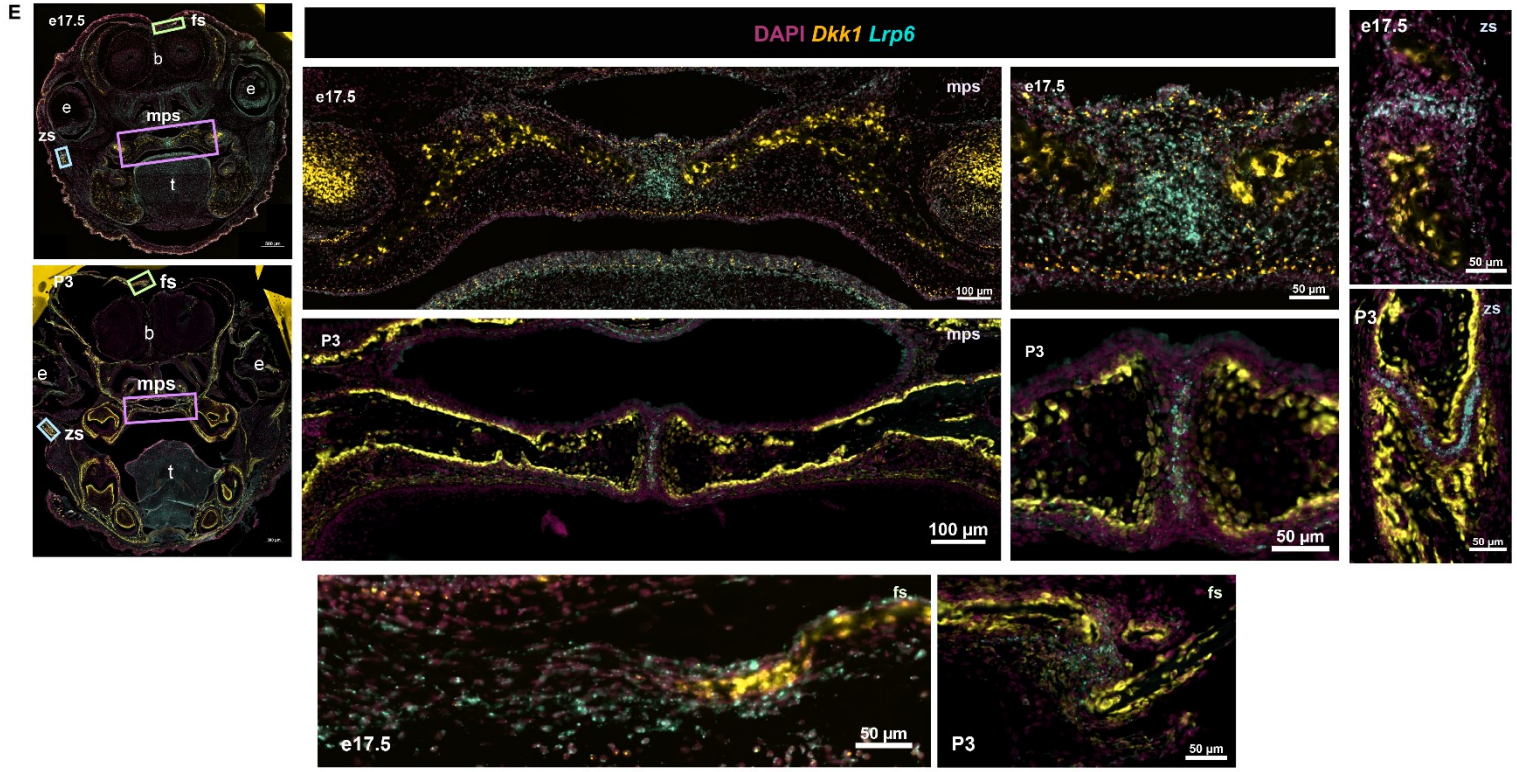
E
e17.5
fs
b
e
e
mps
zs
t
P3
fs
b
e
e
mps
zs
t
DAPI Dkk1 Lrp6
e17.5
mps
100 µm
e17.5
50 µm
e17.5
zs
50 µm
P3
mps
100 µm
P3
50 µm
P3
zs
50 µm
fs
e17.5
50 µm
fs
P3
50 µm

Figure 6.5 Mid-palatal suture midline mesenchyme marker genes have dynamic expression in cranial sutures, growing more restricted over time.
(A) e15.5 coronal palate pentachrome histological stain at low magnification, with major components of the midline mesenchyme annotated in lower magnified panel. MES: Midline Epithelial Seam. (B) Seurat clusters from graph-based clustering of e15.5 palatal shelf, with yellow (cluster 4) marking the midline mesenchyme on visual assessment. Top panel: spatial dimplot, bottom panel: UMAP. Each circular barcode includes whole transcriptome sequencing information for 3-10 adjacent cells. (C) Expression of selected midline mesenchyme markers genes identified from Visium e15.5 cluster 4 targets using the FindMarkers() Seurat function: *Sfrp2* and *Tnn.* (D) Joint FeaturePlot expression of *Sfrp2, Tnn,* or both (*Sfrp2_Tnn)* in scRNA-seq UMAP plots generated for e16, e18, P10, and P28 frontal sutures. Red color indicates *Sfrp2* expression, green indicates *Tnn* expression, and yellow points highlight co-expression of both genes. Plots are labeled with categorical annotation of mes (mesenchymal clusters) or other (remaining clusters). Yellow points are mainly found in mesenchymal clusters across all ages. (E-H) RNAscope *in situ* hybridization for *Dkk1* (yellow) and *Lrp6* (cyan) mRNA on coronal samples through the middle plane of palate sectioning at e17.5 and P3, overview in E. Note high expression of *Lrp6*, a component of the Wnt signaling pathway, in the midline mesenchyme of all sutures. Colored rectangles indicate regions of magnification for panels F (mid-palatal suture), G (frontal suture), and H (zygomatic suture). DAPI nuclear counterstain is dark violet. b: brain; e: eye; fs: frontal suture; mps: mid-palatal suture; t: tongue; zs: zygomatic suture

6.3.6 Tenocyte-like cells interface with specific midline mesenchyme

Analysis of the e15.5 midline mesenchyme *in situ* revealed further discrete expression of genes associated with orofacial clefting and Wnt signaling (*Pax9*, for example) (Fig. 6.6A). Interestingly, the TLC extending from the *Dmp1*+ bone appeared to directly interface with the *Pax9*+ midline. Stratified expression of extracellular matrix genes radiated from the bone edge (*Mkx, Tnn, Thbs1*) toward midline expression of other important developmental growth factors (*Tgfb2*, *Gsc, Bmp2*) (Fig. 6.6B). Many core gene regulatory networks of suture development are similarly stratified in expression between the bone and midline, including Bmp, Fgf, Hh, Mmp, Igf, Tgfb, and Wnt pathways.

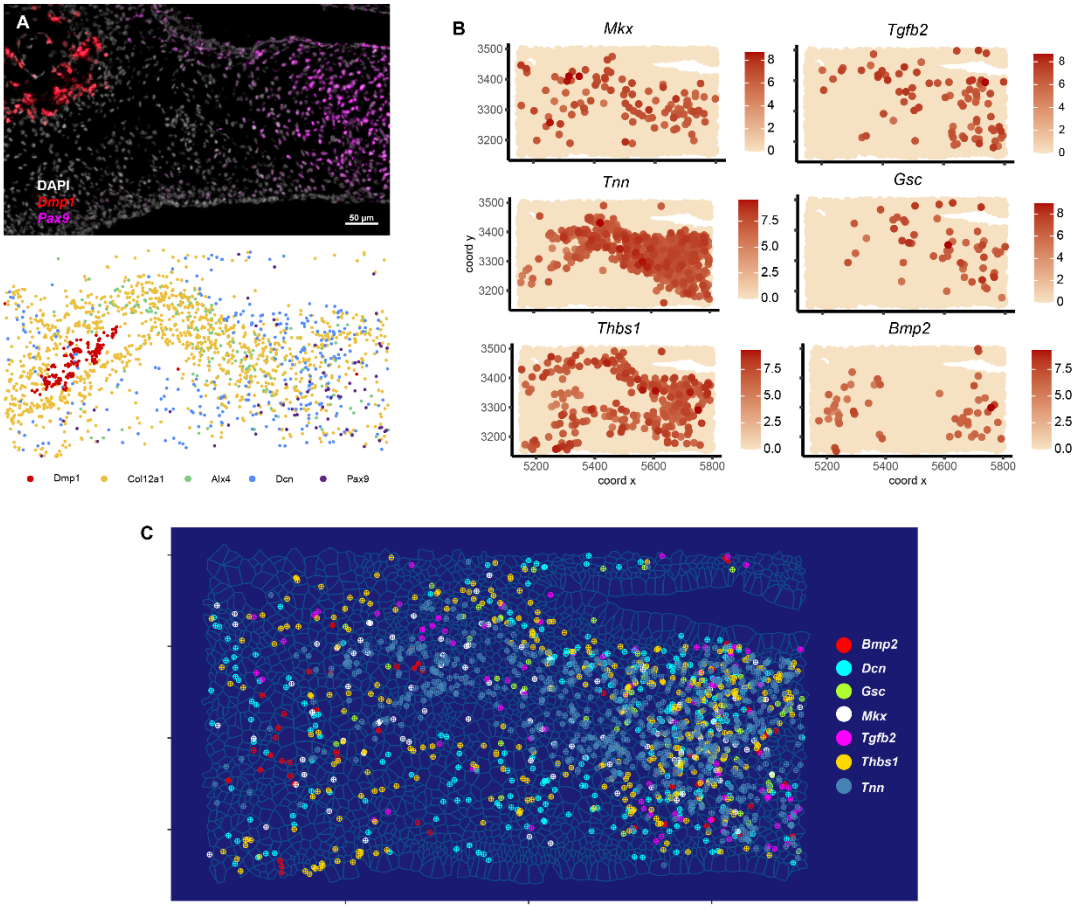

Figure 6.6 Tenocyte-like cells interface with transcriptionally distinct midline mesenchyme in the palate.

(A) RNAscope Manual Assay targeting *Dmp1* (representing immature osteocytes and late osteoblasts) and *Pax9*, a transcription factor that is expressed highly in the mid-palatal midline mesenchyme. Lower panel: spatial plot of transcripts identified in e15.5 mid-palatal suture Xenium assay demonstrating gradient of gene expression (*Col12a1, Dcn, Alx4)* between bone (*Dmp1*) and midline mesenchyme (*Pax9*). (B) Giotto spatplot visualization of Xenium targets localized between the mineralizing bone and midline, including TLC, midline mesenchyme, or both (*Mkx, Tnn, Thbs1, Tgfb2, Gsc, Bmp2*). (C) Spatial co-localization (Xenium) of *Bmp2, Dcn, Gsc, Mkx, Tgfb2, Thbs1,* and *Tnn* in the context of the e15.5 palatal shelf demonstrating the interface between TLC and the midline mesenchyme. Predicted cell shape polygons are outlined in light blue.

6.4 Discussion

This study assessed the establishment of the mid-palatal suture according to cellular and molecular properties established for the cranial suture to characterize the mid-palatal suture according to cranial suture definitions to enable investigation of its midline mesenchyme as a mediator of suture establishment and patency. Through multimodal transcriptomic

techniques spanning single-cell RNA sequencing to spatial transcriptomics, we characterized the architectural and transcriptomic landscape of the palate at e15.5. We identified the presence of cells with a tendon-related molecular signature and provided evidence for a cell hierarchy in the advancing osteogenic front similar to what has been described for cranial sutures. We also characterized the presence of several candidate "patency factors" in the midline mesenchyme of the palate which are also expressed in cranial sutures, decreasing over time, specifically *Sfrp2* and *Tnn.* Our characterization of the shared features of the mid-palatal suture and cranial sutures supports further efforts toward translation between the palate and cranial vault, both clinically and foundationally.

6.4.1 Tenocyte-like cells form a pseudo-neotendon in the palate

Several patterns of spatially correlated gene expression patterns emerged from our Xenium analysis, but one pattern of "metafeats" in particular seemed to bridge the mineralizing bone with the midline of the palate and showed enriched expression of genes that have been associated with tendons. Tenocytes are specialized tendon fibroblasts which are important for maintenance and transduction of tensile force between bony structures and can be identified by *Scx* expression (Shukunami et al., 2018). It is well established that mesenchymal stromal cell (MSC) differentiation is influenced by mechanical cues. MSCs cultured on a stiffer matrix tend toward myocyte and osteoblast fate (Petzold & Gentleman, 2021), and cyclic stretching can cause MSC to tenocyte differentiation (Morita et al., 2018). Tenocytes expanded *in vitro*, referred to as "tenocyte-like cells" (TLC), express multipotential genes similar to mesenchymal stromal cells (MSCs) but maintain a potential to differentiate into osteogenic cells (Darrieutort-Laffite et al., 2019; de Mos et al., 2007; Klatte-Schulz et al., 2012). Previous studies have examined the muscular posterior palate at these ages (Grimaldi et al., 2015; Kouskoura et al., 2016; Nara et al., 2017). However, tenocytes have not been characterized in the medial plane of the palate as in this study, a region with no direct muscle attachment occurs.

Previous studies using rat embryonic fibroblasts (REF) showed a propensity to condense on soft substrates. This "condensation tendency" could provide meaningful insight into the formation of the palatal neotendon between the stiff palatine process of the maxilla and the soft midline mesenchyme (T. Xie et al., 2021). In REF, there is an element of tensile prestretch induced by the substrate – an isotropic stretch which causes tissue

contraction when released. Xie et al conclude that biomechanical principles are important in defining pattern boundaries, such as between inner and outer boundary cells. A similar principle may underly the patterning of the developing bone front, initiating neotendon formation and creating a stiffer scaffold or path along which osteogenesis may proceed. Along these lines, cells at the edges of islands on microfabricated cell sheets along a gradient of traction forces undergo rapid proliferation, with observable cell cycle differences, a function that would cause changes in cell signaling (C. M. Nelson et al., 2005). In the e15.5 palate, we observed a collagen-rich neotendon-like cluster of densely packed stromal cells resembling TLC (based on gene expression) with a border of comparatively more sparse cells. This architecture is reminiscent of a neotendon (referred to henceforth as PNT for simplicity). The formation of a PNT could be guided by and/or instructive for the biomechanical nature of the palate, as tendons and ligaments are in other musculoskeletal sites (Y. Liu et al., 2017). This concept underlies recent innovation in regenerative tendon therapy, which may be leveraged for craniofacial applications in mechanically loaded settings (Citro et al., 2023).

6.4.2 Extracellular matrix in the PNT and cranial suture mesenchyme

A major component of cell migration and force propagation, integrin-mediated activation, is dictated by organization of collagen fibrils (Doyle et al., 2015). The PNT is enriched for genes encoding several collagens with clinical relevance for the palate. In our Xenium spatial dataset, we observed a coordinated pattern of collagen-expressing cells, in addition to other interacting proteoglycans and ECM proteins. Mutations in *Col6a1* and *Col12a1* both affect musculature and result in high arched palate (OMIM 616471, (N. L. Baker et al., 2005)). *Col11a1,* most significantly decreased in *Scx-/-* tendons (H. Liu et al., 2021), is also associated with cleft palate in Pierre Robin and Stickler Syndromes (Lavrin et al., 2001) in addition to reports of nonsyndromic CL/P prevalence in COL11A1/2 deficient patients (L. Guo et al., 2017; Melkoniemi et al., 2003). It should be noted that clefts observed in PRS are usually due to inability of the tongue to contract preventing timely palatal shelf elevation. Interestingly, tongue contraction is dependent on muscle attachment to the mandible, which appears to be compromised in several Pierre Robin Sequence (PRS) mouse models (Kouskoura et al., 2013, 2016; Lavrin et al., 2001). We observed focal expression of genes encoding key proteoglycans that are associated with early

palatogenesis within and directly surrounding the PNT, including *Lum* and *Dcn.* Defects in these proteoglycans also have profound effects on tendons with implications for clefting (Hammond et al., 2018; H. Liu et al., 2021). Previous cranial suture sequencing has shown the presence of tendon-associated genes like *Scx, Mkx, Lum, Fmod, Dcn,* and *Col12a1* in the suture mesenchyme at e16.5 and e18.5, suggesting a mechanoresponsive role (Holmes et al., 2020). Farmer et al. discuss and characterize 'ligament-like mesenchyme' cell populations in the developing calvarial sutures as being related to suture flexibility, or speculatively playing a role in mechanotransduction with relevance to brain growth (Farmer et al., 2021). These tendon/ligament-like populations were reported to express *Tnmd, Chodl, Scx,* and *Mkx* – all of which were also identified in the TLC herein. Our study supports a central role for tenocyte-like cells in both cranial sutures and the developing mid-palatal suture. Both structures share several features beyond the presence of TLC, such as tensile loading and rapid MSC-related changes allowing coordinated osteogenesis.

6.4.3 Maintenance of suture patency

A major outstanding question in cranial suture pathology is still the definition of factors responsible for maintenance of suture patency. This is relevant, as re-synostosis following suture repair is often observed indicating that re-opening of a suture may not be sufficient to establish all suture characteristics. A reconstructed replacement suture should replicate the *in vivo* signalling environment as closely as possible. Similarly, the mid-palatal suture engineered upon CL/P repair, or even surgically assisted rapid maxillary expansion, should recapitulate the conditions for intact mechanoreception, osteogenic differentiation, and resilience to forces/mechanical disruption. This study aimed to investigate some of these uncharacterized elements of palate biology. We found a transcriptional identity of midline mesenchyme of the palate characterized by genes associated with extracellular matrix assembly and composition, growth factor signaling, and transcriptional control. *Lrp6* and *Pax9* marked the definitive midline mesenchyme after e15.5. *Lrp6,* which encodes one of two transmembrane Wnt signaling receptors, was similarly expressed in the midline mesenchyme of cranial sutures and showed a notable compression in its expression domain to the center of the suture mesenchyme in older mice. This finding was interesting to us for two reasons. First, it confirmed that the mid-palatal suture shares key mesenchymal characteristics with other cranial sutures. Also, its continuous yet increasingly restricted

expression in the compressed center of the midline of sutures invoked the concept of suture patency. Interestingly, the zygomatic and mid-palatal sutures had higher and more focal expression of *Lrp6* than the frontal sutures – perhaps reflective of the overlapping anatomy of the frontal bones. Furthermore, we identified midline mesenchyme expression of *Pax9* as early as e15.5 in a similar expression domain to *Lrp6*. *Pax9* has been associated with CP; however, due to the severe phenotype observed following its deletion, late embryonic to early postnatal studies have not been performed (Ichikawa et al., 2006; Jia et al., 2020; Sweat et al., 2020). Induction of *Pax9* in the dental mesenchyme during mesenchymal condensation has been reported, linking its expression to cellular compression resulting in changes to extracellular matrix composition (Mammoto et al., 2015). We found a spatial relationship of *Pax9* with PNT marker genes in the palate, forming a gradient between the mineralizing palatine process of the maxilla and the *Pax9/Lrp6*-expressing midline mesenchyme. We hypothesize that the induction of midline mesenchyme-enriched factors, like *Lrp6, Tnn,* or *Pax9*, is a function of cell compression due to the approximation of extracellular matrix-enriched osteogenic fronts. The relationship between mesenchymal cell compression, suture establishment, and patency is not yet established (Alves-Afonso et al., 2021) and a more detailed study of these factors may be informative.

6.4.4 Clinical implications

Mid-palatal suture establishment is complex and must be considered when developing clinical interventions involving this structure. The integration of biomechanical stimuli (mastication, suckling, brain expansion), osteogenesis, odontogenesis, and midfacial growth should be central to these considerations. Cell differentiation is guided by several signaling networks, including WNT, BMP, TGFs, Hh, and FGF pathways. Development and maintenance of the heterogeneous components in the developing palate such as mineralizing bone, vasculature, nerves, epithelium, and cartilage likely not only involve coordinated signaling for lineage differentiation (M. Chen et al., 2021; Y. Han et al., 2018; Novoseletskaya et al., 2023; Picoli et al., 2024; Tower et al., 2021), but must also include mechanosensitive elements. Thus, it is important to consider how changes in the mechanical environment following surgical intervention might alter the growth potential of the target tissue. Our data suggests a close physical relationship between expanding palatine bone and the patent midline mesenchyme involving a neotendon-like structure,

which may be a critical component for formation of a functional suture. Avoiding damage to the palatopharyngeal muscular structures, like scarring of the pterygomandibular ligament, is a key consideration in palatoplasty (Tschopp, 1974). It has been reported that even superficial disruption of the mid-palatal suture impedes midface expansion, and midface hypoplasia is still a potential outcome following CL/P repair (Celie et al., 2024; Freng, 1978; Fudalej et al., 2008; J. Li et al., 2015). The use of MSC-centered/derived therapies for bone regeneration and tendon healing, especially with adjunctive indiscriminate application of rhBmp2, should be revisited under the lens of our findings (Makar et al., 2021; H. Shen et al., 2022; Takagi & Urist, 1982).

CHAPTER 7
DISCUSSION AND CONCLUSIONS

7.1 Summary

This thesis explored the fundamental drivers of osteogenic biology from a holistic perspective, spanning from molecular level to large-scale craniofacial changes, and the intricate synergy between cellular behaviour and environmental cues across several anatomical structures involved in midfacial growth. The etiology of midface hypoplasia (MFH) and its correlation with calvarial suture malformation, cranial base deficiency, and cleft lip/palate repair are still unknown, necessitating further study of midfacial sutures and craniofacial growth zones. The study aimed to contextualize mechanotransduction in cranial suture physiology and relate findings from non-calvarial studies to provide further insight into the physiology of midfacial growth. The data chapters explored distinct physiological processes within the midfacial sutures and cranial base to identify core developmental paradigms for craniofacial growth. This inquiry also addressed the role of suture malformation in the development of MFH in mice, demonstrating the consequences of disruption of fine regulation of osteogenesis.

Chapter 4 investigated the precise regulatory role of Bmp7 in maintaining symmetry within the internasal suture, demonstrating how its absence from neural crest cells leads to significant nasal bone deviations with physiological ramifications. In Chapter 5, I used *Bmp2* and *Bmp7* deletion from Gli1+ cells to investigate the different roles of these Bmps in endochondral ossification at the cranial base and overall control of craniofacial bone morphology. Notably, the deletion of either *Bmp2* or *Bmp7* yielded different phenotypes. Together, these studies highlighted the nuanced roles of Bmp2 and Bmp7 in the control of craniofacial growth. Both proteins are associated with osteogenesis and have a clinical history of use for bone regeneration, with little distinction between them. Retrospective study of successful rhBMP treatment is complicated by the fact that ICD-9 (International Classification of Diseases, 9th Revision) codes did not distinguish between the type of BMP used in the procedure (Ong et al., 2010). The discontinuity between clinical considerations and my findings of their independent significance underscores the contribution this thesis makes to the BMP and bone regenerative literature.

The concepts of suture establishment and the influence of tissue organization on the patterning of mechanically loaded structures were integrated in Chapter 6 through my characterization of the mid-palatal suture. The heterogeneous mesenchymal sub-populations in the palate were organized into an ECM-rich tendon-like structure that linked the midline mesenchyme with the developing bone, each of which had transcriptional evidence of distinct signaling environments. To my knowledge, this is the first spatial transcriptomic characterization of a pseudo-neotendon in the developing mid-palatal suture preceding the osteogenic front. The presence of a tendon- or ligament-like structure in developing sutures has been reported in other cranial suture sequencing studies, further bolstering the validity of my results (Farmer et al., 2021; Holmes et al., 2020).

Together, the data chapters in this thesis paint a portrait of complex inter-regulation of the extracellular environment and osteochondrogenic cell differentiation, molding the developing sutures and synchondroses into functional units of secondary osteogenic growth. In line with the hypothesis, there is evidence of critical cell-environment relationships in the midfacial sutures, synchondroses, and mid-palatal suture across different stages of growth. This data emphasizes the importance of consideration of biomechanical control of growth zone development and function during clinical interventions and broader craniofacial research.

7.2 Mechanical environment and developmental influences

The transduction of an extrinsic mechanical impulse to a functional change in a cell is underappreciated as a highly physical process with several mechanisms in place for adaptive refinement. To this end, it is useful to think of the cell as a machine composed of physically interacting components (Sheetz & Yu, 2018). For example, the plasma membrane is directly connected to the cytoskeleton (intermediary filaments, microtubules, actin) through membrane-anchoring proteins (Uray & Uray, 2021). The nucleus and chromatin within are also physically linked with the cytoskeleton through LINC complexes, facilitating physical deformation of the nucleus and subsequent changes to chromatin accessibility (van Steensel & Belmont, 2017), import and export of mechanoregulatory factors (Elosegui-Artola et al., 2017), and DNA damage (dos Santos & Toseland, 2021). Within this framework the individual genes regulating specific outcomes

are less important than the processes and principles enabling cell biology overall within which they converge. Genes, like *Bmp2* or *7,* contribute to processes, like osteochondrogenesis, to make evolution reproducible, stable, and adaptable (Hallgrimsson et al., 2014; G. P. Wagner, 1996). While genetic variation at the level of molecular pathways can be overwhelmingly vast, combinations of genes and effects are funnelled into increasingly constricted contributors to development through the limited number of cellular (and increasingly restricted) tissue-level processes. As such, foundational and clinical research should continue to move away from a gene-centric approach, just as the one gene: one enzyme theory has evolved (Strauss, 2016).

Mechanical transduction and the signaling milieu of mechanoresponsive structures are interwoven at several hierarchical layers of inter-regulation. New studies continue to introduce relationships between key developmental gene regulatory networks like Bmp, Fgf, Wnt, and Hh, with an increasing body of work manipulating Yap/Taz in different biological systems (Abuammah et al., 2018; J. M. Collins et al., 2023; da Silva Madaleno et al., 2020; Dupont et al., 2011; Roth, Souter, et al., 2022; Wei et al., 2020). The developing craniofacial complex is an exceptionally dynamic system subject to a multitude of rapidly shifting mechanical stresses and strains, i.e. midface expansion, cranial base growth, mastication, intracranial pressure, suckling, and so on. The effects of these forces on form and function of the skull are well known (Markey & Marshall, 2007). However, there is still a need to unravel the macroscopic anatomical and microscopic cellular connection. The dynamic physical changes to suture morphology provide a suitable system to test and observe the links between tissue-level morphological tuning and cellular mechanical dynamics through osteogenic differentiation and signaling. Similarly, the precise organization of differentiating chondrocytes in the synchondroses of the cranial base readily reveal perturbations to sub-structural cell biology. This thesis benefitted from these features to interpret craniofacial pathology and development of osteochondrogenic growth zones.

7.3 Shared characteristics of these unusual growth zones

In this thesis, I presented several examples of phenotypic variation and pathology across craniofacial growth zones as a result of gene-level changes. Superficially, the

synchondroses and midfacial sutures appear to be independent due to their distinct locations in the skull and mode of osteogenesis. However, each of the structures discussed in this work is related to the others in a number of ways. Most importantly, I believe, is that all are mechanically loaded, dynamic structures. The cranial sutures are viscoelastic structures under tension, compression, and/or torsion, depending on location and developmental stage. The same forces apply to the comparatively less flexible endochondral cranial base, with pressure exerted from the dorsally located brain, masticatory forces, geometric changes to the skull and its mechanical environment, and connection with the spinal column. Mechanical loading can also be intrinsic to the cell through force generation to "feel" the stiffness of the surrounding extracellular matrix or environment. Cell-cell contact can similarly produce a mechanical response. This central theme explains many of their other shared traits: the importance of extracellular matrix (production, organization, composition), morphogenesis and patterning over development (differentiation and behaviour of mechanosensitive progenitors), and shared gene regulatory networks (BMP, FGF, Hh, Wnt, etc.), to name a few.

Cranial sutures and synchondroses are useful as a clear read-out of pathology: the bone or cartilage is or isn't formed, or looks unusual. This visual cue to investigate a certain process may streamline functional analysis of a particular disorder or variant. My work on a pre-clinical model of KBG syndrome, the Ankrd11 neural crest knockout (Ankrd11 ncko) mouse, demonstrated this principle (Roth, Baddam, et al., 2021). KBG syndrome is categorized as a Neurodevelopmental Disorder (NDD), but clinicians have indicated a characteristic craniofacial gestalt as a diagnostic criterion. In our mouse model, we investigated the loss of epigenetic regulator *Ankrd11* with a focus on tangible craniofacial changes leading to the overall phenotype. By looking at osteogenesis and, later, tooth morphogenesis as a readout, we were able to posit new hypotheses regarding *Ankrd11*'s implications in human health. While craniofacial appearance may be one of the most outwardly readily recognizable indicators of genetic variation, not all signs of altered osteochondrogenic function are obvious. In the case of the Bmp7:Gli1-CreERT2 (Bmp7 cko) mice in Chapter 5, my decision to examine the internasal suture at histological resolution was informed by previous Bmp7 ncko nasal septum-internasal suture abutment observations outlined in Chapter 4. The sutures are largely straight and patent in Bmp7 cko

mice, but close examination revealed a hidden change in the abutment which future studies may benefit from exploring. I anticipate that this minor endocranial internasal suture deviation (but not Bmp2 cko mice) may be rooted in impaired mechanoregulatory tuning of osteogenesis upon *Bmp7* deletion, even if only in osteoprogenitors. Thorough histochemical characterization of this region in both mouse lines could reveal further functional differences between BMPs in suture biology. Specifically, it would be informative to query readouts for mechanoregulatory pathways (e.g. Yap, Piezo1, Rock2), assess matrix composition (Fmod, collagens, fibronectin), and cross-analyze other fibrous structures (i.e. mid-palatal suture, periodontal ligament, cranial vault sutures).

Furthermore, familiarity with drivers of normal craniofacial growth zone behaviour and its characteristics enables us to detect sometimes overlooked pathology at a subtle, clinically-relevant scale (Aponte et al., 2021). The genetic models in this thesis are examples of osteogenic structures that are pathologically affected without complete obliteration by bone. These studies have taught me that there is significant value in studying the intact or superficially normal system.

7.4 Patency in sutures

The birth of a cranial suture begins sometime after the craniofacial bones start to expand from nucleating ossification centers, reaching over and around the developing head towards each other. The exact moment at which a previously soft, wide connection between bone can be defined as a suture is up for debate. Has the suture formed when bones are 4 cells apart? When osteoclast-mediated remodeling is detected? Perhaps any change to the extracellular matrix in the location between the ossification center and destination of the suture is sufficient to define its existence. This gap of knowledge complicates the definition of early cranial suture development and establishment. What is less debated is the designation of a synostosed or completely ossified suture. Most cranial sutures fuse or synostose physiologically in humans; in mice, only the posterior frontal suture fuses. The remaining sutures are categorically defined as “patent”. However, depending on the level at which a suture is assessed, this definition could change. A highly interdigitated suture in which the bone has been remodeled so extensively that the fingerlike projections are too numerous to count with the naked eye may be called “fused” in the eyes of an orthodontist

deciding between miniscrew-anchored rapid maxillary expansion and a surgical approach. The same suture, decalcified and sectioned for staining, may be interpreted by a keen histologist as patent due to the presence of bone-lining osteoblasts under microscopy. While there is no question that the skull of a child with congenital craniosynostosis must be corrected, there is room to consider improvement of imprecise terminology when referring to the range of "patent" functional states in suture development.

This thesis does not answer the question of how sutures are established. It does, however, introduce possible elements at play in the early stages of the formation of an abutting suture, as in the mid-palatal suture. Based on my histochemical and transcriptomic analysis undertaken in Chapter 6 comparing the mid-palatal suture with early frontal suture data from G. Holmes et al, it is likely that tenocyte-like mesenchymal cells play a role in advancing osteogenic fronts, especially in abutting sutures. I cannot conclude whether the midline mesenchyme "patency" factors I identified attract the bone, prevent synostosis upon approximation of the bone fronts, or are simply induced upon compression of the mesenchyme as the bone expands. I suspect a combination of these three is involved. However, I can definitively say that the establishing suture is not synostosed and is undergoing active growth.

This description also applies to the early postnatal development of internasal sutures investigated in Chapter 4. Mice undergo a period of rapid midfacial expansion and dimensional changes from birth to about 3 weeks of age. At this time, all of the sutures are canonically patent and are actively facilitating appositional midfacial growth along bone edges. I observed a partial failure to fulfill this task in the case of Bmp7 neural crest knockout (Bmp7 ncko) mice; the bone on one side of the internasal suture was growing while the other was lagging, causing internasal suture deviation. The initial insult in the Bmp7 ncko suture was more complex; we concluded that the phenotype was the magnification of an initial inability to respond to an early asymmetric extrinsic force. But this example of an unfused, yet insufficiently active suture at a critical time brought patency into question again: how many sutures are assessed visually in the clinic or animal models and deemed normal due to the absence of synostosis? These would-be patent sutures could have an intrinsic growth defect preventing functional growth.

There is a third outcome in this line of thinking: sutures which are not fused, are not actively responsible for functional growth, *but could be*. This third example of a healthy patent suture is common in adult rodents, in which long-term unfused sutures are important (White et al., 2021). Mechanical studies have established that repetitive or sustained extrinsic force applied to sutures in adult animals is sufficient to re-activate progenitors and recruit bone-resorbing osteoclasts to remodel the bone and alleviate the perceived stress or strain (reviewed in Chapter 2). However, without extraordinary stimulus, the main task of quiescent sutures is to stay as they are – unfused. This is not necessarily a passive process, as demonstrated in Chapter 5 with conditional deletion of Bmp7 from progenitors in young adult mice. Until the moment of Tamoxifen injection, Bmp7:Gli1-CreERT2 (Bmp7 cko) mice were as normal as their control littermates. However, roughly one month after disruption of the baseline suture microenvironment, Bmp7 cko mice had established endocranial internasal suture malformation. At the time of injection, Bmp7 cko mice had fully developed skulls, defined sutures, and were not undergoing rapid functional growth at sutures. These quiescent patent sutures were still susceptible to dysregulation of the suture signaling environment.

The nuance of suture establishment, functional growth, and quiescence is not captured with the single catch-all term “patency”. While it is useful to simply separate synostosed sutures from those that are not, there is a spectrum of diverse physiological and pathological states which fall under this umbrella which are worthy of investigation. Growth deficiencies, like MFH, are not always characterized by synostosis of midfacial sutures. However, even subtly reduced functional growth at these sites may play an underappreciated role in observable craniofacial differences. This thesis contributes to understanding of the foundational principles underlying coordinated growth zone function, providing further avenues for innovation regarding growth zone hypoplasia or dysmorphology. A great deal is left to be explained about suture patency.

7.5 Conclusions

Midfacial growth is still incompletely understood at a biophysical level. While anatomic contributors are frequently discussed in the literature, the actual molecular mechanisms involved in cell differentiation and behaviour in this geometrically dynamic

space are unclear. In particular, the effects of extracellular mediators of cell differentiation, like matrix stiffness, growth factor production and sequestration, genetic factors, and mechanical environment, are not integrated in the current MFH discourse. My data supports the overarching hypothesis that the reciprocal interactions of these mediators are central in the physiology of contributors to midfacial growth. The nasal bone deviation in Bmp7 ncko mice began as a subtle asymmetry in osteogenic differentiation and mechanical response at birth and, through mechanically-regulated bone remodeling, magnified to severe nasal obstruction. In the cranial base, conditional loss of Bmp2 or Bmp7 affected chondrocyte differentiation with cartilage and bone consequences, including morphogenesis of the sphenoid bone *in utero*. The interaction of pre-osteogenic mesenchymal cells with their physical environment was demonstrated in the developing mid-palatal suture, revealing an additional biomechanical contributor to palatogenesis and expansion of osteogenic centers.

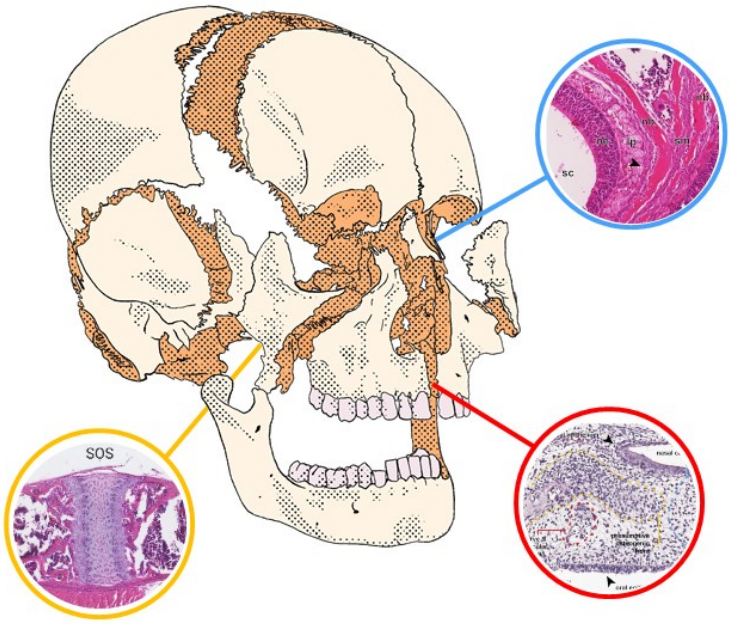

Figure 7.1 Illustration of human skull expanded along craniofacial sutures.
Drawing of an anatomical specimen with craniofacial bones separated along sutures to highlight the numerous planes along which suture appositional growth may occur. Colored circles indicate the general location of the three regions discussed in this thesis in detail: the synchondroses of the cranial base (yellow), mid-palatal suture and its establishment (red), and internasal suture (blue). Illustrated in Procreate by DMR.

At its core, this work is centered around the importance of understanding normal physiology of sutures to enable the clinical translation and interpretation of pathology. Throughout these investigations, I have taken notice of a significant gap in translation between and within disciplines, ranging from clinical phenotype interpretation to long bone physiology, cranial base development, and cranial suture mechanoregulation. There is a clear lapse in both vertical and horizontal communication of findings relating to pathology of mechanosensitive growth zones. The first two chapters of this thesis aimed to bridge these gaps of knowledge at several levels. My review on pathologically widened cranial sutures in Chapter 1 drew high-level connections between basic suture physiology and clinical interpretation of suture-related pathology. Chapter 2 was focused on horizontal translation between models of mechanotransduction in foundational studies for application to cranial sutures, and vice versa. These two studies informed my direction for the data chapters to follow, providing context for the application of my animal model findings in human health and identification of discontinuities in the literature.

This rift is particularly important given the association between growth deficiencies like midface hypoplasia and maxillary insufficiency with syndromic cases of craniosynostosis and orofacial clefting. Several studies have correlated long-term midfacial growth complications with the repair of cleft lip and/or palate, suggesting potential disruption to critical growth zones or yet-unknown coordinating structures (Celie et al., 2024; Naidu et al., 2021; Turri de Castro Ribeiro et al., 2018). Interventions affecting the palatal pseudo-neotendon identified in Chapter 6 of this thesis could be involved in these adverse outcomes. This thesis contains three cautionary tales of intrinsic or induced biological changes which, over time, magnify to severe physiological consequences. Similarly, patients with genetic differences involved in the processes required to facilitate a given treatment may experience greater incidence of adverse effects or reversion of the

intervention. Case reports of failed craniofacial repair or midface advancement, especially in association with other craniofacial differences, are sadly not uncommon (Celie et al., 2024; Cha et al., 2018; Herring et al., 2024; Lacerda & Vieira, 2021). Innate cellular differences likely influence the outcomes of any treatment modalities which take advantage of physiology to correct growth deficiency, including distraction osteogenesis, Le Fort midface hypoplasia correction, suture replacement, CL/P repair, and maxillary expansion. My findings revealed a complexity not previously described *in vivo*. Understanding the precise mechanisms of osteogenesis and cell differentiation is crucial, particularly as regenerative therapies gain traction. Cranial suture research significantly informs current approaches in cell-laden tissue engineering; however, replicating the optimal environment for mesenchymal stem/stromal cell survival and function remains a challenge.

My results challenge the current paradigms of suture patency, midfacial growth, and clinical applications of exogenous factors like Bone Morphogenetic Proteins. In each of these cases, I found that the morphology of midfacial structures was tightly regulated at several levels by spatiotemporally restricted growth factors, extracellular matrix heterogeneity and contribution, and mechanically regulated processes. This data does not support indiscriminate use of BMPs in supraphysiological doses and provides evidence for careful consideration of biophysical contributors to the development of structures involved in midfacial growth and other craniofacial growth deficiencies. I found that the regulation of midfacial growth is more complex than is currently appreciated (summarized in Figure 7.2). Understanding of molecular mechanisms of osteochondrogenesis in craniofacial growth zones must be further developed to fully explain the incidence of midface hypoplasia and its correlation with other craniofacial growth anomalies.

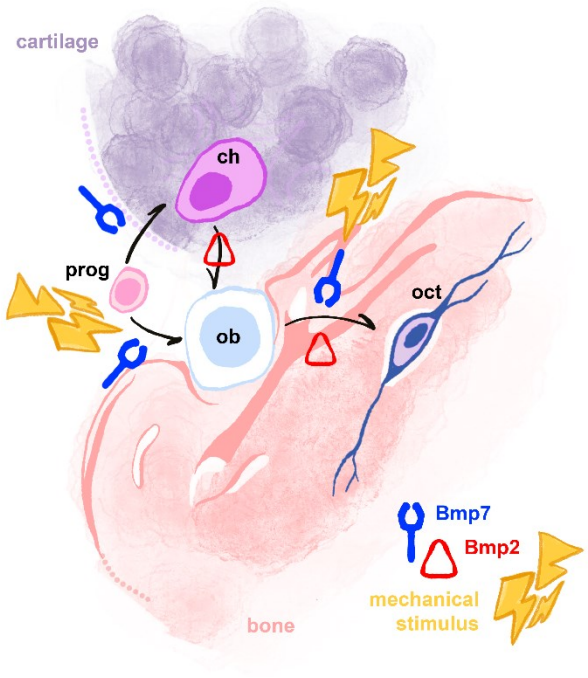

Figure 7.2 BMP signaling in tuning of osteochondrogenic differentiation. Graphic representation of osteochondrodifferentiation from progenitor cells (prog) to chondrocytes (ch) or osteoblasts (ob) and osteocytes (oct). The data in this thesis, spanning several osteochondrogenic growth zones in the skull, supports a framework of fine control of cell differentiation in osteogenesis. Blue icons represent modulation of osteodifferentiation by Bmp7 in response to mechanical stimuli (yellow polygons), including progenitor to osteoblast differentiation and osteoblast to osteocyte maturation. Red icons show stages affected by *Bmp2* knockdown, including chondrocyte to osteoblast transdifferentiation and osteocyte maturation. Illustrated in Procreate by DMR.

7.6 Limitations

This study revealed many novel aspects of suture development and generated a large body of data. However, the breadth of this study and cost limitations did not allow for complete interpretation or follow-up on several of these findings. For example, none of the sequencing experiments in this thesis were conducted in technical triplicate – though each experiment used pooled biological replicate samples. In Chapter 5, the Parse Biosciences sequencing experiment was only done as a pilot study on Bmp2 ncko intersphenoidal synchondroses.

All spatial transcriptomic experiments (Visium, Xenium) were done using wild type mouse sections as they were conducted at the National Institutes of Health. Thus, Figure 4.4 in Chapter 4 is mainly useful for hypothesis generation for theoretical application in Bmp7 ncko mice. Furthermore, Visium expression analysis is limited in condensed structures like the internasal suture due to its low resolution, capturing multi-cell trends rather than sub-cellular transcriptomic profiles. While its power as a whole-transcriptome profiler is evident, a targeted Xenium sub-cellular panel may have been more informative for the internasal suture. This approach would enable comparison of the genetic profiles of the left and right nasal bones beyond my individual RNAscope *in situ* hybridization

experiments. In Chapter 6, multiple planes of sectioning and ages were included for the Xenium mid-palatal suture experiment. However, only one timepoint (e15.5) was used for analysis in this thesis. This small sample size was supported with multimodal data from Visium expression analysis and RNAscope experiments.

In my initial pilot experiments for the Gli1-CreERT2 cranial base story in Chapter 5, I aimed to induce *Bmp2* or *Bmp7* deletion in embryos at e15 and study the effects over late embryogenesis and early postnatal development, beginning at the time of internasal suture formation. Unfortunately, in our hands dams injected with Tamoxifen were highly susceptible to dystocia during birth, which has been previously reported as an adverse effect (Ilchuk et al., 2022). The main study was redesigned to collect e15-injected embryos at e19.5, before birth. Following the establishment of the mouse line, testing injection, and initial characterization, I was only able to collect one litter of Bmp7:Gli1CreERT2 mice from this approach. I did not collect any Bmp2:Gli1CreERT2 embryos. The sphenoid bone morphogenesis portion of the study, shown in Figure 5.4, would be improved with more Bmp7 cko embryos and additional analysis of Bmp2 cko and Bmp2/7 cko mice. This work is ongoing.

For most histological assessments in these studies, at least 3 FFPE sections were analyzed per stain and mouse to account for staining and sectioning artifacts. Some experiments should be repeated to increase sample size as any histological artifacts (such as tears , bubbles, or debris) prevented semi-automated ImageJ quantification according to my current methodology. The cranial base study, however, provided several unique challenges. First, the number of sagittal sections that can be collected from comparable regions of the embryonic cranial base is quite limited due to the small size of the synchondroses at e18.5. Additionally, proper orientation of the block during embedding and sectioning is critical to maximize usable sections and capture the cranial base morphology. This was particularly prohibitive in the postnatal Tamoxifen studies due to the severity of the ISS malformation. I faced significant difficulty in collecting sagittal sections of the cranial base that contained both the ISS and SOS in a single plane. Due to the limited tissue at my disposal and sectioning challenges, I opted to focus on the SOS for this thesis in histochemical analysis. The ISS was also analyzed in neighbouring sections,

but not to sufficient n values for inclusion in this study. All CT scan analyses were performed for both synchondroses.

A limitation shared between the studies in this thesis is the lack of separation between cause and consequence. We characterized phenotypes like the Bmp7 ncko internasal suture early to track the development of deviation and loss of osteoblasts but did not definitively isolate these effects from early programming changes to cells or coincident effects. In the cranial base study, all histochemical analysis was done at the end-point; to separate these effects, it would be important to additionally section early and mid-stage skulls from the experiment. Our identification of the tendon-like mesenchymal cells in the developing palate reveals a structural heterogeneity amongst mesenchymal cells and implies an ECM-modulatory element to mid-palatal suturogenesis but could not be proven as such. We did not determine whether the mesenchymal cells form on a tendon-like matrix scaffold and adopt the fate, generate it, align along force gradients in the tissue, or if their behaviour reflects some combination of these possibilities. Based on my results, I predict that bidirectional feedback between cells and their environment shapes the structure and signaling milieu in all of these examples.

7.7 Future implications

The work in this thesis generated many new hypotheses related to craniofacial growth zones and mechanoregulation of osteochondrogenic cell biology. For example, my data supports further study of causes and etiology of the cranial base morphological differences due to deletion of different Bone Morphogenetic Proteins. One approach may be to continue sequencing the synchondroses from all combinations of BMP variants presented in our CT scan analysis to identify candidates for disrupted genes shared by Bmp7 mutant mice leading to basisphenoid notches or holes that are not seen in Bmp2 ncko mice. Similarly, which genes are associated with fragmentation of the basisphenoid bone in the absence of a notch, as seen in Bmp2 mutant mice? These high-throughput techniques, while cost-prohibitive during my studies, would enable curation of a targeted RNAscope of Xenium probe panel to spatially contextualize variable genes across development and between genetic models.

Another intriguing direction to pursue following this work is the pseudoneotendon (PNT) in the developing mid-palatal suture. I collected data for multiple ages in this region and several planes of sectioning but limited my analysis and presentation in this study to e15.5 in the middle of the palate. It would be prudent to continue this analysis for other ages and regions to build a complete picture of the extracellular matrix composition and behavior of the PNT over time. Given my observations of the similarities between the mid-palatal suture and other craniofacial sutures, this study should be extended to include high resolution spatial transcriptomic analysis (or, at least, multiplex probe hybridization) of the same genes in other sutures. Ideally, the Xenium experiment designed for Chapter 6 would be applied to cranial sutures like the internasal suture, zygomatic-maxillary suture, and frontal suture, to name a few. I did not have the opportunity to conduct any intervention experiments for the work presented in Chapter 6, but a fascinating direction would be to disrupt one or more of the components involved in the PNT-midline mesenchyme interface at different ages. For example, inhibition of collagen crosslinking with an agent like BAPN or genetic knockdown of *Pax9* (enriched in the midline) at different ages conditionally would further shed light on the involvement of these hypothesized regulators of suture establishment. An interesting genetic model would be conditional deletion of a mechanotransducive element like *Yap* in *Pax9*^{pos} cells to reduce responsiveness of the midline mesenchyme to mechanical stimuli. I predict that this condition may yield a disorganized PNT, which could manifest as a broad osteogenic insufficiency due to impaired force conduction or sensation. Alternatively, the inability of *Pax9*-expressing cells to transduce mechanical signals could result in fusion or synostosis of sutures. The timing of intervention would likely be an important variable in design of this study.

This thesis explored concepts in cell regulation in mechanically loaded craniofacial tissue through the lens of bone and osteochondrodifferentiation. An interesting axis for translation of these concepts that has emerged as I contextualize my findings is the series of events in cancer metastasis to bone (M. Wang et al., 2020). First, tumor cells travel to the site of metastasis. The cells must then extravasate, or squeeze through, the walls of the blood vessel to reach the target tissue. This stage involves diverse mechanical stresses on the cell both in exiting the blood vessel and encountering the new extracellular matrix environment. It has been hypothesized that these mechanical signals contribute to the

ability of cancer to metastasize and tune its environment for survival (V. Kumar et al., 2024). Furthermore, they may partially explain the tendency of prostate cancer to preferentially metastasize to bone sites (Langley & Fidler, 2011). Development of anti-metastatic therapies is rapidly evolving, and further advances depend on a fundamental understanding of cell biology at interfaces between bone and variable extracellular matrix composition. In many ways, the establishment of a bone-tumor microenvironment is similar to embryonic development of osteogenic centers and sutures (Ben-Porath et al., 2008). In particular, the work described in Chapter 6 could prove to be a useful platform on which to build further translational connections, especially based on the local microenvironment surrounding newly formed bone.

Future studies should closely consider the success of biology-driven treatments in relation to genetics of patients, especially with the aid of personalized medicine. Innovation on this front will depend on enthusiastic cooperation, collaboration, and creativity. Many of the principles discussed in this thesis are key in non-mineralized organ systems and cancer biology, especially the relationship between mechanoregulation and cell differentiation. With inspiration from physiology and pathology, challenging the limitations of current dogma provides new opportunities to improve and innovate for meaningful impact in human health.

REFERENCES

Abuammah, A., Maimari, N., Towhidi, L., Frueh, J., Chooi, K. Y., Warboys, C., & Krams, R. (2018). New developments in mechanotransduction: Cross talk of the Wnt, TGF-β and Notch signalling pathways in reaction to shear stress. *Current Opinion in Biomedical Engineering*, *5*, 96–104. https://doi.org/10.1016/j.cobme.2018.03.003

Ahn, S., & Joyner, A. L. (2004). Dynamic Changes in the Response of Cells to Positive Hedgehog Signaling during Mouse Limb Patterning. *Cell*, *118*(4), 505–516. https://doi.org/10.1016/j.cell.2004.07.023

Alamer, O. B., Jimenez, A. E., & Azad, T. D. (2021). Single-suture craniosynostosis and the epigenome: Current evidence and a review of epigenetic principles. *Neurosurgical Focus*, *50*(4), E10. https://doi.org/10.3171/2021.1.FOCUS201008

Albiol, L., Büttner, A., Pflanz, D., Mikolajewicz, N., Birkhold, A. I., Kramer, I., Kneissel, M., Duda, G. N., Checa, S., & Willie, B. M. (2020). Effects of Long-Term Sclerostin Deficiency on Trabecular Bone Mass and Adaption to Limb Loading Differ in Male and Female Mice. *Calcified Tissue International*, *106*(4), 415–430. https://doi.org/10.1007/s00223-019-00648-4

Alblowi, J., Kayal, R. A., Siqueria, M., McKenzie, E., Krothapalli, N., McLean, J., Conn, J., Nikolajczyk, B., Einhorn, T. A., Gerstenfeld, L., & Graves, D. T. (2009). High Levels of Tumor Necrosis Factor-α Contribute to Accelerated Loss of Cartilage in Diabetic Fracture Healing. *The American Journal of Pathology*, *175*(4), 1574–1585. https://doi.org/10.2353/ajpath.2009.090148

Alquicira-Hernandez, J., & Powell, J. E. (2021). Nebulosa recovers single-cell gene expression signals by kernel density estimation. *Bioinformatics*, *37*(16), 2485–2487. https://doi.org/10.1093/bioinformatics/btab003

Al-Rekabi, Z., Cunningham, M. L., & Sniadecki, N. J. (2017). Cell Mechanics of Craniosynostosis. *ACS Biomaterials Science & Engineering*, *3*(11), 2733–2743. https://doi.org/10.1021/acsbiomaterials.6b00557

Al-Rekabi, Z., Wheeler, M. M., Leonard, A., Fura, A. M., Juhlin, I., Frazar, C., Smith, J. D., Park, S. S., Gustafson, J. A., Clarke, C. M., Cunningham, M. L., & Sniadecki, N. J. (2016). Activation of the IGF1 pathway mediates changes in cellular contractility and motility in single-suture craniosynostosis. *Journal of Cell Science*, *129*(3), 483–491. https://doi.org/10.1242/jcs.175976

Alves-Afonso, D., Ryan, A. Q., Lahola-Chomiak, A., Prakash, M., Jug, F., Modes, C. D., & Tabler, J. M. (2021). *Tissue scale properties of the extracellular matrix regulates nuclear shape, organisation and fate in the embryonic midline sutures* (p. 2021.09.03.458867). bioRxiv. https://doi.org/10.1101/2021.09.03.458867

Ambrosi, T. H., Longaker, M. T., & Chan, C. K. F. (2019). A Revised Perspective of Skeletal Stem Cell Biology. *Frontiers in Cell and Developmental Biology*, *7*. https://doi.org/10.3389/fcell.2019.00189

An, Y. H., Moreira, P. L., Kang, Q. K., & Gruber, H. E. (2003). Principles of Embedding and Common Protocols. In Y. H. An & K. L. Martin (Eds.), *Handbook of Histology Methods for Bone and Cartilage* (pp. 185–197). Humana Press. https://doi.org/10.1007/978-1-59259-417-7_11

Andrade, F., Howell, L., Percival, C. J., Richtsmeier, J. T., Marcucio, R. S., Hallgrímsson, B., & Cheverud, J. M. (2024). Genetic architecture of trait variance in craniofacial morphology. *Genetics*, *226*(4), iyae028. https://doi.org/10.1093/genetics/iyae028

Andrew, T. W., Koepke, L. S., Wang, Y., Lopez, M., Steininger, H., Struck, D., Boyko, T., Ambrosi, T. H., Tong, X., Sun, Y., Gulati, G. S., Murphy, M. P., Marecic, O., Telvin, R., Schallmoser, K., Strunk, D., Seita, J., Goodman, S. B., Yang, F., … Chan, C. K. F. (2022). Sexually dimorphic estrogen sensing in skeletal stem cells controls skeletal regeneration. *Nature Communications*, *13*, 6491. https://doi.org/10.1038/s41467-022-34063-5

Anvarian, Z., Mykytyn, K., Mukhopadhyay, S., Pedersen, L. B., & Christensen, S. T. (2019). Cellular signalling by primary cilia in development, organ function and disease. *Nature Reviews. Nephrology*, *15*(4), 199–219. https://doi.org/10.1038/s41581-019-0116-9

Aponte, J. D., Katz, D. C., Roth, D. M., Vidal Garcia, M., Liu, W., Andrade, F., Roseman, C. C., Murray, S. A., Cheverud, J., Graf, D., Marcucio, R. S., & Hallgrimsson, B. (2021). Relating multivariate shapes to genescapes using phenotype-biological process associations for craniofacial shape. *eLife*, *10*, e68623. https://doi.org/10.7554/eLife.68623

Appelman-Dijkstra, N. M., & Papapoulos, S. E. (2016). From disease to treatment: From rare skeletal disorders to treatments for osteoporosis. *Endocrine*, *52*, 414–426. https://doi.org/10.1007/s12020-016-0888-7

Aragona, M., Panciera, T., Manfrin, A., Giulitti, S., Michielin, F., Elvassore, N., Dupont, S., & Piccolo, S. (2013). A mechanical checkpoint controls multicellular growth through YAP/TAZ regulation by actin-processing factors. *Cell*, *154*(5), 1047–1059. https://doi.org/10.1016/j.cell.2013.07.042

Aryaei, A., & Jayasuriya, A. C. (2015). The effect of oscillatory mechanical stimulation on osteoblast attachment and proliferation. *Materials Science & Engineering. C, Materials for Biological Applications*, *52*, 129–134. https://doi.org/10.1016/j.msec.2015.03.024

Astudillo, P. (2020). Extracellular matrix stiffness and Wnt/β-catenin signaling in physiology and disease. *Biochemical Society Transactions*, *48*(3), 1187–1198. https://doi.org/10.1042/BST20200026

Azzolin, L., Panciera, T., Soligo, S., Enzo, E., Bicciato, S., Dupont, S., Bresolin, S., Frasson, C., Basso, G., Guzzardo, V., Fassina, A., Cordenonsi, M., & Piccolo, S. (2014). YAP/TAZ incorporation in the β-catenin destruction complex orchestrates the Wnt response. *Cell*, *158*(1), 157–170. https://doi.org/10.1016/j.cell.2014.06.013

Baddam, P., Biancardi, V., Roth, D. M., Eaton, F., Thereza-Bussolaro, C., Mandal, R., Wishart, D. S., Barr, A., MacLean, J., Flores-Mir, C., Pagliardini, S., & Graf, D. (2021). Neural crest-specific loss of Bmp7 leads to midfacial hypoplasia, nasal airway obstruction and disordered breathing, modeling obstructive sleep apnea. *Disease Models & Mechanisms*, *14*(2), dmm047738. https://doi.org/10.1242/dmm.047738

Baddam, P., Young, D., Dunsmore, G., Nie, C., Eaton, F., Elahi, S., Jovel, J., Adesida, A. B., Dufour, A., & Graf, D. (2021). Nasal Septum Deviation as the Consequence of BMP-Controlled Changes to Cartilage Properties. *Frontiers in Cell and Developmental Biology*, *9*, 696545. https://doi.org/10.3389/fcell.2021.696545

Baek, R.-M., & Song, Y.-T. (2006). Overgrowth of a costochondral graft in reconstruction of the temporomandibular joint. *Scandinavian Journal of Plastic and Reconstructive Surgery and Hand Surgery*, *40*(3), 179–185. https://doi.org/10.1080/02844310600763725

Bai, S., Shi, X., Yang, X., & Cao, X. (2000). Smad6 as a Transcriptional Corepressor. *Journal of Biological Chemistry*, *275*(12), 8267–8270. https://doi.org/10.1074/jbc.275.12.8267

Baker, A. H., & Péault, B. (2016). A Gli(1)ttering Role for Perivascular Stem Cells in Blood Vessel Remodeling. *Cell Stem Cell*, *19*(5), 563–565. https://doi.org/10.1016/j.stem.2016.10.011

Baker, N. L., Mörgelin, M., Peat, R., Goemans, N., North, K. N., Bateman, J. F., & Lamandé, S. R. (2005). Dominant collagen VI mutations are a common cause of Ullrich congenital muscular dystrophy. *Human Molecular Genetics*, *14*(2), 279–293. https://doi.org/10.1093/hmg/ddi025

Bala, K., Cuellar, A., Herren, A. W., & Boyadjiev, S. A. (2021). Identification of differentially expressed proteins between fused and open sutures in sagittal nonsyndromic craniosynostosis during suture development by quantitative proteomic analysis. *Proteomics. Clinical Applications*, *15*(2–3), e2000031. https://doi.org/10.1002/prca.202000031

Baldwin, M. C., Zarudnaya, D., Liu, Z.-J., & Herring, S. W. (2023). The nasal septum and midfacial growth. *The Anatomical Record*. https://doi.org/10.1002/ar.25214

Balemans, W., & Van Hul, W. (2007). The genetics of low-density lipoprotein receptor-related protein 5 in bone: A story of extremes. *Endocrinology*, *148*(6), 2622–2629. https://doi.org/10.1210/en.2006-1352

Bancroft, J. D., & Layton, C. (2019). 12—Connective and other mesenchymal tissues with their stains. In S. K. Suvarna, C. Layton, & J. D. Bancroft (Eds.), *Bancroft's Theory and Practice of Histological Techniques (Eighth Edition)* (pp. 153–175). Elsevier. https://doi.org/10.1016/B978-0-7020-6864-5.00012-8

Barberini, F., Bruner, E., Cartolari, R., Franchitto, G., Heyn, R., Ricci, F., & Manzi, G. (2008). An unusually-wide human bregmatic Wormian bone: Anatomy, tomographic description, and possible significance. *Surgical and Radiologic Anatomy*, *30*(8), 683. https://doi.org/10.1007/s00276-008-0371-0

Barrallo-Gimeno, A., & Nieto, M. A. (2006). Evolution of the Neural Crest. In J.-P. Saint-Jeannet (Ed.), *Neural Crest Induction and Differentiation* (pp. 235–244). Springer US. https://doi.org/10.1007/978-0-387-46954-6_15

Barreto, S., González-Vázquez, A., Cameron, A. R., O'Brien, F. J., & Murray, D. J. (2017). Identification of stiffness-induced signalling mechanisms in cells from patent and fused sutures associated with craniosynostosis. *Scientific Reports*, *7*(1), 1–12. https://doi.org/10.1038/s41598-017-11801-0

Basalom, S., & Rauch, F. (2020). Bone Disease in Patients with Ehlers-Danlos Syndromes. *Current Osteoporosis Reports*, *18*(2), 95–102. https://doi.org/10.1007/s11914-020-00568-5

Basel-Vanagaite, L., Kornreich, L., Schiller, O., Yacobovich, J., & Merlob, P. (2008). Yunis–Varon syndrome: Further delineation of the phenotype. *American Journal*

of Medical Genetics Part A, *146A*(4), 532–537. https://doi.org/10.1002/ajmg.a.32135

Basten, S. G., & Giles, R. H. (2013). Functional aspects of primary cilia in signaling, cell cycle and tumorigenesis. *Cilia*, *2*(1), 6. https://doi.org/10.1186/2046-2530-2-6

Baulac, S., Lenk, G. M., Dufresnois, B., Bencheikh, B. O. A., Couarch, P., Renard, J., Larson, P. A., Ferguson, C. J., Noé, E., Poirier, K., Hubans, C., Ferreira, S., Guerrini, R., Ouazzani, R., Hachimi, K. H. E., Meisler, M. H., & Leguern, E. (2014). Role of the phosphoinositide phosphatase FIG4 gene in familial epilepsy with polymicrogyria. *Neurology*, *82*(12), 1068–1075. https://doi.org/10.1212/WNL.0000000000000241

Behr, B., Longaker, M. T., & Quarto, N. (2011). Craniosynostosis of Coronal Suture in Twist1+/− Mice Occurs Through Endochondral Ossification Recapitulating the Physiological Closure of Posterior Frontal Suture. *Frontiers in Physiology*, *2*, 37. https://doi.org/10.3389/fphys.2011.00037

Behr, B., Longaker, M. T., & Quarto, N. (2013). Absence of Endochondral Ossification and Craniosynostosis in Posterior Frontal Cranial Sutures of Axin2−/− Mice. *PLOS ONE*, *8*(8), e70240. https://doi.org/10.1371/journal.pone.0070240

Bemmels, H., Biesecker, B., Schmidt, J. L., Krokosky, A., Guidotti, R., & Sutton, E. J. (2013). Psychological and Social Factors in Undergoing Reconstructive Surgery Among Individuals With Craniofacial Conditions: An Exploratory Study. *The Cleft Palate-Craniofacial Journal : Official Publication of the American Cleft Palate-Craniofacial Association*, *50*(2), 158–167. https://doi.org/10.1597/11-127

Ben-Porath, I., Thomson, M. W., Carey, V. J., Ge, R., Bell, G. W., Regev, A., & Weinberg, R. A. (2008). An embryonic stem cell-like gene expression signature in poorly differentiated aggressive human tumors. *Nature Genetics*, *40*(5), 499–507. https://doi.org/10.1038/ng.127

Bharadwaj, R., Cunningham, K. M., Zhang, K., & Lloyd, T. E. (2016). FIG4 regulates lysosome membrane homeostasis independent of phosphatase function. *Human Molecular Genetics*, *25*(4), 681–692. https://doi.org/10.1093/hmg/ddv505

Bialy, I. E., Jiskoot, W., & Nejadnik, M. R. (2017). Formulation, Delivery and Stability of Bone Morphogenetic Proteins for Effective Bone Regeneration. *Pharmaceutical Research*, *34*(6), 1152. https://doi.org/10.1007/s11095-017-2147-x

Blanco-Carmona, E. (2022). *Generating publication ready visualizations for Single Cell transcriptomics using SCpubr* (p. 2022.02.28.482303). bioRxiv. https://doi.org/10.1101/2022.02.28.482303

BMP-2 Evaluation in Surgery for Tibial Trauma (BESTT) Study Group, Govender, S., Csimma, C., Genant, H. K., Valentin-Opran, A., Amit, Y., Arbel, R., Aro, H., Atar, D., Bishay, M., Börner, M. G., Chiron, P., Choong, P., Cinats, J., Courtenay, B., Feibel, R., Geulette, B., Gravel, C., Haas, N., … Wisniewski, T. (2002). Recombinant Human Bone Morphogenetic Protein-2 for Treatment of Open Tibial Fractures: A Prospective, Controlled, Randomized Study of Four Hundred and Fifty Patients. *JBJS*, *84*(12), 2123.

Bok, S., Yallowitz, A. R., Sun, J., McCormick, J., Cung, M., Hu, L., Lalani, S., Li, Z., Sosa, B. R., Baumgartner, T., Byrne, P., Zhang, T., Morse, K. W., Mohamed, F. F., Ge, C., Franceschi, R. T., Cowling, R. T., Greenberg, B. H., Pisapia, D. J., …

Greenblatt, M. B. (2023). A multi-stem cell basis for craniosynostosis and calvarial mineralization. *Nature*, *621*(7980), 804–812. https://doi.org/10.1038/s41586-023-06526-2

Boran, P., Oğuz, F., Furman, A., & Sakarya, S. (2018). Evaluation of fontanel size variation and closure time in children followed up from birth to 24 months. *Journal of Neurosurgery: Pediatrics*, *22*(3), 323–329. https://doi.org/10.3171/2018.3.PEDS17675

Borgiani, E., Duda, G. N., Willie, B. M., & Checa, S. (2021). Bone morphogenetic protein 2-induced cellular chemotaxis drives tissue patterning during critical-sized bone defect healing: An in silico study. *Biomechanics and Modeling in Mechanobiology*, *20*(4), 1627–1644. https://doi.org/10.1007/s10237-021-01466-0

Bouchard, A. L., Dsouza, C., Julien, C., Rummler, M., Gaumond, M.-H., Cermakian, N., & Willie, B. M. (2022). Bone adaptation to mechanical loading in mice is affected by circadian rhythms. *Bone*, *154*, 116218. https://doi.org/10.1016/j.bone.2021.116218

Bourgeois, P., Bolcato-Bellemin, A.-L., Danse, J.-M., Bloch-Zupan, A., Yoshiba, K., Stoetzel, C., & Perrin-Schmitt, F. (1998). The Variable Expressivity and Incomplete Penetrance of the twist-Null Heterozygous Mouse Phenotype Resemble Those of Human Saethre-Chotzen Syndrome. *Human Molecular Genetics*, *7*(6), 945–957. https://doi.org/10.1093/hmg/7.6.945

Boyle, E. I., Weng, S., Gollub, J., Jin, H., Botstein, D., Cherry, J. M., & Sherlock, G. (2004). GO::TermFinder—Open source software for accessing Gene Ontology information and finding significantly enriched Gene Ontology terms associated

with a list of genes. *Bioinformatics (Oxford, England)*, *20*(18), 3710–3715. https://doi.org/10.1093/bioinformatics/bth456

Buchanan, E., Xue, Y., Xue, A., Olshinka, A., & Lam, S. (2017). Multidisciplinary care of craniosynostosis. *Journal of Multidisciplinary Healthcare*, *Volume 10*, 263–270. https://doi.org/10.2147/JMDH.S100248

Bush, J. O., & Jiang, R. (2012). Palatogenesis: Morphogenetic and molecular mechanisms of secondary palate development. *Development*, *139*(2), 231–243. https://doi.org/10.1242/dev.067082

Byron, C. D., Borke, J., Yu, J., Pashley, D., Wingard, C. J., & Hamrick, M. (2004). Effects of increased muscle mass on mouse sagittal suture morphology and mechanics. *The Anatomical Record. Part A, Discoveries in Molecular, Cellular, and Evolutionary Biology*, *279*(1), 676–684. https://doi.org/10.1002/ar.a.20055

Byun, M. R., Hwang, J.-H., Kim, A. R., Kim, K. M., Hwang, E. S., Yaffe, M. B., & Hong, J.-H. (2014). Canonical Wnt signalling activates TAZ through PP1A during osteogenic differentiation. *Cell Death & Differentiation*, *21*(6), Article 6. https://doi.org/10.1038/cdd.2014.8

Cai, G., Nguyen, A., Bashirzadeh, Y., Lin, S.-S., Bi, D., & Liu, A. P. (2022). Compressive stress drives adhesion-dependent unjamming transitions in breast cancer cell migration. *Frontiers in Cell and Developmental Biology*, *10*. https://doi.org/10.3389/fcell.2022.933042

Calandrelli, R., Pilato, F., D'Apolito, G., Panfili, M., & Colosimo, C. (2021). Normal Growth of the Sutures of the Skull. In M. Turgut, R. S. Tubbs, A. T. Turgut, & A. S. Dumont (Eds.), *The Sutures of the Skull: Anatomy, Embryology, Imaging, and*

Surgery (pp. 77–96). Springer International Publishing. https://doi.org/10.1007/978-3-030-72338-5_7

Calandrelli, R., Pilato, F., Massimi, L., D'Apolito, G., & Colosimo, C. (2023). Facial skeleton dysmorphology in syndromic craniosynostosis: Differences between FGFR2 and no-FGFR2-related syndromes and relationship with skull base and facial sutural patterns. *Child's Nervous System: ChNS: Official Journal of the International Society for Pediatric Neurosurgery*, *39*(11), 3235–3247. https://doi.org/10.1007/s00381-023-05962-9

Campeau, P. M., Lenk, G. M., Lu, J. T., Bae, Y., Burrage, L., Turnpenny, P., Román Corona-Rivera, J., Morandi, L., Mora, M., Reutter, H., Vulto-van Silfhout, A. T., Faivre, L., Haan, E., Gibbs, R. A., Meisler, M. H., & Lee, B. H. (2013). Yunis-Varón Syndrome Is Caused by Mutations in FIG4, Encoding a Phosphoinositide Phosphatase. *American Journal of Human Genetics*, *92*(5), 781–791. https://doi.org/10.1016/j.ajhg.2013.03.020

Cao, X., Lenk, G. M., & Meisler, M. H. (2023). Altered phenotypes due to genetic interaction between the mouse phosphoinositide biosynthesis genes Fig4 and Pip4k2c. *G3 Genes|Genomes|Genetics*, jkad007. https://doi.org/10.1093/g3journal/jkad007

Carinci, P., Becchetti, E., & Bodo, M. (2000). Role of the extracellular matrix and growth factors in skull morphogenesis and in the pathogenesis of craniosynostosis. *The International Journal of Developmental Biology*, *44*(6), 715–723.

Caron, M. M. J., Emans, P. J., Cremers, A., Surtel, D. A. M., Coolsen, M. M. E., van Rhijn, L. W., & Welting, T. J. M. (2013). Hypertrophic differentiation during

chondrogenic differentiation of progenitor cells is stimulated by BMP-2 but suppressed by BMP-7. *Osteoarthritis and Cartilage*, *21*(4), 604–613. https://doi.org/10.1016/j.joca.2013.01.009

Carter, D. R., Beaupré, G. S., Giori, N. J., & Helms, J. A. (1998). Mechanobiology of skeletal regeneration. *Clinical Orthopaedics and Related Research*, *355 Suppl*, S41-55. https://doi.org/10.1097/00003086-199810001-00006

Carthew, J., Abdelmaksoud, H. H., Hodgson-Garms, M., Aslanoglou, S., Ghavamian, S., Elnathan, R., Spatz, J. P., Brugger, J., Thissen, H., Voelcker, N. H., Cadarso, V. J., & Frith, J. E. (2021). Precision Surface Microtopography Regulates Cell Fate via Changes to Actomyosin Contractility and Nuclear Architecture. *Advanced Science (Weinheim, Baden-Wurttemberg, Germany)*, *8*(6), 2003186. https://doi.org/10.1002/advs.202003186

Cedars, M. G., Linck, D. L., Chin, M., & Toth, B. A. (1999). Advancement of the midface using distraction techniques. *Plastic and Reconstructive Surgery*, *103*(2), 429–441. https://doi.org/10.1097/00006534-199902000-00010

Celie, K.-B., Wlodarczyk, J., Naidu, P., Tapia, M. F., Nagengast, E., Yao, C., & Magee, W. (2024). Sagittal Growth Restriction of the Midface Following Isolated Cleft Lip Repair: A Systematic Review and Meta-Analysis. *The Cleft Palate-Craniofacial Journal: Official Publication of the American Cleft Palate-Craniofacial Association*, *61*(1), 20–32. https://doi.org/10.1177/10556656221116005

Cha, B. K., Choi, D. S., Jang, I. S., Yook, H. T., Lee, S. Y., Lee, S. S., & Lee, S. K. (2018). Aberrant growth of the anterior cranial base relevant to severe midface hypoplasia

of Apert syndrome. *Maxillofacial Plastic and Reconstructive Surgery*, *40*(1), 40. https://doi.org/10.1186/s40902-018-0179-8

Chaisrisawadisuk, S., Constantine, S., Lottering, N., Moore, M. H., & Anderson, P. J. (2021). Incidence of persistent metopic suture in Australia: Findings from 1034 three-dimensional computed tomography scans. *Child's Nervous System: ChNS: Official Journal of the International Society for Pediatric Neurosurgery*. https://doi.org/10.1007/s00381-021-05313-6

Chan, C. K. F., Gulati, G. S., Sinha, R., Tompkins, J. V., Lopez, M., Carter, A. C., Ransom, R. C., Reinisch, A., Wearda, T., Murphy, M., Brewer, R. E., Koepke, L. S., Marecic, O., Manjunath, A., Seo, E. Y., Leavitt, T., Lu, W.-J., Nguyen, A., Conley, S. D., … Longaker, M. T. (2018). Identification of the Human Skeletal Stem Cell. *Cell*, *175*(1), 43-56.e21. https://doi.org/10.1016/j.cell.2018.07.029

Chan, C. K. F., Seo, E. Y., Chen, J. Y., Lo, D., McArdle, A., Sinha, R., Tevlin, R., Seita, J., Vincent-Tompkins, J., Wearda, T., Lu, W.-J., Senarath-Yapa, K., Chung, M. T., Marecic, O., Tran, M., Yan, K. S., Upton, R., Walmsley, G. G., Lee, A. S., … Longaker, M. T. (2015). Identification and specification of the mouse skeletal stem cell. *Cell*, *160*(1–2), 285–298. https://doi.org/10.1016/j.cell.2014.12.002

Chappard, D., Alexandre, C., & Riffat, G. (1983). Histochemical identification of osteoclasts. Review of current methods and reappraisal of a simple procedure for routine diagnosis on undecalcified human iliac bone biopsies. *Basic and Applied Histochemistry*, *27*(2), 75–85.

Chen, F., Bi, D., Cheng, C., Ma, S., Liu, Y., & Cheng, K. (2019). Bone morphogenetic protein 7 enhances the osteogenic differentiation of human dermal-derived

CD105+ fibroblast cells through the Smad and MAPK pathways. *International Journal of Molecular Medicine*, *43*(1), 37–46. https://doi.org/10.3892/ijmm.2018.3938

Chen, G., Deng, C., & Li, Y.-P. (2012). TGF-β and BMP Signaling in Osteoblast Differentiation and Bone Formation. *International Journal of Biological Sciences*, *8*(2), 272–288. https://doi.org/10.7150/ijbs.2929

Chen, K. G., Johnson, K. R., McKay, R. D. G., & Robey, P. G. (2018). Conceptualizing Paralogous Stem-Cell Niches and Unfolding Bone Marrow Progenitor Cell Identities. *Stem Cells (Dayton, Ohio)*, *36*(1), 11–21. https://doi.org/10.1002/stem.2711

Chen, L., Li, D., Li, C., Engel, A., & Deng, C.-X. (2003). A Ser250Trp substitution in mouse fibroblast growth factor receptor 2 (Fgfr2) results in craniosynostosis. *Bone*, *33*(2), 169–178. https://doi.org/10.1016/S8756-3282(03)00222-9

Chen, M., Li, Y., Huang, X., Gu, Y., Li, S., Yin, P., Zhang, L., & Tang, P. (2021). Skeleton-vasculature chain reaction: A novel insight into the mystery of homeostasis. *Bone Research*, *9*(1), 1–20. https://doi.org/10.1038/s41413-021-00138-0

Chen, Q., Shou, P., Zheng, C., Jiang, M., Cao, G., Yang, Q., Cao, J., Xie, N., Velletri, T., Zhang, X., Xu, C., Zhang, L., Yang, H., Hou, J., Wang, Y., & Shi, Y. (2016). Fate decision of mesenchymal stem cells: Adipocytes or osteoblasts? *Cell Death & Differentiation*, *23*(7), 1128–1139. https://doi.org/10.1038/cdd.2015.168

Chen, Z., Zhang, Y., Zhao, F., Yin, C., Yang, C., Huai, Y., Liang, S., Liu, S., Xu, X., Wu, Z., Tian, Y., Li, Y., Hu, L., & Qian, A. (2021). miR-138-5p negatively regulates osteoblast differentiation through inhibiting β-catenin under simulated

microgravity in MC3T3-E1 cells. *Acta Astronautica*, *182*, 240–250. https://doi.org/10.1016/j.actaastro.2021.01.052

Chenard, K. E., Teven, C. M., He, T.-C., & Reid, R. R. (2012). Bone morphogenetic proteins in craniofacial surgery: Current techniques, clinical experiences, and the future of personalized stem cell therapy. *Journal of Biomedicine & Biotechnology*, *2012*, 601549. https://doi.org/10.1155/2012/601549

Cheng, S. S. W., Chan, P. K. J., Luk, H.-M., Mok, M. T.-S., & Lo, I. F. M. (2021). Adult Chinese twins with Kenny-Caffey syndrome type 2: A potential age-dependent phenotype and review of literature. *American Journal of Medical Genetics. Part A*, *185*(2), 636–646. https://doi.org/10.1002/ajmg.a.61991

Chirathivat, S., & Post, M. J. (1980). CT demonstration of dural metastases in neuroblastoma. *Journal of Computer Assisted Tomography*, *4*(3), 316–319. https://doi.org/10.1097/00004728-198006000-00005

Christensen, S. T., Clement, C. A., Satir, P., & Pedersen, L. B. (2012). Primary cilia and coordination of receptor tyrosine kinase (RTK) signalling. *The Journal of Pathology*, *226*(2), 172–184. https://doi.org/10.1002/path.3004

Cisarova, K., Garavelli, L., Caraffi, S. G., Peluso, F., Valeri, L., Gargano, G., Gavioli, S., Trimarchi, G., Neri, A., Campos-Xavier, B., & Superti-Furga, A. (2022). A monoallelic SEC23A variant E599K associated with cranio-lenticulo-sutural dysplasia. *American Journal of Medical Genetics. Part A*, *188*(1), 319–325. https://doi.org/10.1002/ajmg.a.62506

Citro, V., Clerici, M., Boccaccini, A. R., Della Porta, G., Maffulli, N., & Forsyth, N. R. (2023). Tendon tissue engineering: An overview of biologics to promote tendon

healing and repair. *Journal of Tissue Engineering*, *14*, 20417314231196275. https://doi.org/10.1177/20417314231196275

Clarkin, C., & Olsen, B. R. (2010). On Bone-forming Cells and Blood Vessels In Bone Development. *Cell Metabolism*, *12*(4), 314. https://doi.org/10.1016/j.cmet.2010.09.009

Collins, J. M., Lang, A., Parisi, C., Moharrer, Y., Nijsure, M. P., Kim, J. H. (Thomas), Szeto, G. L., Qin, L., Gottardi, R. L., Dyment, N. A., Nowlan, N. C., & Boerckel, J. D. (2023). YAP and TAZ couple osteoblast precursor mobilization to angiogenesis and mechanoregulated bone development. *bioRxiv*, 2023.01.20.524918. https://doi.org/10.1101/2023.01.20.524918

Collins, M. T., Marcucci, G., Anders, H.-J., Beltrami, G., Cauley, J. A., Ebeling, P. R., Kumar, R., Linglart, A., Sangiorgi, L., Towler, D. A., Weston, R., Whyte, M. P., Brandi, M. L., Clarke, B., & Thakker, R. V. (2022). Skeletal and extraskeletal disorders of biomineralization. *Nature Reviews Endocrinology*, *18*(8), Article 8. https://doi.org/10.1038/s41574-022-00682-7

da Silva Madaleno, C., Jatzlau, J., & Knaus, P. (2020). BMP signalling in a mechanical context – Implications for bone biology. *Bone*, *137*, 115416. https://doi.org/10.1016/j.bone.2020.115416

Dai, R., Wu, Z., Chu, H. Y., Lu, J., Lyu, A., Liu, J., & Zhang, G. (2020). Cathepsin K: The Action in and Beyond Bone. *Frontiers in Cell and Developmental Biology*, *8*, 433. https://doi.org/10.3389/fcell.2020.00433

Daluiski, A., Engstrand, T., Bahamonde, M. E., Gamer, L. W., Agius, E., Stevenson, S. L., Cox, K., Rosen, V., & Lyons, K. M. (2001). Bone morphogenetic protein-3 is a

negative regulator of bone density. *Nature Genetics*, *27*(1), 84–88. https://doi.org/10.1038/83810

Danielian, P. S., Muccino, D., Rowitch, D. H., Michael, S. K., & McMahon, A. P. (1998). Modification of gene activity in mouse embryos in utero by a tamoxifen-inducible form of Cre recombinase. *Current Biology: CB*, *8*(24), 1323–1326. https://doi.org/10.1016/s0960-9822(07)00562-3

Darrieutort-Laffite, C., Arnolfo, P., Garraud, T., Adrait, A., Couté, Y., Louarn, G., Trichet, V., Layrolle, P., Le Goff, B., & Blanchard, F. (2019). Rotator Cuff Tenocytes Differentiate into Hypertrophic Chondrocyte-Like Cells to Produce Calcium Deposits in an Alkaline Phosphatase-Dependent Manner. *Journal of Clinical Medicine*, *8*(10), 1544. https://doi.org/10.3390/jcm8101544

de Mos, M., Koevoet, W. J., Jahr, H., Verstegen, M. M., Heijboer, M. P., Kops, N., van Leeuwen, J. P., Weinans, H., Verhaar, J. A., & van Osch, G. J. (2007). Intrinsic differentiation potential of adolescent human tendon tissue: An in-vitro cell differentiation study. *BMC Musculoskeletal Disorders*, *8*, 16. https://doi.org/10.1186/1471-2474-8-16

Delgado-Ruiz, R. A., Calvo-Guirado, J. L., & Romanos, G. E. (2019). Effects of occlusal forces on the peri-implant-bone interface stability. *Periodontology 2000*, *81*(1), 179–193. https://doi.org/10.1111/prd.12291

Deng, R., Li, C., Wang, X., Chang, L., Ni, S., Zhang, W., Xue, P., Pan, D., Wan, M., Deng, L., & Cao, X. (2022). Periosteal CD68+ F4/80+ Macrophages Are Mechanosensitive for Cortical Bone Formation by Secretion and Activation of

TGF-β1. *Advanced Science (Weinheim, Baden-Wurttemberg, Germany)*, *9*(3), e2103343. https://doi.org/10.1002/advs.202103343

Di Pietro, L., Barba, M., Palacios, D., Tiberio, F., Prampolini, C., Baranzini, M., Parolini, O., Arcovito, A., & Lattanzi, W. (2021). Shaping modern human skull through epigenetic, transcriptional and post-transcriptional regulation of the RUNX2 master bone gene. *Scientific Reports*, *11*(1), Article 1. https://doi.org/10.1038/s41598-021-00511-3

Di Rocco, F., Baujat, G., Cormier-Daire, V., Rothenbuhler, A., & Linglart, A. (2017). Craniosynostosis and hypophosphatasia. *Archives De Pediatrie: Organe Officiel De La Societe Francaise De Pediatrie*, *24*(5S2), 5S89-85S92. https://doi.org/10.1016/S0929-693X(18)30022-8

Diah, E., Lo, L.-J., Huang, C.-S., Sudjatmiko, G., Susanto, I., & Chen, Y.-R. (2007). Maxillary growth of adult patients with unoperated cleft: Answers to the debates. *Journal of Plastic, Reconstructive & Aesthetic Surgery*, *60*(4), 407–413. https://doi.org/10.1016/j.bjps.2006.10.004

Dimitri, P., De Franco, E., Habeb, A. M., Gurbuz, F., Moussa, K., Taha, D., Wales, J. K. H., Hogue, J., Slavotinek, A., Shetty, A., & Balasubramanian, M. (2016). An emerging, recognizable facial phenotype in association with mutations in GLI-similar 3 (GLIS3). *American Journal of Medical Genetics Part A*, *170*(7), 1918–1923. https://doi.org/10.1002/ajmg.a.37680

Dimopoulos, V. G., Kapsalakis, I. Z., & Fountas, K. N. (2007). Skull morphology and its neurosurgical implications in the Hippocratic era. *Neurosurgical Focus*, *23*(1), E10. https://doi.org/10.3171/foc.2007.23.1.10

Discher, D. E., Smith, L., Cho, S., Colasurdo, M., García, A. J., & Safran, S. (2017). MATRIX MECHANOSENSING: From Scaling Concepts in 'Omics Data to Mechanisms in the Nucleus, Regeneration, and Cancer. *Annual Review of Biophysics*, *46*, 295–315. https://doi.org/10.1146/annurev-biophys-062215-011206

Doro, D., Liu, A., Grigoriadis, A. E., & Liu, K. J. (2019). The Osteogenic Potential of the Neural Crest Lineage May Contribute to Craniosynostosis. *Molecular Syndromology*, *10*(1–2), 48–57. https://doi.org/10.1159/000493106

Doro, D., Liu, A., Lau, J. S., Rajendran, A. K., Healy, C., Krstic, M., Grigoriadis, A. E., Iseki, S., & Liu, K. J. (2024). Cranial suture lineage and contributions to repair of the mouse skull. *Development*, *151*(3), dev202116. https://doi.org/10.1242/dev.202116

dos Santos, Á., & Toseland, C. P. (2021). Regulation of Nuclear Mechanics and the Impact on DNA Damage. *International Journal of Molecular Sciences*, *22*(6), 3178. https://doi.org/10.3390/ijms22063178

Dossani, R. H., Yates, D. M., Kalakoti, P., Nanda, A., Notarianni, C., Woerner, J., & Ghali, G. E. (2017). Cranium Bifidum Occultum Associated with Hypertelorism Treated with Posterior Vault Reconstruction and Orbital Box Osteotomies: Case Report and Technical Note. *World Neurosurgery*, *107*, 40–46. https://doi.org/10.1016/j.wneu.2017.05.032

Doyle, A. D., Carvajal, N., Jin, A., Matsumoto, K., & Yamada, K. M. (2015). Local 3D matrix microenvironment regulates cell migration through spatiotemporal dynamics of contractility-dependent adhesions. *Nature Communications*, *6*(1), 8720. https://doi.org/10.1038/ncomms9720

Dries, R., Zhu, Q., Dong, R., Eng, C.-H. L., Li, H., Liu, K., Fu, Y., Zhao, T., Sarkar, A., Bao, F., George, R. E., Pierson, N., Cai, L., & Yuan, G.-C. (2021). Giotto: A toolbox for integrative analysis and visualization of spatial expression data. *Genome Biology*, *22*(1), 78. https://doi.org/10.1186/s13059-021-02286-2

Driessen, C., Rijken, B., Doerga, P., Dremmen, M., Joosten, K., & Mathijssen, I. (2017). The effect of early fusion of the spheno-occipital synchondrosis on midface hypoplasia and obstructive sleep apnea in patients with Crouzon syndrome. *Journal of Cranio-Maxillofacial Surgery*, *45*(7), 1069–1073. https://doi.org/10.1016/j.jcms.2017.03.024

Du, J., Yang, J., He, Z., Cui, J., Yang, Y., Xu, M., Qu, X., Zhao, N., Yan, M., Li, H., & Yu, Z. (2020). Osteoblast and Osteoclast Activity Affect Bone Remodeling Upon Regulation by Mechanical Loading-Induced Leukemia Inhibitory Factor Expression in Osteocytes. *Frontiers in Molecular Biosciences*, *7*, 585056. https://doi.org/10.3389/fmolb.2020.585056

Du, W., Bhojwani, A., & Hu, J. K. (2021). FACEts of mechanical regulation in the morphogenesis of craniofacial structures. *International Journal of Oral Science*, *13*, 4. https://doi.org/10.1038/s41368-020-00110-4

Dudley, A. T., & Robertson, E. J. (1997). Overlapping expression domains of bone morphogenetic protein family members potentially account for limited tissue defects in BMP7 deficient embryos. *Developmental Dynamics*, *208*(3), 349–362. https://doi.org/10.1002/(SICI)1097-0177(199703)208:3<349::AID-AJA6>3.0.CO;2-I

Dupin, E., Creuzet, S., & Le Douarin, N. M. (2006). The Contribution of the Neural Crest to the Vertebrate Body. In J.-P. Saint-Jeannet (Ed.), *Neural Crest Induction and Differentiation* (pp. 96–119). Springer US. https://doi.org/10.1007/978-0-387-46954-6_6

Dupont, S., Morsut, L., Aragona, M., Enzo, E., Giulitti, S., Cordenonsi, M., Zanconato, F., Le Digabel, J., Forcato, M., Bicciato, S., Elvassore, N., & Piccolo, S. (2011). Role of YAP/TAZ in mechanotransduction. *Nature*, *474*(7350), 179–183. https://doi.org/10.1038/nature10137

Elosegui-Artola, A., Andreu, I., Beedle, A. E. M., Lezamiz, A., Uroz, M., Kosmalska, A. J., Oria, R., Kechagia, J. Z., Rico-Lastres, P., Roux, A.-L. L., Shanahan, C. M., Trepat, X., Navajas, D., Garcia-Manyes, S., & Roca-Cusachs, P. (2017). Force Triggers YAP Nuclear Entry by Regulating Transport across Nuclear Pores. *Cell*, *171*(6), 1397-1410.e14. https://doi.org/10.1016/j.cell.2017.10.008

Elsberg, C. A. (1931). The Edwin Smith Surgical Papyrus. *Annals of Medical History*, *3*(3), 271–279.

Eltoum, I., Fredenburgh, J., Myers, R. B., & Grizzle, W. E. (2001). Introduction to the Theory and Practice of Fixation of Tissues. *Journal of Histotechnology*, *24*(3), 173–190. https://doi.org/10.1179/his.2001.24.3.173

Engler, A. J., Sen, S., Sweeney, H. L., & Discher, D. E. (2006). Matrix Elasticity Directs Stem Cell Lineage Specification. *Cell*, *126*(4), 677–689. https://doi.org/10.1016/j.cell.2006.06.044

Enlow, D. H., & Hunter, W. S. (1966). A differential analysis of sutural and remodeling growth in the human face. *American Journal of Orthodontics*, *52*(11), 823–830. https://doi.org/10.1016/0002-9416(66)90251-X

Eswarakumar, V. P., Horowitz, M. C., Locklin, R., Morriss-Kay, G. M., & Lonai, P. (2004). A gain-of-function mutation of Fgfr2c demonstrates the roles of this receptor variant in osteogenesis. *Proceedings of the National Academy of Sciences*, *101*(34), 12555–12560. https://doi.org/10.1073/pnas.0405031101

Etchevers, H. C., Dupin, E., & Le Douarin, N. M. (2019). The diverse neural crest: From embryology to human pathology. *Development*, *146*(5), dev169821. https://doi.org/10.1242/dev.169821

Fan, X., Masamsetti, V. P., Sun, J. Q., Engholm-Keller, K., Osteil, P., Studdert, J., Graham, M. E., Fossat, N., & Tam, P. P. (2021). TWIST1 and chromatin regulatory proteins interact to guide neural crest cell differentiation. *eLife*, *10*, e62873. https://doi.org/10.7554/eLife.62873

Fang, H., Liu, S., Wang, Y., Chiang, C., Liu, C., & Lin, C. (2019). Phenotypic features of a microdeletion in chromosome band 20p13: A case report and review of the literature. *Molecular Genetics & Genomic Medicine*, *7*(7), e00739. https://doi.org/10.1002/mgg3.739

Fariña, R., Lolas, J., Moreno, E., Alister, J. P., Uribe, M. F., Pantoja, R., Valladares, S., & Arrué, C. (2022). Cleft Lip and Palate Midfacial Hypoplasia: Criteria to Choose the Treatment. *Journal of Craniofacial Surgery*, *33*(2), 496. https://doi.org/10.1097/SCS.0000000000007973

Fariña, R., Valladares, S., Raposo, A., & Silva, F. (2018). Modified Le Fort III osteotomy: A simple solution to severe midfacial hypoplasia. *Journal of Cranio-Maxillo-Facial Surgery: Official Publication of the European Association for Cranio-Maxillo-Facial Surgery*, *46*(5), 837–843. https://doi.org/10.1016/j.jcms.2018.03.010

Farmer, D. T., Mlcochova, H., Zhou, Y., Koelling, N., Wang, G., Ashley, N., Bugacov, H., Chen, H.-J., Parvez, R., Tseng, K.-C., Merrill, A. E., Maxson, R. E., Wilkie, A. O. M., Crump, J. G., & Twigg, S. R. F. (2021). The developing mouse coronal suture at single-cell resolution. *Nature Communications*, *12*(1), Article 1. https://doi.org/10.1038/s41467-021-24917-9

Farrow, E., Nicot, R., Wiss, A., Laborde, A., & Ferri, J. (2018). Cleidocranial Dysplasia: A Review of Clinical, Radiological, Genetic Implications and a Guidelines Proposal. *The Journal of Craniofacial Surgery*, *29*(2), 382–389. https://doi.org/10.1097/SCS.0000000000004200

Fedorov, A., Beichel, R., Kalpathy-Cramer, J., Finet, J., Fillion-Robin, J.-C., Pujol, S., Bauer, C., Jennings, D., Fennessy, F., Sonka, M., Buatti, J., Aylward, S., Miller, J. V., Pieper, S., & Kikinis, R. (2012). 3D Slicer as an Image Computing Platform for the Quantitative Imaging Network. *Magnetic Resonance Imaging*, *30*(9), 1323–1341. https://doi.org/10.1016/j.mri.2012.05.001

Feng, X.-H., & Derynck, R. (2005). Specificity and versatility in TGF-β signaling through Smads. *Annual Review of Cell and Developmental Biology*, *21*(Volume 21, 2005), 659–693. https://doi.org/10.1146/annurev.cellbio.21.022404.142018

Ferlias, N., Gjørup, H., Aagaard Doherty, M., Haagerup, A., & Klit Pedersen, T. (2021). Three-dimensional analysis of craniofacial morphology in patients with pycnodysostosis. *Orthodontics & Craniofacial Research*, *24*(4), 568–574. https://doi.org/10.1111/ocr.12479

Finch-Edmondson, M., & Sudol, M. (2016). Framework to function: Mechanosensitive regulators of gene transcription. *Cellular & Molecular Biology Letters*, *21*, 28. https://doi.org/10.1186/s11658-016-0028-7

Fioravanti, G., Hua, P. Q., & Tomlinson, R. E. (2021). The TrkA agonist gambogic amide augments skeletal adaptation to mechanical loading. *Bone*, *147*, 115908. https://doi.org/10.1016/j.bone.2021.115908

Foster, B. L., Ramnitz, M. S., Gafni, R. I., Burke, A. B., Boyce, A. M., Lee, J. S., Wright, J. T., Akintoye, S. O., Somerman, M. J., & Collins, M. T. (2014). Rare bone diseases and their dental, oral, and craniofacial manifestations. *Journal of Dental Research*, *93*(7 Suppl), 7S-19S. https://doi.org/10.1177/0022034514529150

Fotouhi, A. R., Chiang, S. N., Peterson, A. M., Doering, M. M., Skolnick, G. B., Naidoo, S. D., Strahle, J. M., McEvoy, S. D., & Patel, K. B. (2022). Neurodevelopment in unilateral coronal craniosynostosis: A systematic review and meta-analysis. *Journal of Neurosurgery: Pediatrics*, *31*(1), 16–23. https://doi.org/10.3171/2022.9.PEDS22283

Franklin, D., & Flavel, A. (2014). Brief Communication: Timing of spheno-occipital closure in modern Western Australians. *American Journal of Physical Anthropology*, *153*(1), 132–138. https://doi.org/10.1002/ajpa.22399

Freng, A. (1978). Growth in Width of the Dental Arches After Partial Extirpation of the Mid-Palatal Suture in Man. *Scandinavian Journal of Plastic and Reconstructive Surgery*, *12*(3), 267–272. https://doi.org/10.3109/02844317809013003

Friedlaender, G. E., Perry, C. R., Dean Cole, J., Cook, S. D., Cierny, G., Muschler, G. F., ZYCH, G. A., CALHOUN, J. H., LAFORTE, A. J., & YIN, S. (2001). Osteogenic Protein-1 (Bone Morphogenetic Protein-7) in the Treatment of Tibial Nonunions. *The Journal of Bone and Joint Surgery. American Volume*, *83-A Suppl 1*(Pt 2), S151–S158.

Fudalej, P., Obloj, B., Miller-Drabikowska, D., Samarcew-Krawczak, A., & Dudkiewicz, Z. (2008). Midfacial Growth in a Consecutive Series of Preadolescent Children with Complete Unilateral Cleft Lip and Palate following a One-Stage Simultaneous Repair. *The Cleft Palate Craniofacial Journal*, *45*(6), 667–673. https://doi.org/10.1597/07-174.1

Fuentealba, L. C., Eivers, E., Ikeda, A., Hurtado, C., Kuroda, H., Pera, E. M., & De Robertis, E. M. (2007). Integrating Patterning Signals: Wnt/GSK3 Regulates the Duration of the BMP/Smad1 Signal. *Cell*, *131*(5), 980–993. https://doi.org/10.1016/j.cell.2007.09.027

Gagan, J. R., Tholpady, S. S., & Ogle, R. C. (2007). Cellular dynamics and tissue interactions of the dura mater during head development. *Birth Defects Research. Part C, Embryo Today: Reviews*, *81*(4), 297–304. https://doi.org/10.1002/bdrc.20104

Gage, G. J., Kipke, D. R., & Shain, W. (2012). Whole Animal Perfusion Fixation for Rodents. *JoVE (Journal of Visualized Experiments)*, *65*, e3564. https://doi.org/10.3791/3564

Galea, G. L., Paradise, C. R., Meakin, L. B., Camilleri, E. T., Taipaleenmaki, H., Stein, G. S., Lanyon, L. E., Price, J. S., van Wijnen, A. J., & Dudakovic, A. (2020). Mechanical strain-mediated reduction in RANKL expression is associated with RUNX2 and BRD2. *Gene*, *763S*, 100027. https://doi.org/10.1016/j.gene.2020.100027

Galea, G. L., Zein, M. R., Allen, S., & Francis-West, P. (2021). Making and shaping endochondral and intramembranous bones. *Developmental Dynamics*, *250*(3), 414–449. https://doi.org/10.1002/dvdy.278

Geiger, B., Spatz, J. P., & Bershadsky, A. D. (2009). Environmental sensing through focal adhesions. *Nature Reviews Molecular Cell Biology*, *10*(1), Article 1. https://doi.org/10.1038/nrm2593

Geng, Y., Zhao, X., Xu, J., Zhang, X., Hu, G., Fu, S.-C., Dai, K., Chen, X., Patrick, Y. S.-H., & Zhang, X. (2020). Overexpression of mechanical sensitive miR-337-3p alleviates ectopic ossification in rat tendinopathy model via targeting IRS1 and Nox4 of tendon-derived stem cells. *Journal of Molecular Cell Biology*, *12*(4), 305–317. https://doi.org/10.1093/jmcb/mjz030

Gerstenfeld, L., Cho, T., Kon, T., Aizawa, T., Tsay, A., Fitch, J., Barnes, G., Graves, D., & Einhorn, T. (2003). Impaired Fracture Healing in the Absence of TNF-α Signaling: The Role of TNF-α in Endochondral Cartilage Resorption*. *Journal of*

Bone and Mineral Research, *18*(9), 1584–1592. https://doi.org/10.1359/jbmr.2003.18.9.1584

Gilbert, P. M., Havenstrite, K. L., Magnusson, K. E. G., Sacco, A., Leonardi, N. A., Kraft, P., Nguyen, N. K., Thrun, S., Lutolf, M. P., & Blau, H. M. (2010). Substrate elasticity regulates skeletal muscle stem cell self-renewal in culture. *Science (New York, N.Y.)*, *329*(5995), 1078–1081. https://doi.org/10.1126/science.1191035

Gipson, G. R., Goebel, E. J., Hart, K. N., Kappes, E. C., Kattamuri, C., McCoy, J. C., & Thompson, T. B. (2020). Structural perspective of BMP ligands and signaling. *Bone*, *140*, 115549. https://doi.org/10.1016/j.bone.2020.115549

Gömleksiz, C., Arslan, E., Arslan, S., Pusat, S., & Arslan, E. A. (2014). Delayed diagnosis of cleidocranial dysplasia in an adult: A case report. *Acta Medica Academica*, *43*(1), 92–96. https://doi.org/10.5644/ama2006-124.106

Gong, S., Ji, F., Wang, B., Zhang, Y., Xu, X., & Sun, M. (2018). Tectonic Proteins Are Important Players in Non-Motile Ciliopathies. *Cellular Physiology and Biochemistry*, *50*(1), 398–409. https://doi.org/10.1159/000494017

Gonzalez Malagon, S. G., Dobson, L., Muñoz, A. M. L., Dawson, M., Barrell, W., Marangos, P., Krause, M., & Liu, K. J. (2019). Dissection, Culture and Analysis of Primary Cranial Neural Crest Cells from Mouse for the Study of Neural Crest Cell Delamination and Migration. *Journal of Visualized Experiments : JoVE*, *152*, 10.3791/60051. https://doi.org/10.3791/60051

Goodship, A. E., Cunningham, J. L., Oganov, V., Darling, J., Miles, A. W., & Owen, G. W. (1998). Bone loss during long term space flight is prevented by the application

of a short term impulsive mechanical stimulus. *Acta Astronautica*, *43*(3), 65–75. https://doi.org/10.1016/S0094-5765(98)00144-1

Goos, J. A. C., Fenwick, A. L., Swagemakers, S. M. A., McGowan, S. J., Knight, S. J. L., Twigg, S. R. F., Hoogeboom, A. J. M., Dooren, M. F. van, Magielsen, F. J., Wall, S. A., Mathijssen, I. M. J., Wilkie, A. O. M., Spek, P. J. van der, & Ouweland, A. M. W. van den. (2016). Identification of Intragenic Exon Deletions and Duplication of TCF12 by Whole Genome or Targeted Sequencing as a Cause of TCF12-Related Craniosynostosis. *Human Mutation*, *37*(8), 732. https://doi.org/10.1002/humu.23010

Gould, N. R., Williams, K. M., Joca, H. C., Torre, O. M., Lyons, J. S., Leser, J. M., Srikanth, M. P., Hughes, M., Khairallah, R. J., Feldman, R. A., Ward, C. W., & Stains, J. P. (2021). Disparate bone anabolic cues activate bone formation by regulating the rapid lysosomal degradation of sclerostin protein. *eLife*, *10*, e64393. https://doi.org/10.7554/eLife.64393

Goyal, M., Gupta, A., Kapoor, S., & Bhandari, A. (2020). Apert Syndrome with Preaxial Polydactyly with FGFR2 Gene Mutation. *The Indian Journal of Pediatrics*, *87*(6), 469–470. https://doi.org/10.1007/s12098-019-03140-x

Graf, D., & Economides, A. N. (2008). Dissection of bone morphogenetic protein signaling using genome-engineering tools. In S. Vukicevic & K. T. Sampath (Eds.), *Bone Morphogenetic Proteins: From Local to Systemic Therapeutics* (pp. 115–139). Birkhäuser. https://doi.org/10.1007/978-3-7643-8552-1_7

Grandi, F., Caroli, J., Romano, O., Marchionni, M., Forcato, M., & Bicciato, S. (2022). popsicleR: A R Package for Pre-processing and Quality Control Analysis of Single

Cell RNA-seq Data. *Journal of Molecular Biology*, *434*(11), 167560. https://doi.org/10.1016/j.jmb.2022.167560

Gregory, K. E., Ono, R. N., Charbonneau, N. L., Kuo, C.-L., Keene, D. R., Bächinger, H. P., & Sakai, L. Y. (2005). The Prodomain of BMP-7 Targets the BMP-7 Complex to the Extracellular Matrix*. *Journal of Biological Chemistry*, *280*(30), 27970–27980. https://doi.org/10.1074/jbc.M504270200

Grimaldi, A., Parada, C., & Chai, Y. (2015). A Comprehensive Study of Soft Palate Development in Mice. *PLOS ONE*, *10*(12), e0145018. https://doi.org/10.1371/journal.pone.0145018

Groeger, M., Spanier, G., Wolf, M., Deschner, J., Proff, P., Schröder, A., & Kirschneck, C. (2020). Effects of histamine on human periodontal ligament fibroblasts under simulated orthodontic pressure. *PloS One*, *15*(8), e0237040. https://doi.org/10.1371/journal.pone.0237040

Guo, L., Elcioglu, N. H., Wang, Z., Demirkol, Y. K., Isguven, P., Matsumoto, N., Nishimura, G., Miyake, N., & Ikegawa, S. (2017). Novel and recurrent COL11A1 and COL2A1 mutations in the Marshall–Stickler syndrome spectrum. *Human Genome Variation*, *4*(1), 1–4. https://doi.org/10.1038/hgv.2017.40

Guo, Y., Yuan, Y., Wu, L., Ho, T.-V., Jing, J., Sugii, H., Li, J., Han, X., Feng, J., Guo, C., & Chai, Y. (2018). BMP-IHH-mediated interplay between mesenchymal stem cells and osteoclasts supports calvarial bone homeostasis and repair. *Bone Research*, *6*(1). https://doi.org/10.1038/s41413-018-0031-x

Gurel, H. G., Memili, B., Erkan, M., & Sukurica, Y. (2010). Long-Term Effects of Rapid Maxillary Expansion Followed by Fixed Appliances. *The Angle Orthodontist*, *80*(1), 5–9. https://doi.org/10.2319/011209-22.1

Hald, J. D., Beck-Nielsen, S., Gregersen, P. A., Gjørup, H., & Langdahl, B. (2023). Pycnodysostosis in children and adults. *Bone*, *169*, 116674. https://doi.org/10.1016/j.bone.2023.116674

Hallgrimsson, B., Mio, W., Marcucio, R. S., & Spritz, R. (2014). Let's Face It—Complex Traits Are Just Not That Simple. *PLOS Genetics*, *10*(11), e1004724. https://doi.org/10.1371/journal.pgen.1004724

Hammond, N. L., Brookes, K. J., & Dixon, M. J. (2018). Ectopic Hedgehog Signaling Causes Cleft Palate and Defective Osteogenesis. *Journal of Dental Research*, *97*(13), 1485–1493. https://doi.org/10.1177/0022034518785336

Han, M.-S., Kim, H.-J., Wee, H.-J., Lim, K.-E., Park, N.-R., Bae, S.-C., van Wijnen, A. J., Stein, J. L., Lian, J. B., Stein, G. S., & Choi, J.-Y. (2010). The cleidocranial dysplasia-related R131G mutation in the Runt-related transcription factor RUNX2 disrupts binding to DNA but not CBF-β. *Journal of Cellular Biochemistry*, *110*(1), 97–103. https://doi.org/10.1002/jcb.22516

Han, Y., You, X., Xing, W., Zhang, Z., & Zou, W. (2018). Paracrine and endocrine actions of bone—The functions of secretory proteins from osteoblasts, osteocytes, and osteoclasts. *Bone Research*, *6*, 16. https://doi.org/10.1038/s41413-018-0019-6

Hao, Y., Hao, S., Andersen-Nissen, E., Mauck, W. M., Zheng, S., Butler, A., Lee, M. J., Wilk, A. J., Darby, C., Zager, M., Hoffman, P., Stoeckius, M., Papalexi, E., Mimitou, E. P., Jain, J., Srivastava, A., Stuart, T., Fleming, L. M., Yeung, B., …

Satija, R. (2021). Integrated analysis of multimodal single-cell data. *Cell*, *184*(13), 3573-3587.e29. https://doi.org/10.1016/j.cell.2021.04.048

Hao, Y., Stuart, T., Kowalski, M. H., Choudhary, S., Hoffman, P., Hartman, A., Srivastava, A., Molla, G., Madad, S., Fernandez-Granda, C., & Satija, R. (2024). Dictionary learning for integrative, multimodal and scalable single-cell analysis. *Nature Biotechnology*, *42*(2), 293–304. https://doi.org/10.1038/s41587-023-01767-y

Haravu, P. N., Gonzalez, M., Nathan, S. L., Ross, C. F., Panagiotopoulou, O., & Reid, R. R. (2023). The biomechanics of chewing and suckling in the infant: A potential mechanism for physiologic metopic suture closure. *PLOS Computational Biology*, *19*(6), e1011227. https://doi.org/10.1371/journal.pcbi.1011227

Hariri, F., Lan, T. H., & Cheung, L. K. (2011). Simultaneous Le Fort III and Le Fort I osteotomies for correction of midface hypoplasia in Crouzon syndrome. *Asian Journal of Oral and Maxillofacial Surgery*, *23*(3), 128–133. https://doi.org/10.1016/j.ajoms.2011.04.002

Haye, D., Dridi, H., Levy, J., Lambert, V., Lambert, M., Agha, M., Adjimi, F., Kohlhase, J., Lipsker, D., & Verloes, A. (2016). Failure of ossification of the occipital bone in mandibuloacral dysplasia type B. *American Journal of Medical Genetics. Part A*, *170*(10), 2750–2755. https://doi.org/10.1002/ajmg.a.37825

He, F., & Soriano, P. (2017). Dysregulated PDGFRα signaling alters coronal suture morphogenesis and leads to craniosynostosis through endochondral ossification. *Development*, *144*(21), 4026–4036. https://doi.org/10.1242/dev.151068

Healy, C., Uwanogho, D., & Sharpe, P. T. (1999). Regulation and role of Sox9 in cartilage formation. *Developmental Dynamics: An Official Publication of the American*

Association of Anatomists, *215*(1), 69–78. https://doi.org/10.1002/(SICI)1097-0177(199905)215:1<69::AID-DVDY8>3.0.CO;2-N

Heldin, C.-H., Miyazono, K., & ten Dijke, P. (1997). TGF-β signalling from cell membrane to nucleus through SMAD proteins. *Nature*, *390*(6659), 465–471. https://doi.org/10.1038/37284

Hepp, N., Frederiksen, A. L., Duno, M., Jørgensen, N. R., & Jensen, J.-E. B. (2022). Biochemical and clinical manifestations in adults with hypophosphatasia: A national cross-sectional study. *Osteoporosis International*, *33*(12), 2595–2605. https://doi.org/10.1007/s00198-022-06536-2

Herisson, F., Frodermann, V., Courties, G., Rohde, D., Sun, Y., Vandoorne, K., Wojtkiewicz, G. R., Masson, G. S., Vinegoni, C., Kim, J., Kim, D.-E., Weissleder, R., Swirski, F. K., Moskowitz, M. A., & Nahrendorf, M. (2018). Direct vascular channels connect skull bone marrow and the brain surface enabling myeloid cell migration. *Nature Neuroscience*, *21*(9), 1209–1217. https://doi.org/10.1038/s41593-018-0213-2

Herring, S. W. (2008). Mechanical Influences on Suture Development and Patency. In D. P. Rice (Ed.), *Frontiers of Oral Biology* (Vol. 12, pp. 41–56). S. KARGER AG. https://doi.org/10.1159/000115031

Herring, S. W., Rafferty, K. L., Shin, D. U., Smith, K., & Baldwin, M. C. (2024). Cyclic loading failed to promote growth in a pig model of midfacial hypoplasia. *Journal of Anatomy*. https://doi.org/10.1111/joa.14043

Herring, S. W., & Teng, S. (2000). Strain in the Braincase and Its Sutures During Function. *American Journal of Physical Anthropology*, *112*(4), 575. https://doi.org/10.1002/1096-8644(200008)112:4<575::AID-AJPA10>3.0.CO;2-0

Herrmann, M., Engelke, K., Ebert, R., Müller-Deubert, S., Rudert, M., Ziouti, F., Jundt, F., Felsenberg, D., & Jakob, F. (2020). Interactions between Muscle and Bone—Where Physics Meets Biology. *Biomolecules*, *10*(3). https://doi.org/10.3390/biom10030432

Hinz, B. (2015). The extracellular matrix and transforming growth factor-β1: Tale of a strained relationship. *Matrix Biology*, *47*, 54–65. https://doi.org/10.1016/j.matbio.2015.05.006

Hirukawa, K., Miyazawa, K., Maeda, H., Kameyama, Y., Goto, S., & Togari, A. (2005). Effect of tensile force on the expression of IGF-I and IGF-I receptor in the organ-cultured rat cranial suture. *Archives of Oral Biology*, *50*(3), 367–372. https://doi.org/10.1016/j.archoralbio.2004.07.003

Hitzert, M. M., van der Crabben, S. N., Baldewsingh, G., van Amstel, H. K. P., van den Wijngaard, A., van Ravenswaaij-Arts, C. M. A., & Zijlmans, C. W. R. (2019). Mandibuloacral dysplasia type B (MADB): A cohort of eight patients from Suriname with a homozygous founder mutation in ZMPSTE24 (FACE1), clinical diagnostic criteria and management guidelines. *Orphanet Journal of Rare Diseases*, *14*(1), 294. https://doi.org/10.1186/s13023-019-1269-0

Hliang, E., Ishihara, Y., Wang, Z., Odagaki, N., & Kamioka, H. (2019). Role of intracellular Ca2+-based mechanotransduction of human periodontal ligament fibroblasts. *FASEB Journal: Official Publication of the Federation of American*

Societies for Experimental Biology, *33*(9), 10409–10424. https://doi.org/10.1096/fj.201900484R

Hollnagel, A., Oehlmann, V., Heymer, J., Rüther, U., & Nordheim, A. (1999). Id Genes Are Direct Targets of Bone Morphogenetic Protein Induction in Embryonic Stem Cells*. *Journal of Biological Chemistry*, *274*(28), 19838–19845. https://doi.org/10.1074/jbc.274.28.19838

Holloway, R. L., Broadfield, D. C., & Carlson, K. J. (2014). New high-resolution computed tomography data of the Taung partial cranium and endocast and their bearing on metopism and hominin brain evolution. *Proceedings of the National Academy of Sciences of the United States of America*, *111*(36), 13022–13027. https://doi.org/10.1073/pnas.1402905111

Holmes, G., Gonzalez-Reiche, A. S., Lu, N., Zhou, X., Rivera, J., Kriti, D., Sebra, R., Williams, A. A., Donovan, M. J., Potter, S. S., Pinto, D., Zhang, B., van Bakel, H., & Jabs, E. W. (2020). Integrated Transcriptome and Network Analysis Reveals Spatiotemporal Dynamics of Calvarial Suturogenesis. *Cell Reports*, *32*(1), 107871. https://doi.org/10.1016/j.celrep.2020.107871

Holmes, G., Jabs, E. W., & van Bakel, H. (2017). Transcriptome atlases of the craniofacial sutures. *FaceBase Consortium*. https://doi.org/10.25550/1WW8

Hordyjewska-Kowalczyk, E., Sowińska-Seidler, A., Olech, E. M., Socha, M., Glazar, R., Kruczek, A., Latos-Bieleńska, A., Tylzanowski, P., & Jamsheer, A. (2019). Functional analysis of novel RUNX2 mutations identified in patients with cleidocranial dysplasia. *Clinical Genetics*, *96*(5), 429–438. https://doi.org/10.1111/cge.13610

Houschyar, K. S., Tapking, C., Borrelli, M. R., Popp, D., Duscher, D., Maan, Z. N., Chelliah, M. P., Li, J., Harati, K., Wallner, C., Rein, S., Pförringer, D., Reumuth, G., Grieb, G., Mouraret, S., Dadras, M., Wagner, J. M., Cha, J. Y., Siemers, F., … Behr, B. (2019). Wnt Pathway in Bone Repair and Regeneration – What Do We Know So Far. *Frontiers in Cell and Developmental Biology*, *6*. https://doi.org/10.3389/fcell.2018.00170

Hruba, E., Kavkova, M., Dalecka, L., Macholan, M., Zikmund, T., Varecha, M., Bosakova, M., Kaiser, J., Krejci, P., Hovorakova, M., & Buchtova, M. (2021). Loss of Sprouty Produces a Ciliopathic Skeletal Phenotype in Mice Through Upregulation of Hedgehog Signaling. *Journal of Bone and Mineral Research: The Official Journal of the American Society for Bone and Mineral Research*, *36*(11), 2258–2274. https://doi.org/10.1002/jbmr.4427

Hu, Z., Zhang, L., Wang, H., Wang, Y., Tan, Y., Dang, L., Wang, K., Sun, Z., Li, G., Cao, X., Zhang, S., Shi, F., & Zhang, G. (2020). Targeted silencing of miRNA-132-3p expression rescues disuse osteopenia by promoting mesenchymal stem cell osteogenic differentiation and osteogenesis in mice. *Stem Cell Research & Therapy*, *11*(1), 58. https://doi.org/10.1186/s13287-020-1581-6

Huang, X., Li, Z., Liu, P., Wu, M., Liu, A.-Q., Hu, C., Liu, X., Guo, H., Yang, X., Guo, X., Li, B., He, X., Xuan, K., & Jin, Y. (2021). Gli1+ Cells Residing in Bone Sutures Respond to Mechanical Force via IP3R to Mediate Osteogenesis. *Stem Cells International*, *2021*, 8138374. https://doi.org/10.1155/2021/8138374

Humphrey, J. D., Dufresne, E. R., & Schwartz, M. A. (2014). Mechanotransduction and extracellular matrix homeostasis. *Nature Reviews. Molecular Cell Biology*, *15*(12), 802–812. https://doi.org/10.1038/nrm3896

Ichikawa, E., Watanabe, A., Nakano, Y., Akita, S., Hirano, A., Kinoshita, A., Kondo, S., Kishino, T., Uchiyama, T., Niikawa, N., & Yoshiura, K. (2006). PAX9 and TGFB3 are linked to susceptibility to nonsyndromic cleft lip with or without cleft palate in the Japanese: Population-based and family-based candidate gene analyses. *Journal of Human Genetics*, *51*(1), 38–46. https://doi.org/10.1007/s10038-005-0319-8

Ilchuk, L. A., Stavskaya, N. I., Varlamova, E. A., Khamidullina, A. I., Tatarskiy, V. V., Mogila, V. A., Kolbutova, K. B., Bogdan, S. A., Sheremetov, A. M., Baulin, A. N., Filatova, I. A., Silaeva, Y. Y., Filatov, M. A., & Bruter, A. V. (2022). Limitations of Tamoxifen Application for In Vivo Genome Editing Using Cre/ERT2 System. *International Journal of Molecular Sciences*, *23*(22), Article 22. https://doi.org/10.3390/ijms232214077

Irianto, J., Pfeifer, C. R., Xia, Y., & Discher, D. E. (2016). SnapShot: Mechanosensing Matrix. *Cell*, *165*(7), 1820-1820.e1. https://doi.org/10.1016/j.cell.2016.06.002

Jabs, E. W., Müller, U., Li, X., Ma, L., Luo, W., Haworth, I. S., Klisak, I., Sparkes, R., Warman, M. L., Mulliken, J. B., Snead, M. L., & Maxson, R. (1993). A mutation in the homeodomain of the human MSX2 gene in a family affected with autosomal dominant craniosynostosis. *Cell*, *75*(3), 443–450. https://doi.org/10.1016/0092-8674(93)90379-5

Jacob, S., Wu, C., Freeman, T. A., Koyama, E., & Kirschner, R. E. (2007). Expression of Indian Hedgehog, BMP-4 and Noggin in Craniosynostosis Induced by Fetal

Constraint. *Annals of Plastic Surgery*, *58*(2), 215–221. https://doi.org/10.1097/01.sap.0000232833.41739.a5

James, A. W., LaChaud, G., Shen, J., Asatrian, G., Nguyen, V., Zhang, X., Ting, K., & Soo, C. (2016). A Review of the Clinical Side Effects of Bone Morphogenetic Protein-2. *Tissue Engineering. Part B, Reviews*, *22*(4), 284–297. https://doi.org/10.1089/ten.teb.2015.0357

Jaruga, A., Hordyjewska, E., Kandzierski, G., & Tylzanowski, P. (2016). Cleidocranial dysplasia and RUNX2-clinical phenotype–genotype correlation. *Clinical Genetics*, *90*(5), 393–402. https://doi.org/10.1111/cge.12812

Jaslow, C. R., & Biewener, A. A. (1995). Strain patterns in the horncores, cranial bones and sutures of goats (Capra hircus) during impact loading. *Journal of Zoology*, *235*(2), 193–210. https://doi.org/10.1111/j.1469-7998.1995.tb05137.x

Jenkins, L. L., & Burg, K. J. L. (2003). Tissue Harvesting and Fixation. In Y. H. An & K. L. Martin (Eds.), *Handbook of Histology Methods for Bone and Cartilage* (pp. 143–157). Humana Press. https://doi.org/10.1007/978-1-59259-417-7_8

Jia, S., Zhou, J., & D'Souza, R. N. (2020). Pax9's dual roles in modulating Wnt signaling during murine palatogenesis. *Developmental Dynamics*, *249*(10), 1274–1284. https://doi.org/10.1002/dvdy.189

Jiang, W., Takeshita, N., Maeda, T., Sogi, C., Oyanagi, T., Kimura, S., Yoshida, M., Sasaki, K., Ito, A., & Takano-Yamamoto, T. (2021). Connective tissue growth factor promotes chemotaxis of preosteoblasts through integrin α5 and Ras during tensile force-induced intramembranous osteogenesis. *Scientific Reports*, *11*(1), 2368. https://doi.org/10.1038/s41598-021-82246-9

Jiang, X., Iseki, S., Maxson, R. E., Sucov, H. M., & Morriss-Kay, G. M. (2002). Tissue Origins and Interactions in the Mammalian Skull Vault. *Developmental Biology*, *241*(1), 106–116. https://doi.org/10.1006/dbio.2001.0487

Jiang, Y., Guan, Y., Lan, Y., Chen, S., Li, T., Zou, S., Hu, Z., & Ye, Q. (2021). Mechanosensitive Piezo1 in Periodontal Ligament Cells Promotes Alveolar Bone Remodeling During Orthodontic Tooth Movement. *Frontiers in Physiology*, *12*. https://www.frontiersin.org/article/10.3389/fphys.2021.767136

Jin, A., Hong, Y., Yang, Y., Xu, H., Huang, X., Gao, X., Gong, X., Dai, Q., & Jiang, L. (2022). FOXO3 Mediates Tooth Movement by Regulating Force-Induced Osteogenesis. *Journal of Dental Research*, *101*(2), 196–205. https://doi.org/10.1177/00220345211021534

Jin, J., Seddiqi, H., Bakker, A. D., Wu, G., Verstappen, J. F. M., Haroon, M., Korfage, J. A. M., Zandieh-Doulabi, B., Werner, A., Klein-Nulend, J., & Jaspers, R. T. (2021). Pulsating fluid flow affects pre-osteoblast behavior and osteogenic differentiation through production of soluble factors. *Physiological Reports*, *9*(12), e14917. https://doi.org/10.14814/phy2.14917

Jing, D., Chen, Z., Men, Y., Yi, Y., Wang, Y., Wang, J., Yi, J., Wan, L., Shen, B., Feng, J. Q., Zhao, Z., Zhao, H., & Li, C. (2022). Response of Gli1+ Suture Stem cells to Mechanical Force upon Suture Expansion. *Journal of Bone and Mineral Research: The Official Journal of the American Society for Bone and Mineral Research*. https://doi.org/10.1002/jbmr.4561

Jirapinyo, C., Deraje, V., Huang, G., Gue, S., Anderson, P. J., & Moore, M. H. (2020). Cleidocranial Dysplasia: Management of the Multiple Craniofacial and Skeletal

Anomalies. *Journal of Craniofacial Surgery*, *31*(4), 908–911. https://doi.org/10.1097/SCS.0000000000006306

Jung, Y. T., Cho, J. I., & Lee, S. P. (2015). Cranioplasty Using a Modified Split Calvarial Graft Technique in Cleidocranial Dysplasia. *Journal of Korean Neurosurgical Society*, *58*(1), 79–82. https://doi.org/10.3340/jkns.2015.58.1.79

Junqueira, L. C. U., Bignolas, G., & Brentani, R. R. (1979). Picrosirius staining plus polarization microscopy, a specific method for collagen detection in tissue sections. *The Histochemical Journal*, *11*(4), 447–455. https://doi.org/10.1007/BF01002772

Juran, C. M., Zvirblyte, J., Cheng-Campbell, M., Blaber, E. A., & Almeida, E. A. C. (2021). Cdkn1a deletion or suppression by cyclic stretch enhance the osteogenic potential of bone marrow mesenchymal stem cell-derived cultures. *Stem Cell Research*, *56*, 102513. https://doi.org/10.1016/j.scr.2021.102513

Justice, C. M., Yagnik, G., Kim, Y., Peter, I., Jabs, E. W., Erazo, M., Ye, X., Ainehsazan, E., Shi, L., Cunningham, M. L., Kimonis, V., Roscioli, T., Wall, S. A., Wilkie, A. O. M., Stoler, J., Richtsmeier, J. T., Heuzé, Y., Sanchez-Lara, P. A., Buckley, M. F., … Boyadjiev, S. A. (2012). A genome-wide association study identifies susceptibility loci for non-syndromic sagittal craniosynostosis near BMP2 and within BBS9. *Nature Genetics*, *44*(12), 1360–1364. https://doi.org/10.1038/ng.2463

Kang, K. S., Lee, S.-J., Lee, H., Moon, W., & Cho, D.-W. (2011). Effects of combined mechanical stimulation on the proliferation and differentiation of pre-osteoblasts. *Experimental & Molecular Medicine*, *43*(6), Article 6. https://doi.org/10.3858/emm.2011.43.6.040

Kang, K. S., & Robling, A. G. (2015). New Insights into Wnt–Lrp5/6–β-Catenin Signaling in Mechanotransduction. *Frontiers in Endocrinology*, *5*. https://www.frontiersin.org/article/10.3389/fendo.2014.00246

Karsenty, G. (2008). Transcriptional Control of Skeletogenesis. *Annual Review of Genomics and Human Genetics*, *9*(1), 183–196. https://doi.org/10.1146/annurev.genom.9.081307.164437

Katoh, K., Kano, Y., & Noda, Y. (2011). Rho-associated kinase-dependent contraction of stress fibres and the organization of focal adhesions. *Journal of The Royal Society Interface*, *8*(56), 305–311. https://doi.org/10.1098/rsif.2010.0419

Katsianou, M. A., Adamopoulos, C., Vastardis, H., & Basdra, E. K. (2016). Signaling mechanisms implicated in cranial sutures pathophysiology: Craniosynostosis. *BBA Clinical*, *6*, 165–176. https://doi.org/10.1016/j.bbacli.2016.04.006

Katsianou, M. A., Papavassiliou, K. A., Zoi, I., Gargalionis, A. N., Panagopoulos, D., Themistocleous, M. S., Piperi, C., Papavassiliou, A. G., & Basdra, E. K. (2021). Polycystin-1 modulates RUNX2 activation and osteocalcin gene expression via ERK signalling in a human craniosynostosis cell model. *Journal of Cellular and Molecular Medicine*, *25*(7), 3216–3225. https://doi.org/10.1111/jcmm.16391

Katsube, M., Yamada, S., Yamaguchi, Y., Takakuwa, T., Yamamoto, A., Imai, H., Saito, A., Shimizu, A., & Suzuki, S. (2019). Critical Growth Processes for the Midfacial Morphogenesis in the Early Prenatal Period. *The Cleft Palate-Craniofacial Journal: Official Publication of the American Cleft Palate-Craniofacial Association*, *56*(8), 1026–1037. https://doi.org/10.1177/1055665619827189

Katzen, J. T., & McCarthy, J. G. (2000). Syndromes Involving Craniosynostosis and Midface Hypoplasia. *Otolaryngologic Clinics of North America*, *33*(6), 1257–1284. https://doi.org/10.1016/S0030-6665(05)70280-2

Kawai, M., Bessho, K., Maruyama, H., Miyazaki, J., & Yamamoto, T. (2006). Simultaneous gene transfer of bone morphogenetic protein (BMP) -2 and BMP-7 by in vivo electroporation induces rapid bone formation and BMP-4 expression. *BMC Musculoskeletal Disorders*, *7*(1), 62. https://doi.org/10.1186/1471-2474-7-62

Kawasaki, K., & Richtsmeier, J. T. (2017). Association of the Chondrocranium and Dermatocranium in Early Skull Formation. In C. J. Percival & J. T. Richtsmeier (Eds.), *Building Bones: Bone Formation and Development in Anthropology* (pp. 52–78). Cambridge University Press. https://doi.org/10.1017/9781316388907.004

Kawatsu, M., Takeshita, N., Takimoto, A., Yoshimoto, Y., Seiryu, M., Ito, A., Kimura, S., Kawamoto, T., Hiraki, Y., Shukunami, C., & Takano-Yamamoto, T. (2021). Scleraxis upregulated by transforming growth factor-β1 signaling inhibits tension-induced osteoblast differentiation of priodontal ligament cells via ephrin A2. *Bone*, *149*, 115969. https://doi.org/10.1016/j.bone.2021.115969

Kaya, N., Seker, E. D., & Yücesoy, T. (2023). Comparison of the effects of different rapid maxillary expansion techniques on craniofacial structures: A finite element analysis study. *Progress in Orthodontics*, *24*(1), 7. https://doi.org/10.1186/s40510-023-00459-2

Kaya, S., Çifter, M., Çekici, A., Olgaç, V., İşsever, H., & Işık, G. (2020). Effects of orthodontic force magnitude on cell apoptosis and RANKL-induced

osteoclastogenesis: Studies in a rat model. *Journal of Orofacial Orthopedics*, *81*(2), 100–112. https://doi.org/10.1007/s00056-019-00205-6

Kegelman, C. D., Nijsure, M. P., Moharrer, Y., Pearson, H. B., Dawahare, J. H., Jordan, K. M., Qin, L., & Boerckel, J. D. (2021). YAP and TAZ Promote Periosteal Osteoblast Precursor Expansion and Differentiation for Fracture Repair. *Journal of Bone and Mineral Research*, *36*(1), 143–157. https://doi.org/10.1002/jbmr.4166

Kelly, D. J., & Jacobs, C. R. (2010). The role of mechanical signals in regulating chondrogenesis and osteogenesis of mesenchymal stem cells. *Birth Defects Research Part C: Embryo Today: Reviews*, *90*(1), 75–85. https://doi.org/10.1002/bdrc.20173

Kespohl, B., Schumertl, T., Bertrand, J., Lokau, J., & Garbers, C. (2021). The cytokine interleukin-11 crucially links bone formation, remodeling and resorption. *Cytokine & Growth Factor Reviews*, *60*, 18–27. https://doi.org/10.1016/j.cytogfr.2021.04.002

Kettunen, P., Nie, X., Kvinnsland, I. H., & Luukko, K. (2006). Histological development and dynamic expression of Bmp2–6 mRNAs in the embryonic and postnatal mousecranial base. *The Anatomical Record Part A: Discoveries in Molecular, Cellular, and Evolutionary Biology*, *288A*(12), 1250–1258. https://doi.org/10.1002/ar.a.20402

Khonsari, R. H., Olivier, J., Vigneaux, P., Sanchez, S., Tafforeau, P., Ahlberg, P. E., Di Rocco, F., Bresch, D., Corre, P., Ohazama, A., Sharpe, P. T., & Calvez, V. (2013). A mathematical model for mechanotransduction at the early steps of suture

formation. *Proceedings of the Royal Society B: Biological Sciences*, *280*(1759), 20122670. https://doi.org/10.1098/rspb.2012.2670

Kiesler, J., & Ricer, R. (2003). The abnormal fontanel. *American Family Physician*, *67*(12), 2547–2552.

Killaars, A. R., Walker, C. J., & Anseth, K. S. (2020). Nuclear mechanosensing controls MSC osteogenic potential through HDAC epigenetic remodeling. *Proceedings of the National Academy of Sciences of the United States of America*, *117*(35), 21258–21266. https://doi.org/10.1073/pnas.2006765117

Kim, B., Shin, H., Kim, W. J., Kim, H., Cho, Y.-D., Yoon, H., Baek, J., Woo, K. M., Lee, Y., & Ryoo, H.-M. (2020). PIN1 Attenuation Improves Midface Hypoplasia in a Mouse Model of Apert Syndrome. *Journal of Dental Research*, *99*(2), 223–232. https://doi.org/10.1177/0022034519893656

Kim, B.-S., Shin, H.-R., Kim, H.-J., Yoon, H., Cho, Y.-D., Choi, K.-Y., Choi, J.-Y., Kim, W.-J., & Ryoo, H.-M. (2021). Septal chondrocyte hypertrophy contributes to midface deformity in a mouse model of Apert syndrome. *Scientific Reports*, *11*(1), Article 1. https://doi.org/10.1038/s41598-021-87260-5

Kim, H.-J., Rice, D. P. C., Kettunen, P. J., & Thesleff, I. (1998). FGF-, BMP- and Shh-mediated signalling pathways in the regulation of cranial suture morphogenesis and calvarial bone development. *Development*, *125*(7), 1241–1251. https://doi.org/10.1242/dev.125.7.1241

Kim, H.-S., Neugebauer, J., McKnite, A., Tilak, A., & Christian, J. L. (2019). BMP7 functions predominantly as a heterodimer with BMP2 or BMP4 during mammalian embryogenesis. *eLife*, *8*, e48872. https://doi.org/10.7554/eLife.48872

Kim, S., Nie, H., Nesin, V., Tran, U., Outeda, P., Bai, C.-X., Keeling, J., Maskey, D., Watnick, T., Wessely, O., & Tsiokas, L. (2016). The polycystin complex mediates Wnt/Ca(2+) signalling. *Nature Cell Biology*, *18*(7), 752–764. https://doi.org/10.1038/ncb3363

Kinoshita, N., Hashimoto, Y., Yasue, N., Suzuki, M., Cristea, I. M., & Ueno, N. (2020). Mechanical Stress Regulates Epithelial Tissue Integrity and Stiffness through the FGFR/Erk2 Signaling Pathway during Embryogenesis. *Cell Reports*, *30*(11), 3875-3888.e3. https://doi.org/10.1016/j.celrep.2020.02.074

Kirk, B., Feehan, J., Lombardi, G., & Duque, G. (2020). Muscle, Bone, and Fat Crosstalk: The Biological Role of Myokines, Osteokines, and Adipokines. *Current Osteoporosis Reports*, *18*(4), 388–400. https://doi.org/10.1007/s11914-020-00599-y

Klatte-Schulz, F., Pauly, S., Scheibel, M., Greiner, S., Gerhardt, C., Schmidmaier, G., & Wildemann, B. (2012). Influence of age on the cell biological characteristics and the stimulation potential of male human tenocyte-like cells. *European Cells & Materials*, *24*, 74–89. https://doi.org/10.22203/ecm.v024a06

Knight, R. D., & Schilling, T. F. (2006). Cranial Neural Crest and Development of the Head Skeleton. In J.-P. Saint-Jeannet (Ed.), *Neural Crest Induction and Differentiation* (pp. 120–133). Springer US. https://doi.org/10.1007/978-0-387-46954-6_7

Knippenberg, M., Helder, M. N., Zandieh Doulabi, B., Wuisman, P. I. J. M., & Klein-Nulend, J. (2006). Osteogenesis versus chondrogenesis by BMP-2 and BMP-7 in

adipose stem cells. *Biochemical and Biophysical Research Communications*, *342*(3), 902–908. https://doi.org/10.1016/j.bbrc.2006.02.052

Ko, H.-M., Moon, J.-S., Shim, H.-K., Lee, S.-Y., Kang, J.-H., Kim, M.-S., Chung, H.-J., & Kim, S.-H. (2020). Inhibitory effect of C-X-C motif chemokine ligand 14 on the osteogenic differentiation of human periodontal ligament cells through transforming growth factor-beta1. *Archives of Oral Biology*, *115*, 104733. https://doi.org/10.1016/j.archoralbio.2020.104733

Kobayashi, T., & Sokabe, M. (2010). Sensing substrate rigidity by mechanosensitive ion channels with stress fibers and focal adhesions. *Current Opinion in Cell Biology*, *22*(5), 669–676. https://doi.org/10.1016/j.ceb.2010.08.023

Koenig, B. B., Cook, J. S., Wolsing, D. H., Ting, J., Tiesman, J. P., Correa, P. E., Olson, C. A., Pecquet, A. L., Ventura, F., & Grant, R. A. (1994). Characterization and cloning of a receptor for BMP-2 and BMP-4 from NIH 3T3 cells. *Molecular and Cellular Biology*, *14*(9), 5961–5974. https://doi.org/10.1128/MCB.14.9.5961

Komatsu, Y., Yu, P. B., Kamiya, N., Pan, H., Fukuda, T., Scott, G. J., Ray, M. K., Yamamura, K.-I., & Mishina, Y. (2013). Augmentation of Smad-dependent BMP signaling in neural crest cells causes craniosynostosis in mice. *Journal of Bone and Mineral Research: The Official Journal of the American Society for Bone and Mineral Research*, *28*(6), 1422–1433. https://doi.org/10.1002/jbmr.1857

Komori, T. (2019). Regulation of Proliferation, Differentiation and Functions of Osteoblasts by Runx2. *International Journal of Molecular Sciences*, *20*(7), Article 7. https://doi.org/10.3390/ijms20071694

Kornak, U., Reynders, E., Dimopoulou, A., van Reeuwijk, J., Fischer, B., Rajab, A., Budde, B., Nürnberg, P., Foulquier, F., Lefeber, D., Urban, Z., Gruenewald, S., Annaert, W., Brunner, H. G., van Bokhoven, H., Wevers, R., Morava, E., Matthijs, G., Van Maldergem, L., & Mundlos, S. (2008). Impaired glycosylation and cutis laxa caused by mutations in the vesicular H+-ATPase subunit ATP6V0A2. *Nature Genetics*, *40*(1), 32–34. https://doi.org/10.1038/ng.2007.45

Kosnik-Infinger, L., Gendron, C., Gordon, C. B., Pan, B. S., Aalst, J. A. van, & Vogel, T. W. (2015). Enzyme replacement therapy for congenital hypophosphatasia allows for surgical treatment of related complex craniosynostosis: A case series. *Neurosurgical Focus*, *38*(5), E10. https://doi.org/10.3171/2015.2.FOCUS14847

Kouskoura, T., El Fersioui, Y., Angelini, M., Graf, D., Katsaros, C., & Chiquet, M. (2016). Dislocated Tongue Muscle Attachment and Cleft Palate Formation. *Journal of Dental Research*, *95*(4), 453–459. https://doi.org/10.1177/0022034515621869

Kouskoura, T., Kozlova, A., Alexiou, M., Blumer, S., Zouvelou, V., Katsaros, C., Chiquet, M., Mitsiadis, T. A., & Graf, D. (2013). The Etiology of Cleft Palate Formation in BMP7-Deficient Mice. *PLoS ONE*, *8*(3), e59463. https://doi.org/10.1371/journal.pone.0059463

Kozlowski, K., Sutcliffe, J., Barylak, A., Harrington, G., Kemperdick, H., Nolte, K., Rheinwein, H., Thomas, P. S., & Uniecka, W. (1976). Hypophosphatasia. Review of 24 cases. *Pediatric Radiology*, *5*(2), 103–117. https://doi.org/10.1007/BF00975316

Krakow, D., Cohn, D. H., Wilcox, W. R., Noh, G. J., Raffel, L. J., Sarukhanov, A., Ivanova, M. H., Danielpour, M., Grange, D. K., Elliott, A. M., Bernstein, J. A., Rimoin, D.

L., Merrill, A. E., & Lachman, R. S. (2016). Clinical and radiographic delineation of Bent Bone Dysplasia-FGFR2 type or Bent Bone Dysplasia with Distinctive Clavicles and Angel-shaped Phalanges. *American Journal of Medical Genetics Part A*, *170*(10), 2652–2661. https://doi.org/10.1002/ajmg.a.37772

Kuehle, R., Ringwald, F., Bouffleur, F., Hagen, N., Schaufelberger, M., Nahm, W., Hoffmann, J., Freudlsperger, C., Engel, M., & Eisenmann, U. (2023). The Use of Artificial Intelligence for the Classification of Craniofacial Deformities. *Journal of Clinical Medicine*, *12*(22), 7082. https://doi.org/10.3390/jcm12227082

Kulczyk, T., Przystańska, A., Rewekant, A., Turska-Malińska, R., & Czajka-Jakubowska, A. (2018). Maxillary sinuses and midface in patients with cleidocranial dysostosis. *Annals of Anatomy - Anatomischer Anzeiger*, *215*, 78–82. https://doi.org/10.1016/j.aanat.2017.08.002

Kumar, N., Nayak B, S., Somayaji, S. N., & Nayak, S. (2012). Role of Dilute Alcohol in the Removal of Fine Wrinkles from Paraffin Sections, a Histo-Technical Study. *International Journal of Morphology*, *30*(1), 45–48. https://doi.org/10.4067/S0717-95022012000100007

Kumar, V., Naqvi, S. M., Verbruggen, A., McEvoy, E., & McNamara, L. M. (2024). A mechanobiological model of bone metastasis reveals that mechanical stimulation inhibits the pro-osteolytic effects of breast cancer cells. *Cell Reports*, *43*(5). https://doi.org/10.1016/j.celrep.2024.114043

Kundu, Z. S., Marya, K. M., Devgan, A., Yadav, V., & Rohilla, S. (2004). Subtrochanteric fracture managed by intramedullary nail in a patient with pycnodysostosis. *Joint Bone Spine*, *71*(2), 154–156. https://doi.org/10.1016/S1297-319X(03)00143-X

Kusumbe, A. P., Ramasamy, S. K., & Adams, R. H. (2014). Coupling of angiogenesis and osteogenesis by a specific vessel subtype in bone. *Nature*, *507*(7492), 323–328. https://doi.org/10.1038/nature13145

Kwee, M. L., Balemans, W., Cleiren, E., Gille, J. J. P., Van Der Blij, F., Sepers, J. M., & Van Hul, W. (2005). An autosomal dominant high bone mass phenotype in association with craniosynostosis in an extended family is caused by an LRP5 missense mutation. *Journal of Bone and Mineral Research: The Official Journal of the American Society for Bone and Mineral Research*, *20*(7), 1254–1260. https://doi.org/10.1359/JBMR.050303

Lacerda, R. H. W., & Vieira, A. R. (2021). Retrognathic maxilla in individuals born with oral clefts is due to intrinsic factors and not only due to early surgical treatment. *The Angle Orthodontist*, *91*(2), 243–247. https://doi.org/10.2319/060620-521.1

Lacombe, J., Karsenty, G., & Ferron, M. (2013). Regulation of lysosome biogenesis and functions in osteoclasts. *Cell Cycle*, *12*(17), 2744–2752. https://doi.org/10.4161/cc.25825

Lan, Y., & Jiang, R. (2022). Mouse models in palate development and orofacial cleft research: Understanding the crucial role and regulation of epithelial integrity in facial and palate morphogenesis. *Current Topics in Developmental Biology*, *148*, 13–50. https://doi.org/10.1016/bs.ctdb.2021.12.003

Langeveld, M., & Hollak, C. E. M. (2018). Bone health in patients with inborn errors of metabolism. *Reviews in Endocrine and Metabolic Disorders*, *19*(1), 81–92. https://doi.org/10.1007/s11154-018-9460-5

Langley, R. R., & Fidler, I. J. (2011). The seed and soil hypothesis revisited—The role of tumor-stroma interactions in metastasis to different organs. *International Journal of Cancer. Journal International Du Cancer*, *128*(11), 2527–2535. https://doi.org/10.1002/ijc.26031

Lavrin, I. O., McLean, W., Seegmiller, R. E., Olsen, B. R., & Hay, E. D. (2001). The mechanism of palatal clefting in the Col11a1 mutant mouse. *Archives of Oral Biology*, *46*(9), 865–869. https://doi.org/10.1016/s0003-9969(01)00044-9

Lawson, L. Y., Brodt, M. D., Migotsky, N., Chermside-Scabbo, C. J., Palaniappan, R., & Silva, M. J. (2022). Osteoblast-Specific Wnt Secretion Is Required for Skeletal Homeostasis and Loading-Induced Bone Formation in Adult Mice. *Journal of Bone and Mineral Research: The Official Journal of the American Society for Bone and Mineral Research*, *37*(1), 108–120. https://doi.org/10.1002/jbmr.4445

Layton, R. G., Bins, G. P., Lor, L., Hemal, K., Pontier, J. F., Waler, A., Motamedi, V., & Runyan, C. M. (2023). Impact of Minor Suture Fusion on Midface Hypoplasia in Syndromic Craniosynostosis. *FACE*, *4*(1), 55–63. https://doi.org/10.1177/27325016231153179

LeBlanc, S., & Savarirayan, R. (2020). Pycnodysostosis. In M. P. Adam, H. H. Ardinger, R. A. Pagon, S. E. Wallace, L. J. Bean, G. Mirzaa, & A. Amemiya (Eds.), *GeneReviews®*. University of Washington, Seattle. http://www.ncbi.nlm.nih.gov/books/NBK563694/

Lee, J. C., & Volpicelli, E. J. (2017). Bioinspired Collagen Scaffolds in Cranial Bone Regeneration: From Bedside to Bench. *Advanced Healthcare Materials*, *6*(17).

https://doi.org/10.1002/adhm.201700232@10.1002/(ISSN)2192-2659.Regenerative-Medicine

Lee, K.-B., Taghavi, C. E., Murray, S. S., Song, K.-J., Keorochana, G., & Wang, J. C. (2012). BMP induced inflammation: A comparison of rhBMP-7 and rhBMP-2. *Journal of Orthopaedic Research*, *30*(12), 1985–1994. https://doi.org/10.1002/jor.22160

Lee, S.-J., Lehar, A., Liu, Y., Ly, C. H., Pham, Q.-M., Michaud, M., Rydzik, R., Youngstrom, D. W., Shen, M. M., Kaartinen, V., Germain-Lee, E. L., & Rando, T. A. (2020). Functional redundancy of type I and type II receptors in the regulation of skeletal muscle growth by myostatin and activin A. *Proceedings of the National Academy of Sciences*, *117*(49), 30907–30917. https://doi.org/10.1073/pnas.2019263117

Lenk, G. M., & Meisler, M. H. (2014). Chapter Fourteen—Mouse Models of PI(3,5)P2 Deficiency with Impaired Lysosome Function. In P. M. Conn (Ed.), *Methods in Enzymology* (Vol. 534, pp. 245–260). Academic Press. https://doi.org/10.1016/B978-0-12-397926-1.00014-7

Lenk, G. M., & Meisler, M. H. (2022). Chloroquine corrects enlarged lysosomes in FIG4 null cells and reduces neurodegeneration in Fig4 null mice. *Molecular Genetics and Metabolism*, *137*(4), 382–387. https://doi.org/10.1016/j.ymgme.2022.11.004

Lewis, A. E., Vasudevan, H. N., O'Neill, A. K., Soriano, P., & Bush, J. O. (2013). The widely used Wnt1-Cre transgene causes developmental phenotypes by ectopic activation of Wnt signaling. *Developmental Biology*, *379*(2), 229–234. https://doi.org/10.1016/j.ydbio.2013.04.026

Li, B., Wang, Y., Fan, Y., Ouchi, T., Zhao, Z., & Li, L. (2021). Cranial Suture Mesenchymal Stem Cells: Insights and Advances. *Biomolecules*, *11*(8), 1129. https://doi.org/10.3390/biom11081129

Li, G., Liang, W., Ding, P., & Zhao, Z. (2021). Sutural fibroblasts exhibit the function of vascular endothelial cells upon mechanical strain. *Archives of Biochemistry and Biophysics*, *712*, 109046. https://doi.org/10.1016/j.abb.2021.109046

Li, J., Johnson, C. A., Smith, A. A., Hunter, D. J., Singh, G., Brunski, J. B., & Helms, J. A. (2016). Linking suckling biomechanics to the development of the palate. *Scientific Reports*, *6*(1), Article 1. https://doi.org/10.1038/srep20419

Li, J., Johnson, C. A., Smith, A. A., Salmon, B., Shi, B., Brunski, J., & Helms, J. A. (2015). Disrupting the intrinsic growth potential of a suture contributes to midfacial hypoplasia. *Bone*, *81*, 186–195. https://doi.org/10.1016/j.bone.2014.04.020

Li, S., Quarto, N., & Longaker, M. T. (2007). Dura mater-derived FGF-2 mediates mitogenic signaling in calvarial osteoblasts. *American Journal of Physiology. Cell Physiology*, *293*(6), C1834-1842. https://doi.org/10.1152/ajpcell.00135.2007

Li, W., Zhao, J., Wang, J., Sun, L., Xu, H., Sun, W., Pan, Y., Wang, H., & Zhang, W.-B. (2020). ROCK-TAZ signaling axis regulates mechanical tension-induced osteogenic differentiation of rat cranial sagittal suture mesenchymal stem cells. *Journal of Cellular Physiology*. https://doi.org/10.1002/jcp.29522

Liang, C., Liang, Q., Xu, X., Liu, X., Gao, X., Li, M., Yang, J., Xing, X., Huang, H., Tang, Q., Liao, L., & Tian, W. (2022). Bone morphogenetic protein 7 mediates stem cells migration and angiogenesis: Therapeutic potential for endogenous pulp

regeneration. *International Journal of Oral Science*, *14*(1), Article 1. https://doi.org/10.1038/s41368-022-00188-y

Liang, Y., Wen, L., Shang, F., Wu, J., Sui, K., & Ding, Y. (2016). Endothelial progenitors enhanced the osteogenic capacities of mesenchymal stem cells in vitro and in a rat alveolar bone defect model. *Archives of Oral Biology*, *68*, 123–130. https://doi.org/10.1016/j.archoralbio.2016.04.007

Liberton, D. K., Verma, P., Almpani, K., Fung, P. W., Mishra, R., Oberoi, S., Şenel, F. Ç., Mah, J. K., Huang, J., Padwa, B. L., & Lee, J. S. (2020). Craniofacial Analysis May Indicate Co-Occurrence of Skeletal Malocclusions and Associated Risks in Development of Cleft Lip and Palate. *Journal of Developmental Biology*, *8*(1), Article 1. https://doi.org/10.3390/jdb8010002

Lines, M. A., Ito, Y., Kernohan, K. D., Mears, W., Hurteau-Miller, J., Venkateswaran, S., Ward, L., Khatchadourian, K., McClintock, J., Bhola, P., Campeau, P. M., Boycott, K. M., Michaud, J., van Kuilenburg, A. B., Ferdinandusse, S., & Dyment, D. A. (2017). Yunis-Varón syndrome caused by biallelic VAC14 mutations. *European Journal of Human Genetics*, *25*(9), 1049–1054. https://doi.org/10.1038/ejhg.2017.99

Liu, A.-Q., Zhang, L.-S., Chen, J., Sui, B.-D., Liu, J., Zhai, Q.-M., Li, Y.-J., Bai, M., Chen, K., Jin, Y., Hu, C.-H., & Jin, F. (2020). Mechanosensing by Gli1+ cells contributes to the orthodontic force-induced bone remodelling. *Cell Proliferation*, *53*(5), e12810. https://doi.org/10.1111/cpr.12810

Liu, H., Xu, J., Lan, Y., Lim, H.-W., & Jiang, R. (2021). The Scleraxis Transcription Factor Directly Regulates Multiple Distinct Molecular and Cellular Processes During

Early Tendon Cell Differentiation. *Frontiers in Cell and Developmental Biology*, *9*, 654397. https://doi.org/10.3389/fcell.2021.654397

Liu, J., Li, Q., Liu, S., Gao, J., Qin, W., Song, Y., & Jin, Z. (2017). Periodontal Ligament Stem Cells in the Periodontitis Microenvironment Are Sensitive to Static Mechanical Strain. *Stem Cells International*, *2017*, 1380851. https://doi.org/10.1155/2017/1380851

Liu, J., Nam, H. K., Campbell, C., Gasque, K. C. da S., Millán, J. L., & Hatch, N. E. (2014). Tissue-nonspecific alkaline phosphatase deficiency causes abnormal craniofacial bone development in the Alpl(-/-) mouse model of infantile hypophosphatasia. *Bone*, *67*, 81–94. https://doi.org/10.1016/j.bone.2014.06.040

Liu, J., Zhao, Z., Li, J., Zou, L., Shuler, C., Zou, Y., Huang, X., Li, M., & Wang, J. (2009). Hydrostatic pressures promote initial osteodifferentiation with ERK1/2 not p38 MAPK signaling involved. *Journal of Cellular Biochemistry*, *107*(2), 224–232. https://doi.org/10.1002/jcb.22118

Liu, T. M., & Lee, E. H. (2013). Transcriptional Regulatory Cascades in Runx2-Dependent Bone Development. *Tissue Engineering. Part B, Reviews*, *19*(3), 254–263. https://doi.org/10.1089/ten.teb.2012.0527

Liu, Y., Suen, C.-W., Zhang, J., & Li, G. (2017). Current concepts on tenogenic differentiation and clinical applications. *Journal of Orthopaedic Translation*, *9*, 28–42. https://doi.org/10.1016/j.jot.2017.02.005

Lo, C. M., Wang, H. B., Dembo, M., & Wang, Y. L. (2000). Cell movement is guided by the rigidity of the substrate. *Biophysical Journal*, *79*(1), 144–152.

Logan, C. Y., & Nusse, R. (2004). The Wnt signaling pathway in development and disease. *Annual Review of Cell and Developmental Biology*, *20*, 781–810. https://doi.org/10.1146/annurev.cellbio.20.010403.113126

Long, F. (2012). Building strong bones: Molecular regulation of the osteoblast lineage. *Nature Reviews Molecular Cell Biology*, *13*(1), 27–38. https://doi.org/10.1038/nrm3254

Lorda-Diez, C. I., Montero, J. A., Choe, S., Garcia-Porrero, J. A., & Hurle, J. M. (2014). Ligand- and Stage-Dependent Divergent Functions of BMP Signaling in the Differentiation of Embryonic Skeletogenic Progenitors In Vitro. *Journal of Bone and Mineral Research*, *29*(3), 735–748. https://doi.org/10.1002/jbmr.2077

Lorthongpanich, C., Thumanu, K., Tangkiettrakul, K., Jiamvoraphong, N., Laowtammathron, C., Damkham, N., U-pratya, Y., & Issaragrisil, S. (2019). YAP as a key regulator of adipo-osteogenic differentiation in human MSCs. *Stem Cell Research & Therapy*, *10*(1), 402. https://doi.org/10.1186/s13287-019-1494-4

Lotlikar, P. P., Creanga, A. G., & Singer, S. R. (2018). Clinical and radiological findings in a severe case of cleidocranial dysplasia. *BMJ Case Reports*, *2018*, bcr-2018-226671. https://doi.org/10.1136/bcr-2018-226671

Low, K., Ashraf, T., Canham, N., Clayton-Smith, J., Deshpande, C., Donaldson, A., Fisher, R., Flinter, F., Foulds, N., Fryer, A., Gibson, K., Hayes, I., Hills, A., Holder, S., Irving, M., Joss, S., Kivuva, E., Lachlan, K., Magee, A., … Smithson, S. (2016). Clinical and genetic aspects of KBG syndrome. *American Journal of Medical Genetics. Part A*, *170*(11), 2835–2846. https://doi.org/10.1002/ajmg.a.37842

Lowe, L. H., Booth, T. N., Joglar, J. M., & Rollins, N. K. (2000). Midface Anomalies in Children. *RadioGraphics*, *20*(4), 907–922. https://doi.org/10.1148/radiographics.20.4.g00jl07907

Lu, Y., & Feng, J. Q. (2011). FGF23 in Skeletal Modeling and Remodeling. *Current Osteoporosis Reports*, *9*(2), 103–108. https://doi.org/10.1007/s11914-011-0053-4

Lucas-Herald, A. K., Zürbig, P., Mason, A., Kinning, E., Brown, C. E., Mansoorian, B., Mullen, W., Ahmed, S. F., & Delles, C. (2019). Proteomic Evidence of Biological Aging in a Child with a Compound Heterozygous ZMPSTE24 Mutation. *Proteomics. Clinical Applications*, *13*(2), e1800135. https://doi.org/10.1002/prca.201800135

Lv, P., Gao, P., Tian, G., Yang, Y., Mo, F., Wang, Z., Sun, L., Kuang, M., & Wang, Y. (2020). Osteocyte-derived exosomes induced by mechanical strain promote human periodontal ligament stem cell proliferation and osteogenic differentiation via the miR-181b-5p/PTEN/AKT signaling pathway. *Stem Cell Research & Therapy*, *11*, 295. https://doi.org/10.1186/s13287-020-01815-3

Machol, K., Mendoza-Londono, R., & Lee, B. (2017). Cleidocranial Dysplasia Spectrum Disorder. In M. P. Adam, H. H. Ardinger, R. A. Pagon, S. E. Wallace, L. J. Bean, G. Mirzaa, & A. Amemiya (Eds.), *GeneReviews®*. University of Washington, Seattle. http://www.ncbi.nlm.nih.gov/books/NBK1513/

Maciel, G. B. M., Maciel, R. M., & Danesi, C. C. (2023). Bone cells and their role in physiological remodeling. *Molecular Biology Reports*. https://doi.org/10.1007/s11033-022-08190-7

Maes, C., Kobayashi, T., Selig, M. K., Torrekens, S., Roth, S. I., Mackem, S., Carmeliet, G., & Kronenberg, H. M. (2010). Osteoblast Precursors, but Not Mature Osteoblasts, Move into Developing and Fractured Bones along with Invading Blood Vessels. *Developmental Cell*, *19*(2), 329. https://doi.org/10.1016/j.devcel.2010.07.010

Maga, A. M. (2016). Postnatal Development of the Craniofacial Skeleton in Male C57BL/6J Mice. *Journal of the American Association for Laboratory Animal Science : JAALAS*, *55*(2), 131–136.

Mai, S., Wei, K., Flenniken, A., Adamson, S. L., Rossant, J., Aubin, J. E., & Gong, S.-G. (2010). The missense mutation W290R in Fgfr2 causes developmental defects from aberrant IIIb and IIIc signaling. *Developmental Dynamics*, *239*(6), 1888–1900. https://doi.org/10.1002/dvdy.22314

Makar, K. G., Buchman, S. R., & Vercler, C. J. (2021). Bone Morphogenetic Protein-2 and Demineralized Bone Matrix in Difficult Bony Reconstructions in Cleft Patients. *Plastic and Reconstructive Surgery Global Open*, *9*(6), e3611. https://doi.org/10.1097/GOX.0000000000003611

Malik, Z., Roth, D. M., Eaton, F., Theodor, J. M., & Graf, D. (2020). Mesenchymal Bmp7 Controls Onset of Tooth Mineralization: A Novel Way to Regulate Molar Cusp Shape. *Frontiers in Physiology*, *11*, 698. https://doi.org/10.3389/fphys.2020.00698

Mammoto, T., Mammoto, A., Jiang, A., Jiang, E., Hashmi, B., & Ingber, D. E. (2015). Mesenchymal condensation-dependent accumulation of collagen VI stabilizes organ-specific cell fates during embryonic tooth formation. *Developmental Dynamics*, *244*(6), 713–723. https://doi.org/10.1002/dvdy.24264

Manokawinchoke, J., Pavasant, P., & Osathanon, T. (2017). Intermittent compressive stress regulates Notch target gene expression via transforming growth factor-β signaling in murine pre-osteoblast cell line. *Archives of Oral Biology*, *82*, 47–54. https://doi.org/10.1016/j.archoralbio.2017.05.020

Manzari-Tavakoli, A., Babajani, A., Farjoo, M. H., Hajinasrollah, M., Bahrami, S., & Niknejad, H. (2022). The Cross-Talks Among Bone Morphogenetic Protein (BMP) Signaling and Other Prominent Pathways Involved in Neural Differentiation. *Frontiers in Molecular Neuroscience*, *15*. https://doi.org/10.3389/fnmol.2022.827275

Markey, M. J., & Marshall, C. R. (2007). Linking form and function of the fibrous joints in the skull: A new quantification scheme for cranial sutures using the extant fish Polypterus endlicherii. *Journal of Morphology*, *268*(1), 89–102. https://doi.org/10.1002/jmor.10504

Maruyama, T., Jeong, J., Sheu, T.-J., & Hsu, W. (2016). Stem cells of the suture mesenchyme in craniofacial bone development, repair and regeneration. *Nature Communications*, *7*(1), 1–11. https://doi.org/10.1038/ncomms10526

Maruyama, T., Stevens, R., Boka, A., DiRienzo, L., Chang, C., Yu, H.-M. I., Nishimori, K., Morrison, C., & Hsu, W. (2021). BMPR1A maintains skeletal stem cell properties in craniofacial development and craniosynostosis. *Science Translational Medicine*, *13*(583), eabb4416. https://doi.org/10.1126/scitranslmed.abb4416

Marzuillo, P., Grandone, A., Perrotta, S., Ruggiero, L., Capristo, C., Luongo, C., Miraglia del Giudice, E., & Perrone, L. (2016). Very early onset of autoimmune thyroiditis

in a toddler with severe hypothyroidism presentation: A case report. *Italian Journal of Pediatrics*, *42*(1), 61. https://doi.org/10.1186/s13052-016-0270-7

Massagué, J. (2000). How cells read TGF-β signals. *Nature Reviews Molecular Cell Biology*, *1*(3), 169–178. https://doi.org/10.1038/35043051

Massagué, J., Seoane, J., & Wotton, D. (2005). Smad transcription factors. *Genes & Development*, *19*(23), 2783–2810. https://doi.org/10.1101/gad.1350705

Matthews, H. S., Penington, A. J., Hardiman, R., Fan, Y., Clement, J. G., Kilpatrick, N. M., & Claes, P. D. (2018). Modelling 3D craniofacial growth trajectories for population comparison and classification illustrated using sex-differences. *Scientific Reports*, *8*(1), 4771. https://doi.org/10.1038/s41598-018-22752-5

Mazzitelli, J. A., Smyth, L. C. D., Cross, K. A., Dykstra, T., Sun, J., Du, S., Mamuladze, T., Smirnov, I., Rustenhoven, J., & Kipnis, J. (2022). Cerebrospinal fluid regulates skull bone marrow niches via direct access through dural channels. *Nature Neuroscience*, *25*(5), 555–560. https://doi.org/10.1038/s41593-022-01029-1

McBratney-Owen, B., Iseki, S., Bamforth, S. D., Olsen, B. R., & Morriss-Kay, G. M. (2008). Development and tissue origins of the mammalian cranial base. *Developmental Biology*, *322*(1), 121–132. https://doi.org/10.1016/j.ydbio.2008.07.016

McGuire, T. P., Gomes, P. P., Lam, D. K., & Sándor, G. K. B. (2007). Cranioplasty for midline metopic suture defects in adults with cleidocranial dysplasia. *Oral Surgery, Oral Medicine, Oral Pathology, Oral Radiology, and Endodontology*, *103*(2), 175–179. https://doi.org/10.1016/j.tripleo.2006.02.014

Mchaile, D., Mrindoko, P., Mselle, M., Meleki, E., Kimambo, E., Likiliwike, A., & Lodhia, J. (2020). Neonatal Polycystic Kidney Disease in a One-Day-Old Baby: A Case Report. *Pediatric Health, Medicine and Therapeutics*, *11*, 445–448. https://doi.org/10.2147/PHMT.S271209

Melkoniemi, M., Koillinen, H., Männikkö, M., Warman, M. L., Pihlajamaa, T., Kääriäinen, H., Rautio, J., Hukki, J., Stofko, J. A., Cisneros, G. J., Krakow, D., Cohn, D. H., Kere, J., & Ala-Kokko, L. (2003). Collagen XI sequence variations in nonsyndromic cleft palate, Robin sequence and micrognathia. *European Journal of Human Genetics*, *11*(3), 265–270. https://doi.org/10.1038/sj.ejhg.5200950

Melville, H., Wang, Y., Taub, P. J., & Jabs, E. W. (2010). Genetic basis of potential therapeutic strategies for craniosynostosis. *American Journal of Medical Genetics. Part A*, *152A*(12), 3007–3015. https://doi.org/10.1002/ajmg.a.33703

Menon, S., Salhotra, A., Shailendra, S., Tevlin, R., Ransom, R. C., Januszyk, M., Chan, C. K. F., Behr, B., Wan, D. C., Longaker, M. T., & Quarto, N. (2021). Skeletal stem and progenitor cells maintain cranial suture patency and prevent craniosynostosis. *Nature Communications*, *12*(1), 4640. https://doi.org/10.1038/s41467-021-24801-6

Merkuri, F., & Fish, J. L. (2019). Developmental processes regulate craniofacial variation in disease and evolution. *Genesis (New York, N.Y.: 2000)*, *57*(1), e23249. https://doi.org/10.1002/dvg.23249

Merrill, A. E., Bochukova, E. G., Brugger, S. M., Ishii, M., Pilz, D. T., Wall, S. A., Lyons, K. M., Wilkie, A. O. M., & Maxson, R. E. (2006). Cell mixing at a neural crest-mesoderm boundary and deficient ephrin-Eph signaling in the pathogenesis of

craniosynostosis. *Human Molecular Genetics*, *15*(8), 1319–1328. https://doi.org/10.1093/hmg/ddl052

Mijanović, O., Jakovleva, A., Branković, A., Zdravkova, K., Pualic, M., Belozerskaya, T. A., Nikitkina, A. I., Parodi, A., & Zamyatnin, A. A. (2022). Cathepsin K in Pathological Conditions and New Therapeutic and Diagnostic Perspectives. *International Journal of Molecular Sciences*, *23*(22), Article 22. https://doi.org/10.3390/ijms232213762

Min Swe, N. M., Kobayashi, Y., Kamimoto, H., & Moriyama, K. (2021). Aberrantly activated Wnt/β-catenin pathway co-receptors LRP5 and LRP6 regulate osteoblast differentiation in the developing coronal sutures of an Apert syndrome (Fgfr2S252W /+) mouse model. *Developmental Dynamics: An Official Publication of the American Association of Anatomists*, *250*(3), 465–476. https://doi.org/10.1002/dvdy.239

Minatogawa, M., Unzaki, A., Morisaki, H., Syx, D., Sonoda, T., Janecke, A. R., Slavotinek, A., Voermans, N. C., Lacassie, Y., Mendoza-Londono, R., Wierenga, K. J., Jayakar, P., Gahl, W. A., Tifft, C. J., Figuera, L. E., Hilhorst-Hofstee, Y., Maugeri, A., Ishikawa, K., Kobayashi, T., … Kosho, T. (2021). Clinical and molecular features of 66 patients with musculocontractural Ehlers−Danlos syndrome caused by pathogenic variants in CHST14 (mcEDS-CHST14). *Journal of Medical Genetics*. https://doi.org/10.1136/jmedgenet-2020-107623

Miyazono, K., Kamiya, Y., & Morikawa, M. (2010). Bone morphogenetic protein receptors and signal transduction. *The Journal of Biochemistry*, *147*(1), 35–51. https://doi.org/10.1093/jb/mvp148

Moazen, M., Hejazi, M., Savery, D., Jones, D., Marghoub, A., Alazmani, A., & Pauws, E. (2022). Mechanical loading of cranial joints minimizes the craniofacial phenotype in Crouzon syndrome. *Scientific Reports*, *12*(1), Article 1. https://doi.org/10.1038/s41598-022-13807-9

Mohn, A., De Leonibus, C., de Giorgis, T., Mornet, E., & Chiarelli, F. (2011). Hypophosphatasia in a child with widened anterior fontanelle: Lessons learned from late diagnosis and incorrect treatment. *Acta Paediatrica (Oslo, Norway: 1992)*, *100*(7), e43-46. https://doi.org/10.1111/j.1651-2227.2011.02228.x

Montecino, M., Carrasco, M. E., & Nardocci, G. (2021). Epigenetic Control of Osteogenic Lineage Commitment. *Frontiers in Cell and Developmental Biology*, *8*, 1759. https://doi.org/10.3389/fcell.2020.611197

Morita, Y., Yamashita, T., Toku, T., & Ju, Y. (2018). Optimization of differentiation time of mesenchymal-stem-cell to tenocyte under a cyclic stretching with a microgrooved culture membrane and selected measurement cells. *Acta of Bioengineering and Biomechanics*, *20*(1), 3–10.

Mornet, E. (2007). Hypophosphatasia. *Orphanet Journal of Rare Diseases*, *2*(1), 40. https://doi.org/10.1186/1750-1172-2-40

Moss, M. L. (1957). Experimental alteration of sutural area morphology. *The Anatomical Record*, *127*(3), 569–589. https://doi.org/10.1002/ar.1091270307

Nahabet, E. H., Gatherwright, J., Vockley, J., Henderson, N., Tomei, K. L., Grigorian, A. P., Kaminski, B., Bass, N., Selman, W. R., & Lakin, G. E. (2016). Postnatal Pancraniosynostosis in a Patient with Infantile Hypophosphatasia. *The Cleft Palate-Craniofacial Journal*, *53*(6), 741–744. https://doi.org/10.1597/15-027

Naidu, P., Celie, K.-B., Wlodarczyk, J., Nagenast, E., Yao, C., & Magee, W. (2021). Sagittal Growth Restriction of the Midface following Cleft Lip Repair: A Systematic Review and Meta-analysis. *Journal of Oral and Maxillofacial Surgery*, *79*(10, Supplement), e64. https://doi.org/10.1016/j.joms.2021.08.090

Nakajima, J., Okamoto, N., Shiraishi, J., Nishimura, G., Nakashima, M., Tsurusaki, Y., Saitsu, H., Kawashima, H., Matsumoto, N., & Miyake, N. (2013). Novel FIG4 mutations in Yunis–Varon syndrome. *Journal of Human Genetics*, *58*(12), Article 12. https://doi.org/10.1038/jhg.2013.104

Nara, M., Kitamura, K., Yamamoto, M., Nagakura, R., Mitomo, K., Matsunaga, S., & Abe, S. (2017). Developmental mechanism of muscle–tendon–bone complex in the fetal soft palate. *Archives of Oral Biology*, *82*, 71–78. https://doi.org/10.1016/j.archoralbio.2017.06.001

Nasrollahi, S., Walter, C., Loza, A. J., Schimizzi, G. V., Longmore, G. D., & Pathak, A. (2017). Past matrix stiffness primes epithelial cells and regulates their future collective migration through a mechanical memory. *Biomaterials*, *146*, 146–155. https://doi.org/10.1016/j.biomaterials.2017.09.012

Naujoks, C., Meyer, U., Wiesmann, H.-P., Jäsche-Meyer, J., Hohoff, A., Depprich, R., & Handschel, J. (2008). Principles of cartilage tissue engineering in TMJ reconstruction. *Head & Face Medicine*, *4*, 3. https://doi.org/10.1186/1746-160X-4-3

Nelke, K. H., Pawlak, W., Kurlej, W., & Gerber, H. (2014). Metopic frontal suture in a patient with severe dentofacial deformity undergoing bimaxillary surgery. *The*

Journal of Craniofacial Surgery, *25*(2), 517–518. https://doi.org/10.1097/SCS.0000000000000681

Nelson, C. M., Jean, R. P., Tan, J. L., Liu, W. F., Sniadecki, N. J., Spector, A. A., & Chen, C. S. (2005). Emergent patterns of growth controlled by multicellular form and mechanics. *Proceedings of the National Academy of Sciences*, *102*(33), 11594–11599. https://doi.org/10.1073/pnas.0502575102

Nelson, D. K., & Williams, T. (2004). Frontonasal process-specific disruption of AP-2α results in postnatal midfacial hypoplasia, vascular anomalies, and nasal cavity defects. *Developmental Biology*, *267*(1), 72–92. https://doi.org/10.1016/j.ydbio.2003.10.033

Newfeld, S. J., Wisotzkey, R. G., & Kumar, S. (1999). Molecular Evolution of a Developmental Pathway: Phylogenetic Analyses of Transforming Growth Factor-β Family Ligands, Receptors and Smad Signal Transducers. *Genetics*, *152*(2), 783–795. https://doi.org/10.1093/genetics/152.2.783

Nguyen, P., Abdirahman, S. M., & Putoczki, T. L. (2019). Emerging roles for Interleukin-11 in disease. *Growth Factors (Chur, Switzerland)*, *37*(1–2), 1–11. https://doi.org/10.1080/08977194.2019.1620227

Nguyen, V., Meyers, C. A., Yan, N., Agarwal, S., Levi, B., & James, A. W. (2017). BMP-2-induced bone formation and neural inflammation. *Journal of Orthopaedics*, *14*(2), 252–256. https://doi.org/10.1016/j.jor.2017.03.003

Nifuji, A., & Noda, M. (1999). Coordinated Expression of Noggin and Bone Morphogenetic Proteins (BMPs) During Early Skeletogenesis and Induction of

Noggin Expression by BMP-7. *Journal of Bone and Mineral Research*, *14*(12), 2057–2066. https://doi.org/10.1359/jbmr.1999.14.12.2057

Novak, S., Madunic, J., Shum, L., Vucetic, M., Wang, X., Tanigawa, H., Ghosh, M., Sanjay, A., & Kalajzic, I. (2023). PDGF inhibits BMP2-induced bone healing. *Npj Regenerative Medicine*, *8*(1), 1–10. https://doi.org/10.1038/s41536-023-00276-5

Novoseletskaya, E. S., Evdokimov, P. V., & Efimenko, A. Y. (2023). Extracellular matrix-induced signaling pathways in mesenchymal stem/stromal cells. *Cell Communication and Signaling : CCS*, *21*, 244. https://doi.org/10.1186/s12964-023-01252-8

Odagaki, N., Ishihara, Y., Wang, Z., Ei Hsu Hlaing, E., Nakamura, M., Hoshijima, M., Hayano, S., Kawanabe, N., & Kamioka, H. (2018). Role of Osteocyte-PDL Crosstalk in Tooth Movement via SOST/Sclerostin. *Journal of Dental Research*, *97*(12), 1374–1382. https://doi.org/10.1177/0022034518771331

Oheim, R., Tsourdi, E., Seefried, L., Beller, G., Schubach, M., Vettorazzi, E., Stürznickel, J., Rolvien, T., Ehmke, N., Delsmann, A., Genest, F., Krüger, U., Zemojtel, T., Barvencik, F., Schinke, T., Jakob, F., Hofbauer, L. C., Mundlos, S., & Kornak, U. (2022). Genetic Diagnostics in Routine Osteological Assessment of Adult Low Bone Mass Disorders. *The Journal of Clinical Endocrinology & Metabolism*, *107*(7), e3048–e3057. https://doi.org/10.1210/clinem/dgac147

O'Loughlin, V. D. (2004). Effects of different kinds of cranial deformation on the incidence of wormian bones. *American Journal of Physical Anthropology*, *123*(2), 146–155. https://doi.org/10.1002/ajpa.10304

Ong, K. L., Villarraga, M. L., Lau, E., Carreon, L. Y., Kurtz, S. M., & Glassman, S. D. (2010). Off-Label Use of Bone Morphogenetic Proteins in the United States Using Administrative Data. *Spine*, *35*(19), 1794. https://doi.org/10.1097/BRS.0b013e3181ecf6e4

Oppenheimer, A. J., Rhee, S. T., Goldstein, S. A., & Buchman, S. R. (2009). Force-Induced Craniosynostosis in the Murine Sagittal Suture. *Plastic and Reconstructive Surgery*, *124*(6), 1840–1848. https://doi.org/10.1097/PRS.0b013e3181bf806c

Opperman, L. A. (2000). Cranial sutures as intramembranous bone growth sites. *Developmental Dynamics: An Official Publication of the American Association of Anatomists*, *219*(4), 472–485. https://doi.org/10.1002/1097-0177(2000)9999:9999<::AID-DVDY1073>3.0.CO;2-F

Opperman, L. A., Passarelli, R. W., Morgan, E. P., Reintjes, M., & Ogle, R. C. (1995). Cranial sutures require tissue interactions with dura mater to resist osseous obliteration in vitro. *Journal of Bone and Mineral Research*, *10*(12), 1978–1987. https://doi.org/10.1002/jbmr.5650101218

Opperman, L. A., Passarelli, R. W., Nolen, A. A., Gampper, T. J., Lin, K. Y. K., & Ogle, R. C. (1996). Dura mater secretes soluble heparin-binding factors required for cranial suture morphogenesis. *In Vitro Cellular & Developmental Biology - Animal*, *32*(10), 627–632. https://doi.org/10.1007/BF02724047

Otaify, G. A., Abdel-Hamid, M. S., Mehrez, M. I., Aboul-Ezz, E., Zaki, M. S., Aglan, M. S., & Temtamy, S. A. (2018). Genetic study of eight Egyptian patients with pycnodysostosis: Identification of novel CTSK mutations and founder effect.

Osteoporosis International, *29*(8), 1833–1841. https://doi.org/10.1007/s00198-018-4555-0

Ovchinnikov, D. A., Deng, J. M., Ogunrinu, G., & Behringer, R. R. (2000). Col2a1-directed expression of Cre recombinase in differentiating chondrocytes in transgenic mice. *Genesis*, *26*(2), 145–146. https://doi.org/10.1002/(SICI)1526-968X(200002)26:2<145::AID-GENE14>3.0.CO;2-C

Ozer, L., Unsal, E., Aktuna, S., Baltaci, V., Celikkol, P., Akyigit, F., Sen, A., Ayvaz, O., & Balci, S. (2016). Mandibuloacral dysplasia and LMNA A529V mutation in Turkish patients with severe skeletal changes and absent breast development. *Clinical Dysmorphology*, *25*(3), 91–97. https://doi.org/10.1097/MCD.0000000000000132

Pakvasa, M., Haravu, P., Boachie-Mensah, M., Jones, A., Coalson, E., Liao, J., Zeng, Z., Wu, D., Qin, K., Wu, X., Luo, H., Zhang, J., Zhang, M., He, F., Mao, Y., Zhang, Y., Niu, C., Wu, M., Zhao, X., … Reid, R. R. (2021). Notch signaling: Its essential roles in bone and craniofacial development. *Genes & Diseases*, *8*(1), 8–24. https://doi.org/10.1016/j.gendis.2020.04.006

Pan, H. C., Lee, S., Ting, K., Shen, J., Wang, C., Nguyen, A., Berthiaume, E. A., Zara, J. N., Turner, A. S., Seim, H. B., Kwak, J. H., Zhang, X., & Soo, C. (2017). Cyst-Like Osteolytic Formations in Recombinant Human Bone Morphogenetic Protein-2 (rhBMP-2) Augmented Sheep Spinal Fusion. *The American Journal of Pathology*, *187*(7), 1485–1495. https://doi.org/10.1016/j.ajpath.2017.03.010

Panos, J. A., Coenen, M. J., Nagelli, C. V., McGlinch, E. B., Atasoy-Zeybek, A., Padilla, C. L. D., Coghlan, R. F., Johnstone, B., Ferreira, E., Porter, R. M., Vega, R. E. D.

la, & Evans, C. H. (2023). IL-1Ra gene transfer potentiates BMP2-mediated bone healing by redirecting osteogenesis toward endochondral ossification. *Molecular Therapy*, *31*(2), 420–434. https://doi.org/10.1016/j.ymthe.2022.10.007

Parsons, J. T., Horwitz, A. R., & Schwartz, M. A. (2010). Cell adhesion: Integrating cytoskeletal dynamics and cellular tension. *Nature Reviews. Molecular Cell Biology*, *11*(9), 633–643. https://doi.org/10.1038/nrm2957

Pascual-Castroviejo, I., Lopez-Martin, V., Rodriguez-Costa, T., & Pascual-Pascual, J. I. (1975). Radiological and anatomical aspects of the cranial metastases of neuroblastomas. *Neuroradiology*, *9*(1), 33–38. https://doi.org/10.1007/BF00330134

Pastrana-Ayala, R., Peña-Castro, G. L., Valencia-Herrera, A. M., Mena-Cedillos, C. A., Toussaint-Caire, S., Akaki-Carreño, Y. I., García-Delgado, C., Morán-Barroso, V. F., & Toledo-Bahena, M. (2017). Craniosynostosis, delayed closure of the fontanelle, anal, genitourinary, and skin abnormalities (CDAGS syndrome): First report in a Mexican patient and review of the literature. *International Journal of Dermatology*, *56*(4), 435–439. https://doi.org/10.1111/ijd.13504

Pereira, A. R., Lipphaus, A., Ergin, M., Salehi, S., Gehweiler, D., Rudert, M., Hansmann, J., & Herrmann, M. (2021). Modeling of the Human Bone Environment: Mechanical Stimuli Guide Mesenchymal Stem Cell–Extracellular Matrix Interactions. *Materials*, *14*(16), Article 16. https://doi.org/10.3390/ma14164431

Petzold, J., & Gentleman, E. (2021). Intrinsic Mechanical Cues and Their Impact on Stem Cells and Embryogenesis. *Frontiers in Cell and Developmental Biology*, *9*. https://www.frontiersin.org/articles/10.3389/fcell.2021.761871

Picoli, C. de C., Birbrair, A., & Li, Z. (2024). Pericytes as the Orchestrators of Vasculature and Adipogenesis. *Genes*, *15*(1), Article 1. https://doi.org/10.3390/genes15010126

Piña, J. O., Raju, R., Roth, D. M., Winchester, E. W., Chattaraj, P., Kidwai, F., Faucz, F. R., Iben, J., Mitra, A., Campbell, K., Fridell, G., Esnault, C., Cotney, J. L., Dale, R. K., & D'Souza, R. N. (2023). Multimodal spatiotemporal transcriptomic resolution of embryonic palate osteogenesis. *Nature Communications*, *14*(1), Article 1. https://doi.org/10.1038/s41467-023-41349-9

Pochedly, C., Sarrafi, G., & Dobbs, J. B. (1974). Widened Cranial Sutures in Metastatic Neuroblastoma. *JAMA*, *227*(6), 659. https://doi.org/10.1001/jama.1974.03230190051023

Poon, B., Kha, T., Tran, S., & Dass, C. R. (2016). Bone morphogenetic protein-2 and bone therapy: Successes and pitfalls. *Journal of Pharmacy and Pharmacology*, *68*(2), 139–147. https://doi.org/10.1111/jphp.12506

Przybyla, L., Lakins, J. N., & Weaver, V. M. (2016). Tissue Mechanics Orchestrate Wnt-Dependent Human Embryonic Stem Cell Differentiation. *Cell Stem Cell*, *19*(4), 462–475. https://doi.org/10.1016/j.stem.2016.06.018

Qin, L., Liu, W., Cao, H., & Xiao, G. (2020). Molecular mechanosensors in osteocytes. *Bone Research*, *8*. https://doi.org/10.1038/s41413-020-0099-y

Qin, X., Jiang, Q., Miyazaki, T., & Komori, T. (2019). Runx2 regulates cranial suture closure by inducing hedgehog, Fgf, Wnt and Pthlh signaling pathway gene expressions in suture mesenchymal cells. *Human Molecular Genetics*, *28*(6), 896–911. https://doi.org/10.1093/hmg/ddy386

Qiu, S., Lavallée-Adam, M., & Côté, M. (2021). Proximity Interactome Map of the Vac14–Fig4 Complex Using BioID. *Journal of Proteome Research*, *20*(11), 4959–4973. https://doi.org/10.1021/acs.jproteome.1c00408

Rafferty, K. L., & Herring, S. W. (1999). Craniofacial sutures: Morphology, growth, and in vivo masticatory strains. *Journal of Morphology*, *242*(2), 167–179. https://doi.org/10.1002/(SICI)1097-4687(199911)242:2<167::AID-JMOR8>3.0.CO;2-1

Ramirez, F., & Rifkin, D. B. (2009). Extracellular microfibrils; contextual platforms for TGFβ and BMP signaling. *Current Opinion in Cell Biology*, *21*(5), 616–622. https://doi.org/10.1016/j.ceb.2009.05.005

Ranade, S. S., Woo, S.-H., Dubin, A. E., Moshourab, R. A., Wetzel, C., Petrus, M., Mathur, J., Bégay, V., Coste, B., Mainquist, J., Wilson, A. J., Francisco, A. G., Reddy, K., Qiu, Z., Wood, J. N., Lewin, G. R., & Patapoutian, A. (2014). Piezo2 is the major transducer of mechanical forces for touch sensation in mice. *Nature*, *516*(7529), 121–125. https://doi.org/10.1038/nature13980

Regan, J., & Long, F. (2013). Notch Signaling and Bone Remodeling. *Current Osteoporosis Reports*, *11*(2), 126–129. https://doi.org/10.1007/s11914-013-0145-4

Rice, D. P. (2008). Developmental Anatomy of Craniofacial Sutures. *Craniofacial Sutures*, *12*, 1–21. https://doi.org/10.1159/000115028

Rigueur, D., Brugger, S., Anbarchian, T., Kim, J. K., Lee, Y., & Lyons, K. M. (2015). The Type I BMP Receptor ACVR1/ALK2 is Required for Chondrogenesis During Development. *Journal of Bone and Mineral Research*, *30*(4), 733–741. https://doi.org/10.1002/jbmr.2385

Rindone, A. N., Liu, X., Farhat, S., Perdomo-Pantoja, A., Witham, T. F., Coutu, D. L., Wan, M., & Grayson, W. L. (2021). Quantitative 3D imaging of the cranial microvascular environment at single-cell resolution. *Nature Communications*, *12*(1), 6219. https://doi.org/10.1038/s41467-021-26455-w

Roberts, T., Stephen, L., & Beighton, P. (2013). Cleidocranial dysplasia: A review of the dental, historical, and practical implications with an overview of the South African experience. *Oral Surgery, Oral Medicine, Oral Pathology and Oral Radiology*, *115*(1), 46–55. https://doi.org/10.1016/j.oooo.2012.07.435

Robinson, J. A., Chatterjee-Kishore, M., Yaworsky, P. J., Cullen, D. M., Zhao, W., Li, C., Kharode, Y., Sauter, L., Babij, P., Brown, E. L., Hill, A. A., Akhter, M. P., Johnson, M. L., Recker, R. R., Komm, B. S., & Bex, F. J. (2006). Wnt/β-Catenin Signaling Is a Normal Physiological Response to Mechanical Loading in Bone. *Journal of Biological Chemistry*, *281*(42), 31720–31728. https://doi.org/10.1074/jbc.M602308200

Romani, P., Valcarcel-Jimenez, L., Frezza, C., & Dupont, S. (2021). Crosstalk between mechanotransduction and metabolism. *Nature Reviews Molecular Cell Biology*, *22*(1), 22–38. https://doi.org/10.1038/s41580-020-00306-w

Romans, M., Sambandam, B., Moses, J., & Pragash, M. (2020). A rare case of pycnodysostosis: Technical difficulties in managing long bone fractures. *Journal of Clinical Orthopaedics and Trauma*, *11*(2), 332–338. https://doi.org/10.1016/j.jcot.2018.09.012

Romanyk, D. L., Liu, S. S., Long, R., & Carey, J. P. (2014). Considerations for determining relaxation constants from creep modeling of nonlinear suture tissue. *International*

Journal of Mechanical Sciences, *85*, 179–186. https://doi.org/10.1016/j.ijmecsci.2014.05.022

Root, A. W., & Levine, M. A. (2023). One half-century of advances in the evaluation and management of disorders of bone and mineral metabolism in children and adolescents. *Journal of Pediatric Endocrinology and Metabolism*, *36*(2), 105–118. https://doi.org/10.1515/jpem-2022-0624

Rosenberg, P., Arlis, H. R., Haworth, R. D., Heier, L., Hoffman, L., & LaTrenta, G. (1997). The role of the cranial base in facial growth: Experimental craniofacial synostosis in the rabbit. *Plastic and Reconstructive Surgery*, *99*(5), 1396–1407. https://doi.org/10.1097/00006534-199704001-00030

Ross, R. B. (1987). Treatment variables affecting facial growth in complete unilateral cleft lip and palate. *The Cleft Palate Journal*, *24*(1), 5–77.

Roth, D. M., Baddam, P., Lin, H., Vidal-García, M., Aponte, J. D., De Souza, S.-T., Godziuk, D., Watson, A. E. S., Footz, T., Schachter, N. F., Egan, S. E., Hallgrímsson, B., Graf, D., & Voronova, A. (2021). The Chromatin Regulator Ankrd11 Controls Palate and Cranial Bone Development. *Frontiers in Cell and Developmental Biology*, *0*. https://doi.org/10.3389/fcell.2021.645386

Roth, D. M., Bayona, F., Baddam, P., & Graf, D. (2021). Craniofacial Development: Neural Crest in Molecular Embryology. *Head and Neck Pathology*, *15*(1), 1–15. https://doi.org/10.1007/s12105-021-01301-z

Roth, D. M., Piña, J. O., MacPherson, M., Budden, C., & Graf, D. (2023). Physiology and Clinical Manifestations of Pathologic Cranial Suture Widening. *The Cleft Palate*

Craniofacial Journal, 10556656231178438. https://doi.org/10.1177/10556656231178438

Roth, D. M., Piña, J. O., Raju, R., Iben, J., Faucz, F. R., Makareeva, E., Leikin, S., Graf, D., & D'Souza, R. N. (2024). *Tendon-associated gene expression precedes osteogenesis in mid-palatal suture establishment* (p. 2024.05.11.590129). bioRxiv. https://doi.org/10.1101/2024.05.11.590129

Roth, D. M., Puttagunta, L., & Graf, D. (2022). Histological Techniques for Sectioning Bones of the Vertebrate Craniofacial Skeleton. In S. Dworkin (Ed.), *Craniofacial Development: Methods and Protocols* (pp. 187–200). Springer US. https://doi.org/10.1007/978-1-0716-1847-9_12

Roth, D. M., Souter, K., & Graf, D. (2022). Craniofacial sutures: Signaling centres integrating mechanosensation, cell signaling, and cell differentiation. *European Journal of Cell Biology*, *101*(3), 151258. https://doi.org/10.1016/j.ejcb.2022.151258

Rys, J. P., Monteiro, D. A., & Alliston, T. (2016). Mechanobiology of TGFβ Signaling in the Skeleton. *Matrix Biology : Journal of the International Society for Matrix Biology*, *52–54*, 413–425. https://doi.org/10.1016/j.matbio.2016.02.002

Sait, H., Srivastava, P., Gupta, N., Kabra, M., Kapoor, S., Ranganath, P., Rungsung, I., Mandal, K., Saxena, D., Dalal, A., Roy, A., Pabbati, J., & Phadke, S. R. (2021). Phenotypic and genotypic spectrum of CTSK variants in a cohort of twenty-five Indian patients with pycnodysostosis. *European Journal of Medical Genetics*, *64*(7), 104235. https://doi.org/10.1016/j.ejmg.2021.104235

Salazar, V. S., Ohte, S., Capelo, L. P., Gamer, L., & Rosen, V. (2016). Specification of osteoblast cell fate by canonical Wnt signaling requires Bmp2. *Development (Cambridge, England)*, *143*(23), 4352–4367. https://doi.org/10.1242/dev.136879

Salles, J. P. (2015). Clinical Forms and Animal Models of Hypophosphatasia. *Sub-Cellular Biochemistry*, *76*, 3–24. https://doi.org/10.1007/978-94-017-7197-9_1

Sampath, T. K., & Reddi, A. H. (1983). Homology of bone-inductive proteins from human, monkey, bovine, and rat extracellular matrix. *Proceedings of the National Academy of Sciences*, *80*(21), 6591–6595. https://doi.org/10.1073/pnas.80.21.6591

Sampath, T. K., & Reddi, A. H. (2020). Discovery of bone morphogenetic proteins—A historical perspective. *Bone*, *140*, 115548. https://doi.org/10.1016/j.bone.2020.115548

Samuels, B. D., Aho, R., Brinkley, J. F., Bugacov, A., Feingold, E., Fisher, S., Gonzalez-Reiche, A. S., Hacia, J. G., Hallgrimsson, B., Hansen, K., Harris, M. P., Ho, T.-V., Holmes, G., Hooper, J. E., Jabs, E. W., Jones, K. L., Kesselman, C., Klein, O. D., Leslie, E. J., … Chai, Y. (2020). FaceBase 3: Analytical tools and FAIR resources for craniofacial and dental research. *Development*, *147*(18), dev191213. https://doi.org/10.1242/dev.191213

Santos, A., Bakker, A. D., Willems, H. M. E., Bravenboer, N., Bronckers, A. L. J. J., & Klein-Nulend, J. (2011). Mechanical Loading Stimulates BMP7, But Not BMP2, Production by Osteocytes. *Calcified Tissue International*, *89*(4), 318–326. https://doi.org/10.1007/s00223-011-9521-1

Sasaki, E., Byrne, A. T., Murray, D. J., & Reardon, W. (2020). Caput membranaceum: A novel clinical presentation of ZIC1 related skull malformation and

craniosynostosis. *American Journal of Medical Genetics. Part A*, *182*(12), 2994–2998. https://doi.org/10.1002/ajmg.a.61882

Scanlon v. Medtronic Sofamor Danek USA Inc., 61 F. Supp. 3d 403 (Dist. Court 2014).

Scarano, A., Iezzi, G., & Piattelli, A. (2003). Common Fixatives In Hard-Tissue Histology. In Y. H. An & K. L. Martin (Eds.), *Handbook of Histology Methods for Bone and Cartilage* (pp. 159–165). Humana Press. https://doi.org/10.1007/978-1-59259-417-7_9

Schilling, A. F., Mülhausen, C., Lehmann, W., Santer, R., Schinke, T., Rueger, J. M., & Amling, M. (2007). High bone mineral density in pycnodysostotic patients with a novel mutation in the propeptide of cathepsin K. *Osteoporosis International*, *18*(5), 659–669. https://doi.org/10.1007/s00198-006-0311-y

Schindelin, J., Arganda-Carreras, I., Frise, E., Kaynig, V., Longair, M., Pietzsch, T., Preibisch, S., Rueden, C., Saalfeld, S., Schmid, B., Tinevez, J.-Y., White, D. J., Hartenstein, V., Eliceiri, K., Tomancak, P., & Cardona, A. (2012). Fiji: An open-source platform for biological-image analysis. *Nature Methods*, *9*(7), 676–682. https://doi.org/10.1038/nmeth.2019

Schlager, S. (2017). Chapter 9 - Morpho and Rvcg – Shape Analysis in R: R-Packages for Geometric Morphometrics, Shape Analysis and Surface Manipulations. In G. Zheng, S. Li, & G. Székely (Eds.), *Statistical Shape and Deformation Analysis* (pp. 217–256). Academic Press. https://doi.org/10.1016/B978-0-12-810493-4.00011-0

Schneider, L., Clement, C. A., Teilmann, S. C., Pazour, G. J., Hoffmann, E. K., Satir, P., & Christensen, S. T. (2005). PDGFRalphaalpha signaling is regulated through the

primary cilium in fibroblasts. *Current Biology: CB*, *15*(20), 1861–1866. https://doi.org/10.1016/j.cub.2005.09.012

Schroeder, T. M., Jensen, E. D., & Westendorf, J. J. (2005). Runx2: A master organizer of gene transcription in developing and maturing osteoblasts. *Birth Defects Research Part C: Embryo Today: Reviews*, *75*(3), 213–225. https://doi.org/10.1002/bdrc.20043

Scolozzi, P. (2008). Distraction osteogenesis in the management of severe maxillary hypoplasia in cleft lip and palate patients. *The Journal of Craniofacial Surgery*, *19*(5), 1199–1214. https://doi.org/10.1097/SCS.0b013e318184365d

Segklia, A., Seuntjens, E., Elkouris, M., Tsalavos, S., Stappers, E., Mitsiadis, T. A., Huylebroeck, D., Remboutsika, E., & Graf, D. (2012). Bmp7 regulates the survival, proliferation, and neurogenic properties of neural progenitor cells during corticogenesis in the mouse. *PloS One*, *7*(3), e34088. https://doi.org/10.1371/journal.pone.0034088

Sekelsky, J. J., Newfeld, S. J., Raftery, L. A., Chartoff, E. H., & Gelbart, W. M. (1995). Genetic characterization and cloning of mothers against dpp, a gene required for decapentaplegic function in Drosophila melanogaster. *Genetics*, *139*(3), 1347–1358. https://doi.org/10.1093/genetics/139.3.1347

Sen, B., Xie, Z., Case, N., Ma, M., Rubin, C., & Rubin, J. (2008). Mechanical strain inhibits adipogenesis in mesenchymal stem cells by stimulating a durable beta-catenin signal. *Endocrinology*, *149*(12), 6065–6075. https://doi.org/10.1210/en.2008-0687

Sharma, V. P., Fenwick, A. L., Brockop, M. S., McGowan, S. J., Goos, J. A. C., Hoogeboom, A. J. M., Brady, A. F., Jeelani, N. u O., Lynch, S. A., Mulliken, J. B.,

Murray, D. J., Phipps, J. M., Sweeney, E., Tomkins, S. E., Wilson, L. C., Bennett, S., Cornall, R. J., Broxholme, J., Kanapin, A., … Wilkie, A. O. M. (2013). Mutations of TCF12, encoding a basic-helix-loop-helix partner of TWIST1, are a frequent cause of coronal craniosynostosis. *Nature Genetics*, *45*(3), 304. https://doi.org/10.1038/ng.2531

Sheehan, D. C., & Hrapchak, B. B. (1980). *Theory and Practice of Histotechnology*. Mosby.

Sheetz, M., & Yu, H. (2018, January 10). *The Cell as a Machine*. Higher Education from Cambridge University Press; Cambridge University Press. https://doi.org/10.1017/9781107280809

Sheikh, Z., Javaid, M. A., Hamdan, N., & Hashmi, R. (2015). Bone Regeneration Using Bone Morphogenetic Proteins and Various Biomaterial Carriers. *Materials*, *8*(4), 1778–1816. https://doi.org/10.3390/ma8041778

Shen, B., Wei, A., Whittaker, S., Williams, L. A., Tao, H., Ma, D. D. F., & Diwan, A. D. (2010). The role of BMP-7 in chondrogenic and osteogenic differentiation of human bone marrow multipotent mesenchymal stromal cells in vitro. *Journal of Cellular Biochemistry*, *109*(2), 406–416. https://doi.org/10.1002/jcb.22412

Shen, H., Li, L., Zhang, C., Chen, Y., Yu, H., Si, J., & Shen, G. (2022). The strategy of composite grafting with BMP2-Loaded calcium phosphate cements and autogenous bone for alveolar cleft reconstruction. *Frontiers in Physiology*, *13*. https://doi.org/10.3389/fphys.2022.1023772

Shi, X., Huang, C., Xiao, F., Liu, W., Zeng, J., & Li, X. (2017). Pycnodysostosis with novel gene mutation and sporadic medullary thyroid carcinoma: A case report. *Medicine*, *96*(50), e8730. https://doi.org/10.1097/MD.0000000000008730

Shi, Y., He, G., Lee, W.-C., McKenzie, J. A., Silva, M. J., & Long, F. (2017). Gli1 identifies osteogenic progenitors for bone formation and fracture repair. *Nature Communications*, *8*(1), 2043. https://doi.org/10.1038/s41467-017-02171-2

Shibusawa, N., Endo, Y., Morimoto, N., Takahashi, I., & Miura, T. (2021). Mathematical modeling of palatal suture pattern formation: Morphological differences between sagittal and palatal sutures. *Scientific Reports*, *11*, 8995. https://doi.org/10.1038/s41598-021-88255-y

Shields, L. B. E., Raque, G. H., Glassman, S. D., Campbell, M., Vitaz, T., Harpring, J., & Shields, C. B. (2006). Adverse Effects Associated With High-Dose Recombinant Human Bone Morphogenetic Protein-2 Use in Anterior Cervical Spine Fusion. *Spine*, *31*(5), 542. https://doi.org/10.1097/01.brs.0000201424.27509.72

Shimizu, J., Iba, K., Emori, M., Sasaki, M., & Yamashita, T. (2021). Reconstruction Using Free Vascularized Fibular Grafts after Wide Resection of Humerus Chondrosarcoma in a Patient with Cleidocranial Dysplasia. *Case Reports in Orthopedics*, *2021*, e2302879. https://doi.org/10.1155/2021/2302879

Shu, B., Zhang, M., Xie, R., Wang, M., Jin, H., Hou, W., Tang, D., Harris, S. E., Mishina, Y., O'Keefe, R. J., Hilton, M. J., Wang, Y., & Chen, D. (2011). BMP2, but not BMP4, is crucial for chondrocyte proliferation and maturation during endochondral bone development. *Journal of Cell Science*, *124*(Pt 20), 3428–3440. https://doi.org/10.1242/jcs.083659

Shukunami, C., Takimoto, A., Nishizaki, Y., Yoshimoto, Y., Tanaka, S., Miura, S., Watanabe, H., Sakuma, T., Yamamoto, T., Kondoh, G., & Hiraki, Y. (2018). Scleraxis is a transcriptional activator that regulates the expression of Tenomodulin, a marker of mature tenocytes and ligamentocytes. *Scientific Reports*, *8*(1), 3155. https://doi.org/10.1038/s41598-018-21194-3

Simons, M., Gloy, J., Ganner, A., Bullerkotte, A., Bashkurov, M., Krönig, C., Schermer, B., Benzing, T., Cabello, O. A., Jenny, A., Mlodzik, M., Polok, B., Driever, W., Obara, T., & Walz, G. (2005). Inversin, the gene product mutated in nephronophthisis type II, functions as a molecular switch between Wnt signaling pathways. *Nature Genetics*, *37*(5), 537–543. https://doi.org/10.1038/ng1552

Skinner, R. A., Hickmon, S. G., Lumpkin, C. K., Aronson, J., & Nicholas, R. W. (1997). Decalcified Bone: Twenty Years of Successful Specimen Management. *Journal of Histotechnology*, *20*(3), 267–277. https://doi.org/10.1179/his.1997.20.3.267

Snider, T. N., & Mishina, Y. (2014). Cranial neural crest cell contribution to craniofacial formation, pathology, and future directions in tissue engineering. *Birth Defects Research Part C: Embryo Today: Reviews*, *102*(3), 324–332. https://doi.org/10.1002/bdrc.21075

Song, A. J., & Palmiter, R. D. (2018). Detecting and Avoiding Problems When Using the Cre/lox System. *Trends in Genetics : TIG*, *34*(5), 333–340. https://doi.org/10.1016/j.tig.2017.12.008

Sonnesen, L., Pawlik, T., & Lauridsen, E. F. (2021). Craniofacial Morphology and Upper Airway Dimensions in Patients with Hypermobile Ehlers-Danlos Syndrome

Compared to Healthy Controls. *Journal of Oral & Maxillofacial Research*, *12*(2), e5. https://doi.org/10.5037/jomr.2021.12205

Sorice, S., Bastidas, N., Nah, A. H.-D., Bartlett, S. P., & Taylor, J. A. (2012). Premature Fusion of the Spheno-Occipital Synchondrosis (SOS) and Midface Hypoplasia in Syndromic Craniosynostosis. *Plastic and Reconstructive Surgery*, *130*(5S-1), 16. https://doi.org/10.1097/01.prs.0000421716.20504.0a

Stamper, B. D., Park, S. S., Beyer, R. P., Bammler, T. K., Farin, F. M., Mecham, B., & Cunningham, M. L. (2011). Differential Expression of Extracellular Matrix-Mediated Pathways in Single-Suture Craniosynostosis. *PLoS ONE*, *6*(10). https://doi.org/10.1371/journal.pone.0026557

Stanton, A. E., Tong, X., & Yang, F. (2019). Extracellular matrix type modulates mechanotransduction of stem cells. *Acta Biomaterialia*, *96*, 310–320. https://doi.org/10.1016/j.actbio.2019.06.048

Stanton, E., Urata, M., Chen, J.-F., & Chai, Y. (2022). The clinical manifestations, molecular mechanisms and treatment of craniosynostosis. *Disease Models & Mechanisms*, *15*(4), dmm049390. https://doi.org/10.1242/dmm.049390

Stevens, H. E., Scuderi, S., Collica, S. C., Tomasi, S., Horvath, T. L., & Vaccarino, F. M. (2023). Neonatal loss of FGFR2 in astroglial cells affects locomotion, sociability, working memory, and glia-neuron interactions in mice. *Translational Psychiatry*, *13*(1), 1–13. https://doi.org/10.1038/s41398-023-02372-y

Strauss, B. S. (2016). Biochemical Genetics and Molecular Biology: The Contributions of George Beadle and Edward Tatum. *Genetics*, *203*(1), 13–20. https://doi.org/10.1534/genetics.116.188995

Stuart, T., Butler, A., Hoffman, P., Hafemeister, C., Papalexi, E., Mauck, W. M., Hao, Y., Stoeckius, M., Smibert, P., & Satija, R. (2019). Comprehensive Integration of Single-Cell Data. *Cell*, *177*(7), 1888-1902.e21. https://doi.org/10.1016/j.cell.2019.05.031

Sun, W., Chi, S., Li, Y., Ling, S., Tan, Y., Xu, Y., Jiang, F., Li, J., Liu, C., Zhong, G., Cao, D., Jin, X., Zhao, D., Gao, X., Liu, Z., Xiao, B., & Li, Y. (2019). The mechanosensitive Piezo1 channel is required for bone formation. *eLife*, *8*, e47454. https://doi.org/10.7554/eLife.47454

Sun, Y., Wan, B., Wang, R., Zhang, B., Luo, P., Wang, D., Nie, J.-J., Chen, D., & Wu, X. (2022). Mechanical Stimulation on Mesenchymal Stem Cells and Surrounding Microenvironments in Bone Regeneration: Regulations and Applications. *Frontiers in Cell and Developmental Biology*, *10*. https://www.frontiersin.org/article/10.3389/fcell.2022.808303

Supek, F., Bošnjak, M., Škunca, N., & Šmuc, T. (2011). REVIGO Summarizes and Visualizes Long Lists of Gene Ontology Terms. *PLOS ONE*, *6*(7), e21800. https://doi.org/10.1371/journal.pone.0021800

Suzuki, J., & Osumi, N. (2015). Neural crest and placode contributions to olfactory development. *Current Topics in Developmental Biology*, *111*, 351–374. https://doi.org/10.1016/bs.ctdb.2014.11.010

Svejcar, J., & Walther, A. (1975). The diagnosis of the early infantile form of hypophosphatasia tarda. *Humangenetik*, *28*(1), 49–56. https://doi.org/10.1007/BF00272482

Sweat, Y. Y., Sweat, M., Mansaray, M., Cao, H., Eliason, S., Adeyemo, W. L., Gowans, L. J. J., Eshete, M. A., Anand, D., Chalkley, C., Saadi, I., Lachke, S. A., Butali, A., & Amendt, B. A. (2020). Six2 regulates Pax9 expression, palatogenesis and craniofacial bone formation. *Developmental Biology*, *458*(2), 246–256. https://doi.org/10.1016/j.ydbio.2019.11.010

Swift, J., Ivanovska, I. L., Buxboim, A., Harada, T., Dingal, P. C. D. P., Pinter, J., Pajerowski, J. D., Spinler, K. R., Shin, J.-W., Tewari, M., Rehfeldt, F., Speicher, D. W., & Discher, D. E. (2013). Nuclear lamin-A scales with tissue stiffness and enhances matrix-directed differentiation. *Science (New York, N.Y.)*, *341*(6149), 1240104. https://doi.org/10.1126/science.1240104

Tabler, J. M., Barrell, W. B., Szabo-Rogers, H. L., Healy, C., Yeung, Y., Perdiguero, E. G., Schulz, C., Yannakoudakis, B. Z., Mesbahi, A., Wlodarczyk, B., Geissmann, F., Finnell, R. H., Wallingford, J. B., & Liu, K. J. (2013). Fuz mutant mice reveal shared mechanisms between ciliopathies and FGF-related syndromes. *Developmental Cell*, *25*(6), 623–635. https://doi.org/10.1016/j.devcel.2013.05.021

Tabler, J. M., Rice, C. P., Liu, K. J., & Wallingford, J. B. (2016). A novel ciliopathic skull defect arising from excess neural crest. *Developmental Biology*, *417*(1), 4–10. https://doi.org/10.1016/j.ydbio.2016.07.001

Tahiri, Y., Paliga, J. T., Vossough, A., Bartlett, S. P., & Taylor, J. A. (2014). The Spheno-Occipital Synchondrosis Fuses Prematurely in Patients With Crouzon Syndrome and Midface Hypoplasia Compared With Age- and Gender-Matched Controls. *Journal of Oral and Maxillofacial Surgery*, *72*(6), 1173–1179. https://doi.org/10.1016/j.joms.2013.11.015

Takagi, K., & Urist, M. R. (1982). The reaction of the dura to bone morphogenetic protein (BMP) in repair of skull defects. *Annals of Surgery*, *196*(1), 100–109.

Takimoto, A., Kawatsu, M., Yoshimoto, Y., Kawamoto, T., Seiryu, M., Takano-Yamamoto, T., Hiraki, Y., & Shukunami, C. (2015). Scleraxis and osterix antagonistically regulate tensile force-responsive remodeling of the periodontal ligament and alveolar bone. *Development*, *142*(4), 787–796. https://doi.org/10.1242/dev.116228

Taqi, S. A., Sami, S. A., Sami, L. B., & Zaki, S. A. (2018). A review of artifacts in histopathology. *Journal of Oral and Maxillofacial Pathology : JOMFP*, *22*(2), 279. https://doi.org/10.4103/jomfp.JOMFP_125_15

ten Dijke, P., Yamashita, H., Ichijo, H., Franzén, P., Laiho, M., Miyazono, K., & Heldin, C.-H. (1994). Characterization of Type I Receptors for Transforming Growth Factor-β and Activin. *Science*, *264*(5155), 101–104. https://doi.org/10.1126/science.8140412

Ten Dijke, P., Yamashita, H., Sampath, T. K., Reddi, A. H., Estevez, M., Riddle, D. L., Ichijo, H., Heldin, C. H., & Miyazono, K. (1994). Identification of type I receptors for osteogenic protein-1 and bone morphogenetic protein-4. *Journal of Biological Chemistry*, *269*(25), 16985–16988. https://doi.org/10.1016/S0021-9258(17)32506-1

Tholpady, S. S., & Ogle, R. C. (2011). Expression of transforming growth factor-β-responsive smads in cranial suture development and closure. *The Journal of Craniofacial Surgery*, *22*(1), 324–328. https://doi.org/10.1097/SCS.0b013e3181f7dfa0

Thomas, G. P. L., Magdum, S. A., Saeed, N. R., & Johnson, D. (2019). Multisuture Craniosynostosis and Papilledema in Pycnodysostosis: A Paradox? *The Journal of Craniofacial Surgery*, *30*(1), 110–114. https://doi.org/10.1097/SCS.0000000000004870

Tiberio, F., Cacciotti, I., Frassanito, P., Nocca, G., Tamburrini, G., Arcovito, A., & Lattanzi, W. (2021). Personalized Bone Reconstruction and Regeneration in the Treatment of Craniosynostosis. *Applied Sciences*, *11*(6), Article 6. https://doi.org/10.3390/app11062649

Tiberio, F., Parolini, O., & Lattanzi, W. (2021). Ciliary Signalling and Mechanotransduction in the Pathophysiology of Craniosynostosis. *Genes*, *12*(7), 1073. https://doi.org/10.3390/genes12071073

Timberlake, A. T., Choi, J., Zaidi, S., Lu, Q., Nelson-Williams, C., Brooks, E. D., Bilguvar, K., Tikhonova, I., Mane, S., Yang, J. F., Sawh-Martinez, R., Persing, S., Zellner, E. G., Loring, E., Chuang, C., Galm, A., Hashim, P. W., Steinbacher, D. M., DiLuna, M. L., … Lifton, R. P. (2016). Two locus inheritance of non-syndromic midline craniosynostosis via rare SMAD6 and common BMP2 alleles. *eLife*, *5*, e20125. https://doi.org/10.7554/eLife.20125

Timberlake, A. T., Junn, A., Flores, R., Staffenberg, D. A., Lifton, R. P., & Persing, J. A. (2022). Genetic Influence on Neurodevelopment in Nonsyndromic Craniosynostosis. *Plastic and Reconstructive Surgery*, *149*(5), 1157. https://doi.org/10.1097/PRS.0000000000008976

Timberlake, A. T., & Persing, J. A. (2018). Genetics of Nonsyndromic Craniosynostosis. *Plastic and Reconstructive Surgery*, *141*(6), 1508–1516. https://doi.org/10.1097/PRS.0000000000004374

Tischfield, M. A., Robson, C. D., Gilette, N. M., Chim, S. M., Sofela, F. A., DeLisle, M. M., Gelber, A., Barry, B. J., MacKinnon, S., Dagi, L. R., Nathans, J., & Engle, E. C. (2017). Cerebral Vein Malformations Result from Loss of Twist1 Expression and BMP Signaling from Skull Progenitor Cells and Dura. *Developmental Cell*, *42*(5), 445-461.e5. https://doi.org/10.1016/j.devcel.2017.07.027

Tolchin, D., Yeager, J. P., Prasad, P., Dorrani, N., Russi, A. S., Martinez-Agosto, J. A., Haseeb, A., Angelozzi, M., Santen, G. W. E., Ruivenkamp, C., Mercimek-Andrews, S., Depienne, C., Kuechler, A., Mikat, B., Ludecke, H.-J., Bilan, F., Le Guyader, G., Gilbert-Dussardier, B., Keren, B., … Zarowiecki, M. (2020). De Novo SOX6 Variants Cause a Neurodevelopmental Syndrome Associated with ADHD, Craniosynostosis, and Osteochondromas. *The American Journal of Human Genetics*, *106*(6), 830–845. https://doi.org/10.1016/j.ajhg.2020.04.015

Tomita, M., Asada, M., Asada, N., Nakamura, J., Oguchi, A., Higashi, A. Y., Endo, S., Robertson, E., Kimura, T., Kita, T., Economides, A. N., Kreidberg, J., & Yanagita, M. (2013). Bmp7 Maintains Undifferentiated Kidney Progenitor Population and Determines Nephron Numbers at Birth. *PLOS ONE*, *8*(8), e73554. https://doi.org/10.1371/journal.pone.0073554

Tong, H., Song, T., Sun, X., Yin, N., Liu, L., Wang, X., & Zhao, Z. (2019). Imaging study of midface growth with bone-borne trans-sutural distraction osteogenesis therapy

in growing cleft lip and palate patients. *Scientific Reports*, *9*(1), 871. https://doi.org/10.1038/s41598-018-37326-8

Tower, R. J., Li, Z., Cheng, Y.-H., Wang, X.-W., Rajbhandari, L., Zhang, Q., Negri, S., Uytingco, C. R., Venkatesan, A., Zhou, F.-Q., Cahan, P., James, A. W., & Clemens, T. L. (2021). Spatial transcriptomics reveals a role for sensory nerves in preserving cranial suture patency through modulation of BMP/TGF-β signaling. *Proceedings of the National Academy of Sciences*, *118*(42), e2103087118. https://doi.org/10.1073/pnas.2103087118

Tresguerres, F. G. F., Torres, J., López-Quiles, J., Hernández, G., Vega, J. A., & Tresguerres, I. F. (2020). The osteocyte: A multifunctional cell within the bone. *Annals of Anatomy - Anatomischer Anzeiger*, *227*, 151422. https://doi.org/10.1016/j.aanat.2019.151422

Tschopp, H. M. (1974). Special problems and techniques of palatoplasty. *Chirurgia Plastica*, *2*(2), 67–81. https://doi.org/10.1007/BF00302684

Tu, Q., Zhang, J., James, L., Dickson, J., Tang, J., Yang, P., & Chen, J. (2007). Cbfa1/Runx2-deficiency delays bone wound healing and locally delivered Cbfa1/Runx2 promotes bone repair in animal models. *Wound Repair and Regeneration : Official Publication of the Wound Healing Society [and] the European Tissue Repair Society*, *15*(3), 404–412. https://doi.org/10.1111/j.1524-475X.2007.00243.x

Tu, X., Rhee, Y., Condon, K. W., Bivi, N., Allen, M. R., Dwyer, D., Stolina, M., Turner, C. H., Robling, A. G., Plotkin, L. I., & Bellido, T. (2012). Sost downregulation and

local Wnt signaling are required for the osteogenic response to mechanical loading. *Bone*, *50*(1), 209–217. https://doi.org/10.1016/j.bone.2011.10.025

Turner, A. E., Abu-Ghname, A., Davis, M. J., Shih, L., Volk, A. S., Streff, H., & Buchanan, E. P. (2020). Kenny-Caffey Syndrome Type 2: A Unique Presentation and Craniofacial Analysis. *The Journal of Craniofacial Surgery*, *31*(5), e471–e475. https://doi.org/10.1097/SCS.0000000000006439

Turri de Castro Ribeiro, T., Petri Feitosa, M. C., Almeida Penhavel, R., Zanda, R. S., Janson, G., Mazzottini, R., & Garib, D. G. (2018). Extreme maxillomandibular discrepancy in unilateral cleft lip and palate: Longitudinal follow-up in a patient with mandibular prognathism. *American Journal of Orthodontics and Dentofacial Orthopedics: Official Publication of the American Association of Orthodontists, Its Constituent Societies, and the American Board of Orthodontics*, *154*(2), 294–304. https://doi.org/10.1016/j.ajodo.2017.03.030

Twigg, S. R. F., Healy, C., Babbs, C., Sharpe, J. A., Wood, W. G., Sharpe, P. T., Morriss-Kay, G. M., & Wilkie, A. O. M. (2009). Skeletal analysis of the Fgfr3P244R mouse, a genetic model for the Muenke craniosynostosis syndrome. *Developmental Dynamics*, *238*(2), 331–342. https://doi.org/10.1002/dvdy.21790

Twigg, S. R. F., & Wilkie, A. O. M. (2015). New insights into craniofacial malformations. *Human Molecular Genetics*, *24*(R1), R50–R59. https://doi.org/10.1093/hmg/ddv228

Uhler, C., & Shivashankar, G. V. (2017). Regulation of genome organization and gene expression by nuclear mechanotransduction. *Nature Reviews Molecular Cell Biology*, *18*(12), 717–727. https://doi.org/10.1038/nrm.2017.101

Uludağ Alkaya, D., Akpınar, E., Bilguvar, K., & Tüysüz, B. (2021). Resolution of sclerotic lesions of dysosteosclerosis due to biallelic SLC29A3 variant in a Turkish girl. *American Journal of Medical Genetics Part A*, *185*(7), 2271–2277. https://doi.org/10.1002/ajmg.a.62198

Uray, I. P., & Uray, K. (2021). Mechanotransduction at the Plasma Membrane-Cytoskeleton Interface. *International Journal of Molecular Sciences*, *22*(21), 11566. https://doi.org/10.3390/ijms222111566

Urist, M. R. (1965). Bone: Formation by Autoinduction. *Science*, *150*(3698), 893–899. https://doi.org/10.1126/science.150.3698.893

Urist, M. R., & Strates, B. S. (1971). Bone Morphogenetic Protein. *Journal of Dental Research*, *50*(6), 1392–1406. https://doi.org/10.1177/00220345710500060601

Vaccaro, A. R., Whang, P. G., Patel, T., Phillips, F. M., Anderson, D. G., Albert, T. J., Hilibrand, A. S., Brower, R. S., Kurd, M. F., Appannagari, A., Patel, M., & Fischgrund, J. S. (2008). The safety and efficacy of OP-1 (rhBMP-7) as a replacement for iliac crest autograft for posterolateral lumbar arthrodesis: Minimum 4-year follow-up of a pilot study. *The Spine Journal*, *8*(3), 457–465. https://doi.org/10.1016/j.spinee.2007.03.012

Vaidya, R., Sethi, A., Bartol, S., Jacobson, M., Coe, C., & Craig, J. G. (2008). Complications in the use of rhBMP-2 in PEEK cages for interbody spinal fusions. *Journal of Spinal Disorders & Techniques*, *21*(8), 557–562. https://doi.org/10.1097/BSD.0b013e31815ea897

van Steensel, B., & Belmont, A. S. (2017). Lamina-associated domains: Links with chromosome architecture, heterochromatin and gene repression. *Cell*, *169*(5), 780–791. https://doi.org/10.1016/j.cell.2017.04.022

Vandenbon, A., & Diez, D. (2023). A universal tool for predicting differentially active features in single-cell and spatial genomics data. *Scientific Reports*, *13*(1), 11830. https://doi.org/10.1038/s41598-023-38965-2

Ved, N., Curran, A., Ashcroft, F. M., & Sparrow, D. B. (2019). Tamoxifen administration in pregnant mice can be deleterious to both mother and embryo. *Laboratory Animals*, *53*(6), 630–633. https://doi.org/10.1177/0023677219856918

Vermeulen, S., Roumans, N., Honig, F., Carlier, A., Hebels, D. G. A. J., Eren, A. D., Dijke, P. ten, Vasilevich, A., & de Boer, J. (2020). Mechanotransduction is a context-dependent activator of TGF-β signaling in mesenchymal stem cells. *Biomaterials*, *259*, 120331. https://doi.org/10.1016/j.biomaterials.2020.120331

Vinchon, M. (2019). The metopic suture: Natural history. *Neurochirurgie*, *65*(5), 239–245. https://doi.org/10.1016/j.neuchi.2019.09.006

Vining, K. H., & Mooney, D. J. (2017). Mechanical forces direct stem cell behaviour in development and regeneration. *Nature Reviews. Molecular Cell Biology*, *18*(12), 728–742. https://doi.org/10.1038/nrm.2017.108

Vion, A.-C., Alt, S., Klaus-Bergmann, A., Szymborska, A., Zheng, T., Perovic, T., Hammoutene, A., Oliveira, M. B., Bartels-Klein, E., Hollfinger, I., Rautou, P.-E., Bernabeu, M. O., & Gerhardt, H. (2018). Primary cilia sensitize endothelial cells to BMP and prevent excessive vascular regression. *Journal of Cell Biology*, *217*(5), 1651–1665. https://doi.org/10.1083/jcb.201706151

Vogiatzi, A., Baltsavia, I., Dialynas, E., Theodorou, V., Zhou, Y., Deligianni, E., Iliopoulos, I., Wilkie, A. O. M., Twigg, S. R. F., & Mavrothalassitis, G. (2021). Erf Affects Commitment and Differentiation of Osteoprogenitor Cells in Cranial Sutures via the Retinoic Acid Pathway. *Molecular and Cellular Biology*, *41*(8), e00149-21. https://doi.org/10.1128/MCB.00149-21

Vora, S. R., Camci, E. D., & Cox, T. C. (2016). Postnatal Ontogeny of the Cranial Base and Craniofacial Skeleton in Male C57BL/6J Mice: A Reference Standard for Quantitative Analysis. *Frontiers in Physiology*, *6*. https://doi.org/10.3389/fphys.2015.00417

Wagner, D. O., Sieber, C., Bhushan, R., Börgermann, J. H., Graf, D., & Knaus, P. (2010). BMPs: From bone to body morphogenetic proteins. *Science Signaling*, *3*(107), mr1. https://doi.org/10.1126/scisignal.3107mr1

Wagner, G. P. (1996). Homologues, Natural Kinds and the Evolution of Modularity1. *American Zoologist*, *36*(1), 36–43. https://doi.org/10.1093/icb/36.1.36

Wambach, J. A., Wegner, D. J., Patni, N., Kircher, M., Willing, M. C., Baldridge, D., Xing, C., Agarwal, A. K., Vergano, S. A. S., Patel, C., Grange, D. K., Kenney, A., Najaf, T., Nickerson, D. A., Bamshad, M. J., Cole, F. S., & Garg, A. (2018). Bi-allelic POLR3A Loss-of-Function Variants Cause Autosomal-Recessive Wiedemann-Rautenstrauch Syndrome. *American Journal of Human Genetics*, *103*(6), 968–975. https://doi.org/10.1016/j.ajhg.2018.10.010

Wang, J., Fu, C., Zhang, S., Luo, J., Ouyang, L., Xie, B., Sun, W., He, S., Su, J., Hu, X., Fei, D., Chen, R., Fan, X., Ou, S., Chen, S., & Shen, Y. (2016). A rare occurrence

of two large de novo duplications on 1q42-q44 and 9q21.12-q21.33. *Gene*, *594*(1), 59–65. https://doi.org/10.1016/j.gene.2016.08.042

Wang, M. M., Haveles, C. S., Zukotynski, B. K., Reid, R. R., & Lee, J. C. (2021). Facial Suture Pathology in Syndromic Craniosynostosis: Human and Animal Studies. *Annals of Plastic Surgery*, *87*(5), 589–599. https://doi.org/10.1097/SAP.0000000000002822

Wang, M. M., Haveles, C. S., Zukotynski, B. K., Reid, R. R., & Lee, J. C. (2022). The 27 Facial Sutures: Timing and Clinical Consequences of Closure. *Plastic and Reconstructive Surgery*, *149*(3), 701–720. https://doi.org/10.1097/PRS.0000000000008816

Wang, M., Xia, F., Wei, Y., & Wei, X. (2020). Molecular mechanisms and clinical management of cancer bone metastasis. *Bone Research*, *8*(1), 1–20. https://doi.org/10.1038/s41413-020-00105-1

Wang, R. N., Green, J., Wang, Z., Deng, Y., Qiao, M., Peabody, M., Zhang, Q., Ye, J., Yan, Z., Denduluri, S., Idowu, O., Li, M., Shen, C., Hu, A., Haydon, R. C., Kang, R., Mok, J., Lee, M. J., Luu, H. L., & Shi, L. L. (2014). Bone Morphogenetic Protein (BMP) signaling in development and human diseases. *Genes & Diseases*, *1*(1), 87–105. https://doi.org/10.1016/j.gendis.2014.07.005

Wang, Z., & Guo, J. (2013). Mechanical Induction of BMP-7 in Osteocyte Blocks Glucocorticoid-Induced Apoptosis Through PI3K/AKT/GSK3β Pathway. *Cell Biochemistry and Biophysics*, *67*(2), 567–574. https://doi.org/10.1007/s12013-013-9543-6

Warren, S. M., Brunet, L. J., Harland, R. M., Economides, A. N., & Longaker, M. T. (2003). The BMP antagonist noggin regulates cranial suture fusion. *Nature*, *422*(6932), 625–629. https://doi.org/10.1038/nature01545

Wei, Q., Holle, A., Li, J., Posa, F., Biagioni, F., Croci, O., Benk, A. S., Young, J., Noureddine, F., Deng, J., Zhang, M., Inman, G. J., Spatz, J. P., Campaner, S., & Cavalcanti-Adam, E. A. (2020). BMP-2 Signaling and Mechanotransduction Synergize to Drive Osteogenic Differentiation via YAP/TAZ. *Advanced Science*, *7*(15), 1902931. https://doi.org/10.1002/advs.201902931

Wharton, K. A., Cook, J. M., Torres-Schumann, S., de Castro, K., Borod, E., & Phillips, D. A. (1999). Genetic analysis of the bone morphogenetic protein-related gene, gbb, identifies multiple requirements during Drosophila development. *Genetics*, *152*(2), 629–640. https://doi.org/10.1093/genetics/152.2.629

Wheway, G., Nazlamova, L., & Hancock, J. T. (2018). Signaling through the Primary Cilium. *Frontiers in Cell and Developmental Biology*, *6*, 8. https://doi.org/10.3389/fcell.2018.00008

White, H. E., Goswami, A., & Tucker, A. S. (2021). The Intertwined Evolution and Development of Sutures and Cranial Morphology. *Frontiers in Cell and Developmental Biology*, *9*. https://doi.org/10.3389/fcell.2021.653579

Whyte, M. P., Greenberg, C. R., Salman, N. J., Bober, M. B., McAlister, W. H., Wenkert, D., Van Sickle, B. J., Simmons, J. H., Edgar, T. S., Bauer, M. L., Hamdan, M. A., Bishop, N., Lutz, R. E., McGinn, M., Craig, S., Moore, J. N., Taylor, J. W., Cleveland, R. H., Cranley, W. R., … Landy, H. (2012). Enzyme-Replacement

Therapy in Life-Threatening Hypophosphatasia. *New England Journal of Medicine*, *366*(10), 904–913. https://doi.org/10.1056/NEJMoa1106173

Wilkie, A. O. M. (1997). Craniosynostosis: Genes and Mechanisms. *Human Molecular Genetics*, *6*(10), 1647–1656. https://doi.org/10.1093/hmg/6.10.1647

Wilkie, A. O. M., Johnson, D., & Wall, S. A. (2017). Clinical Genetics of Craniosynostosis. *Current Opinion in Pediatrics*, *29*(6), 622–628. https://doi.org/10.1097/MOP.0000000000000542

Williams, B. J. D., Currimbhoy, S., Silva, A., & O'Ryan, F. S. (2012). Complications following surgically assisted rapid palatal expansion: A retrospective cohort study. *Journal of Oral and Maxillofacial Surgery: Official Journal of the American Association of Oral and Maxillofacial Surgeons*, *70*(10), 2394–2402. https://doi.org/10.1016/j.joms.2011.09.050

Wolff, J. (1986). *The Law of Bone Remodelling*. Springer Berlin Heidelberg. https://doi.org/10.1007/978-3-642-71031-5

Wrana, J. L., Attisano, L., Wieser, R., Ventura, F., & Massagué, J. (1994). Mechanism of activation of the TGF-beta receptor. *Nature*, *370*(6488), 341–347. https://doi.org/10.1038/370341a0

Wu, T., Chen, G., Tian, F., & Liu, H.-X. (2017). Contribution of cranial neural crest cells to mouse skull development. *The International Journal of Developmental Biology*, *61*(8–9), 495–503. https://doi.org/10.1387/ijdb.170051gc

Wu, X., Hu, J., Li, G., Li, Y., Li, Y., Zhang, J., Wang, F., Li, A., Hu, L., Fan, Z., Lü, S., Ding, G., Zhang, C., Wang, J., Long, M., & Wang, S. (2020). Biomechanical stress

regulates mammalian tooth replacement via the integrin β1-RUNX2-Wnt pathway. *The EMBO Journal*, *39*(3), e102374. https://doi.org/10.15252/embj.2019102374

Wyatt, A. W., Osborne, R. J., Stewart, H., & Ragge, N. K. (2010). Bone morphogenetic protein 7 (BMP7) mutations are associated with variable ocular, brain, ear, palate, and skeletal anomalies. *Human Mutation*, *31*(7), 781–787. https://doi.org/10.1002/humu.21280

Xia, C., Ge, Q., Fang, L., Yu, H., Zou, Z., Zhang, P., Lv, S., Tong, P., Xiao, L., Chen, D., Wang, P., & Jin, H. (2020). TGF-β/Smad2 signalling regulates enchondral bone formation of Gli1+ periosteal cells during fracture healing. *Cell Proliferation*, *53*(11), e12904. https://doi.org/10.1111/cpr.12904

Xie, T., St Pierre, S. R., Olaranont, N., Brown, L. E., Wu, M., & Sun, Y. (2021). Condensation tendency and planar isotropic actin gradient induce radial alignment in confined monolayers. *eLife*, *10*, e60381. https://doi.org/10.7554/eLife.60381

Xie, Y., Su, N., Yang, J., Tan, Q., Huang, S., Jin, M., Ni, Z., Zhang, B., Zhang, D., Luo, F., Chen, H., Sun, X., Feng, J. Q., Qi, H., & Chen, L. (2020). FGF/FGFR signaling in health and disease. *Signal Transduction and Targeted Therapy*, *5*(1), 1–38. https://doi.org/10.1038/s41392-020-00222-7

Xing, C., Kanchwala, M., Rios, J. J., Hyatt, T., Wang, R. C., Tran, A., Dougherty, I., Tovar-Garza, A., Purnadi, C., Kumar, M. G., Berk, D., Shinawi, M., Irvine, A. D., Toledo-Bahena, M., Agim, N. G., & Glass, D. A. (2021). Biallelic variants in RNU12 cause CDAGS syndrome. *Human Mutation*, *42*(8), 1042–1052. https://doi.org/10.1002/humu.24239

Xu, J., Wang, Y., Gomez-Salazar, M. A., Hsu, G. C.-Y., Negri, S., Li, Z., Hardy, W., Ding, L., Peault, B., & James, A. W. (2021). Bone-forming perivascular cells: Cellular heterogeneity and use for tissue repair. *Stem Cells (Dayton, Ohio)*, *39*(11), 1427–1434. https://doi.org/10.1002/stem.3436

Xu, J., Zhang, Z., Zhao, J., Meyers, C. A., Lee, S., Qin, Q., & James, A. W. (2022). Interaction between the nervous and skeletal systems. *Frontiers in Cell and Developmental Biology*, *10*. https://doi.org/10.3389/fcell.2022.976736

Yang, J., Shi, P., Tu, M., Wang, Y., Liu, M., Fan, F., & Du, M. (2014). Bone morphogenetic proteins: Relationship between molecular structure and their osteogenic activity. *Food Science and Human Wellness*, *3*(3), 127–135. https://doi.org/10.1016/j.fshw.2014.12.002

Yankee, T. N., Oh, S., Winchester, E. W., Wilderman, A., Robinson, K., Gordon, T., Rosenfeld, J. A., VanOudenhove, J., Scott, D. A., Leslie, E. J., & Cotney, J. (2023). Integrative analysis of transcriptome dynamics during human craniofacial development identifies candidate disease genes. *Nature Communications*, *14*(1), 4623. https://doi.org/10.1038/s41467-023-40363-1

Yannakoudakis, B. Z., & Liu, K. J. (2013). Common skeletal features in rare diseases: New links between ciliopathies and FGF-related syndromes. *Rare Diseases (Austin, Tex.)*, *1*, e27109. https://doi.org/10.4161/rdis.27109

Yao, Q., Sandhurst, E. S., Liu, Y., & Sun, H. (2017). BBP-Functionalized Biomimetic Nanofibrous Scaffold Can Capture BMP2 and Promote Osteogenic Differentiation. *Journal of Materials Chemistry. B, Materials for Biology and Medicine*, *5*(26), 5196–5205. https://doi.org/10.1039/C7TB00744B

Ye, B., Wu, Y., Zhou, Y., Jing, H., Hu, J., & Zhang, G. (2015). A comparative cephalometric study for adult operated cleft palate and unoperated cleft palate patients. *Journal of Cranio-Maxillofacial Surgery*, *43*(7), 1218–1223. https://doi.org/10.1016/j.jcms.2015.04.015

Yen, H.-Y., Ting, M.-C., & Maxson, R. E. (2010). Jagged1 functions downstream of Twist1 in the specification of the coronal suture and the formation of a boundary between osteogenic and non-osteogenic cells. *Developmental Biology*, *347*(2), 258–270. https://doi.org/10.1016/j.ydbio.2010.08.010

Yi, S. E., Daluiski, A., Pederson, R., Rosen, V., & Lyons, K. M. (2000). The type I BMP receptor BMPRIB is required for chondrogenesis in the mouse limb. *Development*, *127*(3), 621–630. https://doi.org/10.1242/dev.127.3.621

Yilmaz, E., Mihci, E., Guzel Nur, B., & Alper, O. M. (2018). A novel AXIN2 gene mutation in sagittal synostosis. *American Journal of Medical Genetics Part A*, *176*(9), 1976–1980. https://doi.org/10.1002/ajmg.a.40373

Yin, L., Du, X., Li, C., Xu, X., Chen, Z., Su, N., Zhao, L., Qi, H., Li, F., Xue, J., Yang, J., Jin, M., Deng, C., & Chen, L. (2008). A Pro253Arg mutation in fibroblast growth factor receptor 2 (Fgfr2) causes skeleton malformation mimicking human Apert syndrome by affecting both chondrogenesis and osteogenesis. *Bone*, *42*(4), 631–643. https://doi.org/10.1016/j.bone.2007.11.019

Ying, X., Sun, Y., & He, P. (2015). Bone Morphogenetic Protein-7 Inhibits EMT-Associated Genes in Breast Cancer. *Cellular Physiology and Biochemistry: International Journal of Experimental Cellular Physiology, Biochemistry, and Pharmacology*, *37*(4), 1271–1278. https://doi.org/10.1159/000430249

Yoon, B. S., Ovchinnikov, D. A., Yoshii, I., Mishina, Y., Behringer, R. R., & Lyons, K. M. (2005). Bmpr1a and Bmpr1b have overlapping functions and are essential for chondrogenesis in vivo. *Proceedings of the National Academy of Sciences*, *102*(14), 5062–5067. https://doi.org/10.1073/pnas.0500031102

Yoshida, T., Vivatbutsiri, P., Morriss-Kay, G., Saga, Y., & Iseki, S. (2008). Cell lineage in mammalian craniofacial mesenchyme. *Mechanisms of Development*, *125*(9), 797–808. https://doi.org/10.1016/j.mod.2008.06.007

Yu, F.-X., & Guan, K.-L. (2013). The Hippo pathway: Regulators and regulations. *Genes & Development*, *27*(4), 355–371. https://doi.org/10.1101/gad.210773.112

Yu, H.-M. I., Jerchow, B., Sheu, T.-J., Liu, B., Costantini, F., Puzas, J. E., Birchmeier, W., & Hsu, W. (2005). The role of Axin2 in calvarial morphogenesis and craniosynostosis. *Development (Cambridge, England)*, *132*(8), 1995–2005. https://doi.org/10.1242/dev.01786

Yu, J. C., Lucas, J. H., Fryberg, K., & Borke, J. L. (2001). Extrinsic tension results in FGF-2 release, membrane permeability change, and intracellular Ca++ increase in immature cranial sutures. *The Journal of Craniofacial Surgery*, *12*(4), 391–398. https://doi.org/10.1097/00001665-200107000-00018

Yu, M., Ma, L., Yuan, Y., Ye, X., Montagne, A., He, J., Ho, T.-V., Wu, Y., Zhao, Z., Sta Maria, N., Jacobs, R., Urata, M., Wang, H., Zlokovic, B. V., Chen, J.-F., & Chai, Y. (2021). Cranial Suture Regeneration Mitigates Skull and Neurocognitive Defects in Craniosynostosis. *Cell*, *184*(1), 243-256.e18. https://doi.org/10.1016/j.cell.2020.11.037

Yu, P. B., Beppu, H., Kawai, N., Li, E., & Bloch, K. D. (2005). Bone morphogenetic protein (BMP) type II receptor deletion reveals BMP ligand-specific gain of signaling in pulmonary artery smooth muscle cells. *The Journal of Biological Chemistry*, *280*(26), 24443–24450. https://doi.org/10.1074/jbc.M502825200

Yu, S., Guo, J., Sun, Z., Lin, C., Tao, H., Zhang, Q., Cui, Y., Zuo, H., Lin, Y., Chen, S., Liu, H., & Chen, Z. (2021). BMP2-dependent gene regulatory network analysis reveals Klf4 as a novel transcription factor of osteoblast differentiation. *Cell Death & Disease*, *12*(2), 1–17. https://doi.org/10.1038/s41419-021-03480-7

Yuste, I., Luciano, F. C., González-Burgos, E., Lalatsa, A., & Serrano, D. R. (2021). Mimicking bone microenvironment: 2D and 3D in vitro models of human osteoblasts. *Pharmacological Research*, *169*, 105626. https://doi.org/10.1016/j.phrs.2021.105626

Zannit, H. M., Brodt, M. D., & Silva, M. J. (2020). Proliferating osteoblasts are necessary for maximal bone anabolic response to loading in mice. *FASEB Journal: Official Publication of the Federation of American Societies for Experimental Biology*, *34*(9), 12739–12750. https://doi.org/10.1096/fj.202000614R

Zara, J. N., Siu, R. K., Zhang, X., Shen, J., Ngo, R., Lee, M., Li, W., Chiang, M., Chung, J., Kwak, J., Wu, B. M., Ting, K., & Soo, C. (2011). High Doses of Bone Morphogenetic Protein 2 Induce Structurally Abnormal Bone and Inflammation In Vivo. *Tissue Engineering Part A*, *17*(9–10), 1389–1399. https://doi.org/10.1089/ten.tea.2010.0555

Zdilla, M. J., Russell, M. L., Koons, A. W., Bliss, K. N., & Mangus, K. R. (2018). Metopism: A Study of the Persistent Metopic Suture. *The Journal of Craniofacial Surgery*, *29*(1), 204–208. https://doi.org/10.1097/SCS.0000000000004030

Zhang, H., Zhang, W., Bai, G., Gao, L., & Li, K. (2021). Bone Morphogenetic Protein-7 (BMP-7) Promotes Neuronal Differentiation of Bone Marrow Mesenchymal Stem Cells (BMSCs) *In Vitro*. *BioMed Research International*, *2021*, e7239783. https://doi.org/10.1155/2021/7239783

Zhang, J.-N., Lu, H.-P., Hou, J., Wang, Q., Yu, F.-Y., Zhong, C., Huang, C.-Y., & Chen, S. (2023). Deep learning-based prediction of mandibular growth trend in children with anterior crossbite using cephalometric radiographs. *BMC Oral Health*, *23*(1), 28. https://doi.org/10.1186/s12903-023-02734-4

Zhang, R., Oyajobi, B. O., Harris, S. E., Chen, D., Tsao, C., Deng, H.-W., & Zhao, M. (2013). Wnt/β-catenin signaling activates bone morphogenetic protein 2 expression in osteoblasts. *Bone*, *52*(1), 145–156. https://doi.org/10.1016/j.bone.2012.09.029

Zhang, T., Wu, Q., Zhu, L., Wu, D., Yang, R., Qi, M., & Huang, X. (2020). A novel SPECC1L mutation causing Teebi hypertelorism syndrome: Expanding phenotypic and genetic spectrum. *European Journal of Medical Genetics*, *63*(4), 103851. https://doi.org/10.1016/j.ejmg.2020.103851

Zhang, Y., Zhao, Y., Xie, Z., Li, M., Liu, Y., & Tu, X. (2022). Activating Wnt/β-Catenin Signaling in Osteocytes Promotes Osteogenic Differentiation of BMSCs through BMP-7. *International Journal of Molecular Sciences*, *23*(24), 16045. https://doi.org/10.3390/ijms232416045

Zhang, Z., Nam, H. K., Crouch, S., & Hatch, N. E. (2021). Tissue Nonspecific Alkaline Phosphatase Function in Bone and Muscle Progenitor Cells: Control of Mitochondrial Respiration and ATP Production. *International Journal of Molecular Sciences*, *22*(3), 1140. https://doi.org/10.3390/ijms22031140

Zhang, Z. Q., & Yang, J. L. (2015). Biomechanical Dynamics of Cranial Sutures during Simulated Impulsive Loading. *Applied Bionics and Biomechanics*, *2015*, e596843. https://doi.org/10.1155/2015/596843

Zhao, H., Feng, J., Ho, T.-V., Grimes, W., Urata, M., & Chai, Y. (2015). The suture provides a niche for mesenchymal stem cells of craniofacial bones. *Nature Cell Biology*, *17*(4), 386–396. https://doi.org/10.1038/ncb3139

Zhong, Z. A., Sun, W., Chen, H., Zhang, H., Lay, Y. E., Lane, N. E., & Yao, W. (2015). Optimizing tamoxifen-inducible Cre/loxp system to reduce tamoxifen effect on bone turnover in long bones of young mice. *Bone*, *81*, 614–619. https://doi.org/10.1016/j.bone.2015.07.034

Zhou, X., Mark, K. von der, Henry, S., Norton, W., Adams, H., & Crombrugghe, B. de. (2014). Chondrocytes Transdifferentiate into Osteoblasts in Endochondral Bone during Development, Postnatal Growth and Fracture Healing in Mice. *PLoS Genetics*, *10*(12). https://doi.org/10.1371/journal.pgen.1004820

Zhou, Y.-X., Xu, X., Chen, L., Li, C., Brodie, S. G., & Deng, C.-X. (2000). A Pro250Arg substitution in mouse Fgfr1 causes increased expression of Cbfa1 and premature fusion of calvarial sutures. *Human Molecular Genetics*, *9*(13), 2001–2008. https://doi.org/10.1093/hmg/9.13.2001

Zhu, L., Liu, Y., Wang, A., Zhu, Z., Li, Y., Zhu, C., Che, Z., Liu, T., Liu, H., & Huang, L. (2022). Application of BMP in Bone Tissue Engineering. *Frontiers in Bioengineering and Biotechnology*, *10*. https://doi.org/10.3389/fbioe.2022.810880

Zouvelou, V., Luder, H.-U., Mitsiadis, T. A., & Graf, D. (2009). Deletion of BMP7 affects the development of bones, teeth, and other ectodermal appendages of the orofacial complex. *Journal of Experimental Zoology Part B: Molecular and Developmental Evolution*, *312B*(4), 361–374. https://doi.org/10.1002/jez.b.21262

Zouvelou, V., Passa, O., Segklia, K., Tsalavos, S., Valenzuela, D. M., Economides, A. N., & Graf, D. (2009). Generation and functional characterization of mice with a conditional BMP7 allele. *The International Journal of Developmental Biology*, *53*(4), 597–603. https://doi.org/10.1387/ijdb.082648vz

Zurowski, C., Jamniczky, H., Graf, D., & Theodor, J. (2018). Deletion/loss of bone morphogenetic protein 7 changes tooth morphology and function in Mus musculus: Implications for dental evolution in mammals. *Royal Society Open Science*, *5*(1), 170761. https://doi.org/10.1098/rsos.170761

APPENDIX A

HISTOLOGICAL TECHNIQUES FOR SECTIONING BONES OF THE VERTEBRATE CRANIOFACIAL SKELETON

The following chapter was written by invitation for a Springer Protocols book titled "Craniofacial Development" in the Methods in Molecular Biology book series, edited by Dr. Sebastian Dworkin. It describes my regular practices in craniofacial tissue processing and histology in practical detail, with an emphasis on the power of basic histological stains and interpretation. I wrote this chapter based on current standards in craniofacial characterization and inspiration from my training with Dr. Lakshmi Puttagunta in clinical pathological specimens and Dr. Daniel Graf in mouse phenotyping. It was published as "Histological Techniques for Sectioning Bones of the Vertebrate Craniofacial Skeleton", by Roth. D.M., Puttagunta, L., and Graf, D.

A1.1 Abstract

Histochemical analysis is an indispensable technique in the field of biology used routinely to characterize pathologies of interest throughout the system. This chapter provides the craniofacial biologist with an introduction to tissue harvesting, embedding, and sectioning as well as a toolkit of useful stains for stromal/mesenchymal tissues including bone and cartilage. Techniques are tailored to decalcified, paraffin embedded mouse tissue; however, these methods are applicable under a broad range of conditions.

A1.2 Introduction

The art of histology is often underappreciated as a powerful means of investigation. With thorough, intentional characterization and an experienced eye, the right suite of stains can reveal a great deal about the pathology in question. The craniofacial biologist is well served to develop the practiced skill of sectioning, staining, and interpreting stains through a qualitative lens. Histological techniques for research are undergoing a renaissance as an accessible and highly efficient tool to rapidly and precisely describe phenotypic changes in gene mutants of model organisms.

This chapter focuses on the analysis of craniofacial structures throughout development with focus on cartilage, bone, and teeth. Emphasis is on decalcified tissues that can be conveniently analyzed using paraffin embedding and microtome sectioning, opening the door to a wide repertoire of established histological stains as well as the use of immunohistochemistry for more detailed molecular analysis.

A1.3 Materials

A1.3.1 Tissue Preparation

1. 1X PBS: Combine 80 g NaCl, 2 g KCl, 14.4 g Na_2HPO_4 (MW 141.96), and 2.4 g KH_2PO_4 (MW 136.08) in a 1 L capacity beaker. Add 800 mL MilliQ water and mix well to dissolve. Adjust volume to 1 L using MilliQ water. PH should be 6.8; adjust using 10 M NaOH or HCl if necessary. Sterilize by autoclaving, and store as 10X PBS at room temperature (RT). For 1X PBS use, dilute 1:10 in MilliQ water (store at 4ºC).
2. Ice.
3. 4% Paraformaldehyde (PFA): For 1 L, heat 800 mL distilled water to 60ºC. Caution: paraformaldehyde is extremely toxic and should be handled under a fume hood. Measure 40 g paraformaldehyde in a 1 L capacity beaker and add heated distilled water under fume hood. Add 5 N NaOH one drop at a time until clear solution forms, stirring continuously on hot plate. Add 100 mL 10X PBS. Mix and add distilled water to bring solution to 1 L volume. Check pH and adjust to 7.4, if necessary. Aliquot and store long term at -20ºC.
4. Dissecting tools (forceps, fine scissors).
5. Petri dish.
6. 0.5 M EDTA, pH 7.4: Dissolve 19 g NaOH in 800 mL MilliQ water completely using a magnetic stir plate. Add 186.1 g EDTA and stir vigorously. Check pH and adjust to 7.4 using NaOH pellets. Sterilize by autoclaving and store at RT. Note: EDTA will only dissolve when pH nears 8.0.
7. Rotator.

A1.3.2 Tissue Processing

1. Tissue cassettes.
2. 50%, 70%, 95%, and 100% ethanol.
3. Xylene.
4. Histology-grade paraffin wax.
5. Automated tissue processor.
6. Paraffin embedder.

7. Forceps.
8. Embedding rings (*see* **Note 5**).
9. Embedding cassettes.

A1.3.3 Sectioning

1. Microtome.
2. Glass slides.
3. Microtome blade.
4. Brush.
5. Forceps.
6. Cold water bath.
7. Hot water bath.
8. Slide drying rack.
9. Slide oven.

A1.3.4 Staining

1. 60ºC oven.
2. Xylene.
3. 70%, 95%, and 100% ethanol.
4. Distilled water.
5. Hematoxylin and eosin: Hematoxylin, running water, bluing agent (3.85 g lithium carbonate, 250 mL distilled water), clarifying agent (1 mL HCl, 199 mL 70% ethanol), and eosin stain stock (0.5 g eosin Y, 10 mL distilled water, 40 mL 95% ethanol).
6. Van Gieson's stain: Hematoxylin, picrofuchsin solution (5 mL 1% aq. acid fuchsin, 95 mL aq. picric acid).
7. Picrosirius red: Hematoxylin, picrosirius red solution (0.5 g Sirius red, 500 mL aq. picric acid), acidified water (5 mL glacial acetic acid, 1 L water).
8. Orcein: Orcein solution (1 g orcein, 100 mL 70% alcohol, 1 mL 25% hydrochloric acid), 56 C water bath, 1% acid alcohol, and 1% methylene blue.
9. Safranin O: Hematoxylin, running water, 1% acetic acid solution, 0.1% Safranin O solution, and 0.02% Fast Green.

10. Tartrate-resistant acid phosphatase (TRAP) staining solution: Mix 25 mL TRAP basic incubation medium pH 5.0 (4.6 g sodium acetate anhydrous, 5.7 g L-(+) tartaric acid, 450 mL distilled water, 1 mL glacial acetic acid, adjusted to pH 5.0 with 5 M NaOH or glacial acetic acid) with 20 mg Fast Red Violet LB salt and 125 µL Naphthol AS-MX phosphate substrate (20 mg Naphthol AS-MX Phosphate, 1 mL ethylene glycol monoethyl ether), and 0.02% Fast Green.
11. 37ºC water bath.
12. Resinous mounting medium.
13. Glass coverslips.
14. Forceps.

A1.4 Methods

A1.3.1 Tissue Preparation

For best results, it is recommended to use tissue perfusion through the heart to achieve deep penetration of fixative. If not possible, after euthanasia of animal, tissue must be immediately dissected into cold 1X PBS and fixed before further processing to preserve cellular integrity and to avoid any artifacts due to tissue autolysis or poor cellular preservation. All figures in this chapter are of mouse tissue.

1. Euthanize the animal using an approved method, decapitate the animal, and transfer the head to a petri dish.
2. Using dissection tools, carefully remove skin and excess tissue from the skull (*see* **Note 2**).

   Optional. If interested in a specific region, the skull can be dissected further to separate anatomical regions such as the calvaria, temporomandibular joint, or molars.
3. Place all dissected tissue into ice-cold 1X PBS.
4. Fix tissue in 4% PFA (*see* **Note 3**) on a rotator for 24–48 h.
5. Wash tissue three times in 1X PBS.
6. Immerse tissue in 0.5 M EDTA (*see* **Note 4**) until sufficiently decalcified.

A1.3.2 Tissue Processing

1. Label tissue cassettes (in pencil) with identifying information (*see* **Note 7**).

2. Place tissue in cassettes (*see* **Note 8**) and soak in 50% ethanol at 4ºC prior to processing.
3. If using an automated tissue processor, program the following parameters (An et al., 2003):

1 h	70% ethanol
1 h	95% ethanol
1 h	100% ethanol
1 h	Xylene
1 h	Xylene
1 h	Xylene
1 h	Paraffin
Vacuum	
1 h	Paraffin
Vacuum	

4. When the processing program is complete, transfer the tissue cassettes to 60–65ºC paraffin bath in the paraffin embedder (*see* **Note 9**).
5. Fill metal or plastic embedding cassettes with melted paraffin on the hot side of the embedder and transfer the sample from the tissue cassette. Balance a labeled embedding ring or tissue cassette on the top.
6. Using forceps or a metal pin, position the sample in its correct orientation against the bottom of the embedding cassette, and hold against the cold surface of the paraffin embedder (*see* **Note 10**). Release sample when stable in cooling wax.
7. Wax will settle as it cools. Before it is fully cooled, top off with additional hot wax to reach the top lip of the cassette.

A1.3.3 Sectioning

1. Warm hot water bath to the desired temperature (*see* **Note 12**).
2. Mount a cooled block in microtome (screw or clip in) (Fig. A1.1B). Insert the microtome blade securely in the blade holder and ensure that all knobs and dials are tightened. Check that the thickness dial/setting is set to 7–10 μm (depending on your preference).
3. Advance the block until it is close to the blade (Fig. A1.1C). Cut the first section, using a brush to catch the leading edge of the paraffin and flatten it against the blade holder (Fig. A1.1D). Note any skewedness once the sample reaches the block face and adjust the angle accordingly using knobs on the block holder.

4. Continue cutting sections, rhythmically and methodically, using forceps to manage the lengthening ribbon (*see* **Notes 14** and **15**)(Fig. A1.1E).
5. Once the ribbon is of desired length, carefully transfer to cold water bath taking care not to trap air bubbles between water and paraffin (*see* **Note 16**).
6. Using forceps, separate sections to be mounted from the ribbon (Fig. A1.1F). Pick up the section with a glass slide and transfer it to the hot water bath.
7. When the paraffin melts slightly and becomes translucent, mount on a glass slide by quickly picking up the floating section with the slide (Fig. A1.1G).
8. Dry slides upright at 37ºC overnight, or at RT until remaining water has evaporated.

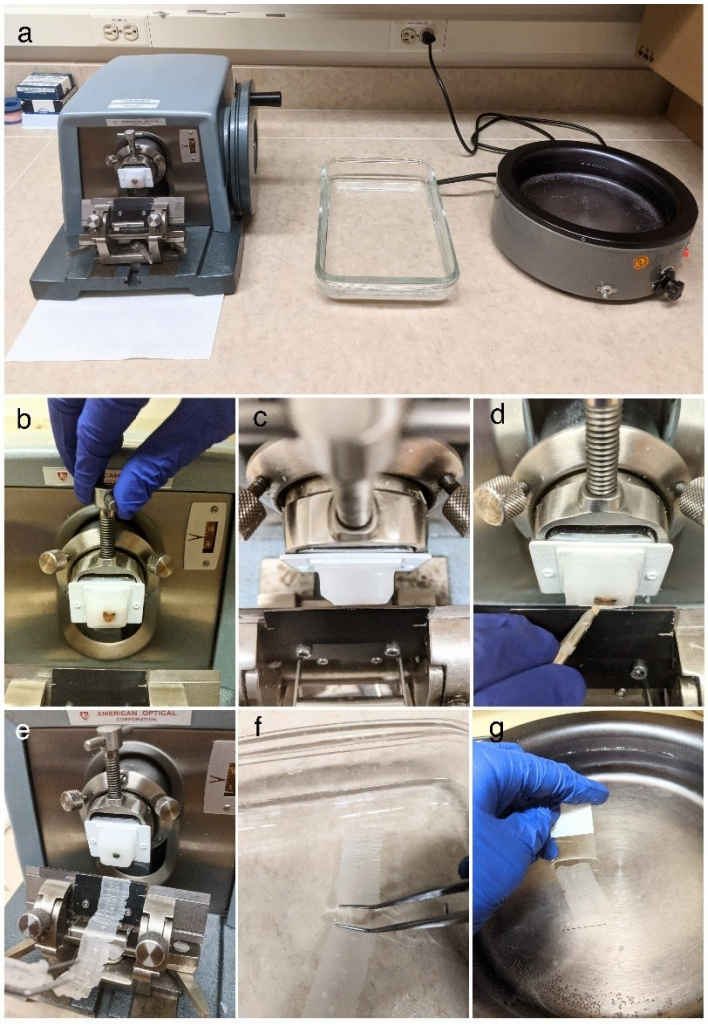

Figure A1.1 Paraffin sectioning technique.
Paraffin sectioning technique. (a) Recommended microtome and water bath workstation. From left to right: microtome, cold water bath, and hot water bath. (b) Firmly secure the paraffin block to the microtome using the plastic embedding ring and screw clamp. Care should be taken not to tighten to the point of cracking. (c) Advance the block until it is almost touching the blade and lock. (d) Cut the first paraffin section, catching the leading

edge with a paintbrush to prevent rolling. (e) Continue cutting paraffin sections, managing the extending ribbon with forceps. (f) Split ribbon in cold water bath into number of sections desired per slide. (g) Lower sections into hot water bath, carefully picking them back up with a glass slide when paraffin is slightly melted.

A1.3.4 Staining

The basic histological stains described in this chapter are optimized for paraffin sections, hence the first stage of each stain is deparaffinization and rehydration (omit if using cryosections).

A1.3.4.1 Deparaffinization and Rehydration

1. Put slides in oven for 10 min, or until wax melts.
2. Wash slides in the following solutions: 2 min xylene, 2 min xylene, 1 min 100% ethanol, 1 min 100% ethanol, 1 min 95% ethanol, 1 min 70% ethanol, and 1 min softly running water bath.

A1.3.4.2 Hematoxylin and Eosin

A commonly used stain for demonstration of tissue morphology and cellular abnormalities. In histopathology, a high proportion of cases can be diagnosed by an experienced pathologist with this stain alone. Nuclei will appear dark purple (hematoxylin), contrasted against a pink (eosin) cytoplasm and background structures (Fig. A1.2A).

1. Deparaffinize and rehydrate slides.
2. Wash slides in the following solutions: 2 min hematoxylin (*see* **Note 18**) and 1 min softly running water bath.
3. Dip slides in clarifying solution three times.
4. Wash slides in the following solutions: 1 min softly running water bath, 1 min bluing agent, 5 min softly running water bath (*see* **Note 19**), and 2–5 min eosin.
5. Dehydrate slides and mount with a resinous mounting medium.

A1.3.4.3 Van Gieson's Stain

Van Gieson's stain is useful for differentiating collagen from other background tissue; collagen/muscle will appear bright pink against a yellow cytoplasmic and other tissue component background (Fig. A1.2B) (Bancroft & Layton, 2019).

1. Deparaffinize and rehydrate slides.
2. Wash slides in the following solutions: 2 min. Hematoxylin, 1 min. Softly running water bath, and 3 min. Picrofuchsin solution.
3. Tap off excess solution and examine for complete staining under microscope.
4. Dehydrate slides and mount with a resinous mounting medium.

A1.3.4.4 Picrosirius Red

Picrosirius Red stains collagen fibers an intense red (Fig. A1.2C). When observed under polarized light, collagen appears bright yellow or orange, due to its enhancement of collagen birefringence (Junqueira et al., 1979). Unlike Van Gieson's stain, picrosirius red also differentiates finer details like reticular fibers (green on polarization), basal laminae of capillaries, and other epithelial-lined structures (red but are not birefringent).

1. Deparaffinize and rehydrate slides.
2. Wash slides in the following solutions: 2 min hematoxylin and 1 h picrosirius red (*see* **Note 20**).
3. Wash slides in 2 changes of acidified water (*see* **Note 21**). Tap off excess solution.
4. Dehydrate slides and mount with a resinous mounting medium.

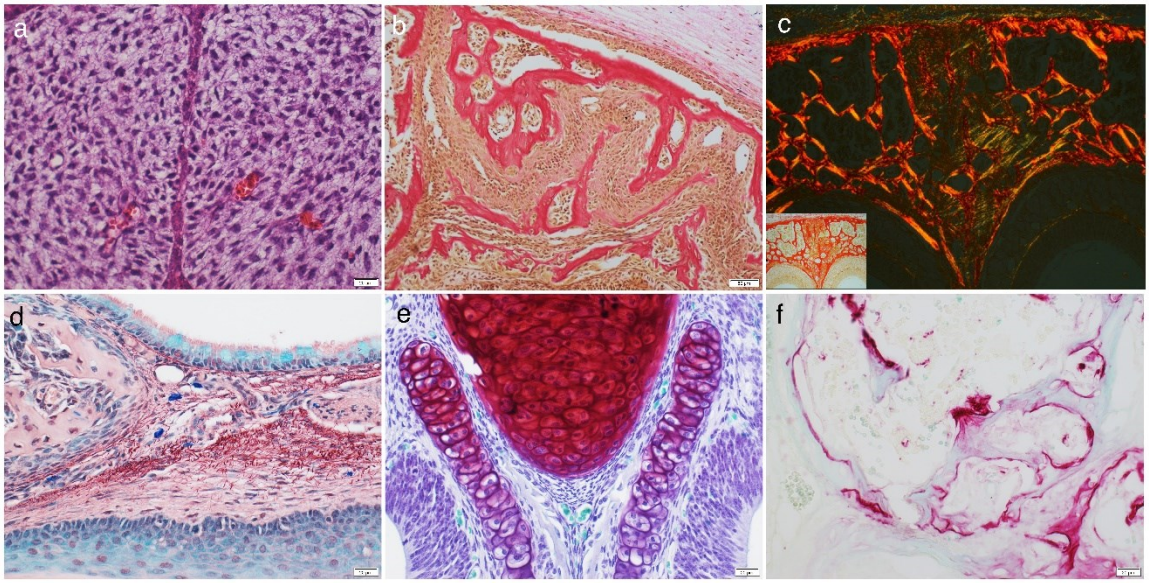

Figure A1.2 Example images of useful stains.
(a) Hematoxylin and eosin stain of epithelial seam in late palate development. Nuclei appear dark purple (hematoxylin), contrasted against a pink (eosin) cytoplasm and background structures. 400X magnification. (b) Van Gieson's stain of interdigitated fronto-maxillary suture, showing pink collagen fibers against yellow/brown nuclei and background structures. 200X magnification. (c) Picrosirius red stain of internasal suture in a 1-month-old mouse, under polarized light. Inset shows red appearance of collagen fibers with bright-field microscopy. 100X magnification. (d) Orcein stain of neonatal palate, exhibiting red-brown elastic fibers in the fusing shelf. Methylene blue counterstain. 400X magnification. (e) Safranin O stain of embryonic nasal septum junction with vomer. Note: deep orange staining chondrocytes counterstained with purple nuclear hematoxylin and faint Fast Green counterstain. 400X magnification. (f) Tartrate-resistant acid phosphatase (TRAP) stain of nasal bone marrow in a 2-week-old mouse. Osteoclasts, multinucleate bone-resorbing cells, stain violet as seen here lining faintly Fast Green-stained bone. 400X magnification

A1.3.4.5 Orcein

Orcein stain, derived from lichen, is used to reveal elastic fibers which stain reddish-brown against a light purple background (Fig. A1.2D) (Sheehan & Hrapchak, 1980). Counterstains can improve contrast; one such stain (methylene blue) is suggested here.

1. Deparaffinize and rehydrate slides.
2. Stain slides in orcein solution at 56ºC for 30 min. Sections should look red.
3. Differentiate in 1% acid alcohol until brown.
4. Wash in softly running water.
5. Counterstain with 1% methylene blue, dipping until nuclei are dark blue.
6. Dehydrate slides and mount with resinous mounting medium.

A1.3.4.6 Safranin O

A classic stain for cartilage, staining chondrocytes orange (Fig. 2e). Mucin will also stain orange with this stain [2]. A suggested counterstain described here is Fast Green, resulting in a pale green background color.

1. Deparaffinize and rehydrate slides.
2. Wash slides in the following solutions: 2 min hematoxylin and 5 min softly running water bath.
3. Rinse slides quickly with 1% acetic acid solution.
4. Wash slides in the following solutions: 5 min 0.1% safranin O solution and 5 min 0.02% Fast Green solution.
5. Dehydrate slides and mount with a resinous mounting medium.

A1.3.4.7 Tartrate-Resistant Acid Phosphatase (TRAP)

TRAP detects bone-resorbing osteoclasts, staining for tartrate-resistant acid phosphatase (Chappard et al., 1983). Multinucleated osteoclasts will appear violet against a pale green counterstain (Fig. A1.2F).

1. Mix fresh TRAP staining solution mix. Pour in a staining dish and prewarm to 37ºC in water bath.
2. Deparaffinize and rehydrate slides.
3. Place slides in prewarmed TRAP Staining Solution Mix and incubate at 37ºC for 40 min, or until control is developed and slightly overstained.
4. Rinse in distilled water.

5. Counterstain with 0.02% Fast Green, checking every 5 min under microscope for staining intensity. Rinse in distilled water.
6. Dehydrate slides and mount with a resinous mounting medium.

A1.3.4.8 Dehydration and Mounting

1. Dip slides in 95% ethanol three times.
2. Wash slides in the following solutions:

1 min	100% ethanol
1 min	100% ethanol
3 min	Xylene
3 min	Xylene

3. Mount coverslip using resinous mounting medium, pushing out any bubbles with a pair of forceps.

A1.5 Notes

1. Consider micro-computed tomography scanning to document hard-tissue morphology of your structure of interest prior to decalcification for histology. This allows correlation of sections throughout the skull using ortho slices or 3D reconstruction.
2. Soft tissue of the head can block penetration of fixative and decalcifying reagents. To maximize penetration, consider removing the tip of the snout, tongue, and/or eyes. Small incisions at the corners of the mouth can also help to open the oral cavity. Postnatal study of internal craniofacial structures often necessitates perfusion of the animal with 1X PBS followed by fixative, to reach deep areas and flush out air-filled cavities (Gage et al., 2012).
3. Our laboratory preserves craniofacial tissue with 4% PFA. However, alternative fixation solutions (e.g., 10% neutral buffered formalin or glutaraldehyde) are a possibility (Eltoum et al., 2001). Some stains are not compatible with certain fixatives, so it is important to check which biochemical properties are affected by the reagent in question. An extensive discussion of fixative/stain compatibility can be found in Jenkins and Burg 2010 (Jenkins & Burg, 2003). Note that over-fixation of tissue can cause shrinkage artifacts.
4. Our laboratory uses 0.5 M EDTA (pH 7.4) to decalcify our samples—a chelator which reacts with calcium (Skinner et al., 1997). Other options may be more practical based on decalcification times, integrity of tissue, or fixative. The

endpoint will depend on the decalcification agent; it is best to empirically determine an optimal time/protocol using extra samples before testing on experimental groups. We generally decalcify adult mouse skulls with EDTA up to 1 month, for roughly as long as the mouse was alive (e.g., 7 days for P7 skulls). For delicate structures, such as sutures, we err on the side of over-decalcification to preserve integrity during sectioning.

5. Depending on the microtome used, you may use different cassettes or embedding rings to mold your wax blocks. For example, our laboratory has the option of classic fully mechanical microtomes (Fig. A1.3C,D), which use white plastic embedding rings with metal embedding cassettes, or newer partially automated microtomes (Fig. A1.3A,B), which are designed for embedding using tissue cassettes themselves.

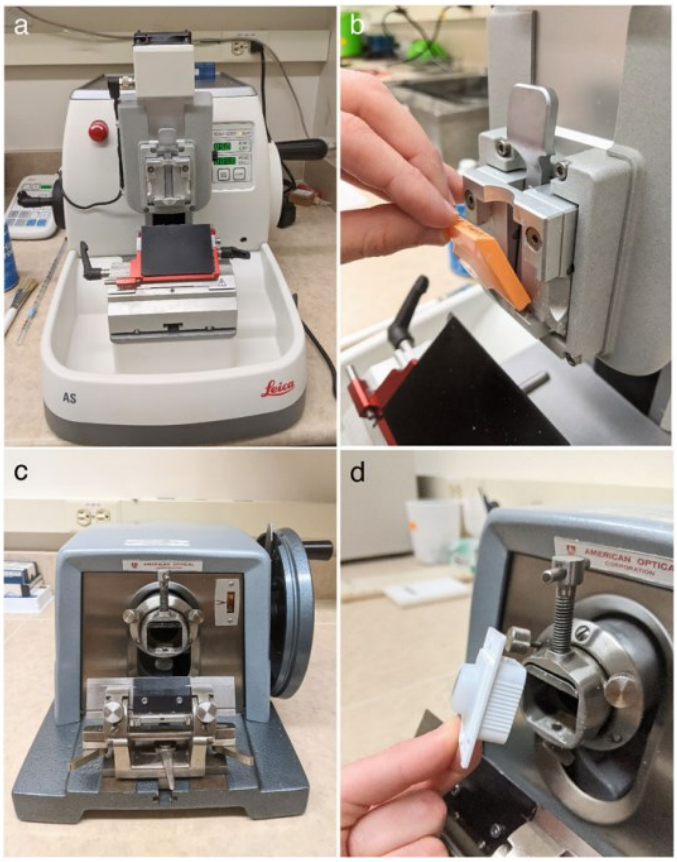

Figure A1.3 Microtome block mounting styles.
(a, b) Paraffin block attachment to automated microtome with clip. Note: design allowing attachment by orange tissue processing cassette. (c, d) Paraffin block attachment to manual microtome with screw clamp attachment, using white plastic embedding rings as anchor.

6. We only discuss paraffin embedding in this chapter, as it is effective for long-term storage, thin sectioning, and study of decalcified hard tissue. However, both cryopreservation and resin-embedding are options with individual benefits and limitations. Cryopreservation allows for study of fresh-frozen soft tissue, with good preservation of RNA and lipid content. To section hard, undecalcified bone, one must embed samples in resin and cut with a diamond-fortified blade. Both techniques require different equipment than paraffin sectioning and embedding.
7. We suggest creating a tissue block log with identifying numbers coded to more specific genotype, age, and orientation information. This is extremely helpful when taking into consideration the limited space for labeling on embedding rings and for effective navigation of a large paraffin block library.
8. Select the appropriate size of tissue processing cassette based on your sample. Tissue should be able to move freely within the cassette unless orientation must be preserved (e.g., sliced brain). For very small samples or to anchor pieces in place, a variety of processing papers or sponges can be used.
9. There are variations on quality and composition of paraffin wax, catering to different melting points or uses. Care must be taken to use the same type of paraffin in all steps. We recommend testing new paraffin brands thoroughly to avoid poor-quality blocks.
10. Orientation of the tissue at the time of embedding is critical to ensure a uniform plane of sectioning. While there is some flexibility on most microtomes to adjust the plane of section slightly, a poorly embedded block may not be salvageable through adjustment alone. Incorrect orientation of the tissue can be misleading, leading to misrepresentation of relative size or form. If a sample is embedded incorrectly, it can be returned to the hot wax bath to melt and re-embedded using the same technique.
11. Paraffin blocks can be stored long term at room temperature but are easier to section when cooled to 4ºC just before use.
12. Hot water bath temperature depends on the melting point of wax used for embedding. Our histology-grade paraffin works best if the water is around 50ºC.

Certain tissue types break down in hot water, so it is important to monitor the quality of sections after mounting and adjust accordingly.

13. It is of critical importance to adhere to a regular microtome maintenance schedule, keeping all parts associated with cutting clean and gears/internal machinery well lubricated.
14. Temperature of the block can influence the quality of sections being cut at this stage. If wax is wrinkling immediately after cutting, the block may need to be cooled more. We keep damp KimWipes on ice to cool the surface of the block for particularly difficult sections. The moisture can also improve flat sectioning of soft tissues, like brain.
15. Check slides periodically under a microscope for more subtle artifacts like knife marks, inconsistent thickness, or small bubbles (Taqi et al., 2018). If these problems arise, first check that the components of the microtome are tightened fully. Replace blades often, especially after cutting ossified structures. Bubbles and wrinkles can be avoided with deliberate handling of sections in and between water baths.
16. Kumar et al., 2012, (N. Kumar et al., 2012) suggest using a 1:15 ethanol and water solution for the cold bath to prevent wrinkles originating between water baths. This technique is very useful for soft tissue, like brain.
17. Deparaffinization and rehydration are only required for paraffin-embedded samples. If using cryosections, thaw first at room temperature and begin from water.
18. . Reagents for the stains described in this chapter can be reused many times. However, this means the user must be aware of the intensity of staining and alter the duration of washes if necessary. This may vary over time under different conditions. Hence, histology is a qualitative measure and must be treated as such—it is prudent to use multiple sections to confirm a suspicion about intensity or distribution of stain before drawing conclusions. It is highly recommended to use sample slides to first validate stains and optimize staining times, to spare experimental sections.
19. At this point, check slides under microscope for differentiation—nuclei should look bright blue and cytoplasm pearl gray. This is an important step after any major

staining component; if the stain is not intense enough, the wash should be repeated/ extended.

20. Agitate picrosirius red solution at least every 15 min during this wash, as the stain tends to settle and stain one end of slides more intensely. Shorter staining periods are not advised, as this protocol is optimized for near-equilibrium staining.
21. This step prevents an observed loss of stain that occurs if these slides are washed in regular water.
22. Note that the stains described in this chapter are for decalcified tissue. Stains like the Von Kossa stain detect calcium deposits, which would be eliminated with EDTA decalcification. Be aware of the intended target of each stain when selecting the best option.
23. Some fixatives interact with certain histochemical stains. Consult Scarano et al. 2010, (Scarano et al., 2003) for stain/fixative combinations to avoid this pitfall.
24. Stains ending in xylene clearing must be mounted with a xylene-compatible mounting medium, not aqueous.
25. We present our laboratory's choices for craniofacial histochemical stains. However, numerous stains exist to differentiate/ highlight the same structures. The following are suggested stains sorted by target:

    Collagen: Van Gieson's, Picrosirius red, Masson's Trichrome, Goldner's.

    Elastic fibers: Elastic van Gieson's, Orcein.

    Bone: Van Gieson's, Picrosirius red, Alizarin red, Toluidine blue, Von Kossa*.

    Cartilage: Safranin O, Alcian blue/PAS, Toluidine blue.

    Osteoclasts: Tartrate-resistant acid phosphatase.

        *stains for calcium deposits, so this stain is not compatible with decalcified tissues.